

Loughborough University  
Institutional Repository

---

*Electroless metallisation of  
glass for electrical  
interconnect applications*

This item was submitted to Loughborough University's Institutional Repository by the/an author.

**Additional Information:**

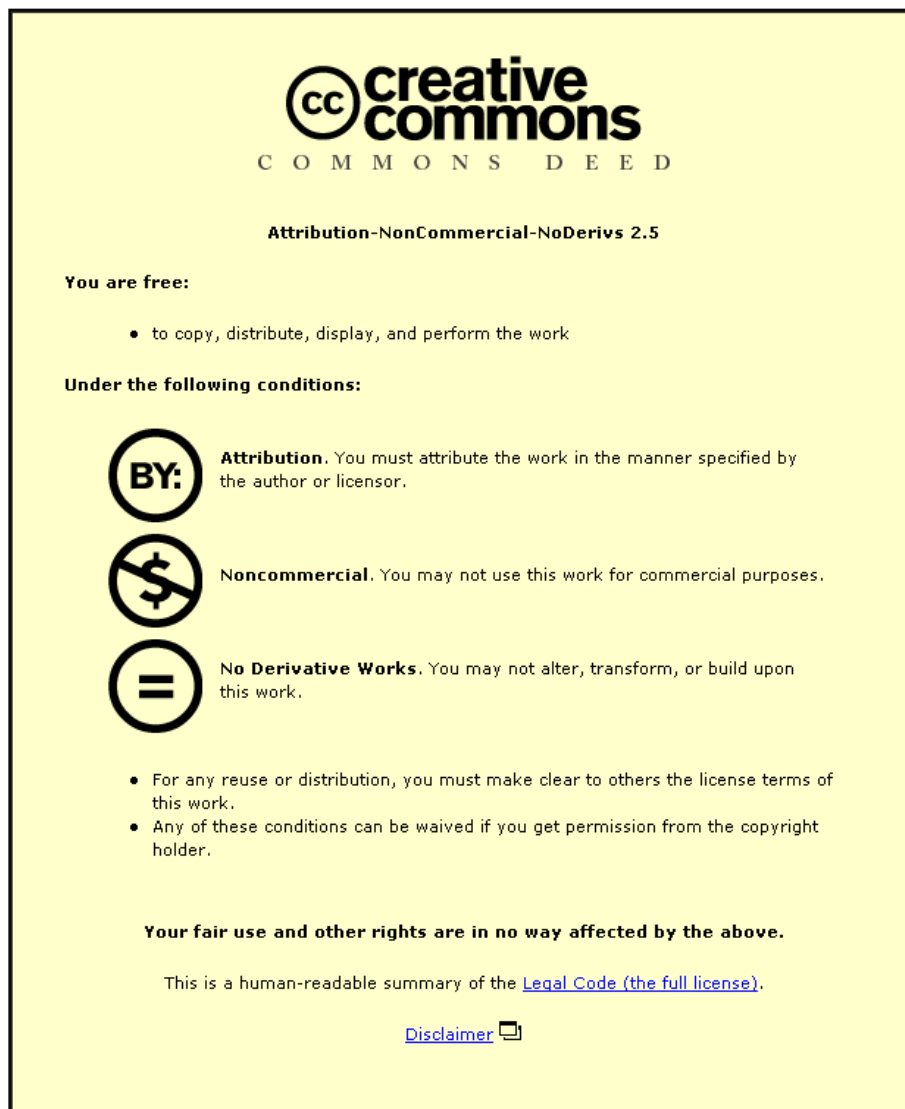
- A Doctoral Thesis. Submitted in partial fulfillment of the requirements for the award of Doctor of Philosophy of Loughborough University.

**Metadata Record:** <https://dspace.lboro.ac.uk/2134/10303>

**Publisher:** © Xiaoyun Cui

Please cite the published version.

This item was submitted to Loughborough University as a PhD thesis by the author and is made available in the Institutional Repository (<https://dspace.lboro.ac.uk/>) under the following Creative Commons Licence conditions.



For the full text of this licence, please go to:  
<http://creativecommons.org/licenses/by-nc-nd/2.5/>



# University Library

Author/Filing Title ..... *CU1, X* .....

.....  
Class Mark ..... *T* .....

**Please note that fines are charged on ALL  
overdue items.**

--	--	--

0403819768





# Electroless Metallisation of Glass for Electrical Interconnect Applications

A Dissertation Presented  
to the Engineering Faculty

By  
XIAOYUN CUI

In Partial Fulfilment of the Requirements for  
the Degree of Doctor of Philosophy in  
Loughborough University



Loughborough  
University  
Pilkington Library

Date 26/2/10

Class T

Acc  
No. 0403819768

## ABSTRACT

The microelectronics industry requires continuous advances due to ever-evolving technology and the corresponding need for higher density substrates with smaller features. Specifically, new dielectric materials with enhanced electrical properties are needed. At the same time, adhesion must be maintained in order to preserve package reliability and mechanical performance. As a result, this research investigates the use of thin glass sheets as an alternative substrate material as it offers a number of advantages including coefficient of thermal expansion similar to silicon, good dielectric properties and optical transparency to assist in the alignment of buried features. As part of this project it was necessary to deposit metallic coatings onto the glass sheets to create electrical tracks, pads and microvias. In order to meet these requirements, the metallisation of both smooth as received glass surfaces and surfaces roughened by laser machining using electroless copper and nickel deposition were investigated. This study resulted in a number of important conclusions about the roles of chemical bonding and mechanical anchoring in both the adhesion and catalyst adsorption, that are key factors in the electroless metallisation process.

Electroless copper and nickel were deposited on glass following several pre-treatment steps, including deposition of a silane self-assembled monolayer (SAM) and subsequent catalyst activation. The effect of the different process steps on the adhesion of the electroless coating to the substrate was investigated. It was found that 3-aminopropyltrimethoxy silane (APTS) treatment to form a SAM on the glass was effective for increasing both catalyst adsorption and adhesion across a range of preparation conditions. The end group of the APTS molecule interacted with the palladium catalyst particles to form strong chemical anchors between the glass surface and the catalyst without the need for high roughness. Analysis of the failure surfaces showed that the failure locus was at the interface between the catalyst and copper. The adhesion of electroless deposits on glass were characterised by qualitative tape peel tests and semi-quantitative scratch tests. The deposition conditions affected the film adhesion and for copper films thicker than 160 nm and NiP films greater than 740 nm the adhesion was not sufficient to pass a tape test. The

different stages of the deposition process were studied using X-ray Photoelectron Spectroscopy (XPS) and Static Secondary Ion Mass Spectrometry (SSIMS) to reveal the structures formed and the behaviour of the catalyst. In addition, the effect of process parameters on the internal film stress was determined by substrate curvature measurements.

In order to deposit thicker films with good adhesion, not only chemical anchors but mechanical anchoring needed to be provided. Glass substrates were excimer laser machined to roughen the surface before metallisation. This process was found to be effective on the glass material with electroless Cu films to 1.5  $\mu\text{m}$  and NiP films to 3.7  $\mu\text{m}$  obtained that passed the tape peel test. For roughened grooves, the Cu thickness could be further built to 8-10  $\mu\text{m}$  by means of Cu electroplating. Finally, combining laser machining with electroless deposition, a novel method to create circuit patterns on glass was demonstrated.

**Key words:** Glass substrate; Electroless copper deposition; Electroless nickel deposition; Thin film adhesion; Micro-mechanical properties; Scratch test; Laser machining;



## ACKNOWLEDGEMENTS

This research was carried out in the Wolfson School of Mechanical and Manufacturing Engineering, Loughborough University. I wish to express my sincere gratitude to my supervisor, Dr David Hutt, who introduced me to the project and who always had time for discussions and gave me invaluable tuition. Also, my second supervisor, Professor Paul Conway, deserves my best compliments because of his encouragement and advice in my work.

There are many people who have made contributions to this work through their direction and support. Mr Andy Sandaver was heavily involved in training and sample preparation for SEM and AFM analysis used in this project, and he deserves my sincere gratitude for helping me with the techniques and fundamentals associated with these measurement tools. Dr Geoff West and Mr John Bates helped with the ion machining of samples by FIB and their subsequent TEM observation. The assistance of Mr Dave Hall for XPS analysis has been of indispensable help. I would like to thank my colleagues, Deepa Bhatt and Fuad Khoshnaw for their cooperation within this project as they were available throughout for discussions and guidance. I would like to extend my appreciation to the University of Nottingham for providing free ToF-SIMS analysis, specifically to Dr David Scurr for his assistance and great patience. I also wish to recognize the other members of the Interconnection Group for graciously lending their expertise on a number of subjects and for keeping the mood around the labs light and enjoyable.

The financial support of the Engineering and Physical Sciences Research Council through the Innovative *Electronics* Manufacturing Research Centre is gratefully acknowledged, as is the technical support of Qioptiq and GE Aviation Systems.

Finally, I would like to thank my parents, for their constant love and support. It has only been with their support and love that I have made it through this period.

---

## Table of contents

---

ABSTRACT .....	ii
ACKNOWLEDGEMENTS .....	iv
Table of contents .....	v
List of tables .....	viii
List of figures .....	x
Glossary .....	xv
Chapter 1 Glass as a Substrate for Printed Circuit Board Manufacture.....	1
1.1 Introduction .....	1
1.2 Limitation of traditional substrate materials.....	2
1.3 Glass as a substrate material.....	4
1.4 Research background.....	6
1.4.1 Selection of deposition material .....	7
1.4.2 Selection of deposition method .....	8
1.5 Research methodology .....	13
Chapter 2 Electroless Cu Deposition Characterisation .....	15
2.1 Introduction .....	15
2.2 Literature survey.....	16
2.2.1 Cu-EDTA-HCHO electroless plating mechanism.....	16
2.2.2 The rate of deposition .....	18
2.2.3 Surface activation .....	19
2.3 Methodology and experimental procedures .....	23
2.3.1 Materials .....	23
2.3.2 Analysis techniques .....	24
2.3.3 Deposition process.....	28
2.4 Results .....	31
2.4.1 Deposition rate.....	31
2.4.2 Appearance of electroless Cu deposits .....	34

2.4.3 Crystal structure and microstructure .....	35
2.4.4 Electrical properties.....	40
2.5 Discussion.....	43
2.6 Conclusion.....	48
Chapter 3 Electroless NiP Deposition Characterisation.....	49
3.1 Introduction .....	49
3.2 Literature survey.....	49
3.2.1 Electroless Nickel (EN) plating mechanism.....	49
3.2.2 Deposition rate and phosphorous content.....	51
3.3 Experimental.....	54
3.3.1 Material.....	54
3.3.2 Electroless NiP process .....	55
3.4 Results and discussion.....	55
3.4.1 Deposition rate and alloy composition .....	55
3.4.2 Microstructure of NiP deposits.....	57
3.4.3 Electrical properties.....	60
3.5 Conclusion.....	61
Chapter 4 Interfacial Adhesion of Electroless Cu and NiP to Glass.....	62
4.1 Introduction .....	62
4.2 Literature review of thin film adhesion.....	63
4.2.1 Introduction .....	63
4.2.2 Adhesion improvement .....	63
4.2.3 Adhesion measurement techniques .....	68
4.3 Methodology and experimental procedure.....	70
4.4 Results and discussion.....	72
4.4.1 Surface analysis of electroless deposition on glass .....	72
4.4.2 Tape test results .....	89
4.4.3 Adhesion failure analysis .....	90
4.4.4 Adhesion between electroless NiP and glass substrate .....	100
4.5 Conclusion.....	103
Chapter 5 Internal Stresses and Mechanical Properties of Cu and NiP Films .....	104
5.1 Introduction .....	104
5.2 Literature survey.....	105
5.2.1 Thin film stress measurement.....	105

5.2.2 Nanoindentation testing.....	107
5.2.3 Scratch testing .....	109
5.3 Methodology and experimental .....	110
5.4 Results .....	112
5.4.1 Internal stress measurement .....	112
5.4.2 Mechanical properties .....	115
5.4.3 Scratch test.....	119
5.5 Discussion.....	124
5.6 Conclusion.....	125
Chapter 6 Catalytic Surface Structure Effects on Electroless Cu plating .....	127
6.1 Introduction .....	127
6.2 Literature review .....	127
6.2.1 Pd based catalysts.....	127
6.2.2 Non-Pd catalysts.....	130
6.3 Methodology and experimental procedures .....	131
6.4 Results .....	132
6.4.1 XPS of catalytic surfaces.....	132
6.4.2 SEM of catalytic surfaces.....	136
6.4.3 TEM observations .....	140
6.4.4 SIMS analysis.....	146
6.5 Discussion.....	156
6.6 Conclusion.....	160
Chapter 7 Metallisation of Laser Machined Glass.....	161
7.1 Introduction .....	161
7.2 Literature review .....	162
7.3 Methodology and Experimental .....	164
7.4 Results and Discussion.....	167
7.4.1 Electroless Cu on tracks and holes .....	167
7.4.2 Further electroplating of Cu on tracks and holes.....	171
7.4.3 Circuit pattern formation .....	174
7.5 Conclusion.....	177
Chapter 8 Conclusion.....	178
References .....	180

---

## List of tables

---

Table 1-1 Basic physical properties for commonly used electronics packaging materials .....	4
Table 1-2 Dielectric properties of different materials .....	5
Table 1-3 Main characteristics of metal films deposited by various techniques.....	11
Table 1-4 Properties of Cu films grown using various techniques .....	12
Table 2-1 Lists of various processes for promoting adhesion of electroless Cu.....	21
Table 2-2 List of Materials and Suppliers .....	24
Table 2-3 Comparison of thickness measurements from Zygo and FIBSEM.....	28
Table 2-4 Experimental process conditions for electroless Cu deposition on glass....	29
Table 2-5 Cu brightness and appearance for different deposition temperatures .....	35
Table 2-6 Joint Committee Powder Diffraction Standards (JCPDS) card for Cu .....	36
Table 2-7 The roughness of different thickness Cu coatings .....	39
Table 3-1 List of materials and suppliers .....	54
Table 3-2 Electroless NiP process route.....	55
Table 3-3 The roughness of different thickness NiP coatings.....	59
Table 4-1 Evolution of some typical silanes coupled onto glass substrates.....	66
Table 4-2 Methods to determine adhesion .....	69
Table 4-3 Contact angle measurement results.....	73
Table 4-4 Surface chemical compositions (at.%) of glass samples following each pre-treatment step.....	85
Table 4-5 Surface compositions (at.%) after different electroless Cu deposition times .....	88
Table 4-6 Tape peel test results for Cu films on glass substrate .....	89
Table 4-7 Tape test results of electroless NiP on glass substrate.....	100
Table 6-1 Examples of Pd based catalysts in electroless deposition.....	129
Table 6-2 Ratios of elemental compositions for different catalyst immersion times	134
Table 6-3 Isotope cluster of Pd and Sn.....	147
Table 6-4 Surface analysis results obtained from SIMS spectra.....	155

Table 7-1 Compositions of typical Cu electroplating baths with various additives .	164
Table 7-2 Compositions and operating conditions of Cu electroplating bath .....	166
Table 7-3 Electroplated Cu thickness on laser machined holes .....	173

---

## List of figures

---

Figure 1-1 Electrical interconnect glass PCB.....	6
Figure 1-2 A suggested route for glass PCB manufacture .....	6
Figure 2-1 Schematic representation of thickness measurement using the Zygo .....	26
Figure 2-2 Example Zygo interferometer image used to determine the thickness of the Cu film on glass .....	26
Figure 2-3 FIBSEM image of cross-section of Cu coating on glass .....	27
Figure 2-4 Process route used for electroless Cu deposition process.....	30
Figure 2-5 Cu thickness as a function of deposition temperature .....	31
Figure 2-6 Cu thickness as a function of deposition time at 40°C .....	32
Figure 2-7 Cu thickness change with different bath aging time.....	33
Figure 2-8 XRD of the electroless deposited Cu on glass substrate.....	35
Figure 2-9 SEM and AFM images of electroless Cu deposits on glass for different plating times: (A) 0.5 min, (B) 1 min, (C) 3 min, (D) 5 min, (E) 25 min.	38
Figure 2-10 The relationship between Cu particle size and film roughness as a function of deposition temperature .....	40
Figure 2-11 Schematic diagram of Four-Point Probe measurement method .....	41
Figure 2-12 Cu resistivity as a function of film thickness, d.....	42
Figure 2-13 Schematic diagram of the Volmer-Weber mode film growth .....	45
Figure 3-1 Schematic diagram of the nickel (II) reduction and hypophosphite oxidation process .....	50
Figure 3-2 Phosphorus content in the NiP electroless film obtained in a wide range of pH adjusted with NH <sub>4</sub> OH .....	52
Figure 3-3 Dependence of deposition rate on bath temperature.....	56
Figure 3-4 NiP thickness as a function of deposition time at 70°C.....	57
Figure 3-5 SEM and AFM images of electroless NiP deposits on glass with different plating time: (A) 30 sec, (B) 3 min, (C) 5 min, (D) 25 min .....	58

Figure 3-6 NiP film resistivity as a function of thickness .....	60
Figure 4-1 Schematic constituents of a SAM-molecule.....	65
Figure 4-2 The reaction of APTS with the surface of glass .....	67
Figure 4-3 Schematic representation of the tape test.....	70
Figure 4-4 Water contact angle as a function of immersion time in the APTS solution .....	73
Figure 4-5 XPS spectra of glass surface (A) as-received, (B) after cleaning with Decon 90 for 8 hours .....	74
Figure 4-6 XPS spectra of the glass surface after immersion in APTS solution for (A) 0.5 hour (B) 1 hour (C) 24 hours .....	76
Figure 4-7 Variation in the surface concentration with APTS treatment .....	77
Figure 4-8 XPS C 1s peak for (A) clean glass, and clean glass modified by APTS immersion for (B) 0.5 h, (C) 1 h, (D) 24 h .....	80
Figure 4-9 XPS O 1s peak for (A) clean glass, and clean glass modified by APTS immersion for (B) 0.5 h, (C) 1 h, (D) 24 h .....	81
Figure 4-10 XPS Si 2p peak for (A) clean glass, and clean glass modified by APTS immersion for (B) 0.5 h, (C) 1 h, (D) 24 h .....	83
Figure 4-11 XPS spectrum of glass surface after pre-dip.....	83
Figure 4-12 XPS spectrum of catalytic glass surface .....	84
Figure 4-13 O 1s level XPS spectra for (A) glass surface before Sn/Pd treatment (B) after 2 min Sn/Pd treatment (C) after 8 min Sn/Pd treatment.....	86
Figure 4-14 Sn core level XPS spectrum on glass after 2 min catalyst treatment.....	87
Figure 4-15 General scan (A) and core level scan (B) of electroless Cu .....	88
Figure 4-16 XPS wide scans of the delaminated surfaces (A) delaminated glass surface (B) Cu on adhesive tape .....	91
Figure 4-17 XPS core level scans of the delaminated glass surface (A) Cu, (B) Pd, (C) Sn .....	92
Figure 4-18 XPS core level scans of the delaminated Cu on adhesive tape (A) Pd, (B) Sn .....	93
Figure 4-19 Diagram of locus of failure of electroless Cu on glass substrate.....	94
Figure 4-20 Corresponding Cu 2p, Cu 2p <sub>3/2</sub> core-levels for (A) original,.....	95
Figure 4-21 C 1s and O 1s core-level spectra of two Cu coatings .....	97
Figure 4-22 SEM images of (A) delaminated glass surface, (B) delaminated Cu surface.....	98



Figure 4-23 SEM images of Cu deposited following different catalyst immersion times after peeling off on adhesive tape .....	99
Figure 4-24 XPS general scans of (A) delaminated glass surface and (B) NiP film on adhesive .....	102
Figure 4-25 SEM image of NiP film on adhesive tape .....	102
Figure 5-1 Load-displacement curve after Briscoe .....	107
Figure 5-2 Schematic diagram of the various scratch test failure modes as a function of coating and substrate hardness ( $H_c$ and $H_s$ , respectively) [136].....	110
Figure 5-3 Curvature measurement of different thickness Cu films deposited on glass .....	112
Figure 5-4 Radius calculation from curvature measurement .....	112
Figure 5-5 Internal stress as a function of electroless Cu thickness.....	113
Figure 5-6 Internal stress as a function of electroless NiP thickness .....	114
Figure 5-7 The force–displacement curves for different thickness NiP films.....	116
Figure 5-8 Hardness distribution as a function of the indentation depth into electroless NiP coatings.....	116
Figure 5-9 The relationship between electroless NiP thickness and Elastic Modulus and hardness.....	117
Figure 5-10 Correlation between elastic modulus, hardness and internal stresses for NiP film .....	118
Figure 5-11 The force–displacement curves for electroless Cu films.....	119
Figure 5-12 Scratch test curves for electroless Cu film .....	120
Figure 5-13 Optical microscopy images of scratched grooves with different loading rates on electroless Cu film (A) 0.5 mN/s, (B) 1 mN/s .....	121
Figure 5-14 AFM section analysis on scratched groove .....	121
Figure 5-15 Critical load as a function of electroless Cu thickness .....	122
Figure 5-16 Scratch test curves for electroless NiP film.....	122
Figure 5-17 Optical micrograph of scratch groove on NiP film .....	123
Figure 5-18 Critical load as a function of NiP thickness.....	123
Figure 6-1 Pd 3d and Sn 3d XPS core-level spectra of the activated substrate for (A) 30 sec (B) 2 min (C) 8 min exposure to the catalyst solution.....	133
Figure 6-2 Pd 3d, Sn 3d XPS core-level spectra after electroless Cu solution exposure for (A) 15 sec (B) 1 min .....	135

Figure 6-3 SEM images of the catalytic surface with different immersion time (A) 30 sec (B,C) 2 min (D,E) 8 min in the catalyst solution.....	137
Figure 6-4 SEM images of the cross-section (left) and plan view (right) of electroless Cu deposited on glass with different catalyst immersion time: (A) 0.5 min (B) 2 min (C) 8 min. ....	139
Figure 6-5 Catalyst immersion time effect on Cu deposition thickness.....	139
Figure 6-6 SEM images of FIB machined TEM sample (A) FIB machined TEM sample adhered to grid, (B) Final thinning of the TEM sample,(C) Finished TEM sample .....	141
Figure 6-7 TEM micrographs of electroless Cu deposited on glass with different catalyst immersion times: (A) 0.5 min, (B) 2 min, (C) 8 min .....	143
Figure 6-8 TEM micrographs and EDX spectra for electroless Cu deposited on glass with different catalyst exposure times: (A) 2 min and (B) 8 min .....	145
Figure 6-9 SIMS spectra of glass surfaces before (A,B) and after (C,D) catalyst steps .....	149
Figure 6-10 Negative ion SIMS spectra of glass surfaces following catalytic step durations of (A) 0.5 min, (B) 2 min, (C) 8 min .....	150
Figure 6-11 Positive ion SIMS of glass surfaces following catalytic step durations of (A) 0.5 min, (B) 2 min, (C) 8 min .....	151
Figure 6-12 The $PdNH^+$ and $SnNH^+$ intensity as a function of catalyst immersion time .....	152
Figure 6-13 Negative and positive ion SIMS spectra of the surface after electroless Cu solution exposure for 15 sec .....	153
Figure 6-14 Positive ion and negative ion spectra for the delaminated glass surface.....	154
Figure 6-15 Schematic diagram of different catalytic structure surfaces.....	157
Figure 6-16 Schematic diagram showing different catalytic surface structures after activation in the electroless Cu bath for a short time (e.g. 15 sec).....	159
Figure 7-1 Schematic diagram showing the main parts of a simple Cu electroplating process .....	165
Figure 7-2 Process flow diagram of electrodeposition of Cu on laser machined glass .....	166
Figure 7-3 Diagram of laser machined groove.....	167

Figure 7-4 Optical microscope image (A) and SEM image (B) of electroless Cu deposited on a groove machined in glass .....	168
Figure 7-5 SEM micrograph of Cu deposited on the laser machined groove and wall (A) view of side wall (B) plan view .....	169
Figure 7-6 Optical and SEM image of electroless Cu metallised through hole (A) and (B,C) blind apertures .....	170
Figure 7-7 Electroless Cu deposition process flow for laser machined glass .....	171
Figure 7-8 Optical microscope images of a cross section through electroplated Cu on a track.....	172
Figure 7-9 Optical microscope images (A,B) and SEM micrographs (C, D) of a via metallised with electroless and electroplated Cu.....	174
Figure 7-10 Process flow diagram showing the fabrication of a Cu or NiP pattern .	175
Figure 7-11 Circuit pattern created using proposed technique and surface morphology .....	176
Figure 7-12 Surface profile of electroless Cu deposited on grooves in glass .....	176

---

## Glossary

---

3DASSM	3D All Silicon System Module
AFM	Atomic Force Microscopy
APCVD	Atmospheric Pressure Chemical Vapour Deposition
APTS	Aminopropyltrimethoxy Silane
ASTM	American Society for Testing and Materials
CA	Contact Angle
CEM	Composite Epoxy Material
CTE	Coefficient of Thermal Expansion
CVD	Chemical Vapour Deposition
DCMS	DC Magnetron Sputtering
DMAB	Dimethylamine Borane
EDTA	Ethylenediaminetetraacetic Acid
EDX	Energy Dispersive X-ray
ELD	Electroless Deposition
EMC	Electro Magnetic Compatibility
EMI	Electromagnetic Interference
EN	Electroless Nickel
EP	Electroplating
FCC	Face Centred Cubic
FIB	Focused Ion Beam
FIBSEM	Focused Ion Beam Scanning Electron Microscopy
FR4	Glass Fibre Epoxy
FWHM	Full Width At Half Maximum
HCHO	Formaldehyde
IBD	Ion Beam Deposition
IC	Integrated Circuit

ICDD	International Centre for Diffraction Data
JCPDS	Joint Committee Powder Diffraction Standards
JGB	Janus Green B
MEMS	Micro-Electro-Mechanical Systems
MOCVD	Metal-Organic Chemical Vapour Deposition
MPTS	Mercaptopropyltrimethoxy Silane
PAMOCVD	Photo Assisted Metal Organic Chemical Vapour Deposition
PCB	Printed Circuit Board
PECVD	Plasma-Enhanced Chemical Vapour Deposition
PEG	Polyethylene Glycol
PLD	Pulse Laser Deposition
PVD	Physical Vapour Deposition
RIE	Reactive Ion Etching
RMS	Root Mean Square
R.T.	Room Temperature
SAM	Self-Assembled Monolayer
SBU <sub>s</sub>	Sequential Build-Up Structures
SCE	Saturated Calomel Electrode
SEM	Scanning Electron Microscopy
SIMS	Secondary Ion Mass Spectrometry
SPS	Bis (3-sulfopropyl) disulfidedisodium
SSIMS	Static Secondary Ion Mass Spectrometry
TEM	Transmission Electron Microscope
TEOS	Ta <sub>2</sub> N <sub>5</sub> /Tetraethylorthosilicate-Oxide/Si
ToF-SIMS	Time of Flight Secondary Ion Mass Spectrum
TU	Thiourea
UBM	Under Bump Metallisation
ULSI	Ultra Large Scale Integration
VTES	Vinyltriethoxysilane
XPS	X-ray Photoelectron Spectroscopy
XRD	X-ray Diffraction
<i>R</i>	Radius of curvature of the specimen after deposition
<i>R</i> <sub>0</sub>	Radius of curvature before deposition
<i>E</i>	Young's modulus

$\nu$	Poisson's ratio
$\sigma$	Internal stress in the thin film
$\rho$	Electrical Resistivity
$t$	Thickness
$\alpha$	Thermal Expansion coefficient

---

# Chapter 1 Glass as a Substrate for Printed Circuit Board Manufacture

---

## **1.1 Introduction**

To meet the increasing demands of advanced electronic products, higher levels of integration of electronic devices are being developed and employed, which is leading to a reduction in package size, but with more and more input/output connections. As a result, in the development of packaging of electronics, the aim is to lower cost, increase the packaging density and improve the performance, while still maintaining or even improving the reliability of the circuits [1, 2].

The concept of flip-chip technology where the semiconductor chip is assembled face down onto the circuit board is ideal for size considerations, as there is no extra area needed for contact outside the component. The performance in high frequency applications is superior to other interconnection methods because the length of the connection path is minimised [3, 4]. A common feature of the joined structures is that the chip is lying face down to the substrate and the connections between the chip and the substrate are made using bumps of electrically conducting material. There are different types of flip chip joints such as solder bump, Au bump, anisotropic conductive adhesive and nonconductive adhesive [5]. However, while flip chip technology is attractive, there is only one level of connection between the chip and the substrate material and this means that the substrate must have features of matching size to the Si chip. This places pressure on the Printed Circuit Board (PCB) manufacturing process.

With increased demand for high data transmission rates in devices, the data transmission speed for electrical circuits is reaching the physical limit for which electro magnetic compatibility (EMC) can be properly controlled [6]. Despite this, the market is still endlessly pursuing smaller, faster, and cheaper products. To make the system smaller and more powerful, low power components and faster devices with smaller footprint and less I/Os are needed [7]. Higher data transmission rates require more parallel I/Os. More I/Os are not compatible with smaller devices.

Based on the analysis above, it would be very difficult to solve all the problems of more advanced technology introduction based on current architectures, because the solutions to each problem drive the technology in opposite directions and conflict with each other. It has already been shown that light as a signal carrier can overcome the disadvantages of electrical transmission in terms of speed and bandwidth with low electromagnetic interference (EMI) [1, 8]. Optical technologies have already been widely employed and shown excellent performance in the communication industry as optical fibres. Extending the idea to PCB level technology, the problems for further advances could be solved by taking advantage of high speed, wide bandwidth and low EMI of optical transmission, leading to reduced I/Os by relying more on high speed serial communication structures. Again, this requires the introduction of new materials and processes into the PCB manufacturing process.

### ***1.2 Limitation of traditional substrate materials***

As electronics manufacturers strive for smaller, faster, more environmentally friendly products, the limits of current manufacturing methods for printed circuit boards (substrates) are being reached. Manufacture using traditional FR4 (glass fibre epoxy composite) or CEM (Composite Epoxy Material) substrates is increasingly difficult, costly and wasteful, as the size of electrical connections on the circuit board becomes comparable to the silicon chip [6]. To meet some of these demands, at the board and package level, sequential build-up structures (SBUs) with alternating dielectric and copper layers and microvias have been integrated into the manufacture of substrates as one means of achieving high density interconnections [4]. However, there are still limitations due to the underlying substrate which is often FR4. Many of these manufacturing difficulties arise from the material properties of the substrate: in order



to meet the requirements of advanced flip chip devices a number of properties are required.

Coefficient of Thermal Expansion (CTE) is one of the most important parameters for a PCB as a mismatch between substrate and components can lead to failure. This is particularly an issue for flip-chip devices where any mismatch can lead to rapid fatigue failure of the small interconnects [3, 9]. Ideally the substrate CTE should be close to that of semiconductor materials, such as silicon or GaAs to minimise this issue. Also, during the manufacturing processes, different temperatures are experienced that can cause misalignment and stress build up. The expansion rate of most circuit board materials increases remarkably when measured at temperatures in excess of the glass transition temperature [5]. Ideally, the expansion of a circuit board material and copper would also not differ significantly. Plated through hole failures during exposure to thermal extremes are a significant risk when the substrate material versus copper Z-axis CTE differential is large [1]. The move to lead free solder materials with higher reflow temperatures is also a concern and leads to more significant stresses between the copper plated vias and glass fibre epoxy materials in multilayer boards.

As mentioned above, input/output connections are growing in number, while the devices must be made smaller in order to satisfy the requirements of consumer markets, therefore, devices with smaller and smaller pin pitches in line with finer bond pad pitches on the components are desired by industry. Current FR4 substrates can support fine pitch (<25  $\mu\text{m}$  track and gap) Cu tracks manufactured using high performance resists and laser imaging [10]. However, the dimensional stability of FR4 during manufacturing is insufficient to provide accurate registration when routing micro-vias to buried capture pads in multilayer boards. Misalignment errors increase towards the edges and corners of large panels reducing the working area. As a result of this, while microvias as small as 50  $\mu\text{m}$  in diameter can be machined using laser techniques, capture pads two or three times this size are often needed to avoid breakout which limits the pitch of the pads that can be achieved [11].

Finally, with the application of more and more powerful devices, thermal management is also becoming very critical during the design of the system. As a very

important and main channel to dissipate heat, the PCB is critical to the system stability and device reliability. However, normal FR4 material is poor in thermal conductivity ( $0.2\text{W/m}\cdot\text{K}$ ) [12], and in various applications with high power devices results in complicated thermal management problems.

### 1.3 Glass as a substrate material

Basic properties of some common electronics packaging materials are summarized in Table 1-1.

**Table 1-1 Basic physical properties for commonly used electronics packaging materials [13]**

Raw Material	Density ( $\text{g/cm}^3$ )	Thermal Conductivity ( $\text{W/m}\cdot\text{K}$ )	CTE ( $10^{-6}/^{\circ}\text{C}$ )
FR4	1.80	0.2	x,y-axis 13-18 z-axis 100-170
Polyimide	1.70	0.3	17
Copper	8.92	385.0	17
Aluminium	2.7	240.0	24
Glasses	2.1-3.0	1.05	3-10
Silicon	2.33	149	2.6-3

As described above, to meet the requirements of advanced packages based on flip chip technology, the substrate should have low CTE, high thermal conductivity, high dimensional stability and good dielectric properties. Many of these requirements are delivered by Si and much work is underway to investigate this as part of the 3D All Silicon System Module (3DASSM) research programme [14]. However, a key issue with Si is that it is not able to carry optical signals and is also electrically conductive such that insulating layers must be grown before use. A potential new substrate material capable of carrying both optical signals and electrically conducting copper tracks is glass, for which there are a number of advantages:

1. The manufacturing processes for glass sheets are fully mature to support the technical requirements, further advances and production volumes.
2. The dielectric constant of glass and low loss tangent is suitable for high frequency applications [15]. Table 1-2 indicates that the dielectric constant of glass could be comparable to that of FR4 and in some cases, could be even better.
3. Glass is very suitable for accurate via machining using optical recognition of buried features.
4. Glass is one of the most stable materials in terms of moisture absorption, aging, and electrical properties, which means that glass could support a more stable electrical performance and enable accurate feature registration during manufacture.
5. The CTE of certain glasses is very close to that of silicon for reduced flip chip joint stress, which is a key point for enabling its use in high density IC packaging technology.
6. Glass shows good thermal conductivity ( $\geq 1\text{W/m}\cdot\text{K}$ ) compared with most non-metallic materials, although it is very poor compared to silicon [12].

**Table 1-2 Dielectric properties of different materials [15]**

Substance	Dielectric Constant (relative)	Loss Tangent
FR-4 (G-10) - low resin	4.9	0.008 @ 100 MHz
- high resin	4.2	0.008 @ 3 GHz
Fused quartz	3.8	0.0002 @ 100 MHz 0.00006 @ 3 GHz
Fused silica (glass)	3.8	
Gallium Arsenide (GaAs)	13.1	0.0016 @ 10 GHz
Germanium	16	
Glass	4 - 10	
Glass (Corning 7059)	5.75	0.0036 @ 10 GHz
Pyrex glass (Corning 7740)	5.1	
Silicon	11.7 - 12.9	0.005 @ 1 GHz 0.015 @ 10 GHz

## 1.4 Research background

Based on the above, a research project was established to investigate glass as a substrate material. The overall aim of the project was to use thin (50-100  $\mu\text{m}$  thick) CMZ glass sheets to manufacture multilayer substrates able to support high density electrical and optical interconnect (CMZ glass is a commercially available glass from Qioptiq company and was chosen due to its close CTE match to Si)[9, 16]. The concept of this new PCB was to produce substrates upon which flip-chip components may be assembled as shown schematically in Figure 1-1.

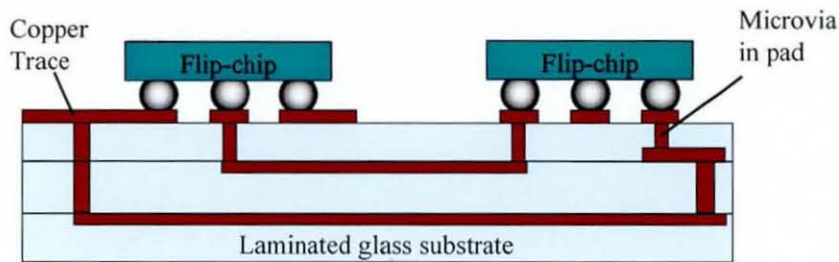


Figure 1-1 Electrical interconnect glass PCB

Figure 1-2 shows a suggested route for the production of a multilayer structure in glass for electrical interconnect.

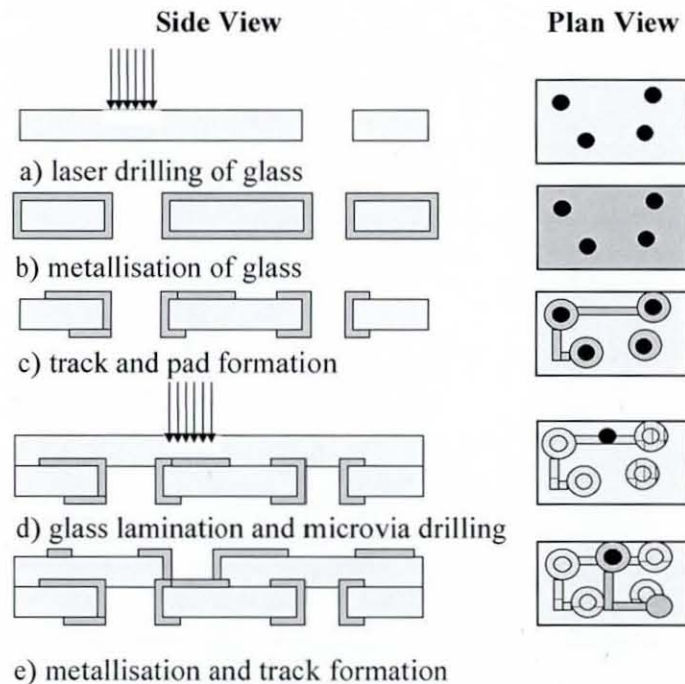


Figure 1-2 A suggested route for glass PCB manufacture

In this process, a laser is employed to machine the tracks and microvias in the glass which is then metallised to produce electrical connections. Layers of glass are laminated together to form multilayer substrates. In order to fulfil this overall objective, three areas of research were necessary: laser machining, glass metallisation and lamination. Within the larger project, each area was investigated by a different PhD student. The work reported in this thesis investigates the metal deposition on glass substrate materials. The main challenge of glass metallisation is to obtain a strong bond between the metallic coating and smooth glass surface, as the adhesion strength is critical for interconnect reliability. In addition, excimer laser machined grooves and micro vias also need to be coated and filled with metal efficiently.

### ***1.4.1 Selection of deposition material***

Initially a suitable material to form the conductive tracks on glass needed to be chosen. Aluminium and its alloys were the standard choice for metallisation in integrated circuits for many years [17, 18]. There are, however, limitations in the use of Al as the interconnect metal, especially used as the conductive layer on a substrate. The relatively low melting temperature of aluminium, in conjunction with its susceptibility to failure processes such as stress-voiding and electromigration, pose uncertainties about the mechanical integrity of aluminium lines, especially lines decreased to micron scales [19]. In addition, the high electrical resistance and low resistance to migration are also not attractive for glass substrate metallisation.

Copper has a lower electrical resistivity and higher melting point than aluminium and, for the same electrical design, it is expected to function as effectively as an aluminium interconnect with roughly double the cross sectional dimensions. It is highly solderable and there is a significant infrastructure for both electroless and electroplating deposition following its widespread use in PCB manufacture [20]. Research into advanced copper interconnect indicates superior performance and reliability of copper, particularly in the context of failure due to stress-voiding and electromigration [21, 22]. Despite these advantages, copper interconnect technology for glass has drawbacks: copper does not adhere well to silicon dioxide and diffuses rapidly into silicon.

Nickel coating has attracted a great deal of interest from the electronics industry and the research community due to its unique characteristics such as its higher thermal stability, corrosion resistance, solderability, magnetic and electrical properties [23, 24]. Similarly to copper it can be easily deposited by electroless and electroplating methods. Ni coating also produces a smooth surface, which is ideal for optical reflectance, and it is already widely used in integrated circuit (IC) interconnections [25, 26], micro-electro-mechanical systems (MEMS) and PCBs [27, 28]. Electroless nickel deposits provide very good protection against corrosion [23], have high abrasion resistance, and have good adhesion to most metals, which makes it an excellent surface finish.

Based on the above, both copper and nickel were chosen as the coating materials to investigate for glass metallisation.

#### **1.4.2 Selection of deposition method**

According to the literature, there are several ways to form a Cu or Ni coating on glass substrates, such as electroless plating, electroplating, CVD and PVD [29]. Each of the following deposition technologies can meet one or two requirements of glass metallisation, but none has yet achieved all requirements [30]. This section will review the different methods to deposit either copper or nickel films on glass or other substrates. Not all of these are suitable for PCB manufacturing. Both physical methods (evaporation, sputtering, ion beam deposition and pulsed laser deposition etc.) and chemical methods (chemical vapour deposition, electroless plating, and electroplating etc.) can be used [31, 32]. Each of these techniques has its own merits and demerits, and the following sections discuss the most relevant to this application.

#### **Evaporation and Sputtering [30, 33]**

Evaporation is a common and simple deposition technology currently used to prepare metal and/or oxide films on various substrates. In this, the metal to be deposited is heated to high temperature in a vacuum chamber such that it evaporates and then condenses on the substrate to be coated. Sputtering is a PVD process involving the removal of material from a solid cathode. The fundamental difference between sputtering as a plasma process and thermally excited thin film preparation methods

(evaporation, CVD) is the much higher energy (typically  $\sim 1\text{-}10$  eV) input on the growing film. Thus, compared with other deposition techniques, the sputtering process produces films with higher purity and density, provides films with greater adhesive strength and homogeneity. Resistivity as low as  $5 \mu\Omega \cdot \text{cm}$  for Cu films and a smooth surface with root mean square (RMS) roughness of  $1\text{-}18$  nm on p-type silicon has been achieved by dc magnetron sputtering [34]. However in general, the deposition rate for sputtering is relatively low and the cost is high.

### Chemical Vapour Deposition (CVD) [30]

CVD is a process in which a chemical reaction involving gaseous reacting species takes place on, or in the vicinity of, a heated substrate surface. A number of variations on and subcategories of CVD techniques have been developed during the past decades, which mainly include metal-organic CVD (MOCVD), plasma-enhanced CVD (PECVD), and atmospheric pressure CVD (APCVD). In general, the surfaces of CVD Cu films are almost always rougher compared with those prepared by PVD methods. Plasma and light are sometimes used to increase the film growth rate and to lower the deposition temperature. For example, Wu et al. [35] found that photo-assisted MOCVD copper films can be deposited on TaN/tetraethylorthosilicate (TEOS)-oxide/Si, but not on TEOS-oxide/Si wafers, at temperatures as low as  $100^\circ\text{C}$ . Kim et al. [36] reported that the adhesion strength of the Cu film deposited on in situ CVD TiN was two times higher than that on air-exposed CVD TiN, which was attributed to formation of  $\text{Cu}(\text{OH})_2$  at the interface.

### Electrochemical Plating [17, 37]

Electrochemical plating is used for a variety of applications in microelectronics, optics, and related fields. The growth of inorganic thin films from liquid phases by chemical reactions is accomplished primarily by electrochemical processes (which include anodisation and electroplating), and by chemical deposition processes (which include reduction plating, electroless plating, conversion coating, and displacement deposition). Electroplating can only be performed on conductive surfaces, but can be used to produce films with thicknesses up to tens of micrometers. In contrast, electroless plating can be deposited on both conductive and non-conductive substrates, but it is usually for thin coatings only. Electroless deposition takes place in simple liquid baths, offering the possibility of batch processing for high throughput. These

baths are less expensive than the equipment required for other deposition techniques such as the vacuum chambers required for sputter deposition. The electroless method is relatively low cost, fast and especially suitable for high volume production.

Table 1-3 compares the main characteristics of metal films deposited by various techniques. For example, sputtering techniques allow the fabrication of high quality films, but they have high equipment cost and relatively low production rates. On the other hand, electroplating is very cheap but the deposition process is less controllable and only suitable for a conductive substrate.

Different deposition techniques grow films with different characteristics. In addition, since the properties of Cu films depend strongly on the microstructure, compositions and the nature of the impurities present, some properties of the Cu films will vary depending on the deposition technique as demonstrated in Table 1-4.

For substrate manufacturing, the Cu must be deposited as lines on the surface, as interlevel connections and in plated through-holes which receive connectors. Vacuum deposition of the Cu is not feasible because of the scale and topography of the board. Electroplating deposition cannot be employed, because the glass is an insulator. Thus, electroless deposition is the favoured technique. As a result of this, electroless copper and nickel were considered in this research for the metallisation of CMZ glass as they are widely used in the PCB industry and their excellent performance as surface coating materials for nonconductive substrates, such as polymers and ceramics, have been demonstrated before.



**Table 1-3 Main characteristics of metal films deposited by various techniques**

<b>Methods</b>	<b>Advantages</b>	<b>Disadvantages</b>	<b>Ref.</b>
Evaporation	Smooth surface Scalability to large areas Good controllability	Vacuum System Medium deposition rate Poor adhesion	[31, 32]
Sputtering	Good adhesion Smooth surface Good thickness uniformity High density of the film Scalability to large areas Good controllability	Vacuum System High cost Medium deposition rate	[29, 32]
Chemical vapour deposition	Low cost High deposition rate Scalability to large areas	High substrate temp. Not suitable for polymer substrates	[31, 32]
Electroless plating	Low substrate temperature Low cost Good filling capability Scalability to large areas	Poor controllability Poor reproducibility Low deposition rate Requires pre-treatment steps for good adhesion	[23, 38]
Electroplating	Low substrate temperature Low cost Good filling capability High deposition rate Scalability to large areas	Only for conductive surfaces	[23, 39, 40]

Note: low deposition rate, medium deposition rate and high deposition rate are typically 1-10 nm/s, 10-30 nm/s and 30-50 nm/s respectively.

Table 1-4 Properties of Cu films grown using various techniques

Methods	Operating Temperature(°C)	Substrate	Thickness (nm)	Roughness (nm)	Resistivity ( $\mu\Omega\text{-cm}$ )	Ref.
Evaporation	RT-400	Si				[41]
DCMS	RT	Si	130-1050	1-18	5	[34]
DCMS	300-480	Si/glass			2	[42]
PLD	RT 500 -Annealing	Glass			41.8 9.2	[43]
IBD		Glass				
CVD	350-500	Si/SiO <sub>2</sub>			3.3	[44]
PAMOCVD	100-125	TaN			2.8	[35]
LPCVD	200	TiN			1.8	
EL	25	Si	500-2000			[26]
EP	RT	Polymer	100-1000	57		[45]
EP	RT	Si		3		[46]
EP	50	Si	20-100	4.2-10	6.23	[19]

Note: DCMS is dc magnetron sputtering, PLD is pulse laser deposition, IBD is ion beam deposition, PAMOCVD is photo assisted metal organic chemical vapour deposition, LPCVD is low pressure chemical vapour deposition, EL is electroless plating, EP is electroplating.

## **1.5 Research methodology**

Based on the background information discussed above, there were a number of key objectives in this research project. Each is a step towards the ultimate goal of glass substrate materials with smooth surfaces and strong adhesion to electroless copper and nickel, as required for future microelectronic devices.

1. The first objective was the investigation of electroless metal deposition on glass with good uniformity and low deposit roughness, for which a detailed study of the process steps for deposition of electroless copper and nickel on glass was carried out using different analysis techniques.

2. The second objective was the development of an understanding of the mechanisms responsible for adhesion at the interface between the electroless coating and the glass: understanding these mechanisms is key to designing processes with optimal conditions in terms of surface roughness and adhesion. Many articles have been published on modifying the glass surface to achieve good coupling, unfortunately all of these attempts only show electroless coating successfully achieved with no systematic investigations of the adhesion as a function of thickness and failure behaviour between the electroless coating and glass substrates. All factors which affected interfacial adhesion including surface morphology, wettability and deposition parameters were investigated. Both chemical methods and mechanical methods were investigated as means to the adhesion improvement. Attention was devoted to the effects of processing on the nucleation and growth of thin films on substrates, the evolution of film microstructure on glass substrates, and the generation of internal stresses during processing.

3. The third important objective was to characterise the mechanical and electrical properties of deposited coatings on glass as satisfactory values of these parameters are essential to further applications in industry.

4. Combined with the laser machining process, glass circuit patterns were to be demonstrated. In addition to the deposition of copper onto the flat glass surface, in this project, excimer laser machined grooves and micro-vias also needed to be coated

and filled with metal. For application in the PCB industry, the metallic plating thickness on glass should be no less than five microns. A limitation of electroless copper is its low deposition rate on the pristine glass surface. Therefore, the use of electroplating after the electroless process to build up the thickness of copper layers was also investigated.

This thesis focuses on understanding and addressing these four objectives in order to develop electroless metallic coating on glass for the fabrication of glass substrates for electrical interconnect. This thesis will present the results of the research carried out towards achieving these objectives in a systematic manner. Chapter 1 has presented an overview of the motivation for the project as well as the relevant background information needed to understand the challenges that must be overcome and the approaches that will be taken. Chapters 2 and 3 focus on the electroless copper and nickel deposition process, respectively. Chapter 4 shows the experimental results and discussion on the adhesion improvement by surface pre-treatment and catalyst processes, together with all the treatment methods used to independently create chemical and morphological changes on the glass surfaces for increased catalyst adsorption. Chapter 5 shows the internal stresses and mechanical properties of deposits on glass substrates, which have great influence on film adhesion. Chapter 6 presents the experimental results and discussion on the catalytic surface structure effects on electroless copper deposition. Chapter 7 presents electroplating applied on laser machined glass after electroless plating to build up the thickness and make multilayers conductive. This chapter also encompasses electroplating on laser machined grooves and microvias. Finally, Chapter 8 offers a summary of the progress made in this research project and offers directions for future work. Thus, a comprehensive understanding of the challenges faced in the electroless plating of Cu and NiP on glass material, as well as a number of approaches for solving these problems, is presented.

---

## Chapter 2 Electroless Cu Deposition Characterisation

---

### ***2.1 Introduction***

The electroless copper plating method is widely used in microelectronics and nano-electronics as it provides uniform metallic coating on either metallic or insulating substrates. For substrate manufacture, the Cu must be deposited on the surface, and into vias as inter level connections. For FR4, this is widely achieved using electroless and electroplating of Cu. Therefore, in order to use a similar process route to produce a glass substrate for high density interconnect, the first step is to deposit a reliable metallic layer on glass.

However, glass metallisation has some difficulties, because of the incompatibility of chemical and mechanical properties between the highly stiff and brittle substrate and the metallic film. The glass substrate is very smooth and the interface between glass and metal deposit is therefore without any mechanical interlocking, so the metal film can easily separate from the substrate. In addition, the CTE is different for the different materials and as a result, strong interfacial stresses appear and may also cause cracking of the metal films. To begin with, a detailed study of the process steps for deposition of electroless copper on glass was carried out in order to understand the surface morphology, deposition rate and electrical conductivity.

## 2.2 Literature survey

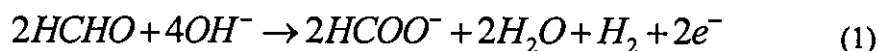
### 2.2.1 Cu-EDTA-HCHO electroless plating mechanism

Electroless copper deposition is an autocatalytic redox process in which cupric ions ( $\text{Cu}^{2+}$ ) are chemically reduced at catalytic surface sites, in the absence of any external current source, to copper metal ( $\text{Cu}^0$ ). The copper deposition reaction is complex because of the number of steps required in order to reduce  $\text{Cu}^{2+}$  to metallic  $\text{Cu}^0$  on the surface.

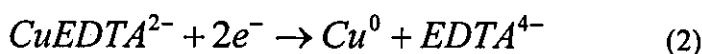
The typical electroless copper bath contains  $\text{CuSO}_4$  (copper source),  $\text{NaOH}$  (pH control), ethylenediaminetetraacetic acid EDTA (complexing agent),  $\text{H}_2\text{O}$  and a reducing agent. Formaldehyde (HCHO) is usually used as a reducing agent because it can give a high deposition rate and leads to excellent mechanical properties of the copper deposits [47-49]. Besides formaldehyde, hypophosphite, borohydride, hydrazine, dimethylamine borane (DMAB), glyoxylic acid and redox-pairs (i.e.  $\text{Fe(II)/Fe(III)}$ ,  $\text{Ti(III)/Ti(IV)}$ ,  $\text{Cr(II)/Cr(III)}$ ,  $\text{V(II)/V(III)}$ ) have been investigated as reducing agents in electroless copper deposition solutions [50-53]. In other work, the hypophosphite modified bath was found to give a better deposition rate, but the mechanical properties such as tensile strength of the deposits decreased compared to those obtained from an HCHO modified bath. Glyoxylic acid baths offered good coating quality, but the operating temperature of  $70^\circ\text{C}$  is high [53].

The Cu-EDTA-HCHO system is the most commonly used for electroless copper deposition. Electroless copper deposition from formaldehyde based plating baths with EDTA as the complexing agent is generally expressed as the coupling of two partial electrochemical reactions as follows [54, 55]:

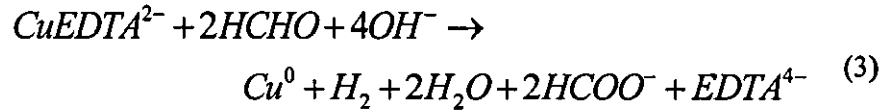
Anodic half reaction



Cathodic half reaction



Overall reaction



The reactions (1) and (2) proceed simultaneously and at separate locations on the activated substrates, in accordance with the mixed-potential theory [56]. In the steady state, at the mixed potential, the rates of reactions (1) and (2) are equal and stay limited by the constant copper ion concentration in the solution and their rate of arrival at the metal substrate [57].

The effects of each component in the bath have been the focus of much research. Zouhou et al. [58] demonstrated that the electroless copper deposition proceeds along two interdependent reactions: the copper reduction and the formaldehyde oxidation. An electrochemical quartz crystal microbalance has been frequently used to measure the partial current of cupric ion reduction as a function of the potential for different concentrations of formaldehyde and to obtain the copper deposition rate. It has been found that increasing the formaldehyde concentration leads to an increase in the reduction current, so the formaldehyde concentration needs to be controlled in the bath [59]. Wiese's group [60] reported that the catalytic oxidation of formaldehyde increases with hydroxide concentration and is only effective at a pH above 11. This is because the methanediolate anion  $\text{H}_2\text{C}(\text{OH})\text{O}^-$  that arises from the formaldehyde as shown in equation (4), is only present in a sufficiently high concentration at a pH above 11.



Weil [61] demonstrated, using an electrochemical quartz crystal microbalance, that the copper reduction current from  $\text{Cu}(\text{EDTA})^{2-}$  solutions at pH 12.5 in the absence of formaldehyde is virtually zero at the working potential of the electroless copper deposition (around -0.65 V vs. saturated calomel electrode SCE). It was concluded from these and related results that adsorbed methanediolate anions catalyse the cathodic reaction.

In addition, the autocatalytic mechanism of both the cathodic and anodic reactions in electroless copper deposition were fully investigated using electrochemical impedance spectroscopy and a polarization technique [62]. It was found that the cathodic reaction produces the catalytic sites for the anodic process, while an intermediate of the anodic process is at the same time an important catalyst for the cathodic partial reaction. During the initial stage of electroless plating high currents occur because of the higher surface concentration and lower polarization. Ramasubramanian's [63] modelling work showed that the concentration of the key components decreased very sharply during the initial period of plating and then recovered slightly due to the arrival of new ions from the solution bulk.

### ***2.2.2 The rate of deposition***

The rate of the copper deposition reaction can be affected by temperature, additives, pH value of the bath, and the substrate material. Temperature affects the kinetics of each partial reaction thereby creating significant changes in reaction and deposition rates [63, 64]. Most of the oxidation and reduction reactions involved in the overall process require energy in the form of heat and therefore increasing the temperature leads to a higher deposition rate. The pH of the solution also has a direct effect on the rate of deposition, mainly due to the role of the OH group as a reactant in the methanediolate anion dissociation reaction.

The plating rate of a typical formaldehyde-based electroless copper bath has been shown to increase nearly ten-fold by increasing pH from 11.5 to 12.5 [63]. Furthermore, the deposition rate was also found to vary with different alkali hydroxides used to adjust the pH. Matsuoka [55] employed three kinds of alkalis as a source of hydroxide ions to investigate the mode of action of the alkali metal cation. The pHs of the baths adjusted using LiOH, NaOH and KOH were found to be 12.5, 12.7 and 13.1, and the corresponding deposition rates of copper were 4.7, 3.4 and 4.2  $\mu\text{m/h}$ , respectively, indicating a nonlinear relationship between the deposition rate and pH. The temperature dependence of the deposition rate was also examined with these baths. The deposition rate of copper increased from 1.52  $\mu\text{m/h}$  to 5.4  $\mu\text{m/h}$  with increasing temperature from 40-70°C in the LiOH system, while it increased from 1.24  $\mu\text{m/h}$  to 3.68  $\mu\text{m/h}$  in the NaOH system.



Some research showed that the HCHO concentration was also a key factor affecting the deposition rate. It was presented that by changing the HCHO concentration in the range of 0.04–0.24 M, both deposition rate and volumetric density rapidly increased followed by a slower increase tending to saturation on the metal surface [48, 54, 57]. Schoenberg et al. [65] also revealed that the deposition rate was constant when the HCHO concentration increased beyond a certain level. This behaviour was because the deposition rate was limited by the HCHO concentration in the first region and limited by the copper concentration in the second region. As the HCHO concentration increases, a higher quantity of electrons are donated to the substrate and the reaction is limited by the arrival of Cu ions at the surface. On the other hand, as the HCHO concentration decreases, a lower quantity of electrons are donated to the metal substrate and the reaction is limited by the arrival of HCHO at the surface. This means that not all complexed copper ions that reach the substrate surface will be reduced and therefore, irregular deposition may occur at different locations on the substrate due to the lack of electrons, and voids may be formed in the Cu film.

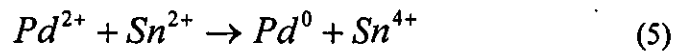
Additives, meanwhile, can have accelerating or decelerating effects on the copper deposition, for example, guanine and adenine have been shown to accelerate plating while other additives such as dipyridyl and NaCN have been shown to have an inhibiting effect on the plating rate [65-67]. These additives also play a role in the microstructure of the copper deposits by affecting copper grain size, and therefore properties such as ductility and resistivity.

### **2.2.3 Surface activation**

The electroless Cu plating process can only take place on a suitable active surface, for example bulk metals such as Cu, Ag and gold [17, 37]. On non-conducting surfaces a catalyst must be used to activate the surface, such as palladium, gold, silver, etc. The range of catalysts used for electroless plating will be reviewed in more detail in chapter 6.

Activation is a catalytic reaction, which is triggered when active colloids on the substrate surface are dipped in an electroless deposition bath. The active catalyst enables the reducing agent to react at the surface and acts as an electron carrier that

supports the transfer of electrons from the reducing agent to the metal ions. A common catalyst is the Pd/Sn colloid catalyst from which Pd catalyst particles are adsorbed on the surface from a solution containing PdCl<sub>2</sub> and SnCl<sub>2</sub> [60]. The Sn in this solution interacts with surface oxygen, adsorbing onto the surface, and enabling the reduction of Pd from Pd<sup>2+</sup> to Pd<sup>0</sup>. The Pd<sup>0</sup> adsorbs on the surface in small clusters of particles and is an active catalyst for the electroless copper deposition reaction [68]:



Once the surface is activated, copper is deposited only where the catalyst is present, making it possible to develop a fully additive build-up process by patterning the initial catalyst deposition.

The adhesion of the catalyst to the surface is also important to ensure consistent plating, and some substrates require additional process steps to allow the attachment of the catalyst. Table 2-1 compares a conventional process and illustrates the range of pre-treatments that can be applied in an improved process. The conventional procedure has been found to be ineffective when attempting to activate the glass surface for electroless copper deposition. Some papers have highlighted that the adhesion between a glass or silicon substrate and metallic layer obtained by conventional electroless plating methods is fairly weak [19, 69, 70]. Therefore, several alternative surface treatments have been attempted in order to activate nonconductive substrates, (such as polymers, glasses, silicon or ceramics) including plasma treatment, reactive ion etching, chemical etching, laser machining, and addition of an intermediate layer, for which examples are given below.

In work performed by Zhang et al. [78], a HF treatment was used to etch a glass surface in order to roughen it. Using the HF as a pre-treatment followed by standard electroless plating improved the adhesion by a factor of five compared to that without pre-treatment. However, HF is difficult to use in many industries due to its high toxicity and corrosive nature making it unattractive for use.

**Table 2-1 Lists of various processes for promoting adhesion of electroless Cu**

Conventional Method	Improved Route	Ref.
1. Cleaning	1. Cleaning	
	2. Pre-treatment (either one or a combination of) plasma treatment reactive ion etch/chemical etch laser machining intermediate layer	[71] [32, 72] [73-75] [32, 76]
2. Pre-Dip Solution 3. Catalyst 4. Post-Activation 5. Electroless Copper	3. Pre-Dip Solution 4. Catalyst 5. Post-Activation 6. Electroless Copper	Activation Activation

Adding an intermediate layer of titanium, cobalt, tantalum, tantalum nitride, tungsten nitride, zinc oxide, indium tin oxide, chromium or vanadium can enhance the adhesion of electroless copper to glass and silicon substrates [79, 80]. These interface metals interact effectively with such oxide substrates. Chromium adheres very well because of oxidation, and the metallic chromium and gold catalyst used in this case interdiffuse to form an interfacial layer which also has very good adhesion [81]. Aithal [19] reported that titanium was used both as a seed layer and barrier layer because it can prevent copper penetration into the substrate at high temperatures and provide good adhesion of copper to dielectrics. Yoshiki [82, 83] prepared an electroless deposited copper layer with strong adhesion to glass substrates by means of a ZnO thin film adhesion layer instead of activation of the substrate surface in a conventional electroless plating process. The main disadvantage of this method is that the structure of the intermediate layer may be changed by acute exposure to conditions such as high temperature or strong magnetic field. In addition, a problem with this approach is the possibility of increased water absorption in the thin metal oxide layer, which can decrease the reliability of the package. Another issue is the effect of the metal layer on the electrical performance of the features since the metals

used for adhesion layers typically have worse electrical properties than copper. Chromium, for instance, has a resistivity of  $12.7 \mu\Omega\text{cm}$  [12], which is nearly eight times higher than copper ( $1.67 \mu\Omega\text{cm}$ ). The increased resistivity of any adhesive metal layer will increase the effective resistance of the signal line. As signal frequency rises and skin depth decreases a larger percentage of the signal will propagate in this thin layer, causing ever-increasing line resistance and signal loss [4]. This effect makes the use of adhesive layers more problematic as off-chip frequencies increase dramatically over the coming years, thus, their use will not be explored in this thesis.

Reactive ion etching (RIE) is a process combining chemical etching and accelerated ion bombardment. It results in etching of the polymer and glass substrate surfaces. Oxygen RIE treatment has been shown to increase the oxygen surface concentration by 70-180% on a polymer surface [84], while oxygen RIE treatment is mainly used to change the surface roughness of glass. Glasses which pass through the RIE process can achieve good adhesion with metals due to this roughness. Laser machining is another useful method to improve adhesion for different substrates by changing the surface roughness [74]. However, the main disadvantages of RIE and laser machining are low speed and high cost, which make them less suitable for high volume production.

Besides the above mentioned methods, one of the most effective ways to improve adhesion to glass is to use a SAM to provide a single molecule thick adhesion promoting layer between the glass and the catalyst [85, 86]. According to the different coupling structures, SAM systems can be divided into two main categories, alkylsilanes and alkanethiols. Thiols ( $\text{R-SH}$ , where R denotes the rest of the molecule) adsorb on metal substrates such as Au, Ag and Pt, while silane-based systems adsorb on silicon oxide and glass. Different siloxane SAMs including those terminated with mercapto-(SH), amino-( $\text{NH}_2$ ), pyridino-(hetero-aromatic,  $\text{C}_5\text{H}_4\text{N}$ ) groups have been successfully formed on the surface of  $\text{SiO}_2$  with a simple one-step dipping process. Organosiloxane SAMs of alkylalkoxysilanes are chemisorbed on a Si substrate that has silanol groups ( $-\text{SiOH}$ ) via Si-O-Si bonds. The aim of the SAM is to form a surface with exposed chemical groups that can interact effectively with the catalyst, thereby coupling it to the glass. Glass surfaces modified with SAMs with increasing

concentration of nitrogen have been shown to result in improved adsorption of the Sn/Pd catalysts [45, 87-89]. Among the most studied systems for glass activation, aminopropyltrimethoxy silane (APTS) and mercaptopropyltrimethoxy silane (MPTS) are the most useful on different hydroxylated surfaces such as oxidized silicon, mica or glass [46, 76, 90]. In the case of silane-based systems, the water content turns out to be crucial for the proper preparation of the SAM, so in most cases a small amount of water is added.

In general, all pre-treatments alter the surface region in different ways, for example, changing the chemical nature of the surface or the surface topography or by removing a weak boundary layer. Silanisation is the most useful method to modify glass surfaces because it is a simple procedure with strong functional groups. Therefore, a silane was used in the present experiment to improve the absorption of Pd based catalyst onto the glass surface.

### ***2.3 Methodology and experimental procedures***

Electroless copper deposition was investigated in this work, including SAM formation, Pd/Sn catalyst and Cu deposition steps.

#### ***2.3.1 Materials***

A list of the materials used in the electroless copper process are summarised in Table 2-2 with the supplier and application specified for each material. In this experiment, CMZ glass with a thickness of 100  $\mu\text{m}$  was used. As mentioned earlier, this was selected due to its close CTE match to Si.

Table 2-2 List of Materials and Suppliers

Product	Supplier	Process Step/Application
CMZ glass	Qioptiq	Glass substrate
Decon 90	Fisher scientific, UK	Cleaning glass
Methanol (laboratory reagent grade)	Fisher scientific, UK	Solvent
3-Aminopropyltrimethoxy silane APTS ( $\geq 97\%$ )	Aldrich	Surface treatment
Circuposit 3340	Rohm and Haas	Pre-dip
Circuposit 3344	Rohm and Haas	Catalyst
Circuposit 4750 part A (Copper sulphate, formaldehyde, hydrogen chloride, methanol)	Rohm and Haas	Electroless Copper
Circuposit 4750 part B (sodium hydroxide)	Rohm and Haas	Electroless Copper
Circuposit 4750 part M (tetrasodium salt of EDTA)	Rohm and Haas	Electroless Copper

### 2.3.2 Analysis techniques

#### Atomic Force Microscopy

In order to characterise the electroless deposited surfaces and their adhesion a number of analysis techniques were utilised. The first of these techniques was atomic force microscopy (AFM), which was used to quantify surface roughness and observe the surface morphology. A Digital Instruments Atomic Force Microscopy (AFM Model Nanoscope III) with Si tip cantilevers of 5–10 nm nominal curvature and a resonance frequency of 247–298 kHz was operated in the tapping mode at a scan rate of 1.0 kHz.

The average copper grain sizes were determined by the AFM software applied to an area of  $500 \times 500 \text{ nm}^2$ , and the roughness was represented as a *Ra* value determined over an area of  $10 \times 10 \text{ }\mu\text{m}^2$ .

## Scanning Electron Microscope

Scanning Electron Microscope (SEM) images of the surfaces were used to aid in qualitative analysis of surface microstructure, deposit thickness, and morphology. SEM images were gathered using two different pieces of equipment: a LEO 1530 VP Field Emission Gun SEM operating at 5 kV and 30 pA was used to investigate the different surface morphologies. For more detailed analysis, including cross-sectioning, an FEI Nova 600 NanoLab was used. This is a dual-beam instrument that integrates ion and electron beams for focused-ion-beam (FIB) and scanning electron microscope (SEM) functionality. The focused ion beam could be used to machine samples for cross sections for which a  $\text{Ga}^+$  ion beam was used at 12 pA and 30 kV. The resulting samples could then be imaged either using the ion beam operating at 11 pA or using the SEM operating at 10kV.

## Film thickness measurement

A Zygo Newview 5000 system was used to measure coating thickness. The Zygo NewView System is a scanning white light interferometer used to image and measure surfaces and provide surface structure analysis without contacting the surface. Light from the microscope divides within the interferometric objective; one portion reflects from the test surface and another portion reflects from an internal, high quality reference surface in the objective. The NewView measures depths with 0.1 nanometer resolution and 0.4 nanometer RMS repeatability.

A requisite to measure the copper coating thickness by using the Zygo was that there were physically different heights or steps in the scan area. To achieve this, the coating on glass was locally removed by partially immersing it in a beaker of nitric acid and leaving for a short time until no coating could be seen. The thickness measurement was then carried out across the step as shown in Figure 2-1.

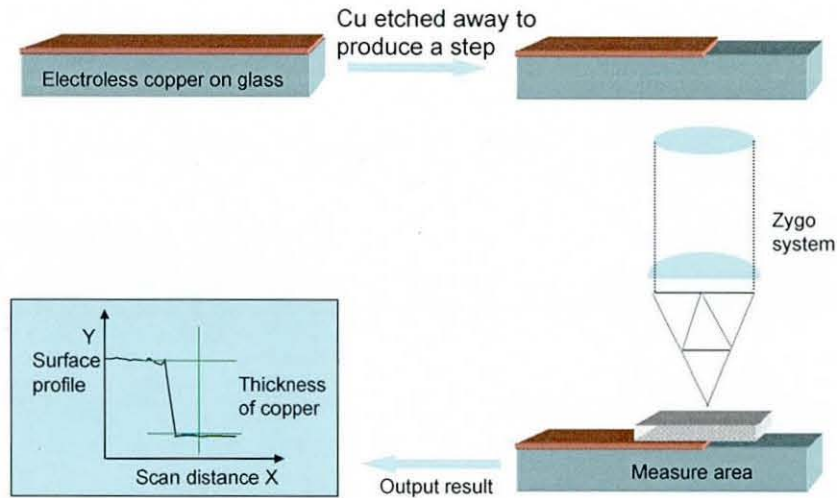


**Figure 2-1 Schematic representation of thickness measurement using the Zygo**

Figure 2-2 is an example of a Zygo image obtained to demonstrate the depth of the step of the electroless copper on glass, where the thickness of the copper coating was measured to be less than 20 nm. Because of the ultra thin copper films, the uncertainty in the thickness measurement was quite large. However, for thicker copper layers (more than 60 nm) the fluctuation was quite small.

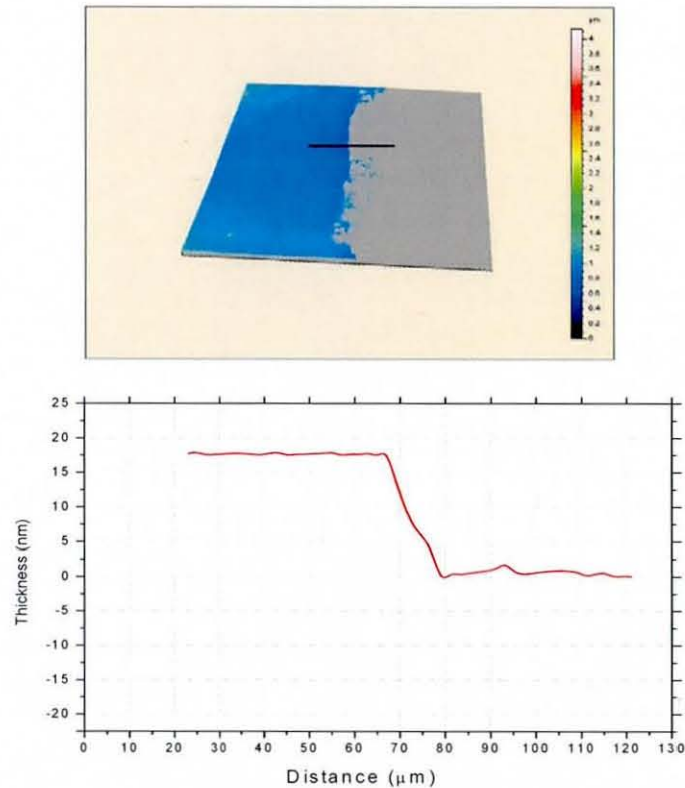


**Figure 2-2 Example Zygo interferometer image used to determine the thickness of the Cu film on glass**



FIB-SEM offers a good way to prepare cross-sections of copper or nickel coating for SEM imaging in a dual beam instrument. The FIB can cut different materials with a high resolution in the required directions. This technique provides site-specific sample preparation and high resolution thickness characterisation. It can resolve morphologic details of less than 5 nm and possesses a depth of focus more than 500 times higher than that of an optical microscope at equivalent magnifications. Figure 2-3 is an example SEM micrograph used to demonstrate the cross section of the electroless copper on glass with different magnification levels, where the thickness of the copper coating was measured to be around 52 nm. This thickness value was an average of ten measurements from different points along the coating. The only requisite to observe the samples by SEM was that they had to be electrically conductive. Metallic samples e.g. copper or nickel deposited on glass, could be placed directly into the SEM chamber.

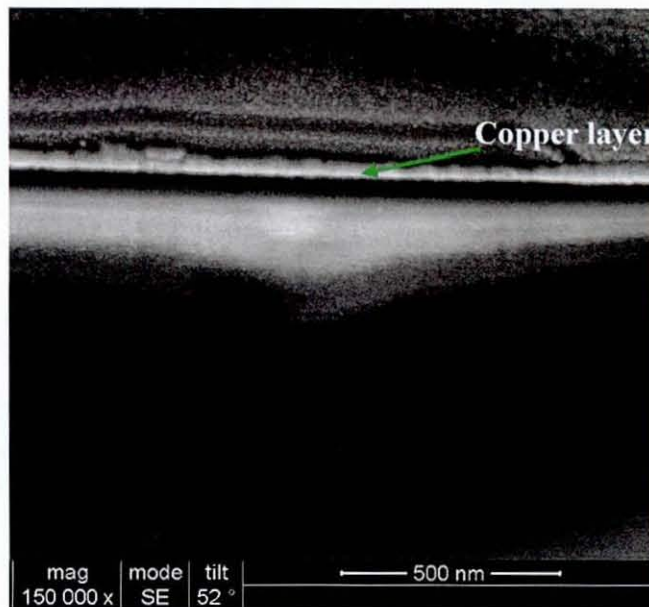


**Figure 2-3 FIBSEM image of cross-section of Cu coating on glass**

Table 2-3 compares thickness measurements from the Zygo and FIB-SEM. Due to the different measurement resolution and alignment of the sample in the instruments, there are some differences in the results which are shown in the table. The thinner the copper coatings, the bigger the disparities. Generally, the measurement results obtained from the SEM were thicker than from the Zygo. However, they were generally consistent and indicated that the measurement techniques were suitable. Considering the relationship between thickness and growth time, this error space is

acceptable. In particular the Zygo was much faster than the SEM and was therefore used for the majority of thickness measurements.

**Table 2-3 Comparison of thickness measurements from Zygo and FIBSEM**

Zygo (nm)	FIB-SEM (nm)	Relative difference
32	41	+21%
47	55	+15%
93	87	- 9%
116	129	+ 9%
140	151	+ 7%
159	171	+ 7%

### **2.3.3 Deposition process**

In this study, the copper deposition process was divided into five main steps, which were Decon cleaning, SAM deposition, pre-dip, catalyst and electroless copper, as shown in Figure 2-4. The electroless copper deposition process details are shown in Table 2-4, which indicates the range of parameters investigated. The major process steps involved in the formation of electroless films on the glass surface are silanisation of the dielectric surface, activation of the silane surface with catalyst particles, and electroless deposition onto the activated SAM surface. Some key parameters of the electroless copper process were varied to investigate the effect of different conditions.

Initially, the glass surface was cleaned by soaking in a Decon 90 solution (2.67 vol.% of Decon 90 in deionised water) for 8 hours. After this, the samples were rinsed with deionised water. Silanisation of the substrates was then accomplished by immersion in a  $5 \times 10^{-3}$  mol/l solution of 3-aminopropyltrimethoxy silane (APTS), in a mixture of methanol (95%) and water (5%), at room temperature for 0 to 24 hours, then rinsed with deionised water. Following the APTS treatment, samples were immersed in an

aqueous pre-dip solution for 1 min then immediately immersed in the catalyst bath, which was maintained at room temperature (R.T.), for 0.5-10 minutes. The samples were thoroughly rinsed with DI water for 3 minutes following catalyst activation. They were then placed in the electroless copper bath at different temperatures for 0-30 min in order to plate a continuous layer of copper on the surface.

The pre-dip, catalyst and electroless copper bath were prepared according to the product operation sheets. 200 ml of Pre-dip solution was prepared by dissolving 54g Circuposit Pre-dip 3340 in 168 ml deionised water. 6 ml of Circuposit catalyst 3344 added to a further 200ml pre-dip solution was used to make the catalyst solution. 200 ml of electroless copper solution was made up of 145.2 ml deionised water, 24 ml of part M, 10.8 ml of part A and 20 ml of part B. As will be seen in chapter 4, through these experiments, some parameters were determined to be the optimum conditions, including APTS SAM formation for 1 hour, 2 min catalyst exposure and 40-45°C for the temperature of the electroless copper bath. In the following sections, if there is no additional information stated for the deposition conditions, it can be assumed that these were the conditions used.

**Table 2-4 Experimental process conditions for electroless Cu deposition on glass**

Step	Main Process	Solution	Time	Temperature
1	Cleaning	Decon 90 (2.67vol.%)	8 hours	R.T.
2	Rinse	DI water	3-5 min	R.T.
3	SAM formation	APTS ( $5 \times 10^{-3}$ mol/l)	0-24 hour	R.T.
4	Rinse	DI water	3-5 min	R.T.
5	Pre-dip	Circuposit 3340	1 min	R.T.
6	Catalyst	Circuposit 3344	0.5 -10 min	R.T.
7	Rinse	DI water	3-5 min	R.T.
8	Electroless Cu	Circuposit Electroless Cu 4750	0-30 min	R.T. to 55°C
9	Rinse and dry	DI water	10 min	R.T.

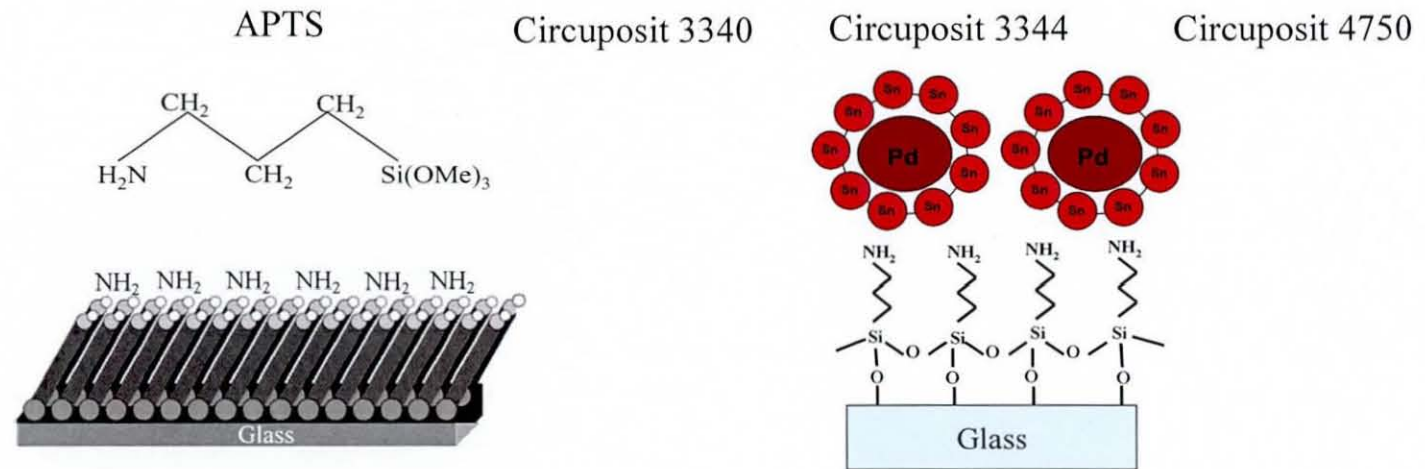
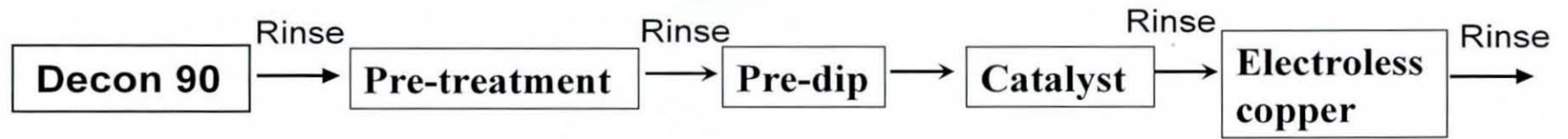


Figure 2-4 Process route used for electroless Cu deposition process

## 2.4 Results

### 2.4.1 Deposition rate

#### Effect of temperature

The effect of temperature on the electroless copper deposition rate was explored over the range of R.T. to 55°C. Figure 2-5 shows the thickness of deposited copper as a function of the plating temperature for a fixed plating time of 30 min. Each point was collected from three samples with a total of at least 10 different measurements. The error bars in this and subsequent figures represent one standard deviation. The copper thickness increased with the plating temperature leading to a deposit thickness of about 310 nm at 50°C. However, the electroless copper solution became unstable when the plating temperature was high, especially when the bath temperature was at 50°C: it was observed that the copper bath decomposed and the transparent solution became turbid quickly. Meanwhile the copper coating roughness and particle size also increased along with the deposition temperature.

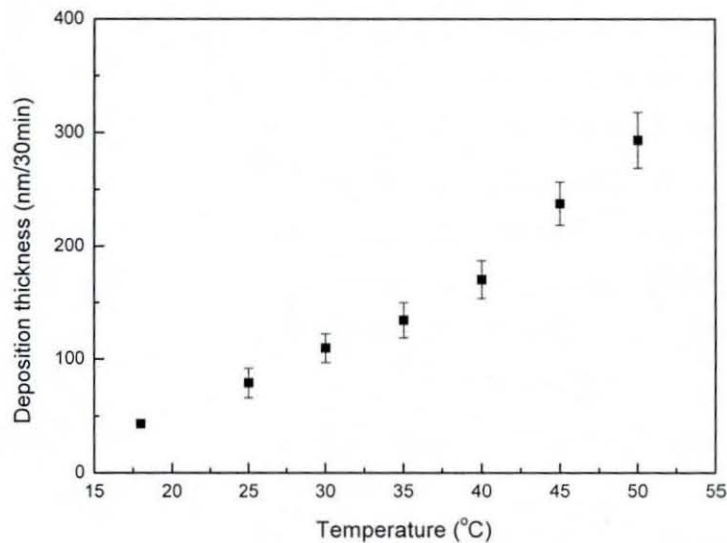


Figure 2-5 Cu thickness as a function of deposition temperature

From the literature and industry patents [55, 64], it was found that deposition rates of electroless copper on FR4 or metallic substrates can be as high as 5  $\mu\text{m}$  in 30 minutes, significantly higher than the rates observed here [21]. Some simple experimental trials

were done to find out the different deposition rates by plating onto polyimide and FR4 substrates using the same process conditions. The copper thickness was built up to  $1.67\ \mu\text{m}$  and  $1.7\ \mu\text{m}$  on the polyimide and FR4 substrates respectively using  $40^\circ\text{C}$  for 30 min. Compared with these substrates, the deposition rate on the glass substrate was fairly slow, which is believed to be due to different surface microstructure and roughness.

While the higher deposition rates at high temperature are attractive for manufacturing, it was found that there was a negative effect on adhesion due to too rapid a reaction. For this reason, accurate temperature control of the electroless copper bath was essential. To balance thickness and adhesion parameters,  $40\text{-}45^\circ\text{C}$  was mainly chosen for further research using glass substrates. Figure 2-6 presents the copper growth as a function of plating time in the electroless copper solution at  $40^\circ\text{C}$ . From the data it can be seen that the copper thickness almost linearly increased along with the plating time from 10 min to 30 min. The average growth rate of the electroless copper plating was about 6 nm per min. However, for the first 10 min, the copper film growth rate was also approximately constant and was higher at around 10 nm per min.

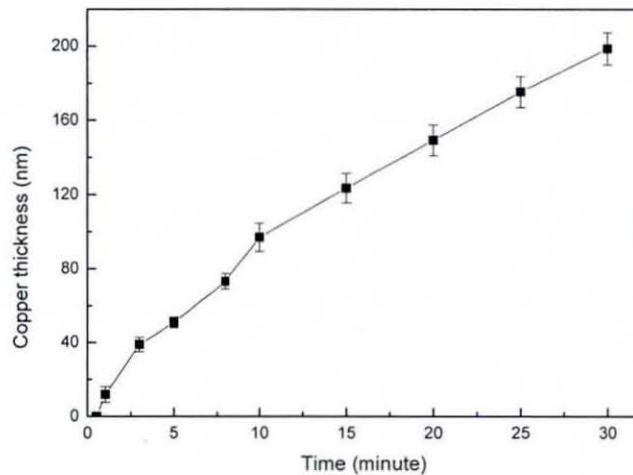
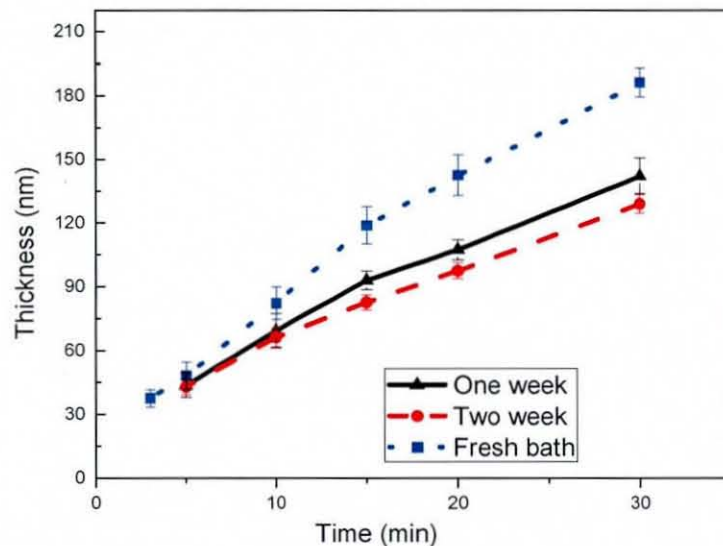


Figure 2-6 Cu thickness as a function of deposition time at  $40^\circ\text{C}$

## Effect of aging of solution

When preparing the electroless copper solution, three separate parts composed of different components were mixed to the suggested concentration. Through thickness measurements, it was found that there was a small difference in plating rate between a fresh bath and an aged electroless bath, especially with longer immersion times. In this case, the aged electroless bath means a freshly prepared bath that was kept at room temperature for a specific period until it was used. In the experiments presented here, only a small amount of solution was used, so to avoid further ageing effects the solution was only used for one or two days of experiments with a total plated area of 20 pieces of 20mm×40mm in size. From an approximate calculation based on 32 full size (70mm×70mm) samples plated to 150 nm thickness, the concentration of cupric ions is expected to decrease by 18% when deposited in this bath. Based on the literature, this is expected to reduce the deposition rate as the cupric ion concentration decreases.



**Figure 2-7 Cu thickness change with different bath aging time**

Figure 2-7 shows that the copper thickness deposited changed with different bath aging time. It was observed that for both the aged solutions during the first 3 min there was no easily measurable coating on the glass. After 5 min of deposition, a slight variation in thickness could be measured. It was found that the deposition speed of the fresh bath was higher than the aged baths. Moreover, this situation was more

obvious for longer deposition times. In general, with the increase in bath aging time, the deposition rate decreased.

### Effect of other parameters

Apart from the above factors, the bath loading, pH value and agitation are also expected to affect the deposition speed in the electroless copper bath. The bath loading is used to define the ratio of the superficial area of work immersed to the volume of solution in the tank. To avoid complex changeable parameters, these three factors were always kept stable. The bath load was set at  $0.75 \pm 0.05 \text{ dm}^2$  of substrate per litre of bath and the pH value was kept at 11.3-11.5.





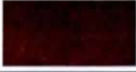

Although agitation of the bath is not absolutely necessary for electroless copper deposition, it is usually advisable [56]. The basis for this is the higher rate of diffusion where the reactants are transported more effectively to the surface of the work to be plated and the spent reaction products are better removed. Magnetic stirring was adopted in the first phase of the experiments. According to Gawrilov [91], the deposition rate in an acid nickel bath is raised by work movement, other conditions remaining constant. This was explained in terms of a raising of pH within the diffusion layer. It appears that this does not apply to the alkaline copper bath used here. Due to the small dimensions of the substrate and low deposition rate, there was no obvious increase in deposit thickness with magnetic stirring. In addition, this required a hot plate to be used as a heating source, for which the fluctuation of temperature was bigger than in a water bath. Consequently, no stirring was used for the electroless copper deposition process and the solution was heated by placing the beaker in a water bath.

#### ***2.4.2 Appearance of electroless Cu deposits***

In terms of the colour of the deposits, appreciable differences were observed between the different electroless deposition temperatures. Table 2-5 lists the dependence of copper brightness and appearance for different deposition temperatures for which the plating time was kept constant at 10 min. At the lowest temperature, the copper was very dull. When the temperature was above  $50^\circ\text{C}$ , the copper colour was brown.



**Table 2-5 Cu brightness and appearance for different deposition temperatures**

Temperature (°C)	Thickness (nm)	Quality	Electroless Cu
30	Very thin	Dull	
35	52	Slightly dull zones	
40	91	Lustrous	
45	140	Lustrous	
50	181	Lustrous	
55	249	Brown and bright	

### 2.4.3 Crystal structure and microstructure

Crystal structure and microstructure of electroless coatings have a significant effect on their physical properties, such as conductivity, hardness and elastic modulus [37].

#### Crystal structure

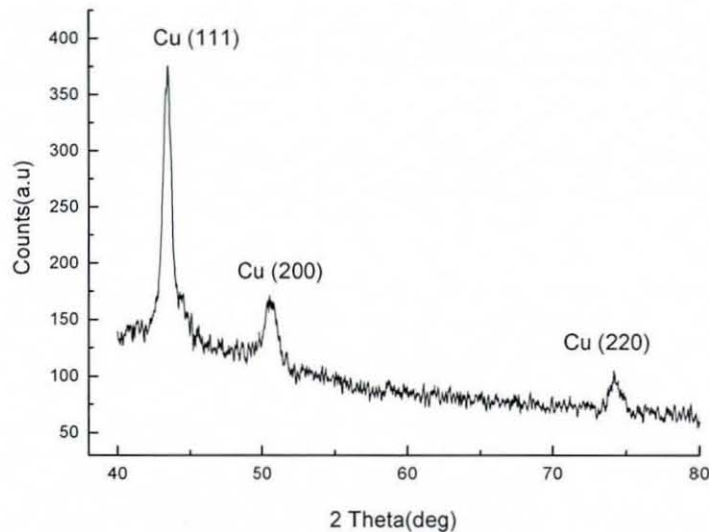


**Figure 2-8 XRD of the electroless deposited Cu on glass substrate**

The electroless copper deposits were found to be polycrystalline in nature and their crystal orientation was characterised by X-ray diffraction (XRD). The XRD patterns

were collected from  $20^\circ$  to  $90^\circ$  at a scan step of  $0.02^\circ$ . Figure 2-8 shows an XRD spectrum of the electroless deposited copper on a glass substrate.

The copper thickness was less than 100 nm, so the baseline was not flat due to a strong effect from the glass substrate. Comparison of the main diffraction peaks (111), (200), (220) and (311) of the deposited copper with the standard International Centre for Diffraction Data (ICDD) JCPDS card [92] for powdered copper (Table 2-6), showed that the strong preferred orientation of the electroless copper grains was (111). There was no indication of oxidation of the film. The peak intensity ratio of  $I(111)/I(200)$  of 2.3 and the full width at half maximum (FWHM) of  $0.20^\circ$  was obtained from the XRD. The (111) diffraction peak (111) of the copper film was at  $43.48^\circ$  which is a shift of about  $0.2^\circ$  from the JCPDS card value and indicates internal stress occurring in the copper layer [93]. Five samples with different Cu thickness were analysed by XPS, and for all, the preferred orientation was (111) in comparison with the preferred orientation of (220) observed in previously reported cases using similar preparation methods [55].

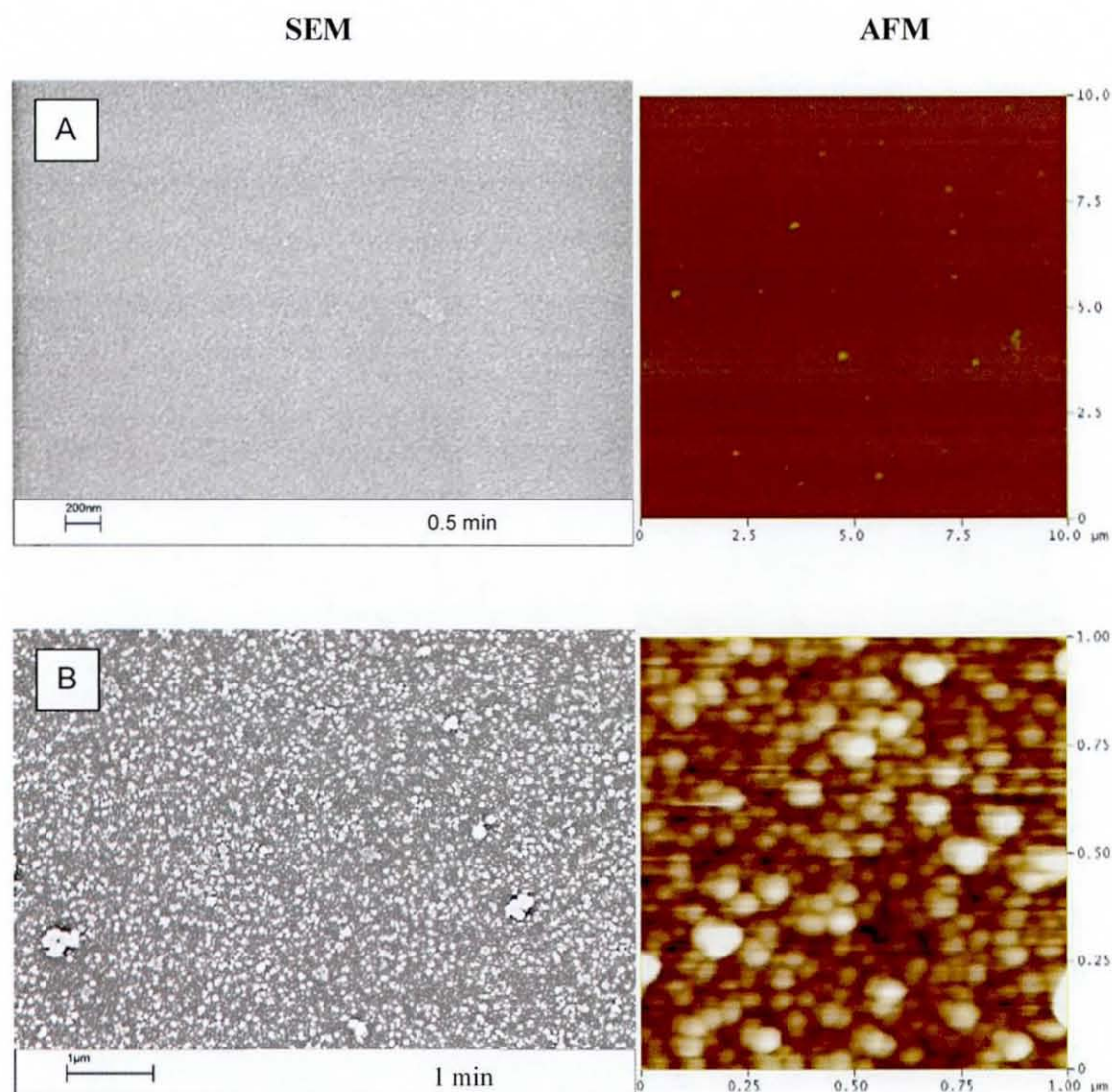
**Table 2-6 Joint Committee Powder Diffraction Standards (JCPDS) card for Cu [92]**

$2\theta$ ( $^\circ$ )	Intensity	(h k l)
43.3	100	(111)
50.4	46	(200)
74.1	20	(220)
89.9	17	(311)

### Microstructure

More detailed investigations of the copper plating by SEM were carried out to characterise how the coating developed with deposition time. Figure 2-9 shows SEM and corresponding AFM images of electroless copper deposits on glass for different plating times. For very short plating times (e.g. 0.5 min), the surface was found to be smooth and there were no obvious copper particles, which was also confirmed later

from XPS results that showed no evidence of copper. More particles appeared on the surface when the plating time was increased to 1 min, for which the average copper grain size was 48 nm with a narrow size distribution. The grain size gradually increased with the plating time such that after 3 min, copper particles were found to be in the range of 70-80 nm. At this stage the film appeared to be uniform and continuous across the surface. After 5 min deposition, the copper particles had grown larger and become polygonal in shape. After 25 min, the copper particles appeared to have merged into a layer and there were no clear particles observed.



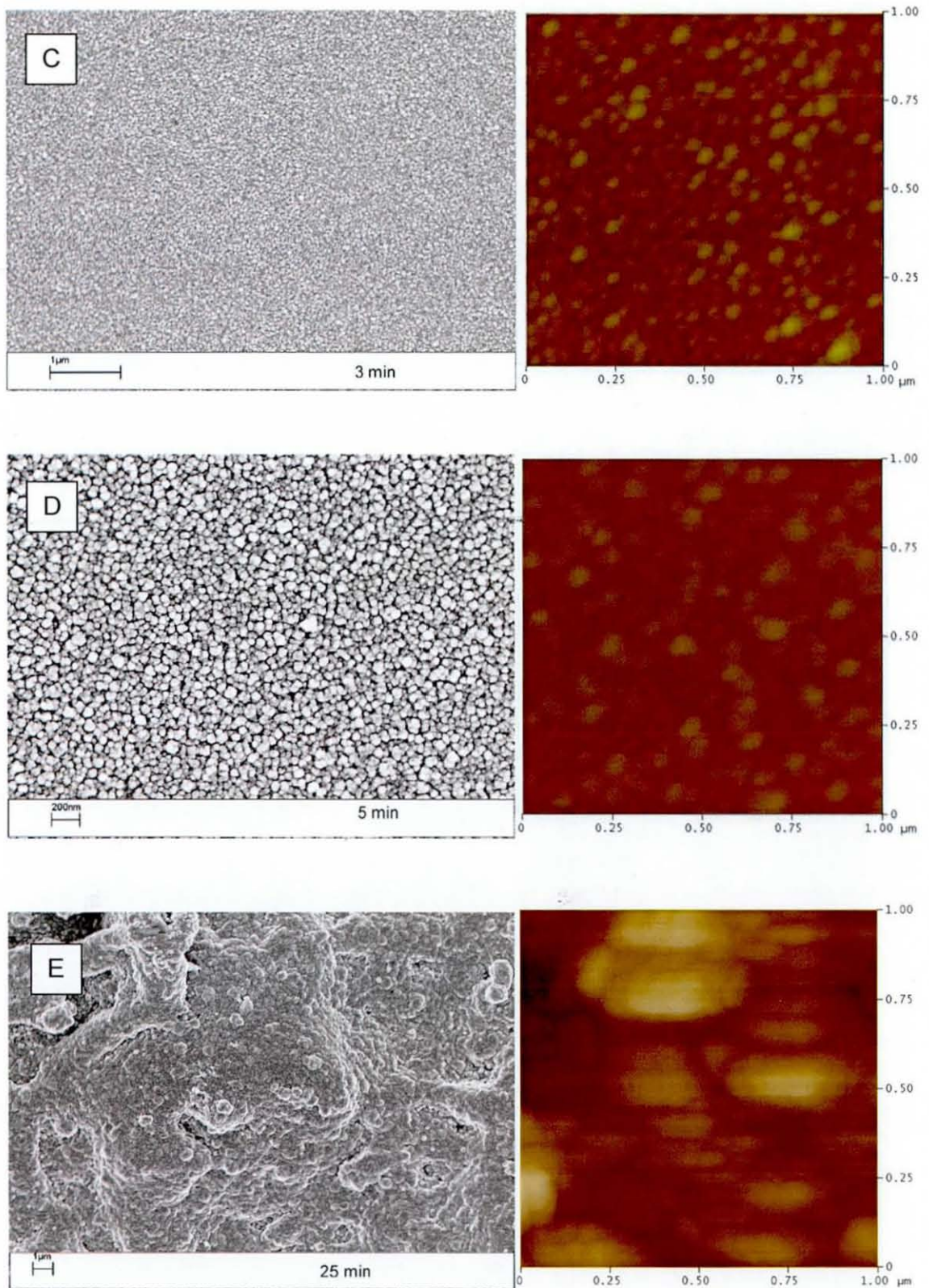


**Figure 2-9 SEM and AFM images of electroless Cu deposits on glass for different plating times: (A) 0.5 min, (B) 1 min, (C) 3 min, (D) 5 min, (E) 25 min.**

The deposited copper roughness was determined directly from the AFM images. Table 2-7 lists the roughness,  $R_a$ , for different thickness films formed at 40°C. As the copper thickness increased from 46 nm to 150 nm, the roughness increased from 5 nm to 12 nm. Meanwhile, there was an overall increase of the grain size with increasing thickness. It is expected that the roughness of the deposit surfaces would increase along with the plating time, except for discontinuous ultra-thin films, which is attributed to grain growth and is in good agreement with that of many other measurements [94].

**Table 2-7 The roughness of different thickness Cu coatings**

Deposition time (min)	Film thickness (nm)	Roughness, $R_a$ (nm)
4	46	$4.8 \pm 0.7$
6	69	$9.4 \pm 1.9$
10	92	$10.6 \pm 1.7$
12	104	$10.3 \pm 2.0$
14	122	$11.3 \pm 1.5$
16	145	$11.9 \pm 2.3$

The coating roughness also varied with deposition temperature. Figure 2-10 presents the relationship between deposition temperature and AFM measurements for a fixed thickness. The measurements revealed that the roughness of the copper coating increased when the bath temperature increased. The copper particle size steadily increased from 50 nm at 30°C to 90 nm at 60°C, while the maximum roughness was still less than 35 nm.

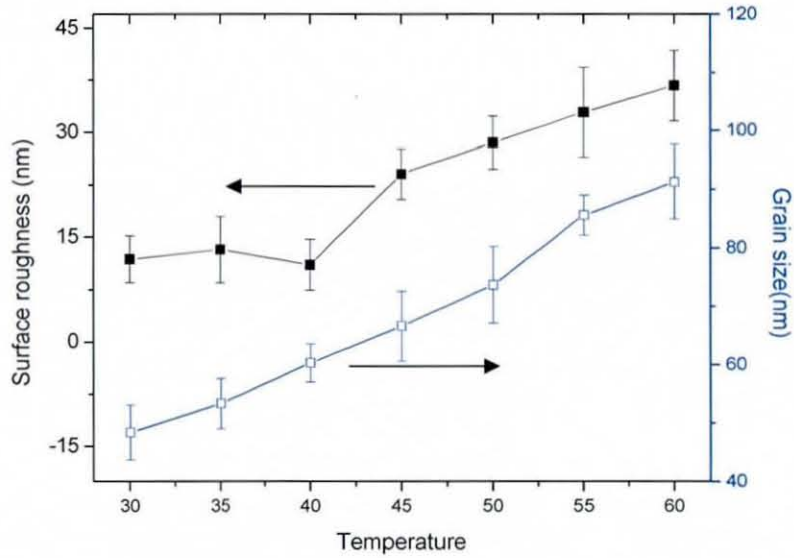


**Figure 2-10 The relationship between Cu particle size and film roughness as a function of deposition temperature**

#### **2.4.4 Electrical properties**

The electrical properties such as resistivity of the Cu interconnects are fundamental properties for PCBs, therefore, experiments were carried out to measure these important parameters. The Four-Point Probe or Kelvin, probe method is the most common way to measure the sheet resistance of shallow layers (as a result of epitaxy, ion-implant, diffusion or sputtering). The schematic representation of the Four-Point Probe is shown in Figure 2-11. This technique involves bringing four equally spaced probes into contact with the material of unknown resistance. The probe array is usually placed in the centre of the material. The theory behind this is that a fixed current is injected into the substrate through the two outer probes, and a voltage is measured between the two inner probes. Using four probes eliminates measurement errors due to the probe resistance, the spreading resistance under each probe, and the contact resistance between each metal probe and the upper material. In this work, the resistivity of the electroless films was measured using a Keithley 580 micro-ohmmeter, and the spacing between the Au probes was 2mm.

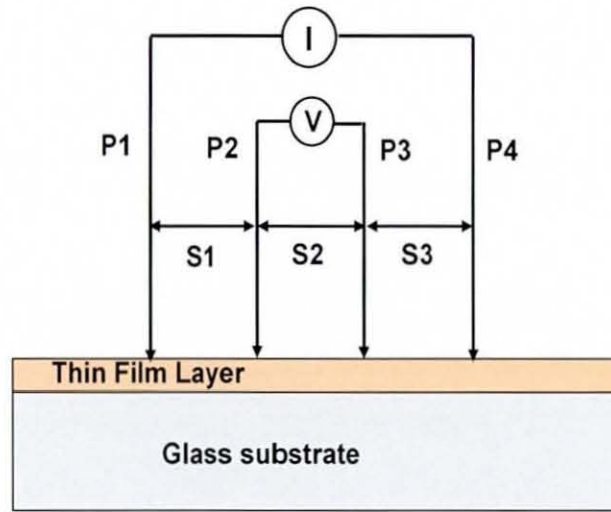


Figure 2-11 Schematic diagram of Four-Point Probe measurement method

If  $d$  represents the thickness of the thin film and if probes with uniform spacing  $s$  are placed on an infinite slab of material, then the resistivity,  $\rho$ , is given by the following equation [10, 34].

If  $s \gg d$ , then

$$\rho = \frac{\pi d}{\ln 2} \times \frac{V}{I} = 4.53d \frac{V}{I} \quad (6)$$

$\rho$  = volume resistivity ( $\mu\Omega\text{cm}$ )

$V$  = the measured voltage (volts)

$I$  = the source current (amperes)

$d$  = the sample thickness (cm)

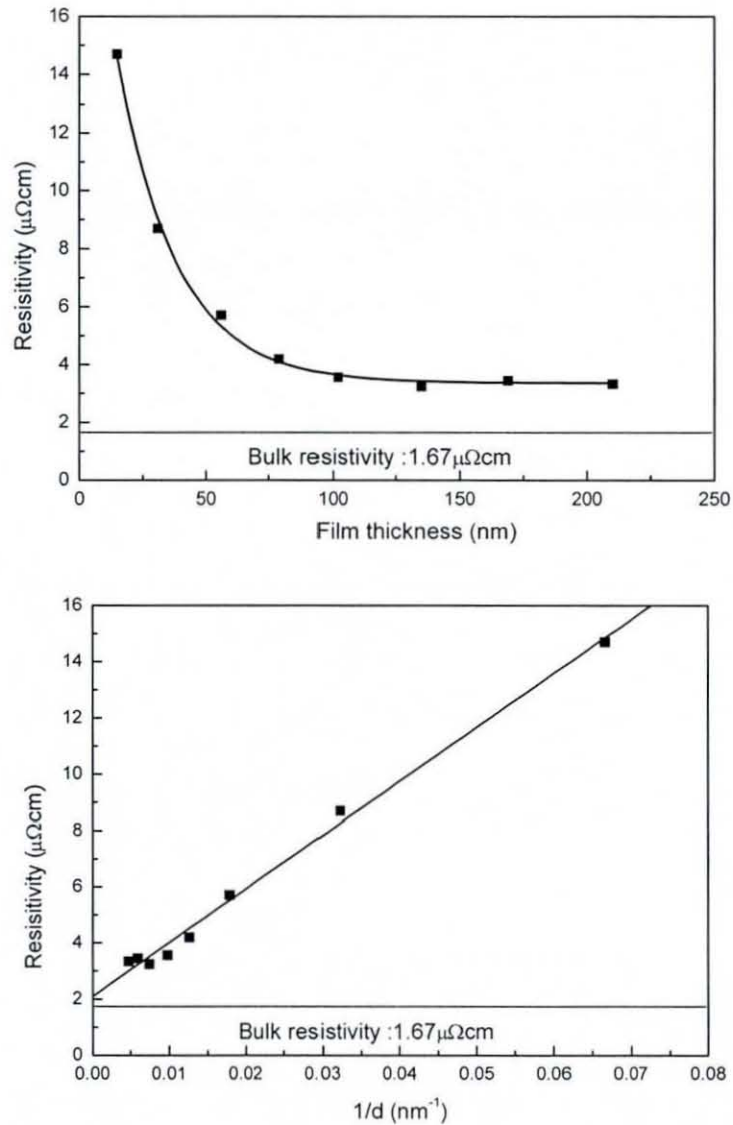


Figure 2-12 Cu resistivity as a function of film thickness,  $d$

To examine the thickness dependence of the Cu film resistivity, the electrical resistivity of the Cu films was measured. For each thickness, at least 10 points from different areas of the sample were measured to get an average value. Figure 2-12 shows the resistivity of the Cu films as a function of the film thickness. The resistivity of the Cu films was found to decrease noticeably with increasing film thickness, with the resistivity dropping from  $14.7 \mu\Omega\text{cm}$  to  $3.21 \mu\Omega\text{cm}$  as the thickness increased from 17 to 209 nm. All values were higher than that of high purity bulk copper for which the resistivity is  $1.67 \mu\Omega\text{cm}$ .



## 2.5 Discussion

### Deposition rate

It is evident that the deposition on the glass substrate measured here is fairly slow, approximately two hundred nanometers thick in 30 min, which is consistent with the deposition rate reported in [20]. Ref. [71] showed that the deposition rate can be 3.9  $\mu\text{m/h}$  if proper plasma treatments are used on polymer surfaces before electroless deposition. In order to find out the reason for this low rate, polyimide and FR4 materials were also plated using the same conditions and the deposit thickness built to around 1.7  $\mu\text{m}$  in 30 min. Clearly, the deposition rate varied greatly with different substrates, not just because of different temperature, pH value and bath recipes. This assumption can be partly supported by Donahue's [64] kinetics research on electroless copper plating, which showed that the substrate plays a role in affecting the nucleus formation during electroless copper deposition. This is because of the different catalytic properties of the substrate surface on which the deposition occurs. It is more difficult to create effective nucleation sites on glass compared with the porous surface of FR4 or other polymer materials. Many researchers have measured the plating rate on different classes of substrates, including metals and sensitised non-conductors with different catalytic (or electrocatalytic) properties. In these studies large differences in plating rates have also been reported from similar baths, e.g. compare Shippey [95] with Goldie [96] and this could be explained by differences in the catalytic activity. However, no method of defining the catalytic properties of the surface was found and the suggestion that differences exist is postulated.

As for Figure 2-6, it was noted that the copper deposition rate was not constant at 40°C. The deposition rate decreased after about 10 min. This phenomenon was also observed in the different aged baths as shown in Figure 2-7. It was clearly seen that the deposition rates of the first 10 min in the aged baths were similar, while deposition rates after 10 min were lower. This could be because of varied catalytic effects along with the plating time. When the reaction started, the catalytic surface could offer enough nucleation sites for cupric ions to react. Later, the nucleation sites became insufficient to maintain this reaction so the deposition rate went down. Once the surface was fully covered with copper, this deposition rate remained stable. Another possible reason is that the deposits may have different initial morphologies

compared to later on, and could have changed during the plating process leading to different plating rates. These were called the "initial" and "final" rates by Dumesic and co-workers [97].

For aged baths, the deposition rate was not the same as that of a fresh bath. One possible reason for this phenomenon is that electroless copper baths are not as intrinsically stable as electroless nickel baths. One of the principal problems in the development of electroless copper plating was spontaneous deposition, and many of the baths had a rather short operating life [98]. The decomposition probably arises from a competing reaction, which is non-catalytic and takes place in the bulk of the solution:



The cuprous oxide ( $Cu_2O$ ) particles can then disproportionate:



Therefore, after one or two weeks' aging storage prior to use, the concentration of components may change, resulting in the reaction speed decreasing and a lower deposition rate. In addition, loss of formaldehyde during storage may also occur leading to a lower concentration and deposition rate. In general, electroless Cu deposition rates are determined by the bath composition, the plated substrate and the temperature of the bath.

### Microstructure

Numerous experimental studies of the mechanism for copper film structure development, such as those of Abermann and Koch [99-101] have shown that the film growth mechanism follows the Volmer-Weber mode, which is defined as the formation of 3-dimensional crystallites of the deposit metal on the substrate which merge together to form a complete layer. The Volmer-Weber mode is popularly accepted for metallic films deposited on substrates by electrochemical methods. Figure 2-13 shows a schematic diagram of the copper film growth from an electroless copper bath.

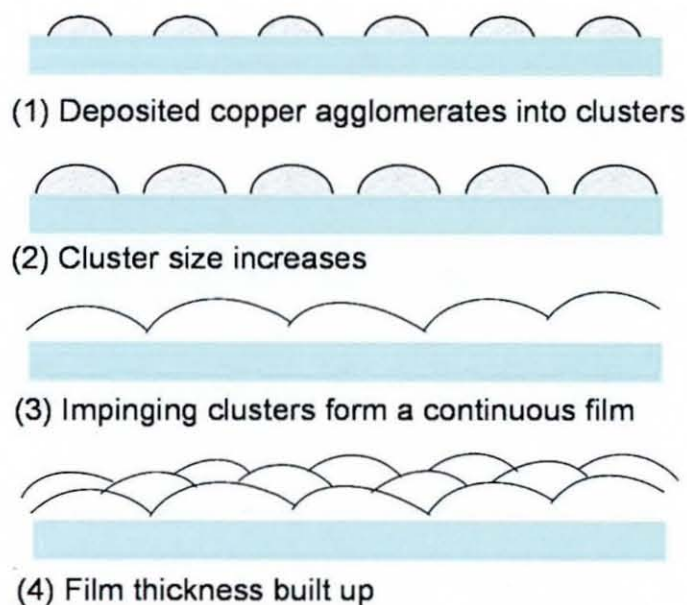


**Figure 2-13 Schematic diagram of the Volmer-Weber mode film growth**

According to the proposed Volmer-Weber mode, the basic assumption is that the deposited copper agglomerates around catalyst particles, forming clusters on the glass substrate surface, then the clusters increase in size until they impinge on each other to form a continuous film. After the glass substrate is completely covered with clusters, they will grow by further incorporation of Cu atoms. When the islands grow together, strong capillary forces appear so that the islands minimize their surface energy by changing their shape. Finally many islands grow together giving a dense coverage of the substrate which changes to a continuous film by taking up further atoms [102]. This model is consistent with the SEM image results of electroless copper deposits for different plating time as shown in Figure 2-9. Some copper particles appeared on the glass surface when the plating time was 1 min (Figure 2-13 Step 1), then the grain size gradually increased as the plating time increased to 3 min (Figure 2-13 Step 2). The copper particles grew larger and became a continuous film in 5 min (Figure 2-13 Step 3), finally the copper thickness was built up by continuous plating (Figure 2-13 Step 4). The deposition rate change observed at 10 min, is likely to correspond to the critical point that the individual copper clusters started to grow and merge into one continuous film.

From the XRD results, the copper film is obviously a polycrystalline structure with a strong (111) peak. Initial crystallographic orientations of the copper film that minimise surface and interface energies are favoured over others, and the nucleation rates for clusters with lower energy orientations are greater than those for others. Eventually, this leads to a strong texture in the microstructure of the film [22]. In face-centred-cubic (fcc) metals, such as Al, Ag and Cu, the higher surface mobility of the adatoms facilitates continued structure evolution during film thickening resulting in most grains being oriented so that the crystallographic direction of the surface is the (111) direction [33].

Electromigration strongly relates to the crystallographic texture in metal interconnects. It has been shown that (111) texture significantly inhibits stress-induced voiding in aluminium interconnects. The (111)-textured copper has higher resistance to electromigration, because highly textured microstructures suppress grain boundary and interfacial diffusion of metal atoms. A lower oxidation rate has also been observed in the (111)-textured copper layer, which implies that a highly textured (111) copper is favourable for interconnect technology in high current density applications [103, 104].

### Electrical properties

Because each of the studies presented in the literature used different substrates and bath components, the reported electrical properties of electroless copper films varies greatly. The 150 nm copper films obtained in Ref. [105] had a resistivity,  $\rho$ , of about 300  $\mu\Omega\text{cm}$  and the authors speculated that such a high  $\rho$  can result from “poor conductivity between Cu particles”, an explanation that was not corroborated by their AFM observations. The 100 nm copper films obtained in Ref. [90] had a resistivity of 12  $\mu\Omega\text{cm}$ , and comparison of these two observations demonstrates high promise in improvement of the quality of Cu films by optimising the experimental parameters. Aithal [19] showed using electroless deposition that the electrical resistivity of the as-plated copper on a Ti seed layer was 6.23  $\mu\Omega\text{cm}$ , which is still significantly higher than that of bulk copper, which is 1.67  $\mu\Omega\text{cm}$ .

Figure 2-12 presents the effect of thickness on electrical resistivity of Cu films in the current experiments. From it, it is clearly seen that the resistivity of Cu thinner than

23 nm was very high and it decreased sharply with increasing thickness. When the copper film was very thin, e.g. 17 nm, it was discontinuous and consisted of small islands [106]. As a consequence, the island boundaries serve as infinite potential barriers resulting in infinite resistance arising from the separation between very small clusters during the early stages of film growth. As the film grows, the Cu islands begin to grow and coalesce, reducing the separation between islands. As a result, there is a rapid increase in the electron mobility from one island to another, thereby, decreasing film resistivity. The resistivity was almost constant if the Cu thickness was over 100 nm, which is because all of the islands had merged into an interconnected network.

For thicknesses greater than 100 nm the resistivity was constant at about  $3.5 \mu\Omega\text{cm}$  and comparing this resistivity with much larger values reported in the literature for 150 nm [105] and 100 nm [90] electroless Cu, it can be concluded that the electroless Cu film deposited here had a better microstructure, such as the particle size, growth mode and crystallographic direction. This resistivity is still two times that of pure bulk Cu. The reason for this lower conductivity is the fact that the Cu film is polycrystalline with small grains and therefore many grain boundaries that scatter electrons, thus reducing the conductivity. Polycrystalline films show a higher resistivity than epitaxial single crystal films and the resistivity of thin films increases with a decrease of the film thickness [107]. Accordingly, to improve conductivity it is necessary to suppress the rate of crystal nucleation and enhance the crystal growth to accelerate grain growth and hence decrease the number of grain boundaries. Aithal [19] also reported the electrical resistivity of copper films decreased from  $6.23 \mu\Omega\text{cm}$  to  $3.3 \mu\Omega\text{cm}$  with increasing annealing time up to 90 min at  $200^\circ\text{C}$ . The decrease in resistivity resulting from the increased annealing time is attributed to the reduction in defects and the number of grain boundaries in the film. In the present study, resistivity measurements were carried out on a few samples annealed in a vacuum oven at  $180^\circ\text{C}$  for 1 hour, however no decrease of resistivity was observed. The resistivity levels obtained here are very close to Cu films deposited by ion beam deposition in Ref. [108], which is often considered to provide one of the best film conductivities.

## **2.6 Conclusion**

A literature survey and experimental studies were performed to investigate the feasibility of electroless copper deposition on a glass surface. Homogenous copper films were deposited on a self-assembled monolayer treated glass substrate by means of electroless plating, but the thickness was very limited. Meanwhile, it was revealed that the deposition rate on the glass substrate is much lower than that on two polymer based substrates. Metallographic studies of the electroless copper deposits reveal that their topographic structures showed uniform and fine particle distribution. Furthermore, it was determined from XRD that the primary crystal orientation of the electroless copper grains is (111) which implies this copper is favourable for interconnect technology in high current density applications.

---

## **Chapter 3    Electroless NiP Deposition Characterisation**

---

### ***3.1 Introduction***

Compared to electroless copper, electroless nickel has several advantages: its corrosion resistance is greater, its thickness distribution is more uniform leading to lower surface roughness and it has a higher deposition rate [23]. As a result of this it has been widely used in electronics packaging applications, for example as an under bump metallisation (UBM) [7]. However, in electroless nickel plating the deposit is not pure nickel, but contains a small amount of another element that forms part of the reducing agent. The most commonly used reducing agent in industrial applications is hypophosphite resulting in a nickel phosphorous deposit [109]. The hardness, corrosion resistance and morphology of the nickel phosphorous deposit varies with the phosphorous content which can be used to control the properties [27]. In this work electroless nickel deposition was carried out to investigate its feasibility for the metallisation of the glass substrate. The evolution of the deposit morphology such as roughness, alloy microstructure and growth rate of electroless nickel deposited on glass are presented.

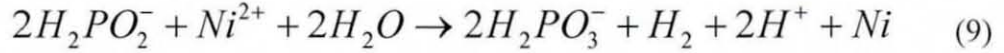
### ***3.2 Literature survey***

#### ***3.2.1 Electroless Nickel (EN) plating mechanism***

Electroless NiP deposits are produced by the autocatalytic electrochemical reduction of nickel ions from the plating solution by means of a chemical redox reaction [23].

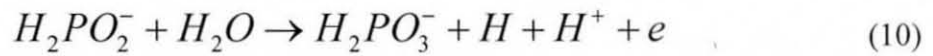
The progress of the electroless nickel plating reaction is depicted in Figure 3-1. In the reaction the deposited nickel is not provided by an anode but by a nickel salt. The salt is dissolved in the aqueous solution resulting in nickel ions. The nickel ions are then reduced by the electrons, not provided by an external current source but by a reducing agent also dissolved into the solution.

For the hypophosphite based EN baths, the overall reaction can be written as:



From an electrochemical point of view, the reaction above can be further divided into an anodic reaction and a cathodic reaction, as below:

Anodic reaction:



Cathodic reaction:

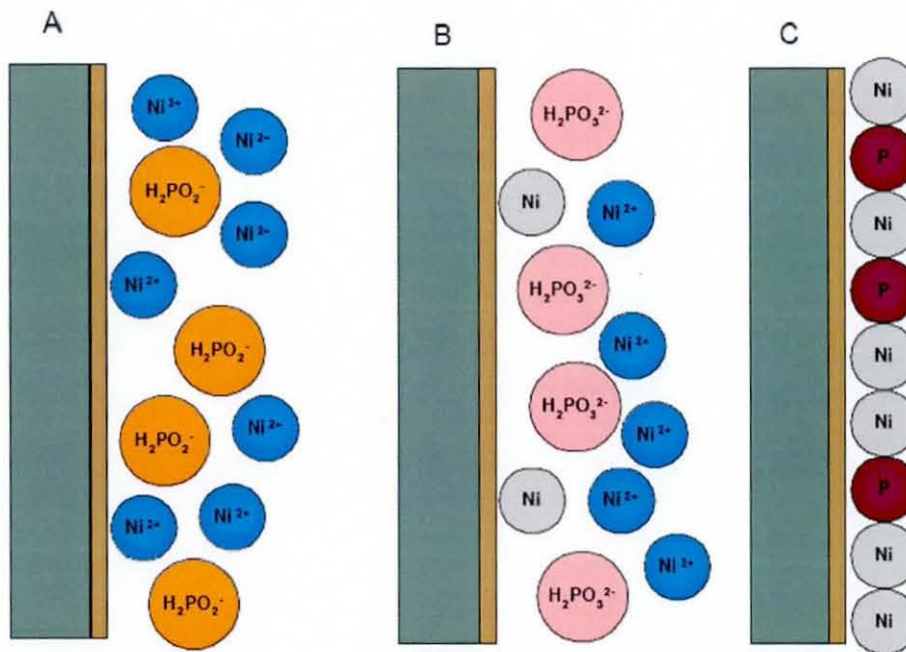


Figure 3-1 Schematic diagram of the nickel (II) reduction and hypophosphite oxidation process



The process includes three main steps: A) the reducing agent ( $H_2PO_2^-$ ) and the nickel source ( $Ni^{2+}$ ) are dissolved in the plating bath; B) the reduction reaction occurs on an active surface where hypophosphite oxidizes into orthophosphate, reducing the nickel ions into atomic nickel; C) during the reaction some reducing agent is also reduced so that the plated nickel film contains some phosphorous.

As the anodic partial reaction is the electron source for the cathodic one, it is the driving force for the whole deposition process. The Ni deposition includes the diffusion towards and adsorption on the catalytic surfaces, the de-adsorption and diffusion of products away from the surface, and the electrochemical reactions on the surface. The nickel deposition rate is mainly decided by the electrode potential and catalytic activity .

### 3.2.2 Deposition rate and phosphorous content

Most of the properties of the coating are structure-dependent and the structure depends on phosphorous content [110]. Phosphorous in the deposit is a result of the reaction between the hypophosphorous acid with a hydrogen radical



Equation (12) and (13) explains the decrease of phosphorous content in the deposit with increasing alkalinity of the bath by means of the equilibrium displacement of the reaction to the left side. In many baths ammonia is added to adjust the pH and the presence of ammonium ions determines the amount of available species to the reduction process according to reaction (14) [27]. pH is one of the most dominant factors, which controls phosphorous content in the deposits. The dependence of the phosphorous content on the pH when adjusted by the ammonia concentration in the solution from literature is shown in Figure 3-2. Typically the amount of non-metallic P in the alloy can vary between 3 and 35 atom percent depending on the experimental conditions [111]. This quantity is strongly dependent on the solution pH, and it is usually reported as increasing with acidity. At low pH values, there is a significant concentration of hypophosphorous acid and a low concentration of  $NH_3$ . Obviously,

the nickel reduction is not favoured by the low pH due to the high concentration of free nickel ions in solution. At medium pH values, the hypophosphorous acid concentration is relatively low and a medium concentration of free nickel ions is present. As a result, the ratio of phosphorous to nickel in the deposit is very low. On the other hand, for strongly alkaline solutions, the concentration of both hypophosphorous acid and free nickel is very low. Due to the lack of both oxidant species, the ratio of phosphorous to nickel in the deposit is significantly low. Kar et al. [112] also reported that the phosphorous content of the deposit decreased, whereas the deposition rate of nickel increased by increasing the pH of the plating bath.

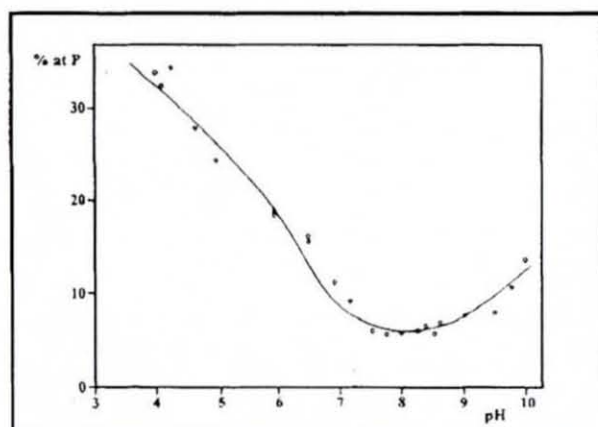


**Figure 3-2 Phosphorus content in the NiP electroless film obtained in a wide range of pH adjusted with  $\text{NH}_4\text{OH}$  [111]**

Temperature is the most important factor to affect the deposition rate [91]. Below  $60^\circ\text{C}$ , the reaction takes considerably more time to start and the coating rate is also very slow. As the temperature increases the deposition rate increases, but at high temperatures the bath can decompose. According to Schlesinger when the temperature of the bath is increased to  $90^\circ\text{C}$ , it becomes very difficult to maintain the pH and the quality of the coating decreases [40], so temperatures over  $90^\circ\text{C}$  are not recommended in the literature.

As with the electroless copper process, the reaction requires a catalytic surface to be present. The adsorption of the reducing agent on the substrate surface must occur in order to promote its oxidation. Palladium based catalysts are the most widely used for

electroless nickel deposition. Nevertheless, the NiP electroless process may occur on other substrate materials under given conditions, for example, stainless steel [113] can become active at suitable temperatures. For metals such as Al, Fe, and Zn, the nickel deposition is initiated by galvanic displacement giving rise to a catalytic surface [28]. The nickel deposition reaction could happen on the surface of particles present in the solution when there are little or no stabilisers. As the formation of these colloid particles is uncontrollable and the nickel deposition process is autocatalytic, the electroless nickel bath can decompose spontaneously, especially in acid baths, so different stabilisers are added to prevent this. However, the mechanism of stabiliser control is also complex, therefore, alkaline hypophosphite baths are often used because a stabiliser is not essential. However, Riedel [23] has reported that the deposition rate is slower in alkaline solutions and the deposits formed are more porous and less corrosion resistant.

Apart from hypophosphite, boron compounds and hydrazine are candidates as reducing species for electroless nickel [23]. Suitable boron compounds include borohydride, diethylamineborane, monomethylamineborane, dimethylamineborane and trimethylamineborane and the deposits formed consist of NiB in this case. Hydrazine acts as a strong reducing agent for electroless nickel, but unfortunately the deposits formed lack many of the attributes of those based on NiP or NiB formed from hypophosphite or boron-containing reducing agents respectively.

Stress in the electroless nickel coating comes from two sources: the mismatch of the coefficient of thermal expansion between the substrate and the EN coating and the coating growth [37]. The stress is connected to many factors during deposition, such as phosphorous content, bath pH value, working life of the solution, and heat treatment. When the P content is reduced or the pH value increases, the intrinsic stress in the coating will change from compressive stress to tensile stress [114, 115]. Compressive stress can benefit the adhesion of the EN coating to the substrate; however, a high level of tensile stress will induce cracks and lead to adhesion failure [114, 116]. With the aging of the plating solution, the intrinsic stress will increase, which is related to the concentration increase of  $H_2PO_3^{2-}$  during the working life of the plating solution. Stress will also increase with the thickness of an EN coating.

### 3.3 Experimental

#### 3.3.1 Material

A list of materials used for the electroless nickel process is summarised in Table 3-1 with manufacturers name and application specified for each material. The deposition route was very similar to that for electroless copper deposition except that for the final step electroless nickel was used instead.

**Table 3-1 List of materials and suppliers**

<b>Product</b>	<b>Supplier</b>	<b>Process Step/Application</b>
CMZ glass	Qioptiq	Glass substrate
Decon 90	Fisher scientific, UK	Glass cleaning
Methanol	Fisher scientific, UK	Solvent
3-Aminopropyltrimethoxy silane	Aldrich	Surface treatment
Circuposit 3340	Rohm and Haas	Pre-dip
Circuposit 3344	Rohm and Haas	Catalyst
Sodium hydroxide	ACROS ORGANICS	Accelerator
Nickel (II) sulphate hexahydrate	Fisher scientific, UK	Electroless Nickel
Sodium hypophosphite monohydrate	ACROS ORGANICS	Electroless Nickel
Tri-sodium citrate dihydrate	Sigma-Aldrich	Electroless Nickel
Ammonium sulphate	Sigma-Aldrich	Electroless Nickel
Ammonium hydroxide water solution	Fisher scientific, UK	Electroless Nickel

### 3.3.2 Electroless NiP process

Experimental pre-treatment details were similar to those for electroless copper, which can be found in Table 3-2. An acceleration step was added after the catalyst step as the EN bath was not self-accelerated. An aqueous 10% sodium hydroxide solution was used as an accelerator for 3 min at room temperature. The compositions and operating conditions of the electroless nickel bath are also shown in Table 3-2, which is a popularly used composition [72, 91]. The  $\text{NH}_4\text{OH}$  was used to adjust the pH value to 9.

**Table 3-2 Electroless NiP process route**

1-7	Same procedure as the electroless copper deposition			R.T.
8	Accelerator	sodium hydroxide	3 min	R.T.
9	Rinse	DI water	3-5 min	R.T.
10	Electroless Nickel	$\text{NiSO}_4 \cdot 6\text{H}_2\text{O}$ (26 g/l) $\text{Na}_3\text{C}_6\text{H}_5\text{O}_7 \cdot 2\text{H}_2\text{O}$ (60 g/l) $\text{NaH}_2\text{PO}_2 \cdot \text{H}_2\text{O}$ (16 g/l) $(\text{NH}_4)_2\text{SO}_4$ (30 g/l) $\text{NH}_4\text{OH}$ (Adjust pH value to 9)	0-30 min	45-90°C controlled in water bath
11	Rinse and dry	DI water	10 min	R.T.

## 3.4 Results and discussion

### 3.4.1 Deposition rate and alloy composition

Temperature is one of the most important parameters affecting the electroless nickel deposition rate since many of the individual reactions only take place significantly above 60°C. Figure 3-3 shows the thickness of deposited nickel as a function of the plating temperature at a fixed plating time of 30 min at a bath pH value of 9. Each point was collected from 3 samples with a total of at least 10 measurements. It can be seen that the deposition rate increased with increasing temperature from 45°C to 90°C, and that there was an approximately parabolic relationship between deposition rate

and temperature above 60°C. It is necessary to point out that the electroless nickel film was not continuous at lower temperatures, such as 45°C and 50°C - these operating temperatures were used only for investigation of the deposition rate. At 90°C it can be seen that a deposition rate of over 2.5  $\mu\text{m}/30\text{min}$  was achieved. While the higher deposition rate makes this region attractive, there is a danger of instability of the bath at this high temperature. Balancing the deposition rate and adhesion strength, a bath temperature of 70°C was mainly used for further electroless nickel research.

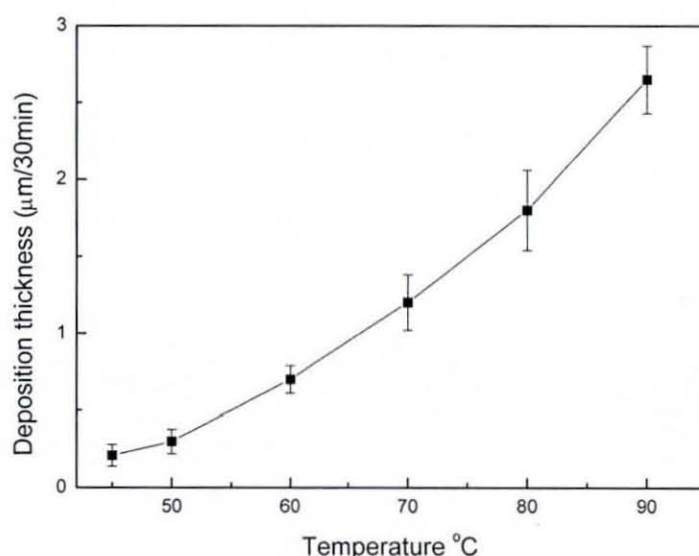


**Figure 3-3** Dependence of deposition rate on bath temperature

Figure 3-4 presents the nickel growth as a function of plating time in the electroless nickel solution at 70°C. It can be seen that the nickel thickness was 1.25  $\mu\text{m}$  after 30 min. Compared with electroless Cu deposition, the EN deposition rate was about three times higher. From the data it can be seen that the nickel deposit thickness linearly increased along with the plating time. The deposition rate was around 40 nm/min.

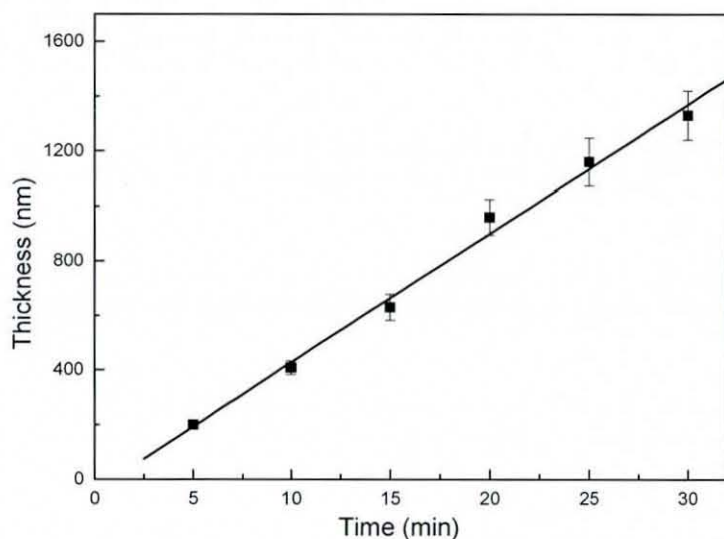
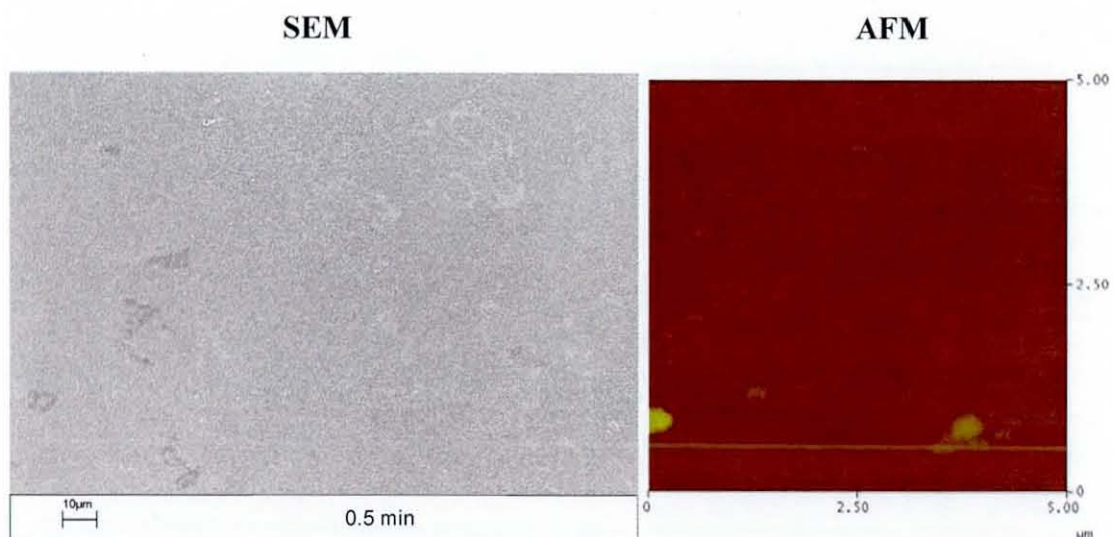
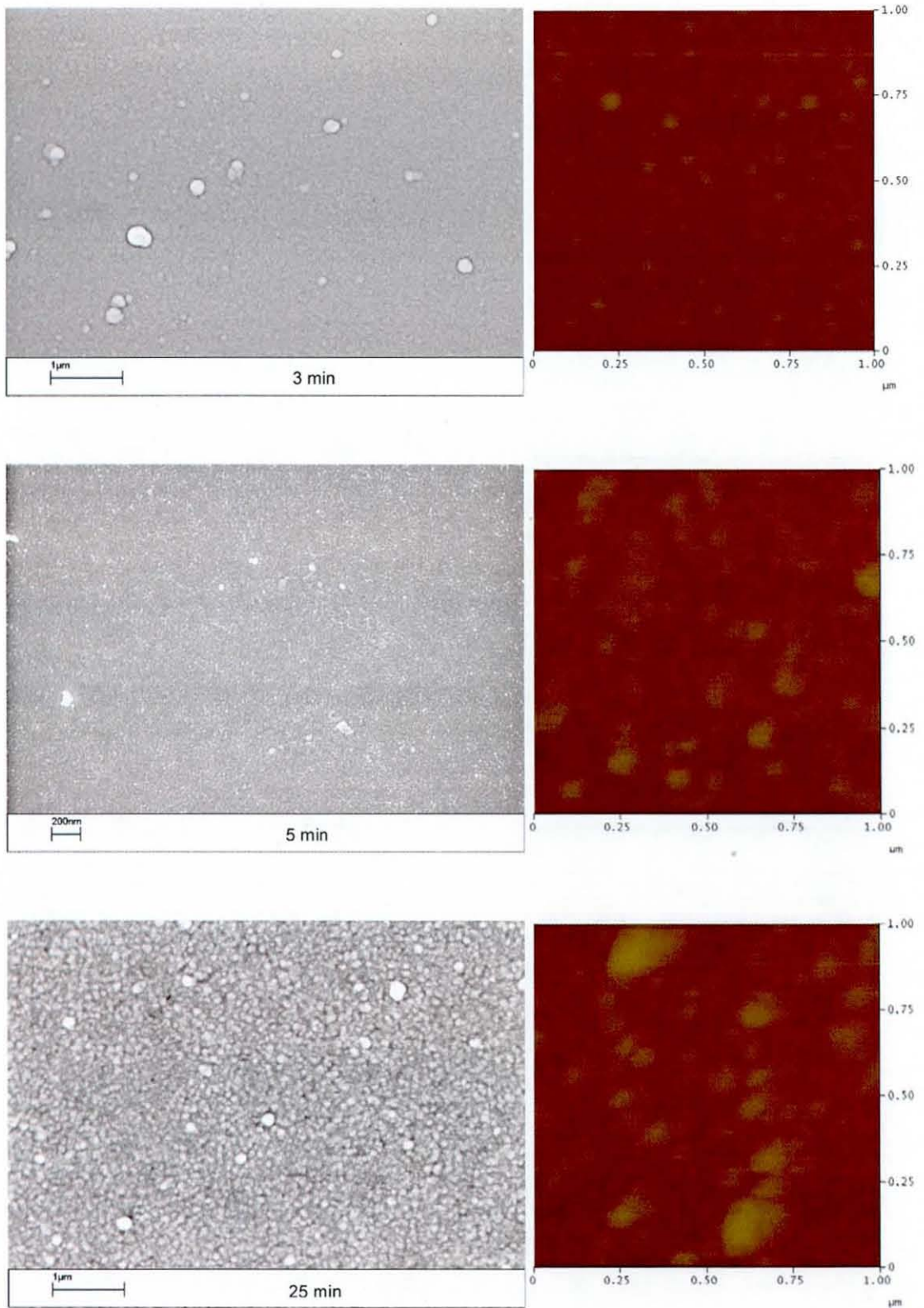


Figure 3-4 NiP thickness as a function of deposition time at 70°C

### 3.4.2 Microstructure of NiP deposits

Electroless deposited NiP coatings were found to be amorphous in terms of X-ray structure determination, which is consistent with the results in the literature [23, 24]. Matsuoka [117] showed that electroless nickel deposits which have not been heat-treated, can have structures ranging from extremely small crystallites (ca 5 nm) to those which are fully amorphous. In the current electroless plating process, the phosphorous content of the deposits was found to be about 8.7 at.%. Figure 3-5 shows the SEM and the corresponding AFM images of electroless nickel deposits for different immersion times. The deposition temperature was kept constant at 70°C.





**Figure 3-5 SEM and AFM images of electroless NiP deposits on glass with different plating time: (A) 30 sec, (B) 3 min, (C) 5 min, (D) 25 min**



The surfaces of the samples for the first 3 min were very similar and there were few differences in the SEM images. Figure 3-5A and B show that the deposit surfaces were very smooth, without any observable voids or breaks on the outer surface of the nickel coating. From Figure 3-5D it was found that, if the plating time was 25 min, the number of voids increased, which was thought to be due to stress in the nickel coatings. The coating roughness was measured over a  $1 \mu\text{m} \times 1 \mu\text{m}$  area after the AFM examination: the average roughness  $Ra$  of these samples prepared at  $70^\circ\text{C}$  are listed in Table 3-3. The AFM measurements reveal that the roughness of the nickel coating was very small when the coating thickness was less than 300 nm. The coating roughness increased with increasing coating thickness. As the nickel thickness increased from 72 nm to 1130 nm, the surface roughness increased from 0.36 nm to 11.7 nm. In the electroless NiP plating process, many factors affect the relationship between the surface roughness and coating thickness such as plating temperature, plating time, bath constituents, etc. It is difficult to establish the specific reason for the relation between roughness and thickness revealed in this experiment, but it is in good agreement with that observed for many plating methods [94, 118].

**Table 3-3 The roughness of different thickness NiP coatings**

Deposition time (min)	Film thickness (nm)	Roughness, $Ra$ (nm)
1	72	$0.36 \pm 0.05$
3	154	$0.64 \pm 0.09$
5	219	$1.2 \pm 0.2$
8	365	$2.7 \pm 0.3$
10	486	$3.2 \pm 0.3$
12	573	$6.7 \pm 0.8$
15	770	$9.5 \pm 1.3$
25	1130	$11.7 \pm 1.6$

### 3.4.3 Electrical properties

The electrical property of the NiP is an important parameter for further application, therefore, experiments were carried out to measure resistivity. As for the electroless Cu coating, a 4-point probe was used for this measurement.

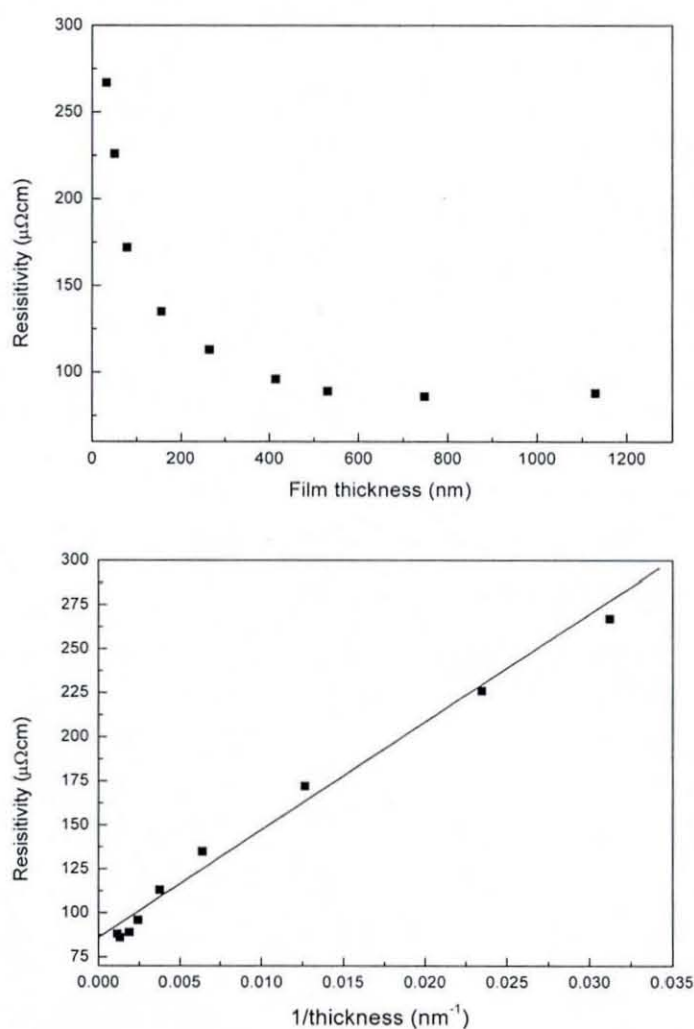


Figure 3-6 NiP film resistivity as a function of thickness

As shown in Figure 3-6 the resistivity of the NiP films decreased rapidly with increasing film thickness, with the resistivity dropping from 260  $\mu\Omega\text{cm}$  to 80  $\mu\Omega\text{cm}$  as the thickness increased from 30 to 1130 nm. The final value of 80  $\mu\Omega\text{cm}$  is slightly smaller than that of Murarka's value [18], 110  $\mu\Omega\text{cm}$  for an amorphous NiP film, but is larger than the reported resistivity of evaporated Ni on glass substrates that ranged

from 46  $\mu\Omega\text{cm}$  at 31 nm down to 18.3  $\mu\Omega\text{cm}$  at 115nm [119]. Yoon [120] reported that the electrical resistivity of the layer increased with increasing P content for which the measured resistivity for Ni-7wt.%P and Ni-10wt.%P were 16.8 and 18.1  $\mu\Omega\text{ cm}$ , respectively. The value of NiP resistivity obtained here is much higher than these values and is possibly related to the extent of the tensile strain, which can give rise to an increased resistivity within the film [31] and may also be due to the amorphous structure. However, this value is consistent with that from Riedel [23].

### **3.5 Conclusion**

Compared with electroless Cu, electroless NiP shows some obvious advantages for glass metallisation for high density interconnection. Firstly, the deposition rate is much faster than that of the electroless Cu process, the nickel thickness could be 1.25  $\mu\text{m}$  when the plating time was 30 min in the electroless nickel bath at 70°C, while the electroless Cu film was only about 150 nm. However, as will be seen later, good adhesion can only be obtained if the thickness is below 740 nm. Secondly, the extremely smooth surface is suitable to reflect the optical signals for use in optical interconnection. It can be seen that the roughness was less than 3 nm when the electroless NiP film was built up to 400 nm. However, electroless NiP also contains some apparent disadvantages, such as low conductivity and poor solder wettability [110], which affects the electrical signal transmission speed and subsequent reflow processes, respectively. So in order to fulfil the aims of this project, further study of electroless deposition of both Cu and NiP was necessary.

---

## **Chapter 4    Interfacial Adhesion of Electroless Cu and NiP to Glass**

---

### ***4.1 Introduction***

The microelectronics industry requires continuous advances due to ever-evolving technology and the corresponding need for higher density substrates with smaller features. New dielectric materials with smoother surfaces (to avoid signal scattering) and enhanced electrical properties (to minimize signal RC delay and loss) are used [1]. At the same time, adhesion between the electrical tracks and substrate must be maintained in order to preserve package reliability and mechanical performance [7]. Although glass exhibits excellent optical and thermophysical properties, the smooth surface and low surface energy results in quite weak metal/glass interfacial adhesion. This has been a dominant problem that has limited the more widespread use of glass.

In order to enable the use of glass materials instead of traditional substrates, two main advances must be made: increased catalyst adsorption and increased adhesion of the catalyst to electroless copper/nickel plating. Some widely used methods to improve surface activation to achieve sufficient catalyst adhesion were briefly reviewed in chapter 2. Among them, SAM formation was considered to be a suitable technique for glass surface modification. This chapter focuses on understanding the SAM modified glass surface and the influence of process parameters on the adhesion of electroless coatings.

## **4.2 Literature review of thin film adhesion**

### **4.2.1 Introduction**

Adhesion is a complex phenomenon relating to the physical effects and chemical reactions at the interface. Mittal [121] defines adhesion in three different forms: (I) Fundamental adhesion, (II) Thermodynamic adhesion and (III) Practical adhesion. Fundamental adhesion is defined as the summation of all interfacial intermolecular interactions between the contacting materials. The thermodynamic adhesion signifies the change in free energy when an interface is formed. The practical adhesion signifies the force required to remove a film from the substrate. The adhesion of a film to the substrate is strongly dependent on the chemical nature, cleanliness, and the microscopic topography of the substrate surface. The adhesion is better for higher values of (1) kinetic energy of the incident species, (2) adsorption energy of the deposit, and (3) initial nucleation density. The presence of contaminants on the substrate surface may increase or decrease the adhesion depending on whether the adsorption energy is increased or decreased, respectively. Also, the adhesion of a film can be improved by providing more nucleation centres on the substrate, for instance, by using a fine-grained substrate or a substrate pre-treated with suitable materials [76].

Based on the above considerations, adhesion of the metal/glass system can be assumed to be enhanced by the following mechanisms: (1) increased interlocking between the metal layer and modified glass surface [122], (2) formation of chemical bonding or adsorption between electropositive metal and electronegative hydrophilic groups on the modified glass surface, (3) removal of any weak boundary layers. This literature review considers the different ways in which the adhesion of electroless coatings can be improved by covering a range of substrates including polymers, glass and silicon.

### **4.2.2 Adhesion improvement**

#### **Electroless coating on polymers**

From the literature, advanced epoxies, polyimides and other high performance materials have been shown to have poor adhesion to electroless copper with traditional pre-treatment steps, mainly because much less surface roughness is created

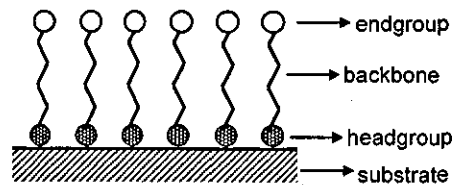
[84, 87, 123]. In order to increase adhesion between these materials and electroless copper, techniques such as plasma surface treatments for chemical and physical modifications of the polymer surface, graft polymerisation to insert adhesion improving groups in the polymer structure, coupling agents, and adhesive metal layers have been widely investigated [85, 124, 125]. These have been applied with varying levels of success, and each approach has advantages and limitations.

One approach is the addition of functional groups onto the surface of polymers through wet-chemical synthesis as well as ultraviolet, thermal, and plasma grafting processes. Wet-chemical synthesis processes have been used to add organosilanes such as 2-(trimethoxysilyl)ethyl-2-pyridine and 2-(diphenylphosphino)ethyltriethoxy silane, which contain nitrogen groups, to polymer surfaces in order to enable electroless nickel deposition [89, 126]. These treatments have the advantage of being more cost effective than plasma treatments, but have not been demonstrated to have the same efficacy. Grafting processes have similarly been used to add nitrogen containing groups to a variety of surfaces, including silicon, glass, polytetrafluoroethylene, polyimide and polyethylene [88, 90].

A common link in many of the plasma and wet-chemical investigations is the addition of nitrogen-containing functional groups on the surface. These groups have been shown to enhance catalyst adsorption and adhesion with electroless copper. In many cases these nitrogen groups are thought to interact with the palladium catalyst used for electroless copper deposition and also with the copper layer itself [88, 126, 127]. Details of the interaction between the modified surface and either palladium catalyst particles or electrolessly deposited copper have not been determined. Previous work [128] indicates that wet-chemically treated or oxygen etched polyimide surfaces react with  $\text{SnCl}_2$  in the bath to produce C-O-Sn linkages. These Sn groups then aid the reduction of  $\text{PdCl}_2$  to Pd(0) on the surface. This surface coverage of catalyst is important for the electroless copper deposition since the Pd on the surface initiates the copper deposition reaction. With sputtered or evaporated metals, however, it is oxygen containing groups that have been found to be more effective in enhancing adhesion [44].

## Electroless coating on glass and silicon

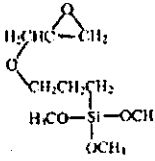
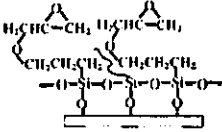
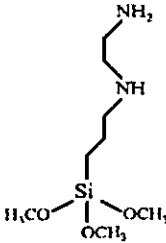
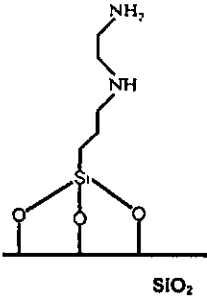
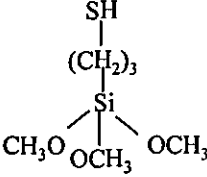
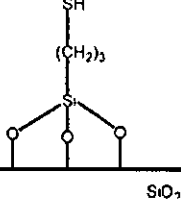
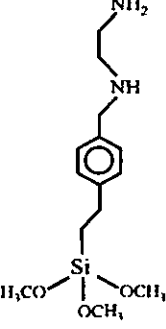
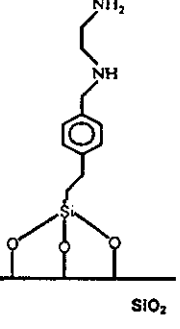
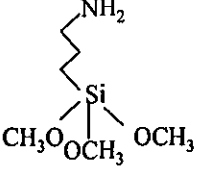
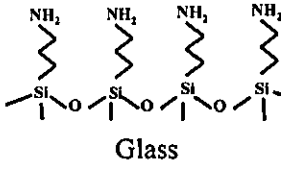
As mentioned before, the self-assembled monolayer is a potential approach to modify the glass surface to improve adhesion [129]. Self-assembled monolayers are ordered molecular assemblies that are formed by the adsorption of a surfactant with a specific affinity of its headgroup to a substrate. The adsorption of the headgroup on the substrate combined with the interactions between the chains from adjacent molecules favour spontaneous formation of a SAM having order and defined chemical composition. The endgroup can be chosen from a variety of chemical functionalities [130]. Figure 4-1 shows a schematic, including the constituents of a SAM.



**Figure 4-1 Schematic constituents of a SAM-molecule**

Self-assembled monolayers have been fabricated on substrates and modified into hydrophilic/ hydrophobic surfaces to act as templates [131]. Metallic patterning can thus be achieved on glass substrates on which patterned SAM are formed. The driving force of the site-selective growth is the difference in wettability of the hydrophilic/ hydrophobic surface. The monolayer is deformable and can relieve internal stresses [132]. Interfacial bonds are broken by hydrolysis, but many then reform, making the bond ductile and permitting stress relaxation. Table 4-1 shows the evolution of several different silanes coupled onto glass substrates. Among the most studied systems of SAM formation, APTS and MPTS are most useful on different hydroxylated surfaces such as oxidized silicon, mica or glass. Ramanath et al. [85] reported that the use of 0.7 nm thick SAMs comprising mercaptopropyl trimethoxy silane molecules inhibited Cu diffusion and enhanced adhesion at the Cu/SiO<sub>2</sub> interface.

Table 4-1 Evolution of some typical silanes coupled onto glass substrates

Materials	Structure	Solution composition	Reaction	Ref.
GPS		1ml GPS, 99ml acetic acid/ sodium acetate buffer solution (pH = 5)		[88]
EDA-Si		1% EDA-Si in water		[132]
MPTS		MPTS:H <sub>2</sub> O: isopropyl alcohol = 1:1:40 (v/v)		[90]
PEDA		solution containing methanol, water and PEDA in the volume ratio 95:4:1 that was slightly acidified with acetic acid to a concentration of 10 <sup>-3</sup> M.		[133]
APTS		1) 1 vol.% APTS added to the solvent acetone, ethanol and toluene 2) 5 × 10 <sup>-3</sup> mol/l of APTS mixed with 95% methanol, 5% water		[46, 76]



Siloxane-type SAMs can be formed on substrates having OH groups such as glass, silicon, metal oxides, or metals having a thin natural oxide surface layer. Organosiloxane SAMs of alkylalkoxysilanes are chemisorbed on a Si substrate that has silanol groups (-SiOH) via Si-O-Si bonds. Figure 4-2 shows the reaction of (3-aminopropyl)-trimethoxysilane, APTS ( $\text{NH}_2\text{-(CH}_2\text{)}_3\text{-Si(OCH}_3\text{)}_3$ ) with the surface of glass. When glass samples are immersed into a dilute APTS solution, there are two major steps to form the self-assembled layer. Firstly, the hydrolysis of  $\text{-Si(OCH}_3\text{)}_3$  to trisilanol-  $\text{Si(OH)}_3$ , which is fast. Secondly, condensation polymerisation of trisilanol and surface  $\text{-OH}$  groups to produce a polysiloxane network that is covalently bonded to the surface, which is a slower reaction. The  $\text{NH}_2$  groups exposed at the surface are free to interact with other materials.

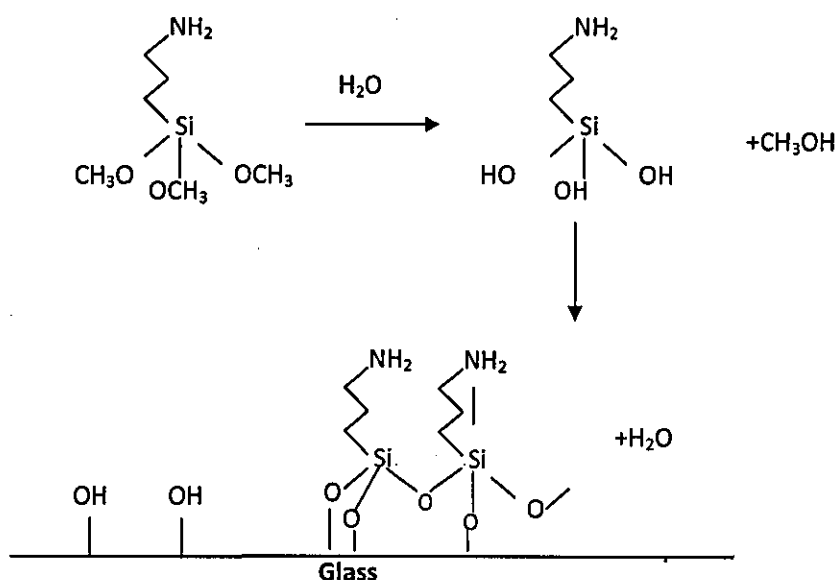


Figure 4-2 The reaction of APTS with the surface of glass

Comyn [76] reported pH 8 is the optimum for APTS formation. Under this condition, glass and silanes bond well. Xu [46] and Chen [88] used XPS to investigate the attachment of Pd catalyst to an APTS SAM. The results indicated that the formation of coordination bonds between Pd ions and nitrogen atoms of APTS SAMs serves as an important binding mechanism. As is well known, the amine group is a strong electron donor and possesses great ligand capability to transition metal ions due to the

lone pair electrons of the nitrogen atom. On the other hand, Pd(II), as a soft metal ion, whose outermost electron is configured as  $4d^85s^05p^0$ , possesses empty lower energy orbitals for accepting electrons [46].

Investigations of the reaction of amine-terminated silanes with silica have shown that the hydroxyl groups deriving from hydrolysis of the alkoxy groups in silanes can form hydrogen bonds with the surface hydroxyl groups of silica, and then a siloxane forms via the condensation between the hydroxyl groups. All of the literature reviewed indicated that APTS is suitable for modifying glass surfaces for the process of electroless deposition [76, 135].

### ***4.2.3 Adhesion measurement techniques***

Techniques to measure the practical adhesion of thin films have been reviewed extensively elsewhere [121, 136, 137]. Table 4-2 lists a number of methods for measuring the adhesion of thin films which have appeared in the literature. Due to the different measurement conditions, the results obtained from the different types of tests are not comparable. Each method has its advantages and disadvantages. The theoretical background for the electromagnetic tensile test, laser spallation test and ultracentrifuge test are quite complex and the interpretation of results difficult. Bend tests and peel tests have been widely used in defining adhesion, but are only applicable to thick films rather than ultrathin films. Tape tests and scratch tests were used for qualitative and quantitative adhesion measurements respectively in this study.

Table 4-2 Methods to determine adhesion

Qualitative	Quantitative
Tape test	Direct pull off method
Abrasion test	Tangential-shear test
Bend and stretch test	Electromagnetic tensile test
Shearing stress test	Laser spallation test
X-ray diffraction test	Ultracentrifuge test
	Ultrasonic test
	Thermal method
	Scratch test

### Tape test

Possibly the most widely used and, certainly the simplest and quickest method of adhesion assessment, is the tape test, shown schematically in Figure 4-3. An adhesive tape is stuck to the film and then removed, a check being made to see if the film adheres to the substrate or is torn off together with the tape. This method gives only qualitative results. The tape test is simple to execute, but peel-strength values are affected by a number of experimental parameters, e.g. angle, rate and width of peel. In practice, the peel test can be applied when the adhesion force is below  $2000 \text{ Nmm}^{-2}$  [121, 137]. 3M Scotch 600 and 3M-56 Tape were used in the tape tests presented here.

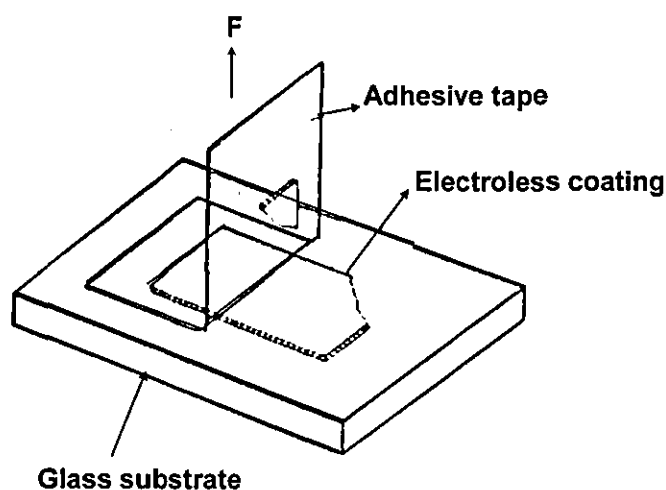


Figure 4-3 Schematic representation of the tape test

### Scratch test

The scratch test has been used to assess the adhesion of thin coatings for some time and is a useful tool for coating development or quality assurance. However, the test is influenced by a number of intrinsic and extrinsic factors which are not adhesion-related and the results of the test are usually regarded as only semi-quantitative. In the test process, a diamond tip is driven over a coated surface to produce a scratch. The load on the diamond tip is increased linearly to induce a shear force in the nearby film that is proportional to the applied load. As the mechanical properties of the film and the substrate are different, there is a discontinuity in the shear stress at the interface which, when sufficiently high, induces adhesive failure at a critical load [138, 139]. This may be identified by an abrupt change in either the depth and /or the friction signal or by identifying the failure point under the microscope. The indenter load at this failure point is then determined and is recorded as a critical load.

### **4.3 Methodology and experimental procedure**

Based on the literature review, there are several possible approaches that can be taken to prepare a glass surface for plating with electroless copper/nickel. Adhesion can be increased through traditional means (surface roughening) or more advanced techniques that take advantage of chemical bonding. The purpose of each of these treatments is to prepare the substrate surface for electroless copper deposition by

creating a surface that is more suitable for catalyst adsorption and adhesion. The literature points to the efficacy of nitrogen-containing functional groups for chemical bonding improvements in terms of both catalyst adsorption and adhesion with electroless copper – for this reason APTS was used to form a SAM prior to catalyst adsorption in this study.

The adhesion of the copper and nickel films to glass was determined using tape tests and scratch tests and the influence of process parameters on adhesion identified. Due to the importance of surface composition and surface energy, X-ray photoelectron spectroscopy (XPS) and contact angle analysis (together with SEM) were used to characterise the glass surface at each stage of the plating process and subsequently the location of the failure interface was determined in order to understand which area of the process required further improvement.

### X-Ray Photoelectron Spectroscopy (XPS)

XPS analysis is a surface sensitive technique that can be used to measure chemical compositions and bonding states in the top 5-10 nm of a sample. XPS measurements were carried out on a VG ESCALAB spectrometer equipped with a hemispherical electron analyser and Al K $\alpha$  X-ray source (1486.6 eV photons). The X-ray source was run at a power of 160 W (20 kV and 8 mA). The samples were mounted on the sample stubs by means of double-sided adhesive tape. The core-level spectra were obtained at the photoelectron takeoff angle, with respect to the sample surface of 90°. The pressure in the analysis chamber was maintained at  $5 \times 10^{-7}$  Torr or lower during each measurement. To compensate for surface charging effects, the binding energies (B.E.) were referenced to the internal C 1s (284.9 eV) standard. The survey scan spectra shown here were collected from 0 eV to 1100 eV using a pass energy of 85 eV, A4 slit size and dwell time of 20 ms, and the core scan spectra were done using a pass energy of 25 eV and dwell time of 50 ms. Surface composition was obtained from survey scans using the instrument software. For more detailed analysis of individual peaks, both B.E. values and peak areas were computed by fitting the curves using XPSPEAK41 software, the line width (full width at half-maximum, FWHM) and Lorentzian-Gaussian ratio of peaks was maintained constant for all components

in a particular spectrum. Surface atomic ratios were calculated from the peak areas normalised by relative atomic sensitivity factors.

## Contact Angle Measurement

Contact angle (CA) measurement is useful for determining wetting behaviour and surface free energy estimation, which is an important parameter for the solution based deposition process. The degree to which a liquid coating wets a solid surface is measured by the contact angle  $\theta$ . Low values of  $\theta$  indicate that the liquid spreads, or wets well, while high values indicate poor wetting. Contact angle measurements were made using a DataPhysics Instruments (Germany) contact angle goniometer. Diiodomethane (obtained from Sigma-Aldrich) and water were used as measurement liquids to define the contact angle. The dosing rate was 2  $\mu\text{l/s}$ , and dosing volume was 1.0  $\mu\text{l}$ . The surface energy was determined from the Ström equation by using the Owen-Wendt-Kaeble method [140].

## **4.4 Results and discussion**

### **4.4.1 Surface analysis of electroless deposition on glass**

#### **4.4.1.1 Contact angle measurements**

Table 4-3 shows the contact angle and surface energy results for glass treated using different solutions including DI water, Decon and APTS silane. The results showed that Decon 90 was more suitable to clean the glass surface than DI water. When glass was immersed in DI water for 16 hours, the contact angle was about  $71^\circ$ , indicating poor wettability, and even if immersed for over 48 hours, the contact angle was still  $70^\circ$ , which indicated that DI water alone was not effective as a cleaning agent. On the other hand, the contact angle of glass which was immersed in Decon 90 for 8 hours decreased to  $42^\circ$ , while the surface energy increased greatly. It can be seen that as a result of cleaning, the dispersive component was stable, but the polar component increased. The key dominating factor in the surface wettability modification is the polar component, which could be increased from 9 mN/m to 30 mN/m.

Table 4-3 Contact angle measurement results

Process	CA(°) Water	CA(°) Diiodomethane	Dispersive Component (mN/m)	Polar Component (mN/m)	Surface Energy Total (mN/m)
DI water- 16h	71.1 ± 2.7	54.9 ± 1.5	31.29	9.57	40.86
DI water- 48h	70.0 ± 2.3	55.3 ± 1.5	31.93	10.58	42.51
Decon 90- 8h	42.5 ± 3.1	55.9 ± 2.6	29.57	27.74	57.31
APTS-2h	38.6 ± 3.0	57.8 ± 3.2	29.85	30.32	60.17

To obtain good conditions for the growth of the self assembled monolayer, the relationship between contact angle and immersion time was investigated for the APTS treatment. Figure 4-4 shows the water contact angle as a function of immersion time in the APTS solution at a concentration of  $5 \times 10^{-3}$  mol/l at room temperature. All the samples were dipped into Decon solution for cleaning before APTS formation. The water contact angle was greatly reduced after the first hour, following which, the contact angle decreased only slightly.

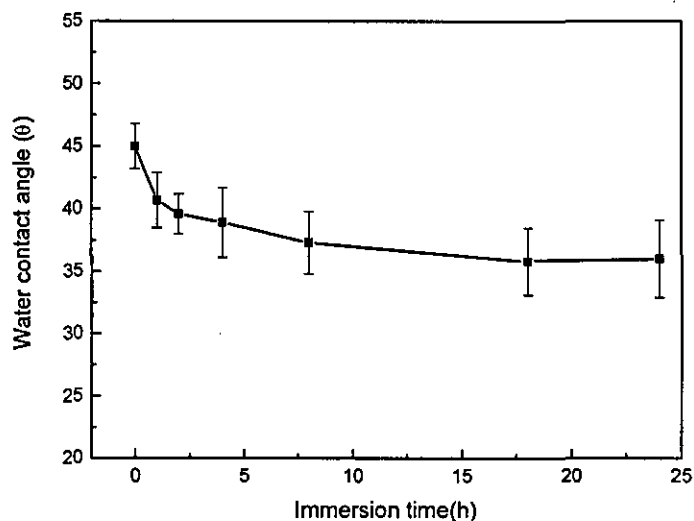


Figure 4-4 Water contact angle as a function of immersion time in the APTS solution

#### 4.4.1.2 XPS analysis

Figure 4-5 presents XPS survey scans of the glass surface after cleaning in Decon 90 for 8 hours and without cleaning. Each scan clearly shows the presence of oxygen, silicon and carbon, with the latter due to contamination adsorbed from the air.

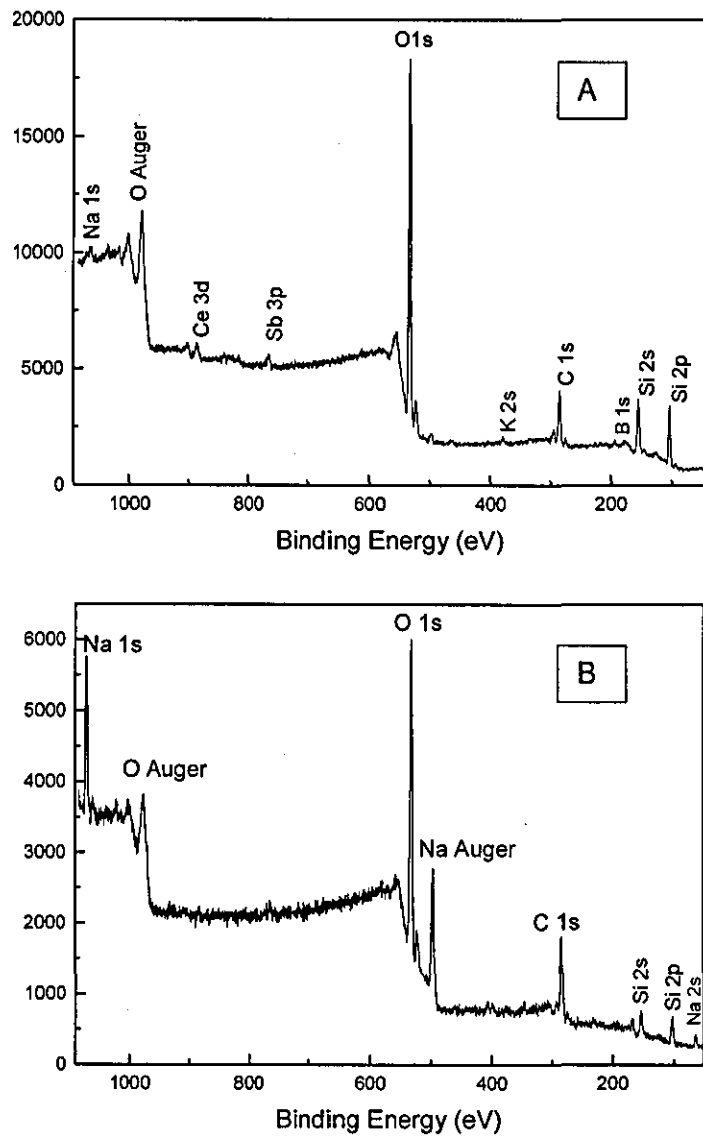


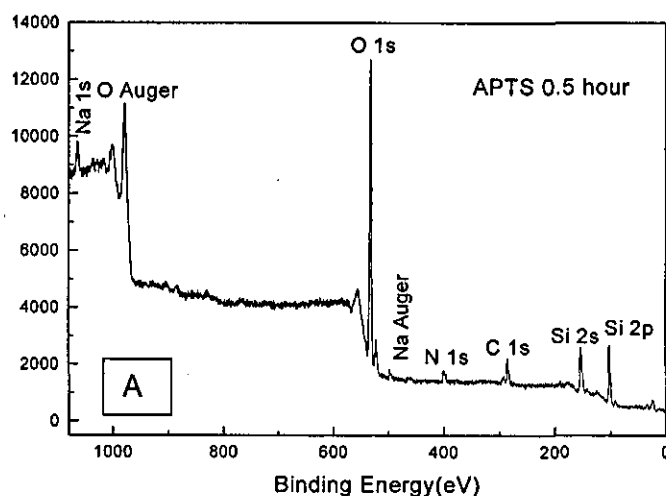
Figure 4-5 XPS spectra of glass surface (A) as-received, (B) after cleaning with Decon 90 for 8 hours

The presence of Ce, B, Sb, Na and K shown in Figure 4-5A was attributed to the chemical content of the glass substrate. After cleaning with Decon solution, the



spectrum reveals strong peaks due to Si and O with additional features associated with other elements present in the original material. The sodium signal at 1071.9 eV increased substantially and was probably left behind by the cleaning process as well as being part of the glass composition.

The XPS spectra of samples immersed in APTS solution for different times are shown in Figure 4-6. The main elements present in the surfaces were N, O, Si and C. The N peak (at 399.0 eV) originates from the amine groups of the APTS silane molecules, indicating their coupling to the glass surface and the formation of a self-assembled monolayer. This is further supported by the disappearance of many of the signals from the lower concentration elements visible in the earlier spectrum, due to their coverage by the silane which attenuates their photoelectron emission. Meanwhile, the C 1s signal intensity in the wide scan spectrum of the glass surface increases substantially after APTS silanisation for an extended immersion time. The O 1s (at 532.3 eV), Si 2s (at 151.3 eV), and Si 2p (at 101.0 eV) signals originate primarily from the glass and to a lesser extent from the grafted silane.



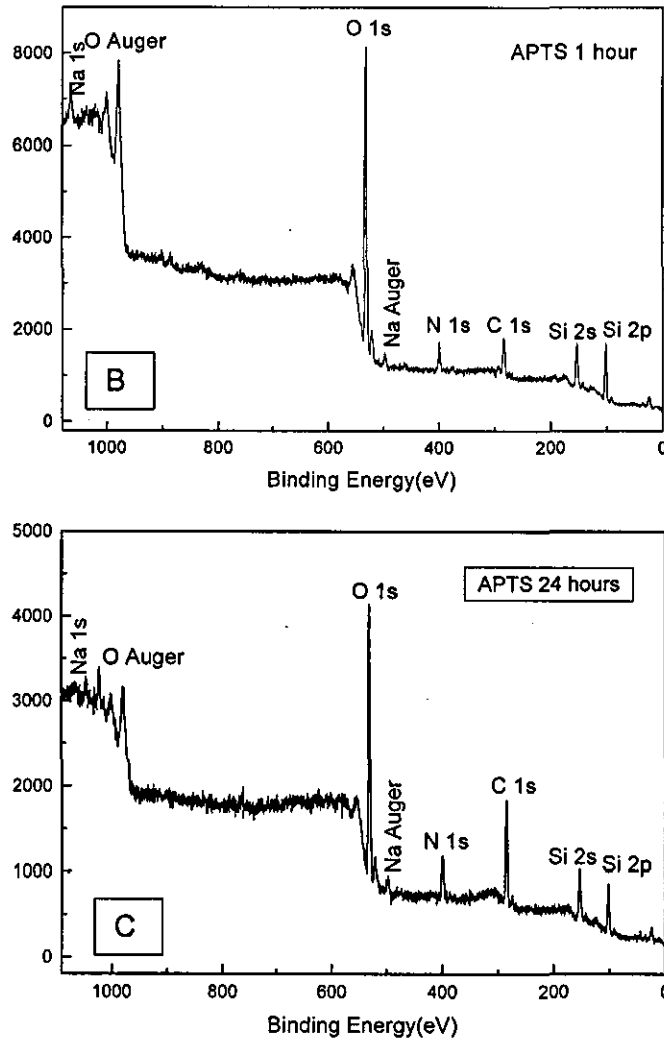


**Figure 4-6 XPS spectra of the glass surface after immersion in APTS solution for (A) 0.5 hour (B) 1 hour (C) 24 hours**

The quantitative results from all the XPS spectra of APTS modified glass with varying immersion time treatments are presented graphically in Figure 4-7.

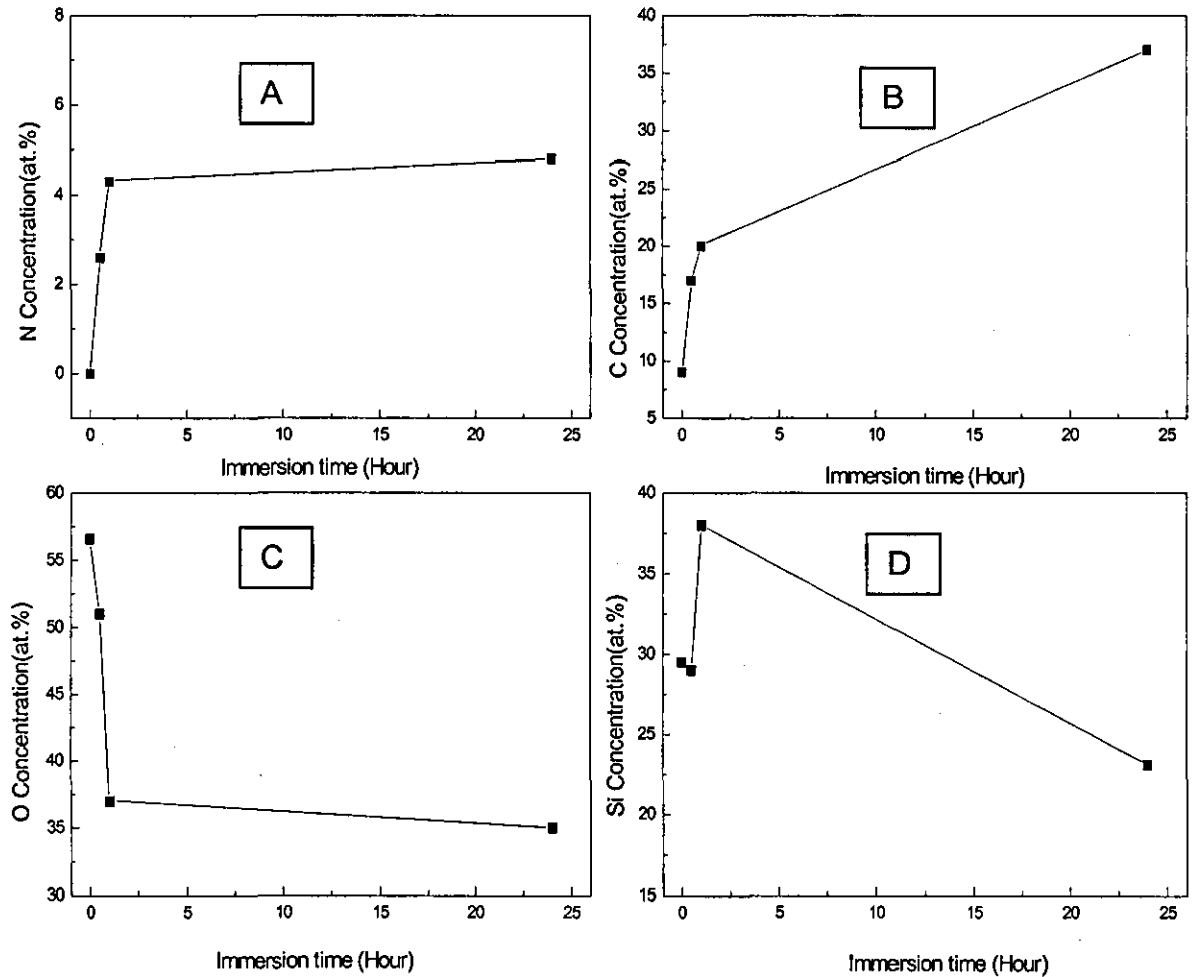
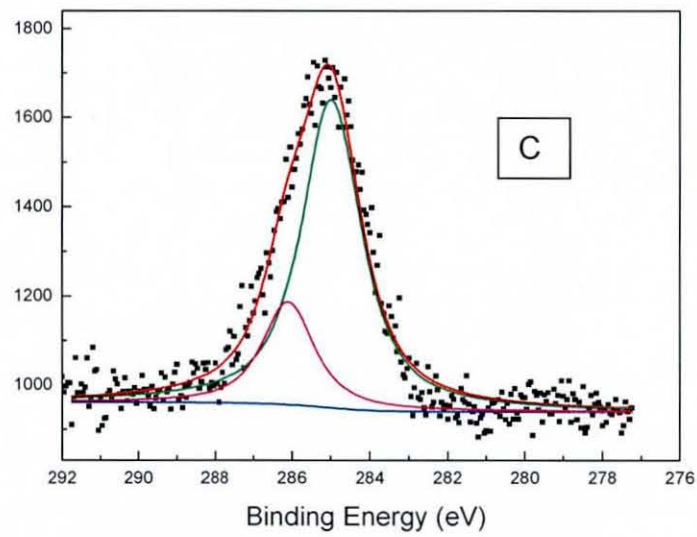
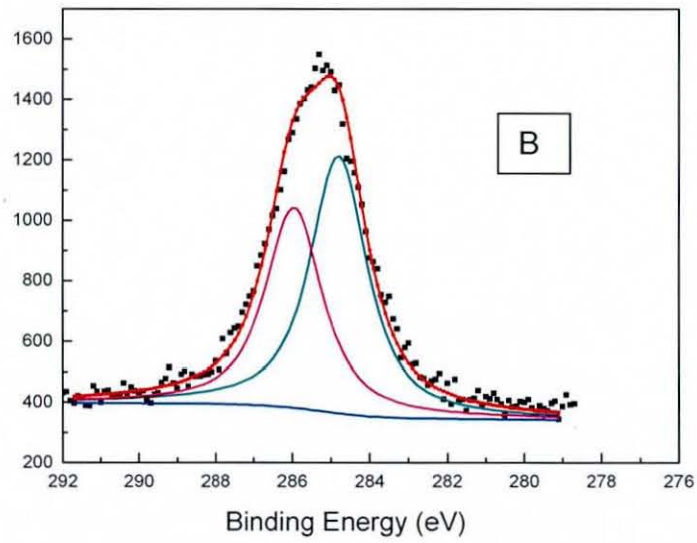
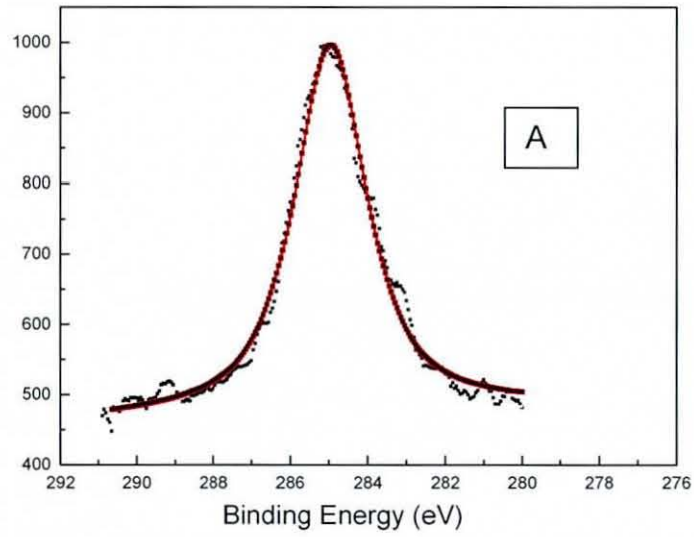


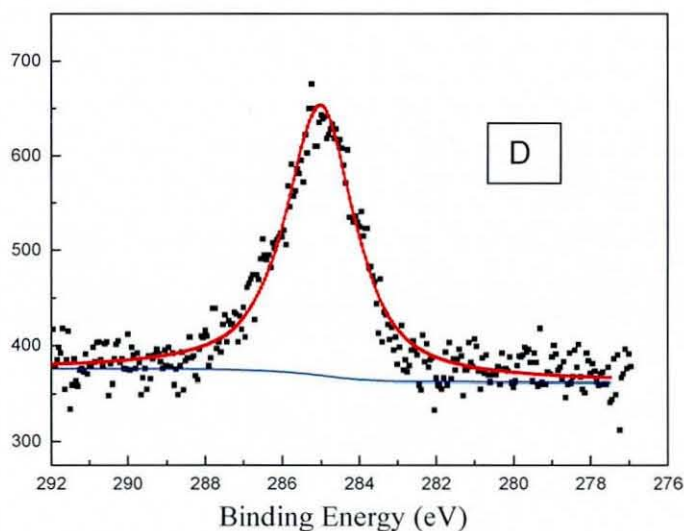
**Figure 4-7** Variation in the surface concentration with APTS treatment

With increasing immersion time the nitrogen content on the glass surface increased (Figure 4-7A). The 0.5 hour APTS-treated surface contained only 2.5 at.% nitrogen, while a 1 hour treatment increased the concentration to 4.2 at.%. This is due to more silane molecules reacting with the surface. As the immersion time increased to 24 hours, only a small further increase of nitrogen concentration, to 4.9 at.%, was observed. The treatment also showed a strong tendency to increase the carbon concentration on the surface (Figure 4-7B), with a 24 hour immersion increasing the carbon concentration to 37 at.%. The oxygen concentration at the surface decreased to 37 at.% after the 1 hour treatment (Figure 4-7C), after which it decreased only slightly more. The Si concentration changed with the immersion time as the glass substrate and the head group ( $-\text{Si}(\text{OCH}_3)_3$ ) from the APTS molecule both contribute to it. AFM measurements of surface roughness were made, for which there was a relatively small

change (0.9 nm – 2.1 nm) resulting from long SAM formation times. The APTS treatment, thus, has been shown to chemically modify the surface, without significant roughness generation.

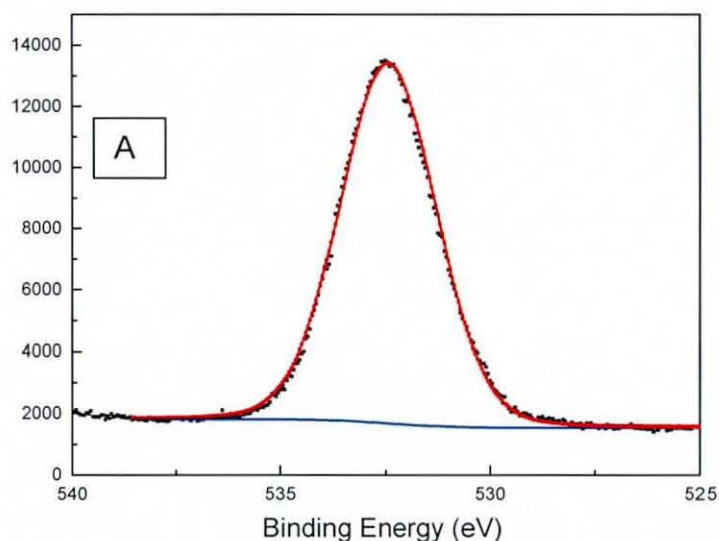
The use of XPS allows the detailed chemical states of the elements on the surface to be analysed. Figure 4-8 shows the C 1s spectra of the cleaned CMZ glass and the glass surface after APTS silanisation for 0.5 hour, 1 hour and 24 hours. On the clean glass, carbon can be found in one bonding state, which is attributed to the adventitious contamination of the surface. The C 1s spectrum of the silanised glass (B) and (C) exhibits two well-defined components revealing the various types of carbon environments: methylene groups in the propyl chain (C1-285.0 eV,  $\text{NH}_2\text{-(CH}_2\text{)}_3\text{-Si(OMe)}_3$ ) and a shoulder at higher binding energy that can be fitted by a second component centred at 286.8eV. This second peak matches the position of methoxy groups (C2-286.8 eV,  $\text{NH}_2\text{-(CH}_2\text{)}_3\text{-Si(OMe)}_3$ ) [135, 141] which is attributed to the remnant APTS on the surface. It was seen that peak C2 decreased with increasing immersion time and there was no methoxy group after 24 hours of silane treatment, indicating that the reaction was completed by this extended immersion time. The corresponding C:N atomic ratios for 0.5 hour, 2 hour, 24 hour treatments were 7.4:1, 8.2:1, 7.7:1, respectively. The theoretical ratio for C:N is 3:1 when all three methoxy groups are totally replaced by siloxane linkages. The obtained values are much higher than this theoretical ratio, which may be due to adsorption of adventitious carbon from the air. The results indicate that at least one of the three methoxy groups ( $\text{-Si(OMe)}_3$ ) reacted with the glass surface, which agrees with that previously proposed [135].

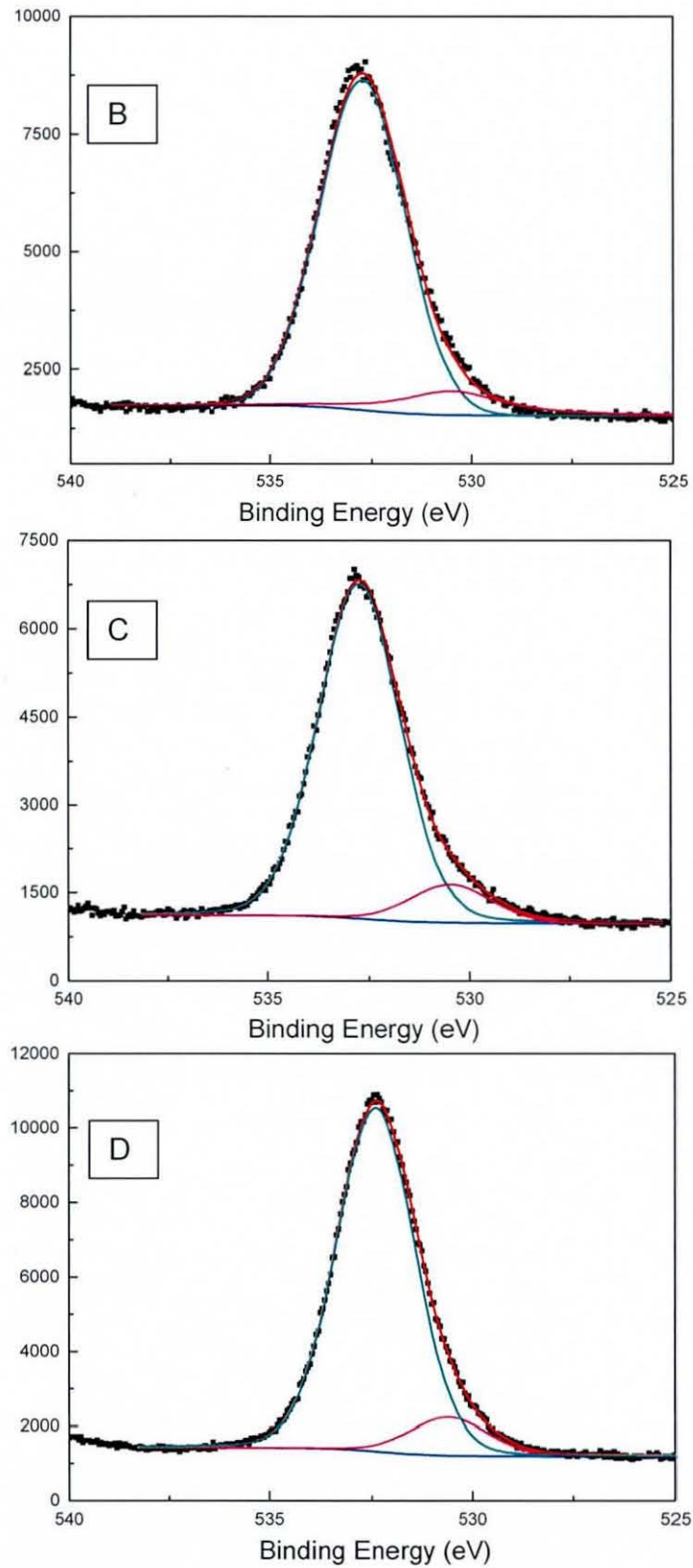




**Figure 4-8 XPS C 1s peak for (A) clean glass, and clean glass modified by APTS immersion for (B) 0.5 h, (C) 1 h, (D) 24 h**

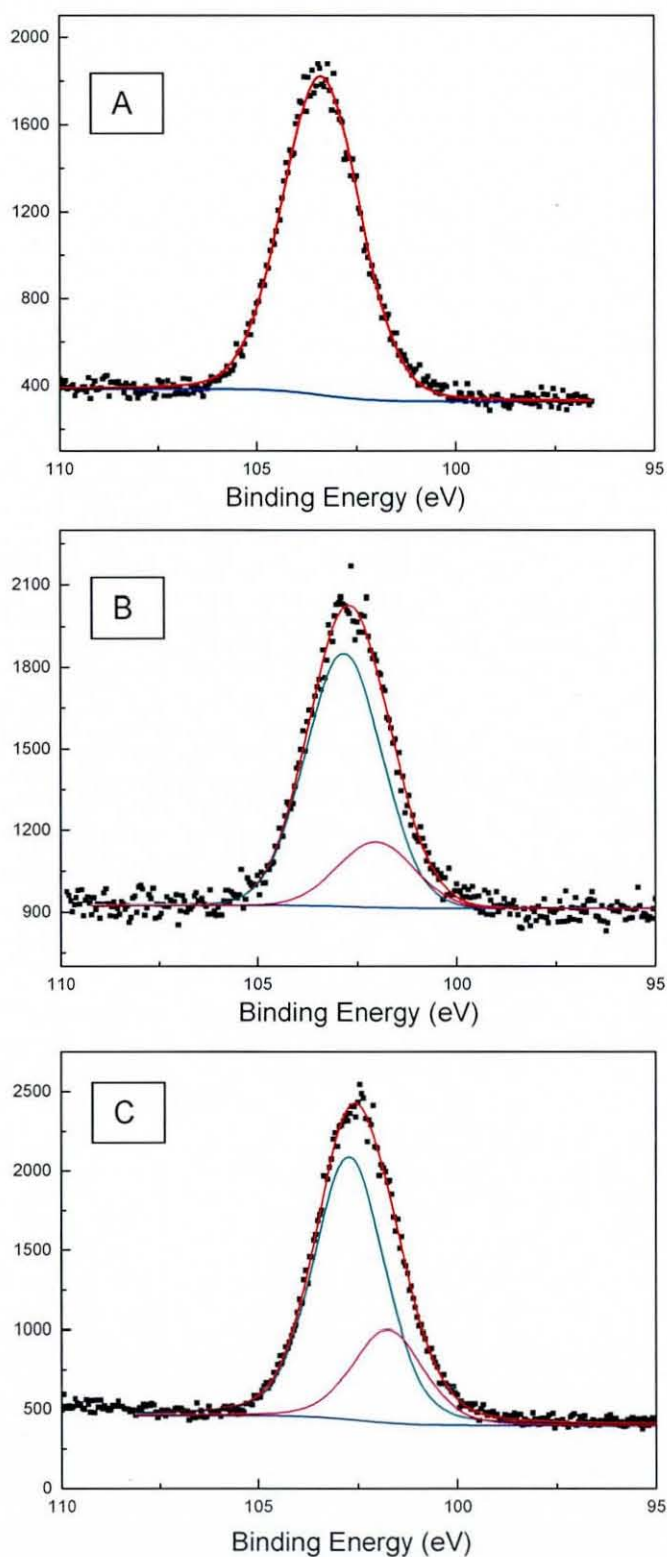
The corresponding O 1s levels are displayed in Figure 4-9. The oxygen spectrum for clean glass only presents one peak at 532.4 eV which can be attributed to the  $\text{SiO}_2$  from the glass substrate. All three silanisation spectra exhibit a main peak signal around 532.3 eV which is still due to the oxygen atoms from the glass substrate, and a weak peak at low B.E. 531.1eV that is due to Si-O-Si that arises from the APTS coupled with the glass surface.





**Figure 4-9 XPS O 1s peak for (A) clean glass, and clean glass modified by APTS immersion for (B) 0.5 h, (C) 1 h, (D) 24 h**

Figure 4-10 presents the XPS silicon core level spectra of clean glass and clean glass modified by APTS. For clean glass, there is one peak at 103.3 eV attributed to the Si in the bulk glass. All APTS treated samples show a peak essentially composed of a large signal around 103-103.2 eV assigned to the glass substrate accompanied by one additional lower binding energy peak assigned to the Si-ethoxy structure ( $-\text{Si}(\text{OMe})_3$ ) bonded to the surface to form O-Si-O.





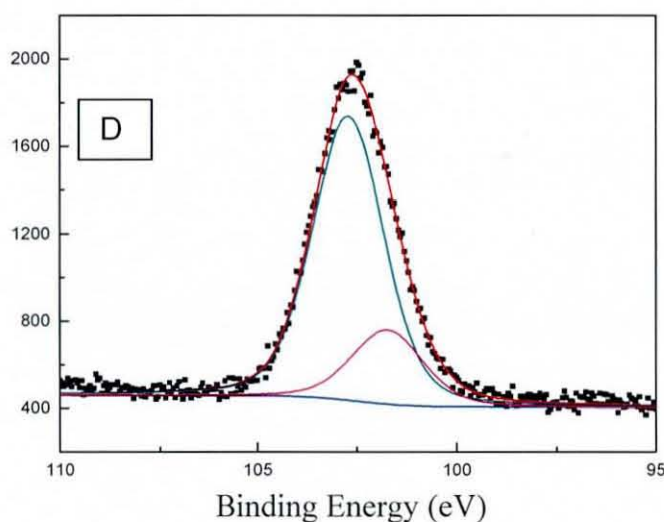


**Figure 4-10 XPS Si 2p peak for (A) clean glass, and clean glass modified by APTS immersion for (B) 0.5 h, (C) 1 h, (D) 24 h**

A pre-dip is an essential step prior to the catalyst. It improves the ability of the catalyst to adhere to the substrate and also prevents dilution of the catalyst from drag-in, so the XPS spectrum (Figure 4-11) shows the surface chemical elements after 1 hour SAM formation and 1 min pre-dip treatment. The main component of the pre-dip solution is sodium hydrogen sulphate. It can be seen that the N 1s peak remained stable after the pre-dip, indicating that this was unaffected. Compared with the SAM treated glass, the elements were almost the same.

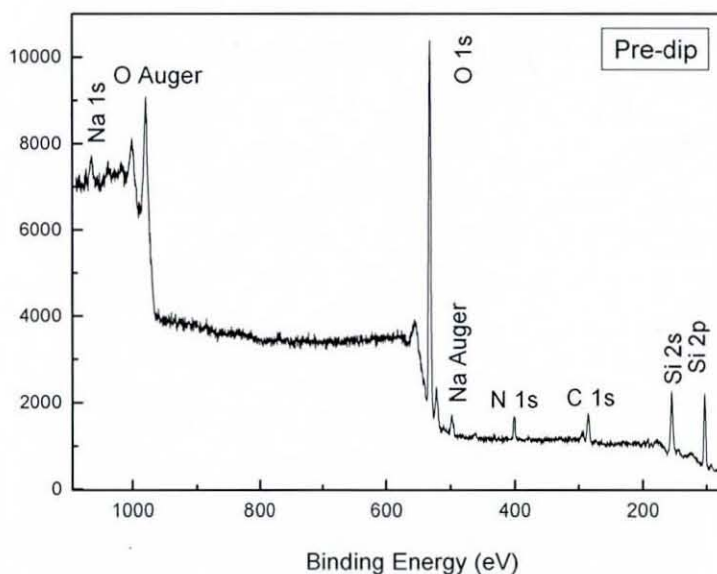


**Figure 4-11 XPS spectrum of glass surface after pre-dip**

After undergoing the APTS and pre-dip treatment described above, glass samples were immersed in a  $\text{SnCl}_2\text{-PdCl}_2$  catalyst bath in order to activate the surface for electroless copper plating. A spectrum of the glass surface after exposure to the catalyst solution for 2 min is shown in Figure 4-12. XPS readily detected Pd 3d (325-345 eV), Sn 3d (475-497 eV), Sn 3p<sub>3/2</sub> (710-720 eV) and 3p<sub>1/2</sub> (750-765 eV) owing to the high sensitivity of this technique to these elements and their position at the surface of the sample. Meanwhile, O 1s, C 1s and Si were also detected, however N could not be easily seen presumably due to the coverage of Pd/Sn, but still could be detected as shown in the inset.

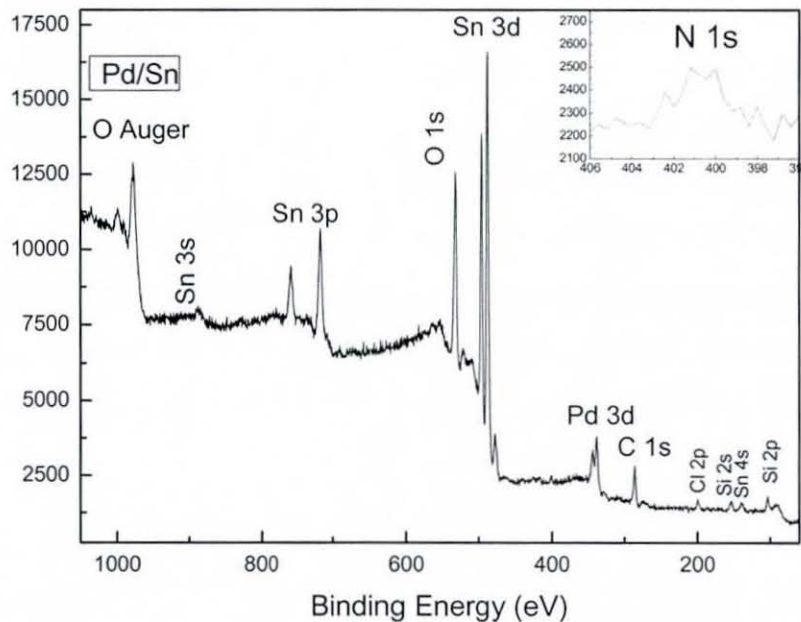


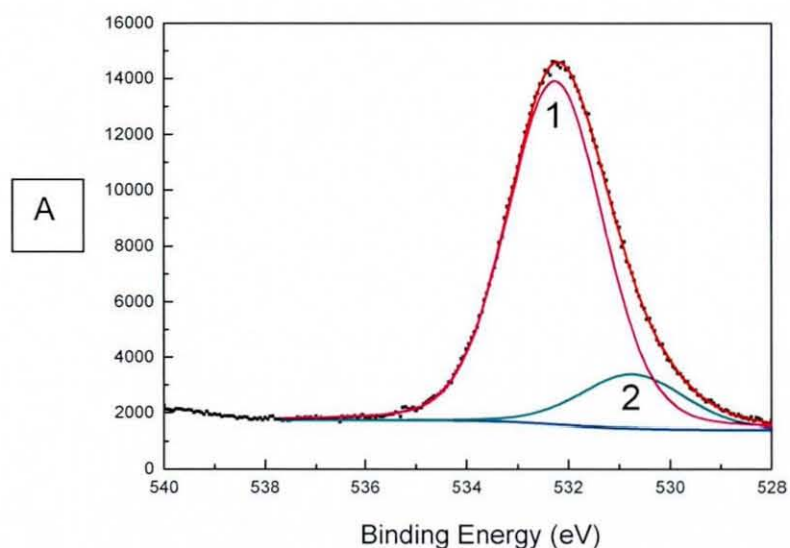
**Figure 4-12 XPS spectrum of catalytic glass surface**

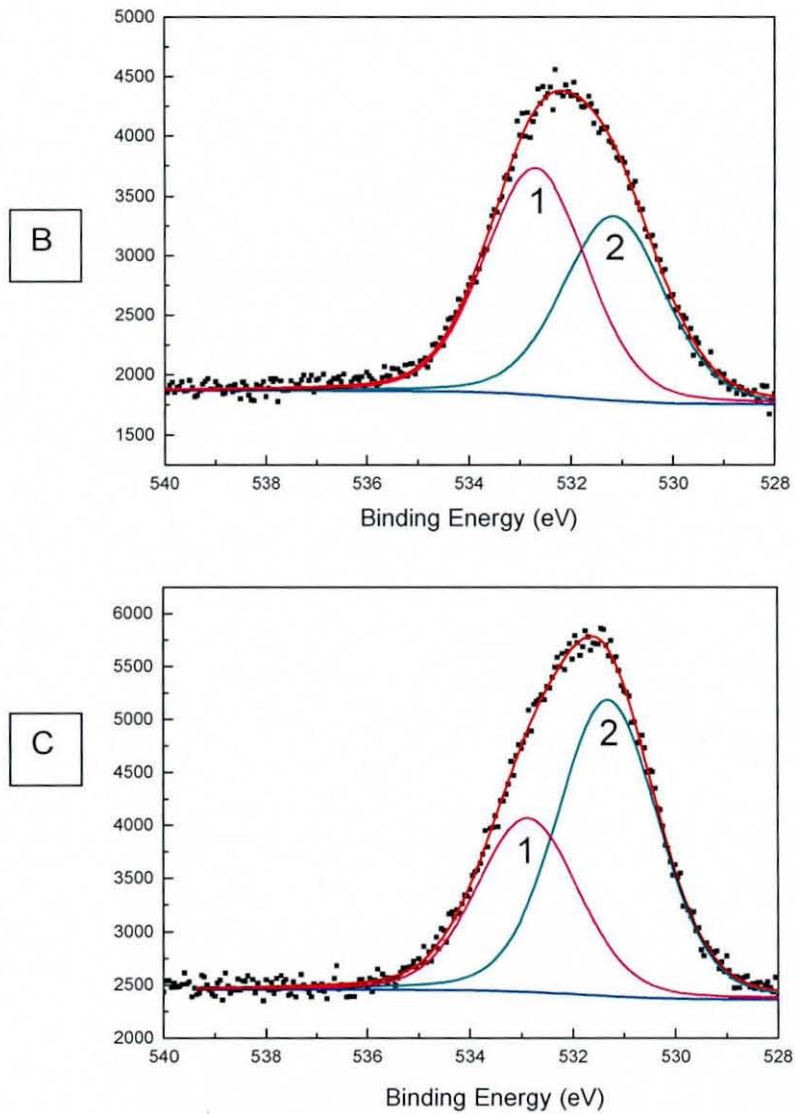
The surface concentrations for each step in the pre-treatment process, are presented in Table 4-4. The concentrations of carbon, nitrogen and silicon decrease following Sn/Pd treatment while the concentration of oxygen increases from 32.6 at.% to 45.1 at.%. The reduction of carbon, nitrogen and silicon concentrations observed following Sn/Pd treatment is likely due to coverage of the surface by the tin and palladium. The oxygen increase is caused by bonding of atmospheric oxygen to tin and oxidation of the tin to higher order oxides. This theory was supported by the oxygen core level spectra, which consistently showed an increase in O-metal bonding.

**Table 4-4 Surface chemical compositions (at.%) of glass samples following each pre-treatment step**

Surface treatment	C	O	Si	N	Sn	Pd	Cu
As received glass	9.4	57.2	24.2				
After cleaning	9.6	56.9	15.7				
APTS 1 hour	22.0	32.6	38.0	4.4			
Pre-dip	18.9	38.1	40.1	4.2			
Catalyst 2 min	15.5	45.1	9.7		17.6	2.1	

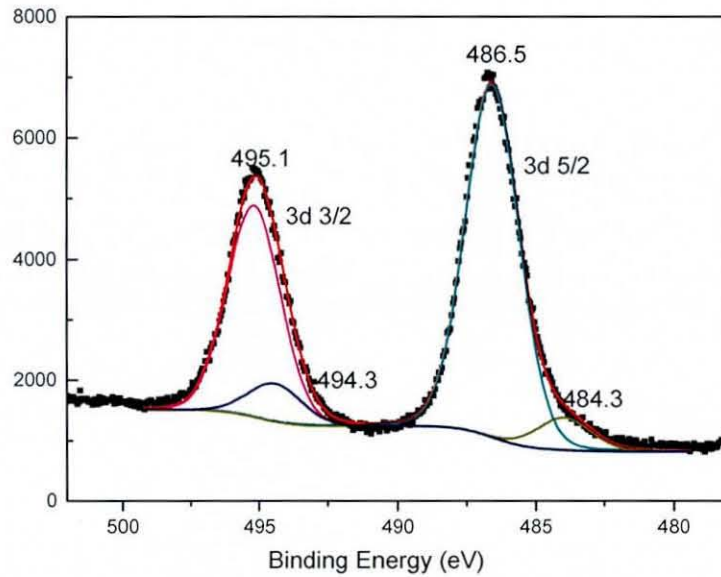
Figure 4-13 shows the oxygen spectra for a sample before and after catalyst treatment. The level of O-metal bonding (peak 2 at 531.1 eV) (which was also attributed to silane coupled on glass earlier), increased from 15.1 % to 63 % of the total peak area due to the increase in Sn-O interactions. A decrease in Si-O from the bonding from the glass substrate (peak 1) from 84.9 % to 37 % was also apparent following the Sn/Pd treatment. This indicates that the catalyst layer with some thickness covered the surface of the treated glass so that the signal from the substrate decreased. The concentration of Pd following the Sn/Pd treatment was much smaller than that of Sn, as expected based on other studies in the literature [128, 129].





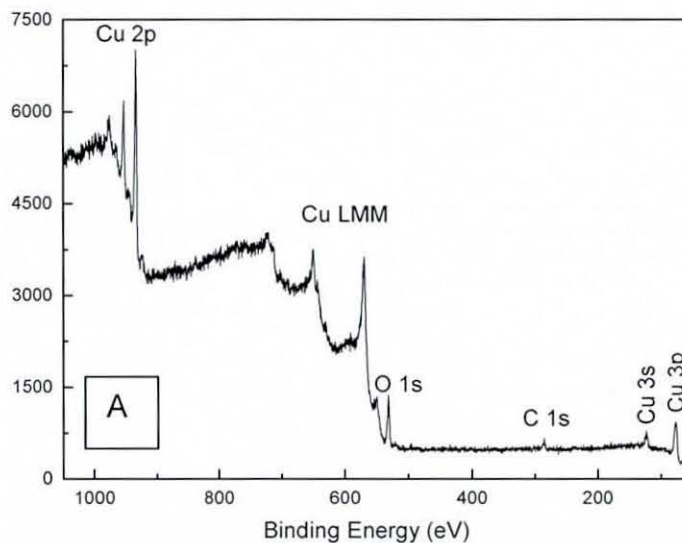
**Figure 4-13 O 1s level XPS spectra for (A) glass surface before Sn/Pd treatment (B) after 2 min Sn/Pd treatment (C) after 8 min Sn/Pd treatment**

The core-level spectrum for Sn following a 2 min catalyst treatment, presented in Figure 4-14, shows two main doublet peaks at 486.5 eV and 495.1 eV with a binding energy difference of 8.6 eV. These peak positions support the conclusion that Sn is reacting with atmospheric oxygen and is present on the surface mainly in the  $\text{Sn}^{4+}$  oxidation state, which corresponds to  $\text{SnO}_2$  bonding. The sample also shows a second smaller bonding state for metallic Sn at 484.6 eV.



**Figure 4-14 Sn core level XPS spectrum on glass after 2 min catalyst treatment**

Following Sn/Pd activation, samples were immersed in an electroless Cu bath for 5 minutes, which was sufficient time to initiate plating resulting in the formation of a continuous copper layer. The sample was then analysed using XPS to produce the survey scan shown in Figure 4-15A. In this spectrum the  $\text{Cu}^0$  peak is located at 932.8 eV. Cu 2p peaks and Cu(LMM) Auger signals were the dominant features. The tiny amount of carbon is believed to be due to contamination from the environment during storage prior to analysis, while the appearance of the O 1s signal indicates some oxidation of the copper coating.



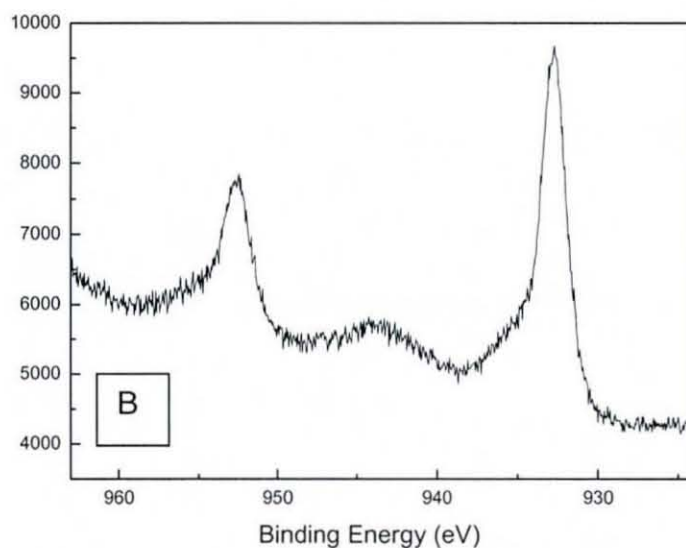


**Figure 4-15 General scan (A) and core level scan (B) of electroless Cu**

The core-level XPS spectrum for Cu is shown in Figure 4-15B. The Cu  $2p_{3/2}$  peak is located at 932.8 eV and Cu  $2p_{1/2}$  peak is at 952.7 eV. By applying deconvolution procedures, the most prevalent bonding state was identified as Cu<sup>0</sup> bonding or Cu(I) located at 932.8 eV and a minor peak of Cu(II) located at 934.8 eV. The Cu(II) assigned to Cu-O bonding is likely due to Cu surface oxidation from atmospheric oxygen.

**Table 4-5 Surface compositions (at.%) after different electroless Cu deposition times**

Electroless plating time (min)	C	O	Si	Sn & Pd (Total)	Cu
0.5	47.9	34.4	14.8	2.8	
1	42.3	35.3	19	0.7	2.7
5	54.5	32			15.6
10	38.9	40.4			20.7
15	22.4	40.1			38.5

The detailed surface composition data on the glass surface after 2 min catalyst treatment followed by different electroless Cu plating times is shown in Table 4-5.

The data (at.%) in this table indicates that Cu coverage is dependent on the electroless plating time. When the plating time is less than 1 min, there was a tiny amount of catalyst detectable in the spectra.

#### 4.4.2 Tape test results

Tape peel tests (mainly according to the ASTM D3359-02 standard test method [142]) were used to qualitatively determine the influence of the deposition process parameters on the adhesion of the films. Quality rating of the adhesion was determined from the fractional area in which a part or the whole coating layer was removed from the substrate. In general, it was found that the APTS pre-treatment step was necessary to enable the coating of the glass - without it, the catalyst could be easily washed from the surface prior to copper plating and almost no deposit was formed. Therefore, APTS immersion time, catalyst immersion time and electroless copper bath temperature were all investigated for their effect on the uniformity and adhesion of copper. Table 4-6 lists qualitative tape test results: “Good” indicates zero or almost no copper removal from the surface, “Average” means approx. 10%-15% copper removal, “Bad” indicates no less than 20% removal of copper.

**Table 4-6 Tape peel test results for Cu films on glass substrate**

APTS Solution Immersion Time (hour)	Pre-dip Immersion Time (min)	Catalyst Immersion Time (min)	Electroless Cu Bath Temp. (°C)	Adhesion (Thickness: nm)		
				< 100	> 120	
-	1	0.5-10	20-55	No film		
1	1	0.5-10	55±3	Bad		
0.5	1	1	40±2	< 100	> 120	
				Good	Bad	
1	1	2	40±2	< 160	170-210	> 220
				Good	Average	Bad
1	1	2	R.T. (19-24)	Very thin layer	< 80	
				Average	Bad	

Copper films were easily peeled off if the electroless bath temperature was 55°C or over, while a short immersion time in the catalyst also resulted in weak adhesion of

very thin coatings. The optimum conditions were found to be: 2 min in catalyst solution and 40°C for the electroless copper bath. However, even with these conditions, the coating adhesion varied with thickness: below 160 nm the coatings showed good adhesion with no material removed during the tape test, while above 220 nm they could be easily peeled off.

#### **4.4.3 Adhesion failure analysis**

To investigate the nature of the linkages among the various layers on the glass surface, an analysis of the failure surfaces was conducted after the tape peeling test using XPS and SEM to investigate the surface chemistry and morphology of the fracture surfaces.

##### **4.4.3.1 XPS of delaminated surfaces**

Figure 4-16 shows a wide scan spectrum obtained from the glass surface after delamination of the electroless copper coating. The spectrum showed features due to Si and O as expected from the underlying substrate, but also showed clear peaks attributed to Pd and Sn, similar to those observed from the catalyst treated surface shown earlier. However, compared to the original catalytic surface, for the delaminated glass, the Sn 3d and 3p signal decreased dramatically, while the Si signal intensity increased. The atomic percentage of Pd was 2.4 at%, while Sn was only 1.8 at%. No Cu signal could be seen. The amount of Sn is much less than that observed after the catalyst solution which indicates that much of the Sn was removed in the electroless plating bath.

Analysis of the copper surface adhered to the tape indicated only the presence of copper. No Pd or Sn could be observed even when detailed scans of the expected peak positions were carried out. Some oxygen was seen, which was associated with oxidation of the exposed copper surface. The extent of oxidation was much less than that seen for the original top copper surface which is consistent with the buried nature of this interface that was only exposed to air for a short period after peeling.



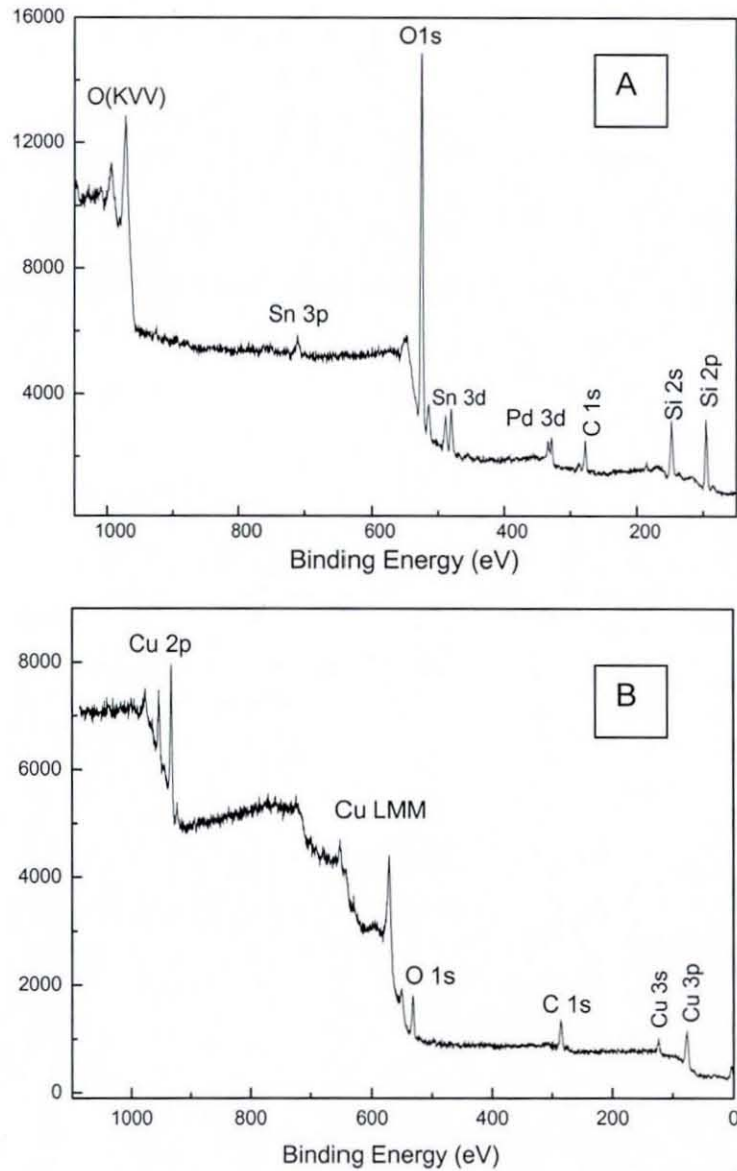


**Figure 4-16 XPS wide scans of the delaminated surfaces (A) delaminated glass surface (B) Cu on adhesive tape**

Comparison of the spectra from the delaminated surfaces with the database of spectra gathered for the deposition process enables some insight into the failure mechanism to be gained. The presence of obvious Si, Sn and Pd 3d signals on the delaminated glass surface, together with the absence of any copper signal, suggests that the failure did not occur in the copper layer as it was cleanly peeled away without any transfer to the glass. However, the presence of a strong copper peak without Pd or Sn signals on the delaminated Cu surface shows that failure occurred at the interface between Cu and catalyst. All of these assumptions were further confirmed by the narrow scan spectra of elements on the delaminated surfaces as shown in Figure 4-17 and Figure 4-18.

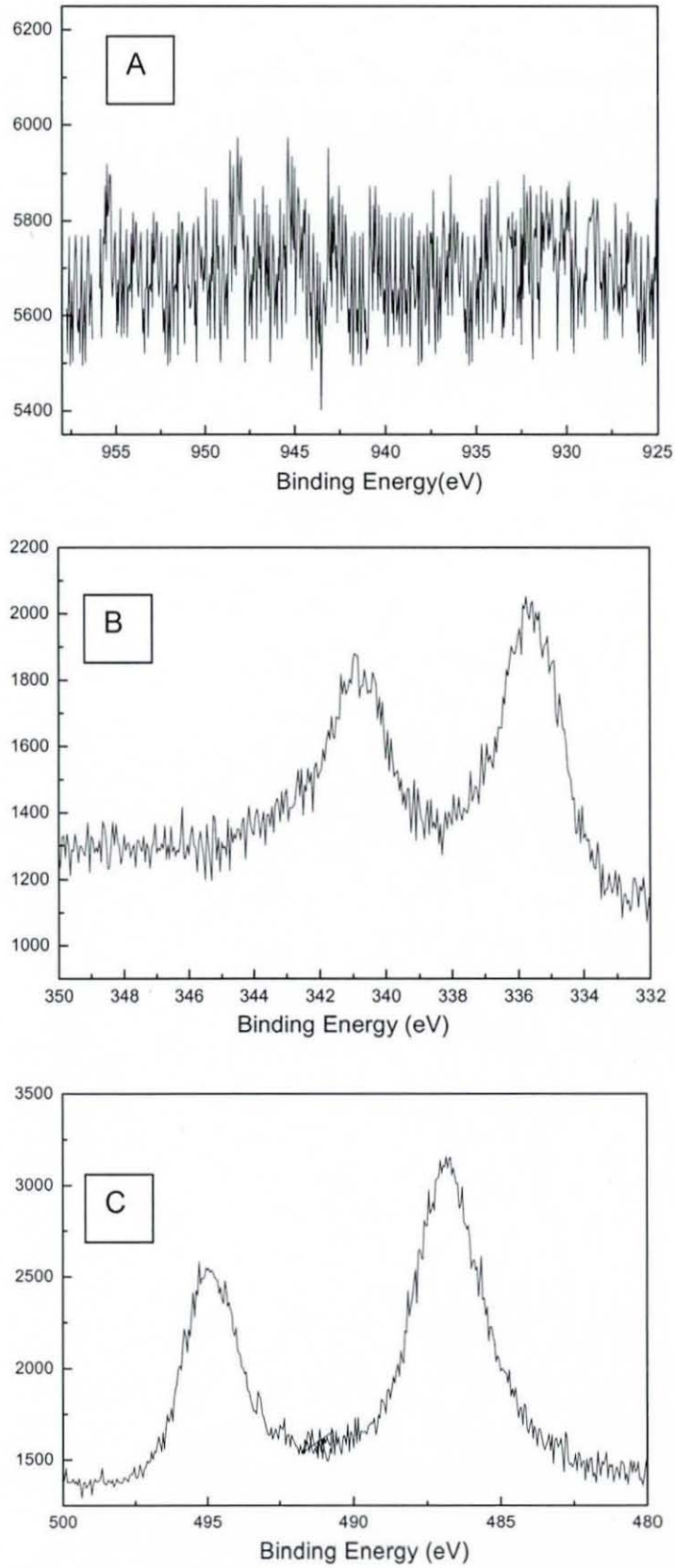
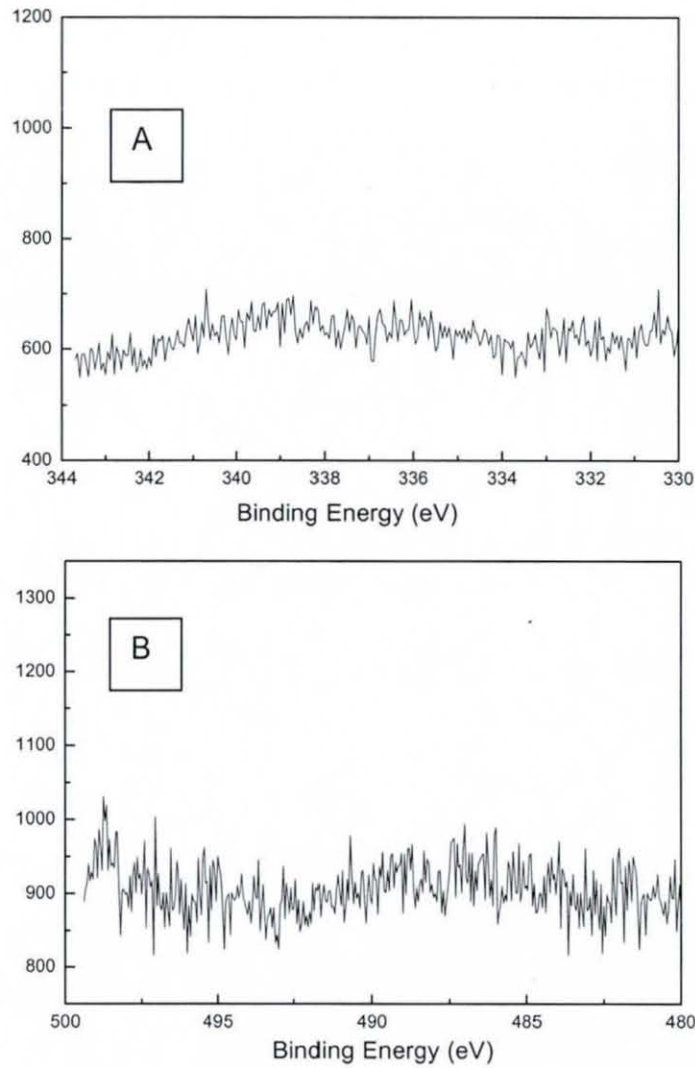
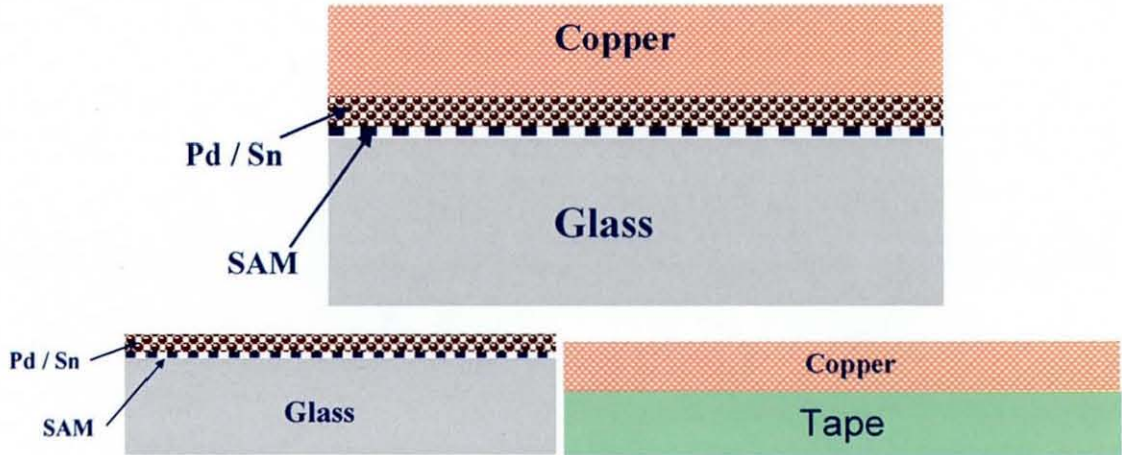


Figure 4-17 XPS core level scans of the delaminated glass surface (A) Cu, (B) Pd, (C) Sn



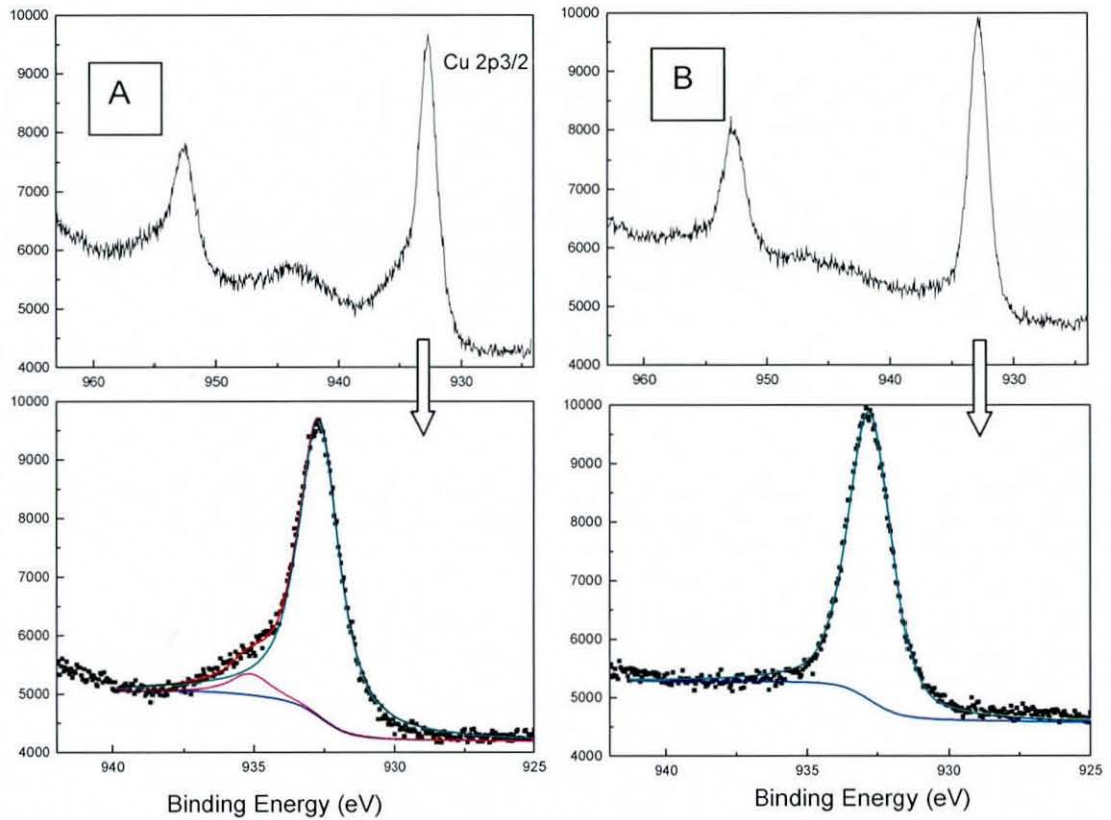
**Figure 4-18 XPS core level scans of the delaminated Cu on adhesive tape (A) Pd, (B) Sn**

From the tape test results, it is easily seen that the adhesion decreased with increasing electroless plating thickness. The tape peel test and XPS results show that the failure location was between the catalyst and electroless Cu (Figure 4-19), which is in contrast to some other observations in the literature where failure appears at the interface between substrate and catalyst [88, 143, 144]. One possible reason is thought to be due to stress developed in the coating which increases with increasing deposition time. In addition, it has been reported that hydrogen and water may be occluded in the deposits with increasing time, degrading the anchoring effect between the substrate and electroless copper [16]. Another possible reason is residual tin ions reacted with copper in the initial period to form an ultrathin brittle layer which is harmful to the interfacial adhesion [85].



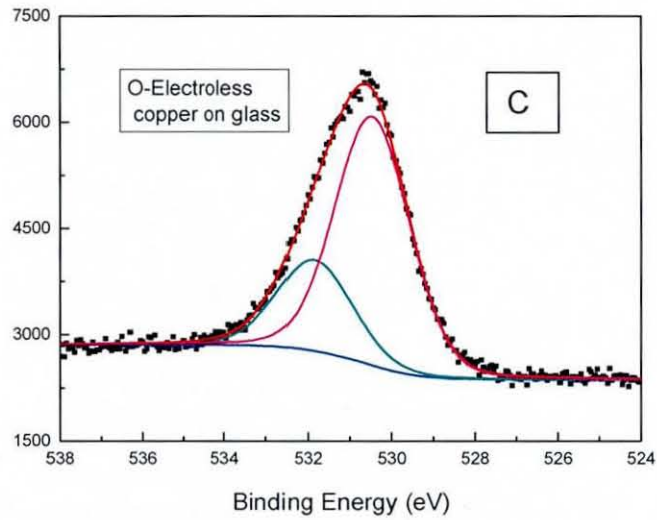
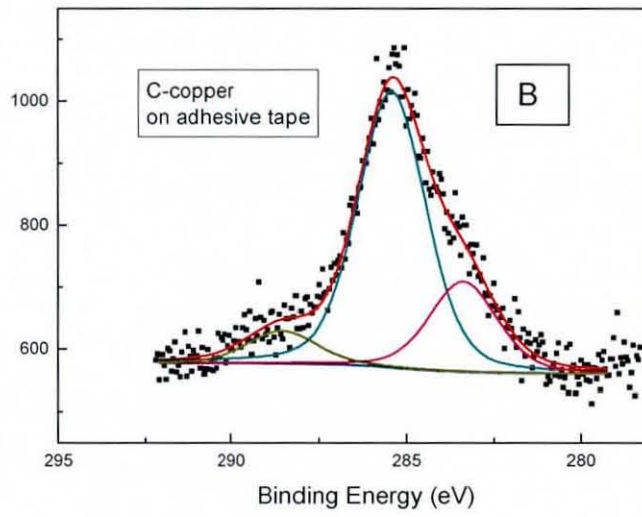
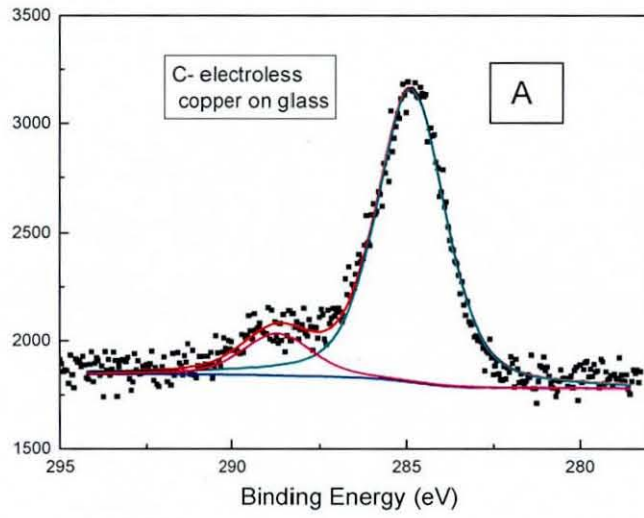
**Figure 4-19 Diagram of locus of failure of electroless Cu on glass substrate**

In order to know more details of the weak interface, more XPS core-level scans were performed. Comparing the XPS general scan of electroless copper on glass and copper on the adhesive tape, there was no obvious difference. Therefore, narrow scans of copper, oxygen and carbon were performed to find out the possible reasons for the weak adhesion between copper and catalyst. The corresponding Cu 2p and Cu 2p<sub>3/2</sub> core-levels from copper deposits and copper on the adhesive tape are displayed in Figure 4-20. From the Cu 2p peak, a clear feature due to oxidation can be seen for the electroless Cu at about 945.2 eV, while on the adhesive tape there was no obvious oxidation. This result means that the electroless plating can form a dense film on the catalyst surface and there is no air penetration to the interlayer during storage. By applying deconvolution procedures both spectra exhibit a main peak signal around 932.8 eV, which is indicative of Cu(0) formed from the electroless process, although Cu(I) has a similar B.E. There is a small peak signal about 935.2 eV for the electroless copper on glass, which is indicative of Cu(II) from oxidation, while only metallic copper (or Cu(I)) was observed on the adhesive.



**Figure 4-20 Corresponding Cu 2p, Cu 2p<sub>3/2</sub> core-levels for (A) original, (B) delaminated Cu surfaces**

Core-level scans of C 1s and O 1s were also investigated for the two different Cu surfaces. Figure 4-21 (A and B) show the respective C 1s core-level spectra of the electroless Cu surface and the delaminated surface. By applying deconvolution procedures both spectra show a major peak at 285.0 eV. There is also another weak peak at 288.7 eV in the C 1s spectrum of electroless Cu on glass, while it was seen that C 1s contains three main peaks for the Cu on the adhesive tape, 285.0 eV (C-C), 288.7 eV (C=O) and 283.6 eV. The peak at 283.6 eV is shifted in an unusual direction and could be due to charging from the adhesive tape or some signal from the tape layer.



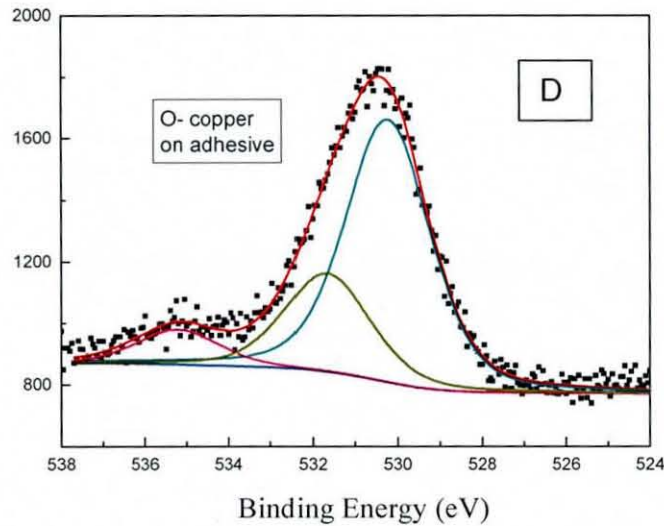


**Figure 4-21 C 1s and O 1s core-level spectra of two Cu coatings**

The XPS oxygen spectrum of the electroless deposit, as shown in Figure 4-21C presents two peaks that correspond to these bonding states: O-Cu found at 530.3 eV and O=C at 531.9 eV. The oxygen spectrum of copper on the adhesive tape shows an added peak at 535 eV, most likely coming from some exposure of the adhesive tape or charging effects.

#### **4.4.3.2 Microstructure of the failure interface**

The adhesion failure position was determined by XPS, moreover, SEM was also used to investigate the morphology of delaminated surfaces. Figure 4-22 shows typical SEM images of delaminated surfaces (both were coated with gold to prevent charging). As can be seen, the glass surface is quite smooth except for little remnant deposits, which are thought to be copper particles. Due to the strength of the peeled adhesive tape applied, many cracks were formed on the delaminated copper layer, as shown in Figure 4-22B.

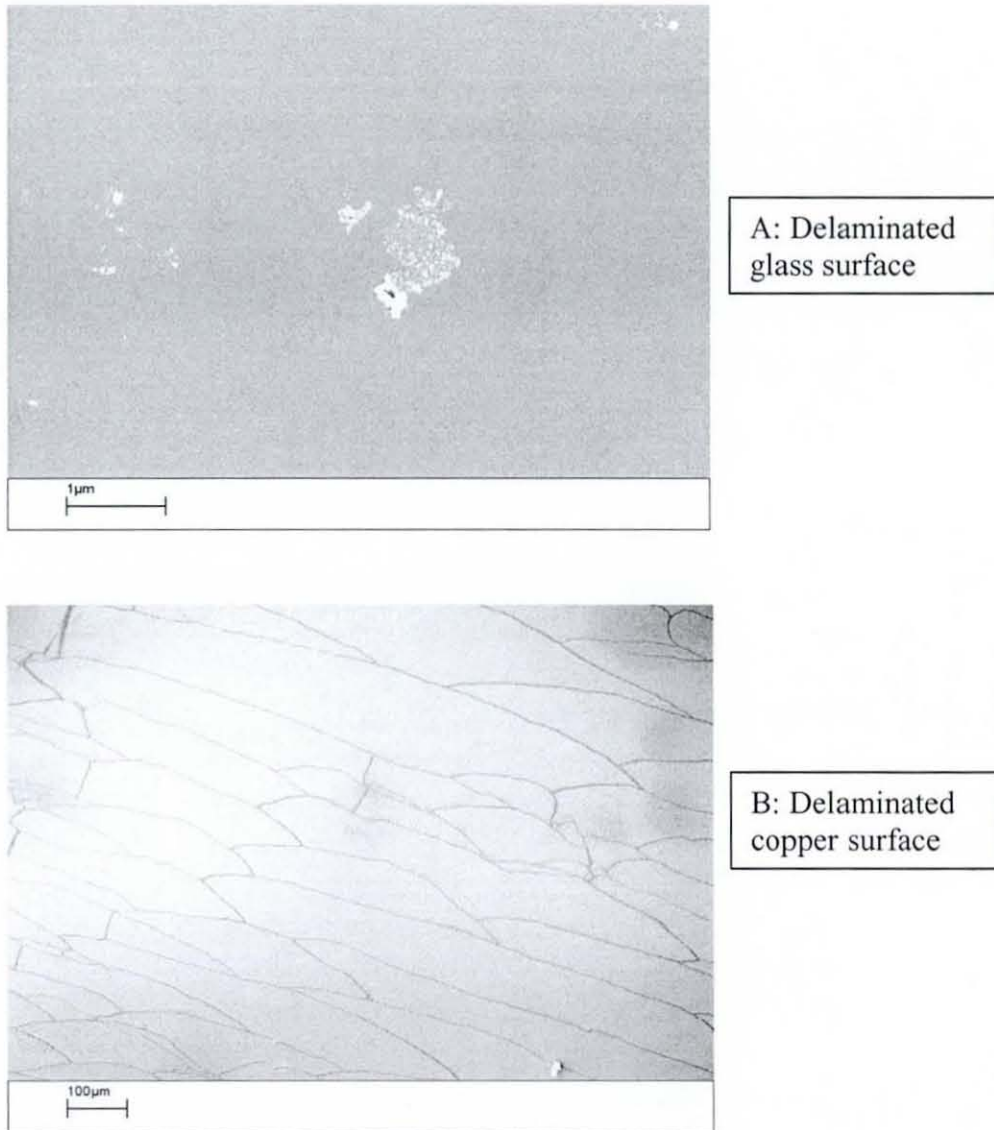


**Figure 4-22 SEM images of (A) delaminated glass surface, (B) delaminated Cu surface**

The electroless Cu layer and delaminated Cu layer were chemically different, as shown by XPS. The morphological images of electroless Cu deposits on glass have been shown in chapter two, the following part emphasises the microstructure of the delaminated Cu layer. Figure 4-23 presents SEM images of peeled off Cu which was deposited using different conditions, specifically 2 minutes and 8 minutes immersion in the catalyst bath. From low magnification images, e.g. Figure 4-22, the delaminated Cu layer looks smooth which indicates homogeneous deposition on the glass surface when the electroless Cu plating started.



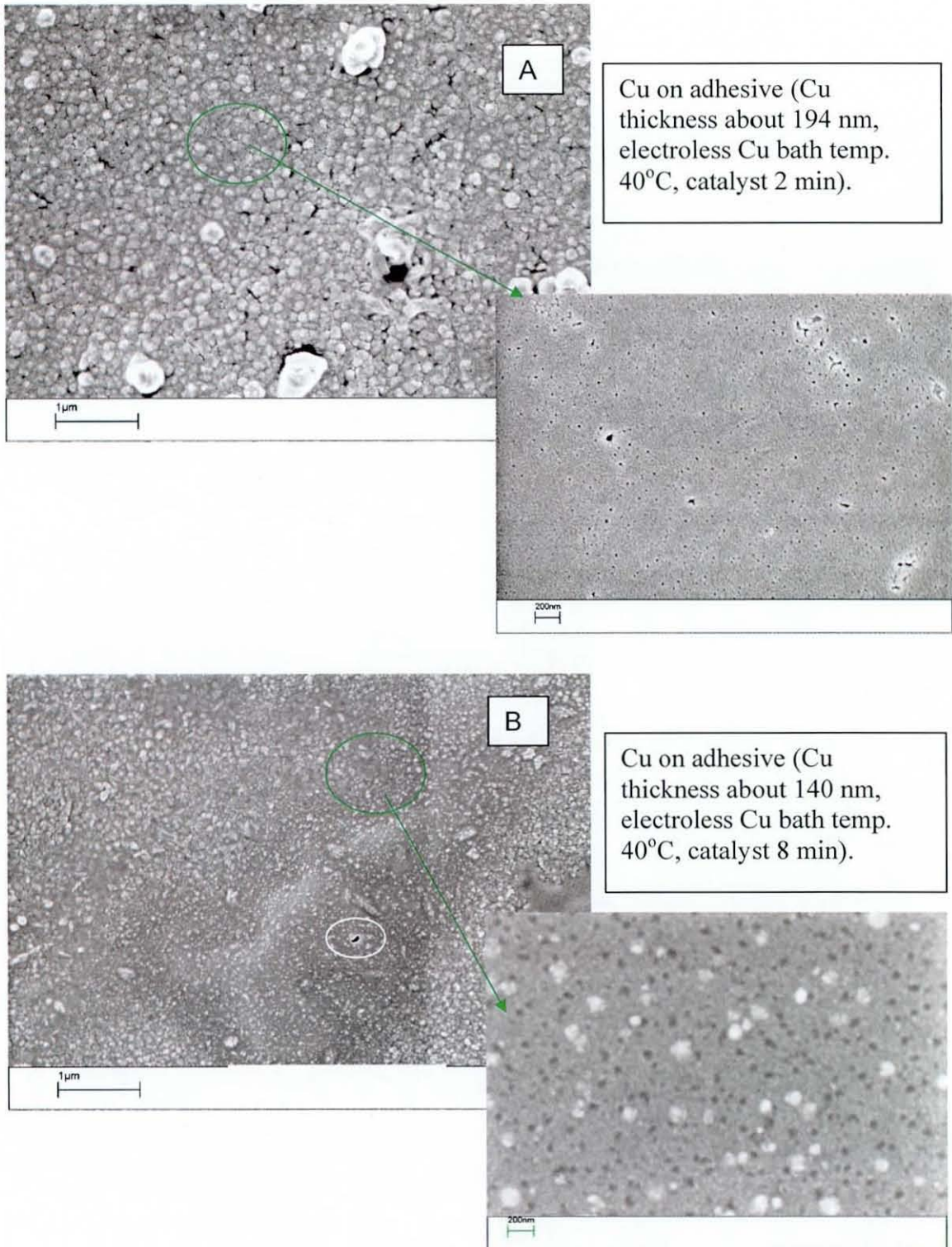


**Figure 4-23 SEM images of Cu deposited following different catalyst immersion times after peeling off on adhesive tape**

Many circular shaped copper deposits are visible in Figure 4-23A, while in Figure 4-23B there was no obvious shape to the copper particles. Moreover, when using high magnification, many voids were found on both delaminated copper layers. According

to Kim et al. [145] there were two types of stress-induced damage observed from images of peeled copper. One type of damage consisted of severe grooves along the grain boundaries, similar to those shown in Figure 4-23A, which was attributed to high stress formed along the surface leading to breaking of the film in weak locations, such as at grain boundaries and contamination remnants. The other type of damage consisted of isolated large voids as presented in Figure 4-23B. The dimension of voids shown above increased with the catalyst immersion time from less than 10 nm at 2 min to about 25 nm at 8 min. These voids probably occurred because of bubbles in the electroless copper plating. With increasing immersion time in the catalyst, this phenomena happened even more as all the metallic Pd served as deposition spots for the electroless copper.

#### **4.4.4 Adhesion between electroless NiP and glass substrate**

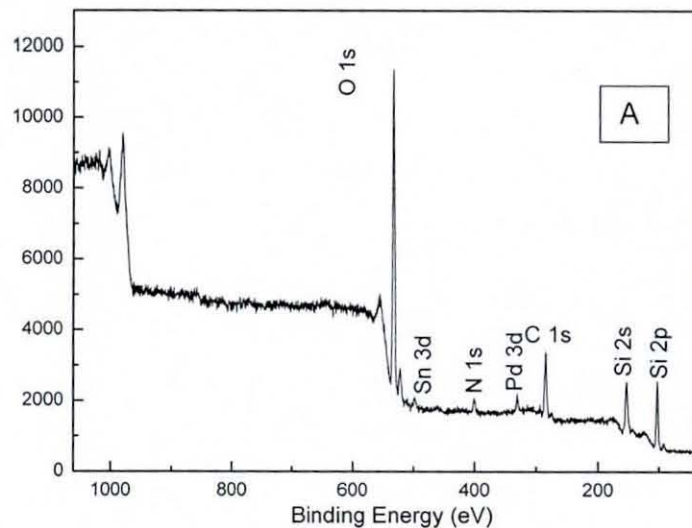
So far, all the results focused on the electroless copper coating. Tape peel testing was also used to determine the influence of the deposition process parameters on the adhesion of the electroless nickel coating. The APTS pre-treatment step was still necessary to enable coating of the glass. Table 4-7 lists qualitative tape test results of electroless NiP coatings. The quality rating grades are the same as those used for the electroless copper film.

**Table 4-7 Tape test results of electroless NiP on glass substrate**

APTS Solution Immersion Time (hour)	Pre-dip Immersion Time (min)	Catalyst Immersion Time (min)	Accelerator Immersion Time (min)	Electroless Nickel Bath Temp.(°C)	Adhesion (Thickness: nm)	
					< 140 average	> 235 weak
-	1	0.5-10	5	70	< 740 Good	> 870 average
1	1	2	5	70	< 550 Good	> 642 weak
1	1	8	5	70	< 417 Good	> 530 weak
0.5	1	8	5	70		

It can be seen that thin NiP films were easily peeled off without the APTS treatment. The NiP thickness could be built up to 740 nm with good adhesion under proper preparation conditions. However, even with these conditions, the coating adhesion became bad when the thickness was over 1 micron.

As for the electroless copper film, the delaminated NiP film and the glass surface after the tape peel test were analysed by XPS and SEM to reveal the surface chemistry and microstructure of the fracture surfaces. Figure 4-24 shows the wide scan spectrum obtained from the glass surface after delamination of the electroless NiP coating. The spectrum is very similar to that of the glass surface after the coating was removed, except for an obvious nitrogen peak at 402 eV. Analysis of the nickel surface adhered to the tape indicated the presence of Ni, C, P and O, but with no evidence of Pd or Sn. These results also show that failure occurred at the interface between the electroless nickel coating and catalyst, which is consistent with the failure locus of the electroless copper coating.



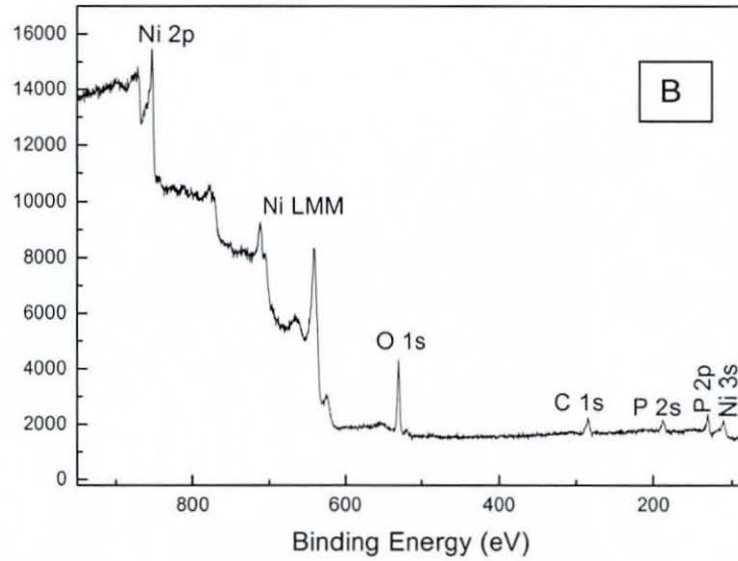


**Figure 4-24 XPS general scans of (A) delaminated glass surface and (B) NiP film on adhesive**

Figure 4-25 shows an SEM image of the delaminated NiP surface. The delaminated NiP surface microstructure looks like fish scales, and there were no obvious cracks formed in the peeled off coating layer, which is different to that seen for the peeled copper coating, under the same magnification.

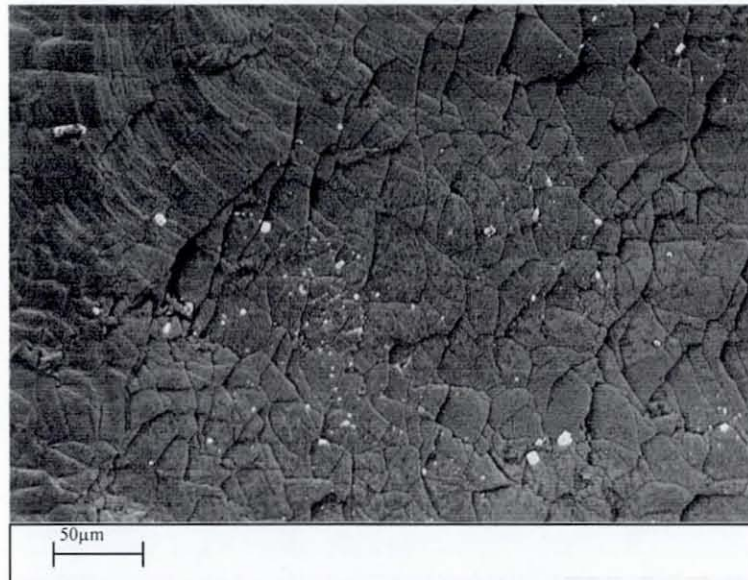


**Figure 4-25 SEM image of NiP film on adhesive tape**

#### **4.5 Conclusion**

The work presented in this chapter has focused on the use of APTS treatment to enhance catalyst adsorption and adhesion between a smooth glass surface and electroless copper and nickel. It has been found that APTS increases nitrogen content on the surface, which is thought to increase the catalyst adsorption during the Sn/Pd activation step and improves the electroless deposition uniformity.

Good adhesion was obtained on a 2 min catalyst treated surface, although this was only possible for copper coatings less than 160 nm thick. The failure locus was revealed by XPS, and it was found that the failure was between the catalyst and the electroless copper or nickel layers. The possible reason for this is remnants of tin ions and some voids resulting from bubbles during the electroless copper reaction, which will be investigated in later chapters of this thesis. Overall, the APTS treatments on glass have been shown to be effective in chemically modifying the surface for catalyst adsorption and electroless plating, but the adhesion has not been adequately enhanced for practical application in industry.

---

## **Chapter 5 Internal Stresses and Mechanical Properties of Cu and NiP Films**

---

### **5.1 Introduction**

As shown in the previous chapter, adhesion between glass and a metallic coating is a major issue for electroless deposition. Thus, it is necessary to assess the adhesion of an electroless Cu or NiP film quantitatively to help understand the mechanism for the interfacial failure. Of all the properties of a thin-film system, adhesion is one of the most important, but one of the most difficult to measure. Practical adhesion refers to the ability of a thin film to resist delamination in a practical setting, under stresses appropriate to the application.

There are many factors that affect the practical thin-film system adhesion, such as film stress, adhesion type and substrate structure. For example, NiP and Cu thin films and glass substrate have different thermal expansion coefficients, so internal stress is produced after deposition. Stress in thin films is known to cause yield and reliability problems in microelectronic devices [146]. Thus, in this chapter, the equipment and experimental procedures for the measurement of the stress of electroless thin films are presented. This is followed by an explanation of the experimental methodologies and some discussion of the nature of stress and adhesion in thin films. Attention is devoted to the effects of processing on the adhesion and application field of thin films on substrates, the evolution of film microstructure in polycrystalline films, and the generation of internal stresses through processing

## **5.2 Literature survey**

### **5.2.1 Thin film stress measurement**

Several methods have been used for mechanical properties measurement on thin metallic films. Reed and Dally [147] used the uniaxial tensile testing method for free standing films. These films were removed from the substrate prior to testing. In this case the effect of the substrate was not included and the removed films were vulnerable, thus the tested mechanical properties may differ from those of the attached films. X-ray diffraction measurements performed on electrochemically grown Cu films on silicon substrate revealed high tensile stress [104]. Yu et al. [93] focused on the internal stress between a Si substrate and Cu film prepared by both metal vapour vacuum arc ion implantation and ion beam assisted deposition. The internal stresses in the Cu films were analysed by X-ray diffraction, which showed that all the Cu films possessed compressive stress, which increased as the film thickness increased. In addition, due to the difference in the thermal expansion coefficients between film and substrate, Shute and Cohen [148] used the X-ray diffraction method to examine the yield strength of Al films on silicon through cooling. Chuang and Kim et al. [145, 149] used the curvature technique to study the stresses in Al and electroplated Cu films. Pienkos et al. [41] studied the stress in thin Ag and Cu films on sapphire by means of curvature measurement. It was revealed that once the film thickness was above 30 nm, the stress changed to compressive for Ag films, but to tensile for Cu films.

In general, almost all of the thin films prepared by different methods possess internal stress. The stress level in microelectronic devices such as integrated circuits is generally recognized as an important issue [93]. Excessive residual stresses in thin films may cause defect formation and delamination at the film–substrate interface. Consequently, the adhesion between the film and substrate will be affected by the stress in the film, leading to a decrease in the stability and reliability of the components and devices. Therefore, it is important to understand the origins of the stresses in the films.

The substrate curvature method is the most commonly used technique for determination of thin film stress, due to its simplicity and non-destructive nature. In

this method, the internal stresses are determined by measuring the change of substrate curvature radius before and after deposition. The deflection measurement can be converted into an internal film stress using Stoney's formula [150]:

$$\sigma_f = \frac{E_s t_s^2}{6 t_f (1 - \nu_s)} \left( \frac{1}{R} - \frac{1}{R_0} \right) \quad (15)$$

where  $\sigma_f$  is the internal stress in the thin film,  $E_s$  and  $\nu_s$  are Young's modulus and Poisson's ratio of the substrate.  $t_f$  and  $t_s$  indicate the film and substrate thicknesses.  $R$  is the radius of curvature of the specimen after deposition, and  $R_0$  is the radius of curvature before deposition. Positive values of  $\sigma_f$  indicate tensile and negative values compressive film stress.

In general, the internal stress in a thin film can be simply divided into two components: an intrinsic stress due to the film growth process and a thermal stress due to the difference in coefficient of thermal expansion between substrate and film material. The thermal stress,  $\sigma_{th}$ , is directly related to the thermal strain,  $\varepsilon_{th}$ , in the film through Hooke's law [151]:

$$\sigma_{th} = \frac{E_{film}}{1 - \nu_{film}} \varepsilon_{th} = \frac{E_{film}}{1 - \nu_{film}} (\alpha_{film} - \alpha_{sub}) \Delta T \quad (16)$$

where  $E_{film}$  and  $\nu_{film}$  are Young's modulus and Poisson's ratio of the film.  $\alpha_{sub}$  and  $\alpha_{film}$  indicate thermal expansion coefficient of the substrate and film, respectively. There are two assumptions in the use of this equation. First, the substrate should be a stiff material, that is, the stress in films on flexible substrates could not be calculated by this law. Secondly, the film is much thinner than the substrate.  $\Delta T$  is the temperature drop from the deposition temperature to room temperature. Gunnars et al. [152] found that the thermal stresses become tensile if the thermal expansion coefficient of the thin film is greater than the value of the substrate.



### 5.2.2 Nanoindentation testing

Due to the importance of mechanical properties as a measure of the quality of thin films, mechanical properties including hardness and elastic modulus are often measured. Mechanical properties of thin films are usually affected by the internal stresses that are induced from the different deposition processes. In the literature, significant research had been focused on the characterisation of thin metallic film properties for which the majority of thicknesses of film are greater than one micron and prepared by a CVD or PVD method [101, 153, 154]. However there has been little systematic research into the electroless NiP or Cu films. Due to the very thin nature of electroless coatings, extreme accuracy is required to measure their mechanical properties, for which nanoindentation is a useful tool.

The nanoindentation method has been developed to evaluate the mechanical properties of metal films, for which the indentation loading curve (Figure 5-1) is employed to determine the yield strength and hardness of a thin film on a substrate [155]. In nanoindentation, the depth of penetration together with the known geometry of the indenter provide an indirect measure of the area of contact at full load and thus hardness is obtained by dividing the maximum applied load by that contact area. In the nanoindentation technique, hardness and Young's modulus can be determined by the Oliver and Pharr method [156].

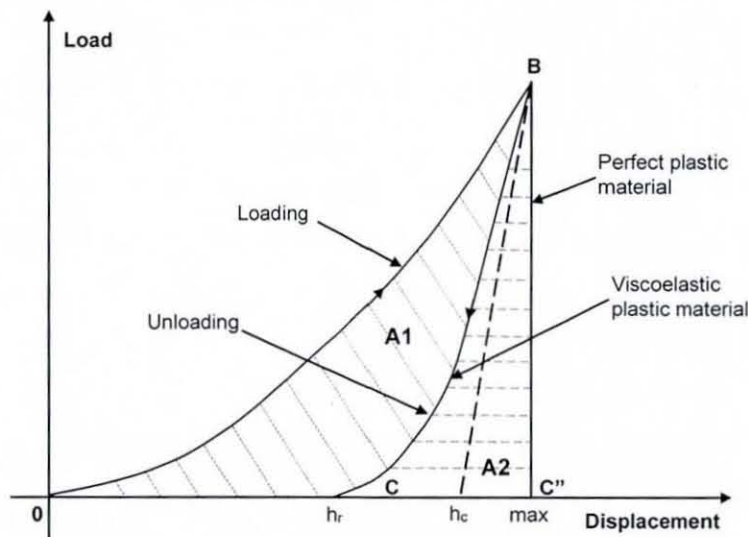


Figure 5-1 Load-displacement curve after Briscoe [155]

Figure 5-1 shows the typical load-displacement curve, showing the values used in the Oliver and Pharr method. In nanoindentation testing, as the indenter presses into the sample, both elastic and plastic deformation occurs, resulting in an imprint that conforms to the indenter shape. During the indenter withdrawal, only the elastic portion of the deformation is recovered. Oliver [156] suggested a method based on the measured indentation load-displacement curves to determine the indenter area function (the cross-sectional area of the indenter as a function of the distance from its tip). The method is based on the idea that, at peak load, the material conforms to the shape of the indenter to some depth, then hardness and modulus were obtained based on the observation that during the initial stages of unloading, the area of contact remains constant as the indenter is unloaded. Therefore, nanoindentation hardness,  $H$  can be defined as:

$$H = \frac{P_{\max}}{A} \quad (17)$$

where  $P_{\max}$  represents the peak load and  $A$  is the contact area. The hardness is the mean pressure that a material can support under load. The relation between the load ( $P$ ) and the depth ( $h$ ) can be represented as:

$$P = \alpha(h - h_f)^m \quad (18)$$

where  $\alpha$  is an indent constant,  $m$  depends on the geometry of the indenter, and  $h_f$  indicates the final depth. The elastic modulus of the indented sample can be inferred from the initial unloading contact stiffness. The relation between the contact stiffness, contact area, and elastic modulus can be derived as:

$$s = 2\beta \sqrt{\frac{A}{\pi}} E_r \quad (19)$$

where  $\beta$  is a constant that depends on the geometry of the indenter,  $\beta = 1.034$  for the commonly used Berkovich indenter, and  $E_r$  is the reduced elastic modulus, which accounts for the elastic deformation that occurs in both the sample and the indenter. Hence,  $E$  is given by equation:

$$\frac{1}{E_r} = \frac{1-\nu^2}{E} + \frac{1-\nu_i^2}{E_i} \quad (20)$$

where  $E$  and  $\nu$  are the elastic modulus and Poisson's ratio for the sample, respectively, and  $E_i$  and  $\nu_i$  are the elastic modulus and Poisson's ratio for the indenter.

### 5.2.3 Scratch testing

Scratch testing is widely used to evaluate film adhesion. The test consists of drawing a stylus (e.g. Rockwell ball or diamond tip) of known radius of curvature over a film under increasing normal loads. The value of the load at which adhesion failure occurs (delamination between the film and the substrate) is known as the critical load,  $L_c$ . If the failure mode is the same, as the adhesion increases, so the value of  $L_c$  increases. Failure may be identified by an abrupt change in either the depth and /or the friction signal, or by identifying the failure point under the microscope. Scratch lines are also investigated by means of optical microscopy and AFM to determine the critical load. For very thin films, the test can be performed using a nanoindenter to carefully control the load and depth.

Many different failures modes can be observed, including coating detachment, through-thickness cracking and plastic deformation or cracking in the coating or substrate [157]. The failure modes observed in the scratch test depend on many factors and are most easily characterised in terms of the hardness of both substrate and coating (Figure 5-2) [136]. For hard coatings on soft substrates deformation of the substrate is predominantly plastic whilst the coating may plastically deform or fracture as it is bent into the track created by plastic deformation of the substrate. Soft coatings on a harder substrate tend to deform by plastic deformation and some extrusion of the coating from between the stylus and the substrate may occur. Considerable thinning of the coating by plastic deformation will occur before plastic deformation and fracture of the substrate becomes significant. For hard coatings on hard substrates plastic deformation is minimal and fracture dominates the scratch response [136].

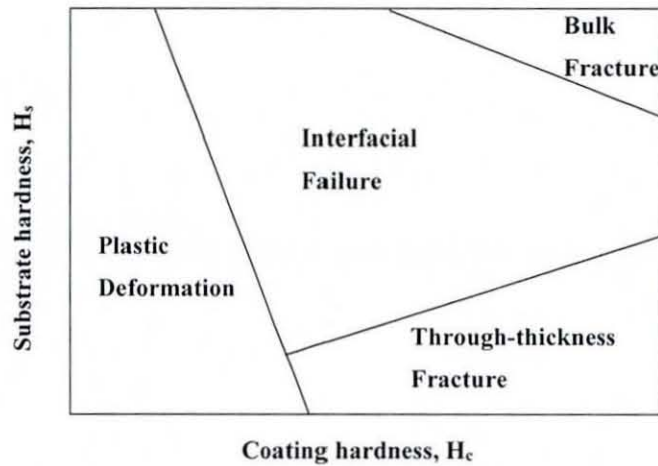


**Figure 5-2 Schematic diagram of the various scratch test failure modes as a function of coating and substrate hardness ( $H_c$  and  $H_s$ , respectively) [136]**

Using this technique Prikryl reported that the critical load is extremely dependent on the loading rate for plasma deposited polymer films of vinyltriethoxysilane (VTES) on planar glass substrates [158]. It was found that the critical load corresponding to the film with a thickness of 190 nm was much higher than that for both thicker or thinner coatings. Ottermann et al. [159] revealed that increasing the film stress decreased the critical load. Tusi et al. [160] have demonstrated that the hardness of sputter deposited aluminum films on silicon or soda-lime glass substrates is constant for indentation depths within the film thickness.

### **5.3 Methodology and experimental**

Although there is no way of measuring the fundamental adhesion directly, there are a number of tests that characterise adhesion practically. Three basic types of quantitative tests can be distinguished: tensile-type adhesion tests, shear-type tests and scratch tests [161]. However for thin films, compared to the other measurement tools, the scratch test provides a useful measure of adhesion [136, 138]. Therefore, in this study scratch tests were performed using a nanoindenter to characterise the adhesion of the electroless coating on glass.

Nanoindentation testing and scratch tests were performed by using a Micro Materials *Nanotest*<sup>TM</sup> machine, which is normally used to measure micro materials properties, hardness and nanotribometry. There were several initial test parameters for the

*Nanotest<sup>TM</sup>* machine that affected the final experiment results, including load rate, maximum load and dwell time, initial force and depth gain. Load rate is the amount the load force increases in each second, which remains constant during the test. Dwell time is the time for which the load is kept constant after the maximum load is reached and the initial force is the load force at which the machine starts to record the experimental data. The depth gain is set to 75% to obtain the best performance in scratch tests. The machine stops increasing load force when either the load force reaches the maximum load or the deformation exceeds the depth gain. It was found that mechanical deformation at the same load rate was not affected by the other test parameters.

In this work, a Berkovich diamond indenter with angle of  $142.3^\circ$  was used for mechanical measurements, and scratch tests were performed with a Rockwell indenter ( $120^\circ$  cone with  $200\ \mu\text{m}$  hemispherical tip). Scratch tests involved moving the indenter across the surface with a steadily increasing load applied. The total scratch length was  $250\ \mu\text{m}$  or  $500\ \mu\text{m}$  and along the length of the scratch the load was ramped to a maximum of  $100\ \text{mN}$ . Tests were conducted at a temperature of  $22 \pm 0.3^\circ\text{C}$  with the samples directly mounted onto a metal stub using cyanoacrylate adhesive. Scratch lines were observed using an optical microscope and AFM.

In addition to scratch tests, substrate curvature was also measured to examine the state of stress in the coatings. Due to the brittle material of the glass substrate, the tensile testing method was not suitable in this work, therefore, an optical system for measuring the sample's curvature was used. A surface profiler (Talysurf CLI 2000) was used to measure the substrate radius of curvature at room temperature. The scan distance was about  $23 \pm 1\ \text{mm}$  and multiple passes were used. The machine resolution was  $0.5\ \text{nm}$  and the radius of curvature was calculated using the Talymp analysis software. All the samples were prepared by the same procedure as in chapters 2 and 3 described with only one side of the glass coated with Cu or NiP. Samples were placed on the machine bed with the coated surface uppermost.

## 5.4 Results

### 5.4.1 Internal stress measurement

Figure 5-3 shows the results of curvature measurements for different thickness electroless Cu films. The x axis represents the measurement distance along the sample, while the y axis shows the displacement from the horizontal. Positive curvature implies that the substrate is concave on the surface on which the film is deposited, which is consistent with a state of residual tension in the film.

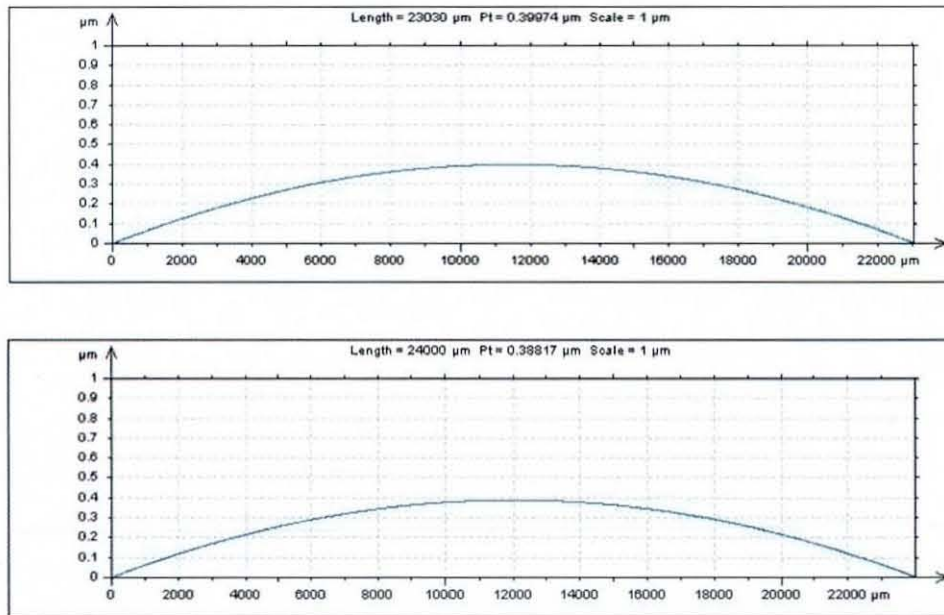


Figure 5-3 Curvature measurement of different thickness Cu films deposited on glass

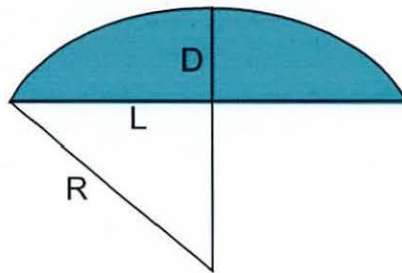
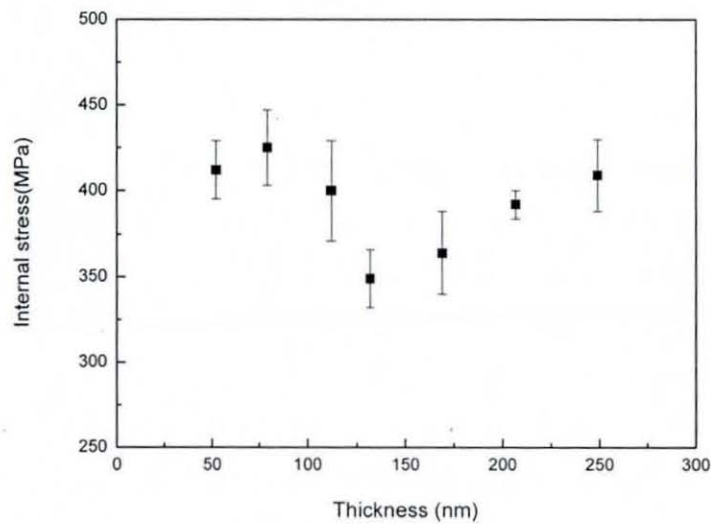


Figure 5-4 Radius calculation from curvature measurement

Figure 5-4 defines the parameters  $D$  and  $L$  that were obtained from the software directly, and then  $R$  was calculated using equation (21):

$$(R - D)^2 + L^2 = R^2 \quad (21)$$

For CMZ glass, values of  $E_s$  and  $\nu_s$  were not available, so values based on borosilicate glass were used with  $E_s = 70.5$  GPa [12]. Poisson's ratio varies for different types of glass, but for borosilicate glass  $\nu_s = 0.2$  [12] which was used here. The glass thickness,  $t_s$ , was 100  $\mu\text{m}$ . According to equation (15) and substituting the curvatures measured before and after deposition, the internal stress in the thin films was calculated. Figure 5-5 shows the internal stresses for different thickness films, in which the plotted stress values are the average of three experimental data points collected from samples prepared under the same conditions.



**Figure 5-5 Internal stress as a function of electroless Cu thickness**

In Cu films with 127-300 nm thickness, the internal stress increased with increasing thickness. The internal stress was 350 MPa at 127 nm and increased to 430 MPa at 250 nm. However, the highest stresses, of up to 450 MPa, were found in films less than 100 nm thickness. This indicates the film deposition induces higher internal stress early in the process, which is consistent with other reports [153].

Figure 5-6 shows the variation of internal stress with thickness for electroless nickel coatings and demonstrates that the internal stress decreased with increasing NiP film

thickness from 110-1120 nm. The internal stress was 770 MPa at 110 nm and decreased to 513 MPa at 1120 nm. The highest internal stress level of 770 MPa was again found in the thinner films.

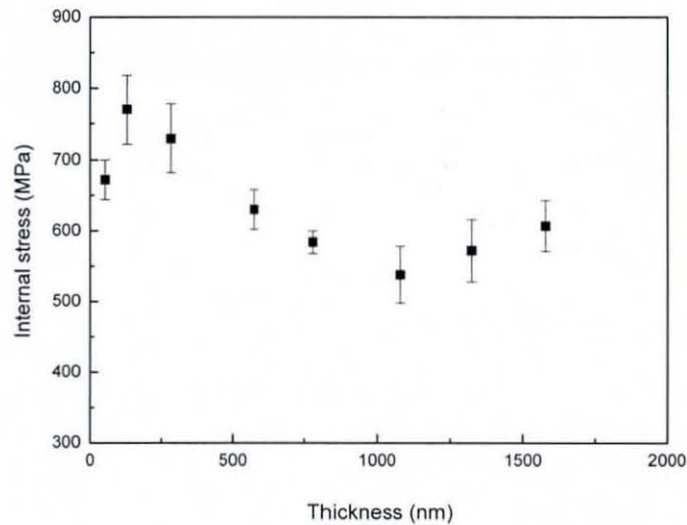


**Figure 5-6 Internal stress as a function of electroless NiP thickness**

The above results describe the total internal stress experienced by the coating which, consists of the intrinsic and thermal component. The thermal residual stress comes from differences in CTE as the sample cools from the deposition temperature and is particularly important in CVD and PVD deposited films because of the high temperatures involved. For electroless methods the thermal residual stress is not as important as the intrinsic stress, due to the low deposition temperature.

The thermal contribution to the total stress was estimated based on equation (15) for which the constants for the Cu film were  $E_{film} = 120$  GPa,  $\nu_{film} = 0.34$ . The thermal expansion coefficient of the Cu thin film ( $16.5 \times 10^{-6}/^{\circ}\text{C}$ ) is larger than that of a borosilicate glass substrate ( $3.5 \times 10^{-6}/^{\circ}\text{C}$ ) [12]. The thermal stress was therefore evaluated to be 52 MPa of tension, which is only 15% of the internal stress measured using the curvature technique. It was the same value for all the samples. The thermal expansion coefficient of the electroless nickel thin film is  $13.6 \times 10^{-6}/^{\circ}\text{C}$ , and applying this equation to the NiP film, the thermal stress was around 149 MPa. Again, it appears that the thermal stresses are only expected to be a small part of the internal stress. Using electroless methods due to the relatively low plating bath operation

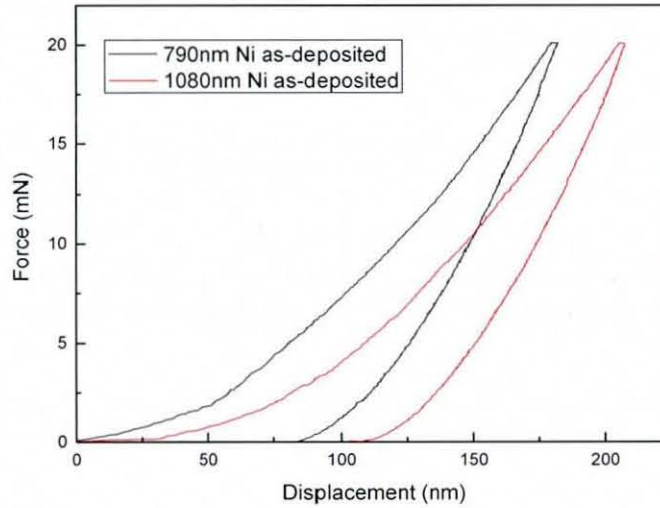


temperature, it seems that intrinsic stress due to the film growth during deposition is the main source of residual stress.

### **5.4.2 Mechanical properties**

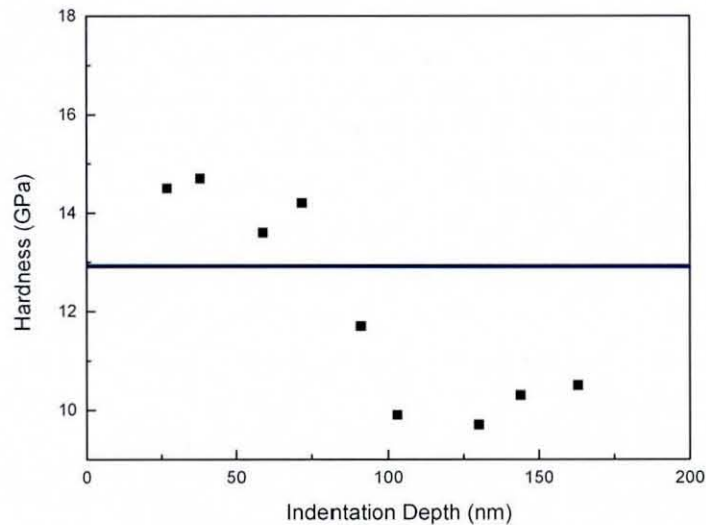
The mechanical properties of the Cu and NiP deposits were measured through nanoindentation tests. The hardness of the films was calculated using the Oliver and Pharr method described earlier. The small thickness of the deposit was considered as an important factor in the nanoindentation measurements as too high an indentation may be influenced by the substrate. To avoid influencing the results, the indentation should be designed purposely to minimise the influence of the glass substrate and therefore indentation must be deep enough to prevent errors from thermal drift, but should not exceed 20% of the deposit thickness. The thicknesses of the NiP deposits were 300-1600 nm and control of the indentation depth was relatively straightforward. The Cu films were thinner and in this case the indentation depths were not easy to control within these limits.

Figure 5-7 presents the force–displacement curves of nanoindentation for different thickness NiP coatings on CMZ glass. Since the peak indentation depths for all the coatings were about 20% of the coating thickness, the effect of the substrate could be ignored. When the initial loading was applied to the samples, the depth control mode was used to precisely control the penetration depth. The indentation load sequence was 20 s loading and 5 s hold, where the peak load was 20 mN. For the NiP film with 790 nm thickness, the maximum displacement was 179.8 nm and the final displacement after removal of the load was 82.2 nm. For the NiP film with 1080 nm thickness, the maximum displacement was 210.8 nm and the final displacement was 112.7 nm. The film plasticity was obtained from the maximum and final displacement, and was found to be 46% and 53% for the 790 nm and 1080 nm films, respectively.



**Figure 5-7 The force–displacement curves for different thickness NiP films**

Typical hardness data for a 1.2  $\mu\text{m}$  thick NiP film as a function of indentation depth are shown in Figure 5-8. It can be seen that there was a decrease in the hardness measured as the load was increased which may be because of the influence of the substrate. In general, there are two different levels in the hardness distribution as shown in Figure 5-8. The highest hardness was 15 GPa at an indentation depth of 36 nm. The hardness of the glass substrate is 10 GPa, so with the increasing indentation depth, the apparent NiP hardness decreased to that of the glass substrate.



**Figure 5-8 Hardness distribution as a function of the indentation depth into electroless NiP coatings**

The hardness and elastic modulus of different thickness NiP films measured at a load of 5 mN are plotted in Figure 5-9. It shows that the elastic modulus increased linearly from 133 GPa to 185 GPa with coating thickness. The experimental modulus is expected to be in good agreement with the literature value for indentation depths of 250 nm or more, but is significantly lower for shallow indentations. This may be because of the co-deposited P that affected the structure of the NiP [158]. In addition, it may be related to stress in the NiP deposits. To support this, the relation between the elastic modulus, hardness and internal stress are shown in Figure 5-10. It shows that both elastic modulus and hardness decrease approximately linearly with internal stress increase. The elastic modulus decreases by 40 GPa and hardness decreases by 3.6 GPa when the internal stress increases by 200 MPa.

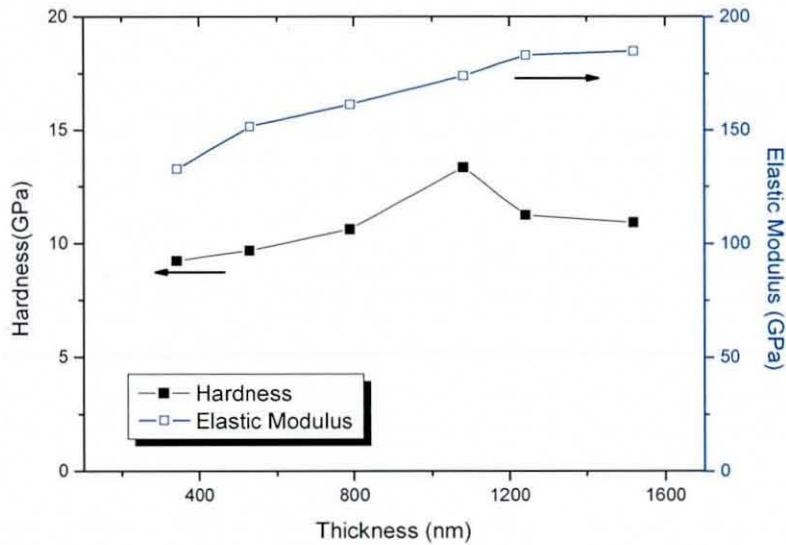


**Figure 5-9 The relationship between electroless NiP thickness and Elastic Modulus and hardness**

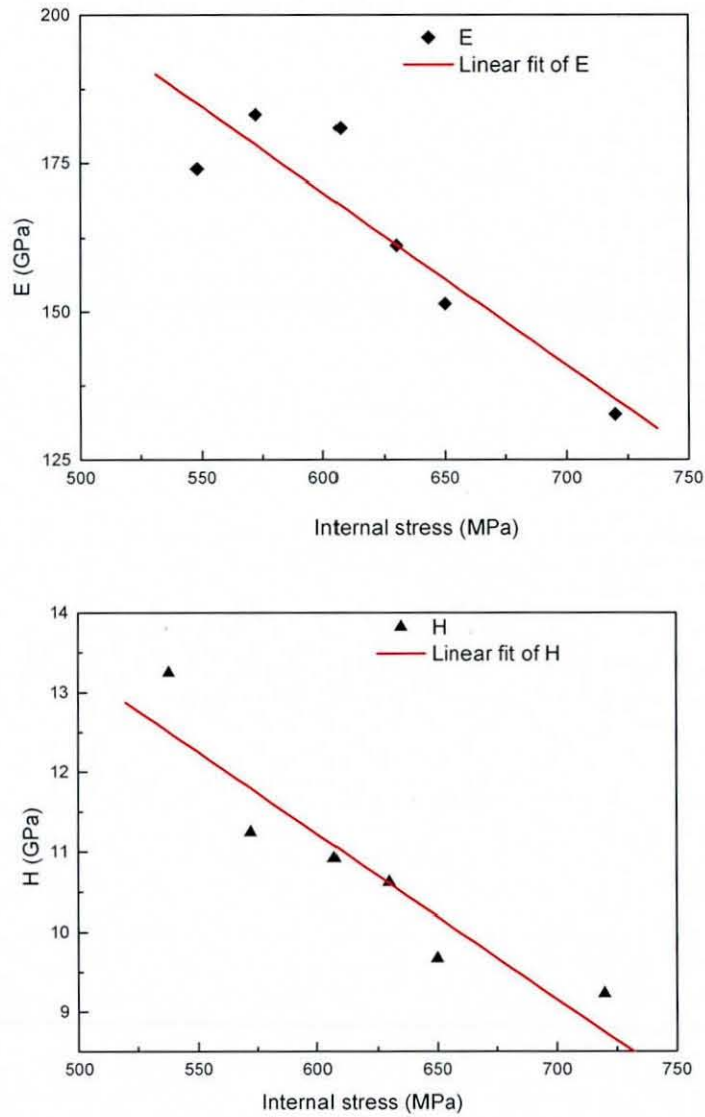


**Figure 5-10 Correlation between elastic modulus, hardness and internal stresses for NiP film**

Testing of the Cu coatings was also carried out, however, due to the limited thickness of the electroless Cu coating, it was difficult to keep the contact depths within 20% using this nanoindenter. Therefore, a maximum 1 mN force was applied to get the lowest indentation depth. Figure 5-11 presents two load-displacement curves obtained for a 168 nm thick Cu film at a maximum load of 0.8 mN. The load-displacement behaviour is typical of that for a soft metal and it is seen that there is very little elastic recovery, indicating that the deformation occurs mainly by plastic processes.

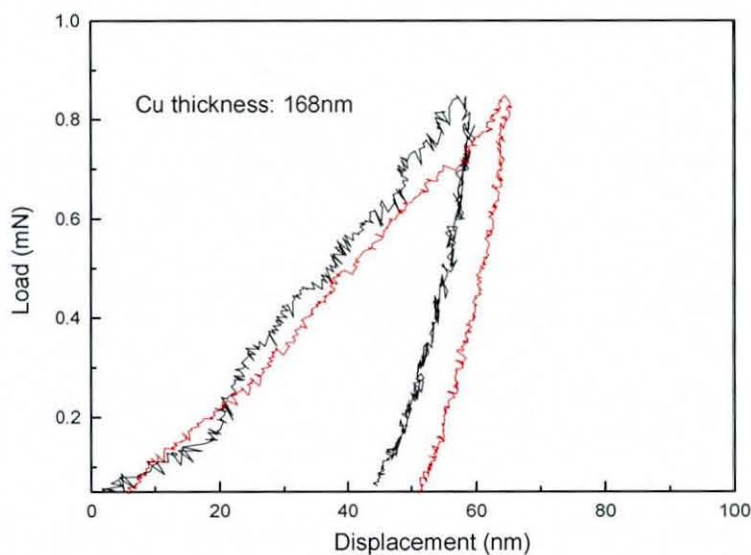


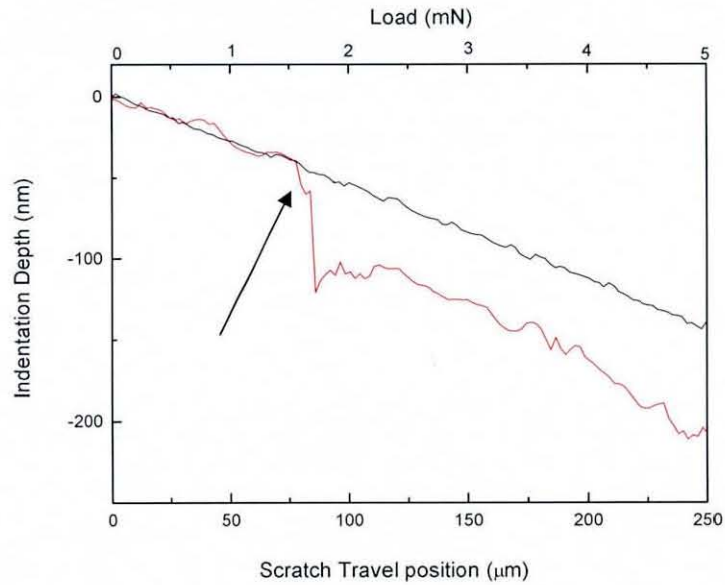
**Figure 5-11 The force–displacement curves for electroless Cu films**

For a 168 nm thick Cu film, the hardness and elastic modulus were 5.69 GPa and 110 GPa respectively. The elastic modulus was very close to that of bulk Cu rather than glass, for which the elastic modulus is only 70.5 GPa. This indicates that the substrate effect did not have a large influence on the measured film elastic modulus for this Cu thickness when a small loading force was applied to the surface. However, for the thinnest film of 70 nm, at the 1 mN applied load, the hardness was equal to the substrate hardness, indicating that the substrate was dominating the hardness behaviour for the ultra thin film system.

### 5.4.3 Scratch test

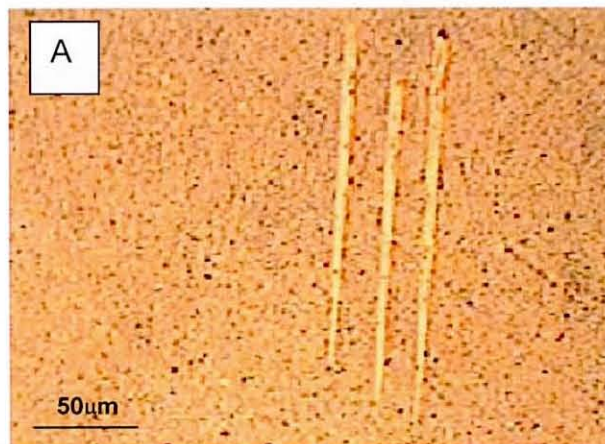
Scratch tests were carried out on all samples using different loads and loading rates. The surface profile as a function of scratch travel distance for a 138 nm thick Cu film at a maximum 5 mN ramped load is shown in Figure 5-12. The linear trace (black) shows the pre-scratch curve result and the red trace shows the scratch curve. The scratch test was performed using the multiple scan mode. First, a pre-scratch curve was recorded by drawing the indenter across the surface with a continuously increasing load. A scratch curve was then recorded by repeating the test, but adding a side to side oscillation perpendicular to the indenter motion. The critical position indicated in the figure is characterised by an abrupt increase in the post-scratch displacement. The increased displacement is directly associated with significant

damage to the Cu film. The corresponding applied normal load is called the critical load, meaning the minimum load for scratch damage with material removal, film fracture and interface delamination. The critical load is approximately 1.7 mN for this sample and the indentation depth is around 75 nm.



**Figure 5-12 Scratch test curves for electroless Cu film**

The scratch damage grooves made at different loading rates in a 138 nm Cu film were investigated by optical microscopy, as shown in Figure 5-13.



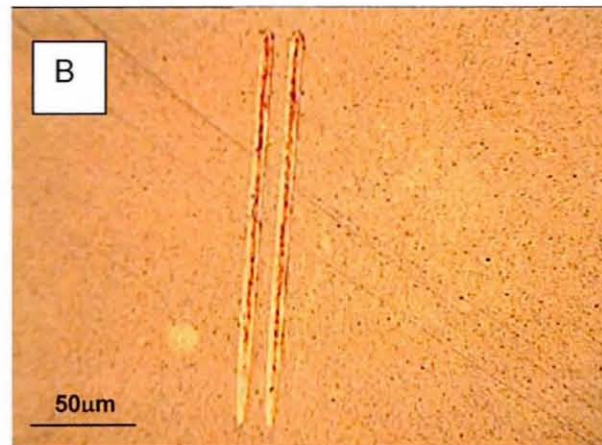


**Figure 5-13 Optical microscopy images of scratched grooves with different loading rates on electroless Cu film (A) 0.5 mN/s, (B) 1 mN/s**

The optical microscope could only show obvious morphology differences in each groove, so AFM was used to obtain valuable information such as the scratch track width and depth. Figure 5-14 shows AFM section analysis for sample A in Figure 5-13. The scratch depth is 80.4 nm and the track width is around 10  $\mu\text{m}$ .

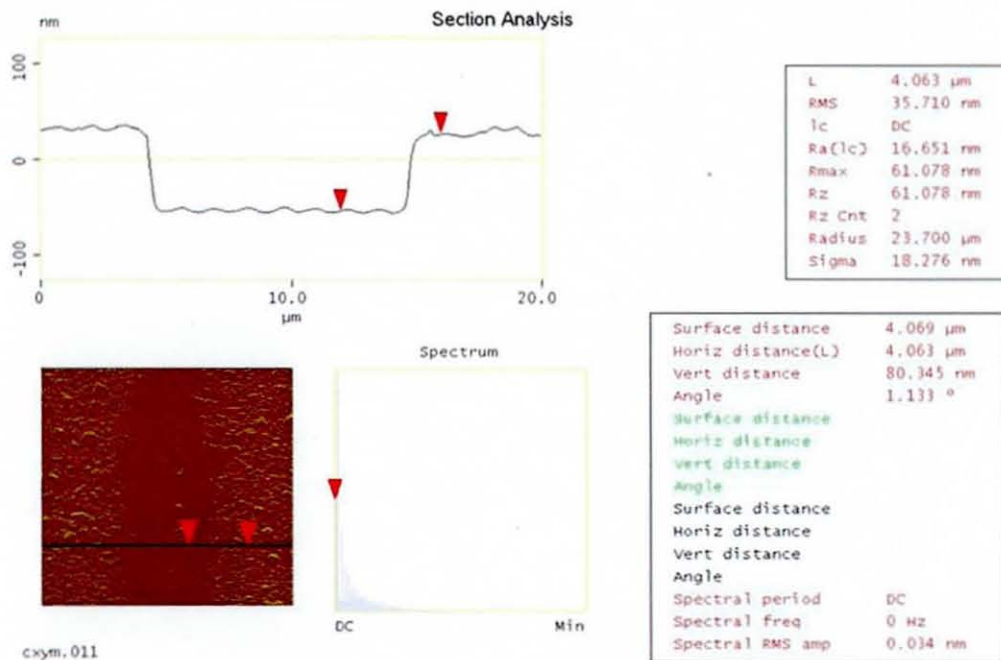


**Figure 5-14 AFM section analysis on scratched groove**

Figure 5-15 shows the relationship between critical load and Cu thickness performed under the same scratch test conditions of loading rate 0.5 mN/s, scan length 250  $\mu\text{m}$ . In this case the Cu was deposited following 1 hour in the APTS solution and 2 min

immersion in the Pd catalyst. The critical load decreased from 2.8 mN to 1.3 mN with increased film thickness. It illustrates that larger critical loads were observed for the thinner film, which is in good agreement with the peel test result.

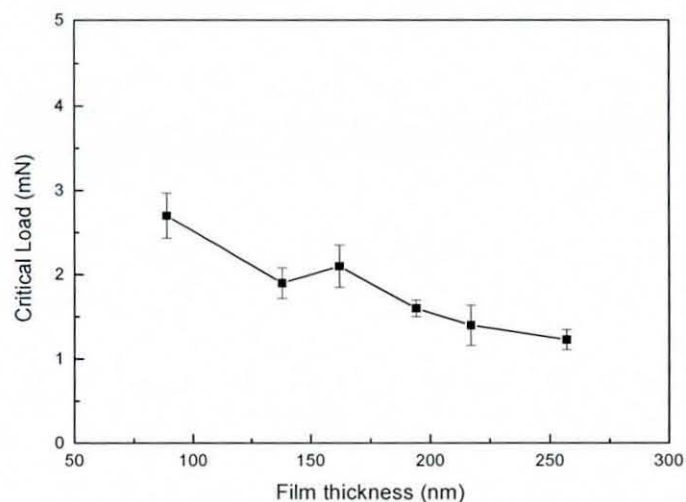


**Figure 5-15 Critical load as a function of electroless Cu thickness**

The electroless NiP film was also scratch tested. The surface profile as a function of scratch travel distance for 970 nm thick Ni at a maximum 20 mN ramped load are shown in Figure 5-16. Sometimes some fluctuations were observed in the scratch at the start of a test as indicated in the figure. This is associated with the initiation of contact between the indenter and the sample surface and some contamination adhered to the surface, but is not thought to be critical damage of the film. The critical load is approximately 14 mN for this sample.

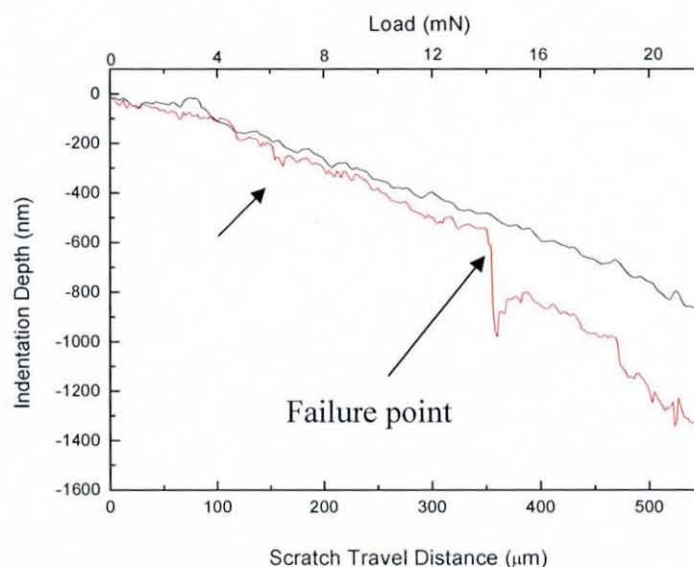


**Figure 5-16 Scratch test curves for electroless NiP film**



The surface of the NiP after the scratch test was examined in an optical microscope to identify the location where failure occurred, as shown in Figure 5-17. It can be clearly seen, the NiP film delaminated from the glass substrate and some films piled up in the track, which indicates the bad wear behaviour of this coating.

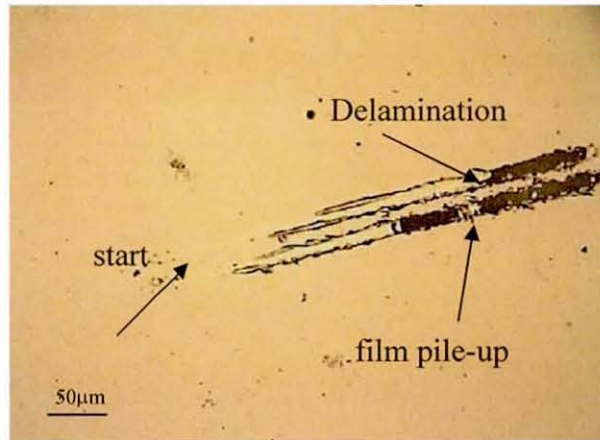


**Figure 5-17** Optical micrograph of scratch groove on NiP film

The critical load as a function of NiP thickness is displayed in Figure 5-18. All the measurements were done at the same test conditions: 0.5 mN/s loading rate, 20 mN maximum loading force and 500  $\mu\text{m}$  scratch length. The critical load is in the range from 7 mN to 17 mN and varies a little with thickness.

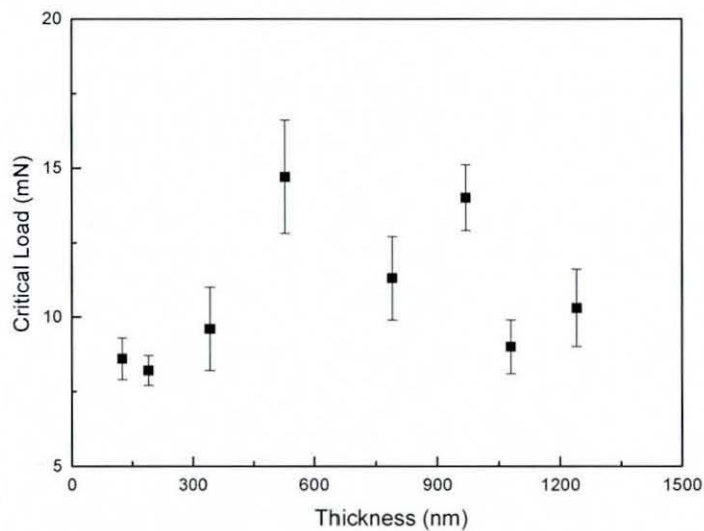


**Figure 5-18** Critical load as a function of NiP thickness

## **5.5 Discussion**

The experimental conditions used in this work made all the Cu and NiP films with a high internal stress. It has been reported by other researchers that films can possess different internal stresses, of different magnitude, when the Cu films are produced by different methods. Electroless Cu films showed internal stresses ranging from 300 to 450 MPa, which is consistent with the reported internal stresses of from 200-500 MPa observed in Cu films prepared by DC magnetron sputtering with thickness from 80-530 nm [153]. In the same work, high tensile stresses of 500-530 MPa were observed in 17-80 nm thick films. In contrast, Okolo et al. [162] showed that compressive stresses from 165 to 223 MPa were induced in 500 nm thick Cu films on amorphous SiO<sub>2</sub> by magnetron sputter deposition. This was explained by relief of the coalescence stress and the atomic peening effect during sputter deposition. Choi [163] showed that internal stresses from 0 to 500 MPa were induced into 1 μm thick Cu films on Si (100) by bias sputtering, which he suggested was due to collapse of pores and thermal effects. From the thermal stress values obtained here, it was elaborated that the films prepared by electroless plating possessed a low thermal stress compared with those reported for PVD and CVD methods.

The hardness of Cu films was also measured by Beegan and Chowdhury et al. [164] by combining the nanoindentation and AFM residual area analysis. It was found that the measured hardness was determined by applied load and thickness of the coating, meanwhile, hardness varied strongly between different measurement methods. Ma et al. indicated that the strength of Cu films is strongly dependent on the deposition technology of the film and that the measured strengths for Cu films are all higher than that of the bulk material [165]. From the measurement results presented here, it can be seen that NiP coatings have higher hardness values than the Cu coatings, which is consistent with that of the bulk material. It was seen that the film shows a high hardness value for low indentation depth and this is because atoms can easily occupy a relatively stress-free configuration with fewer structural defects for short plating times [165].

The results shown in Figure 5-10 illustrate that the increasing internal stress will decrease the measured mechanical properties of thin films, including elastic modulus

and hardness. This phenomenon can be interpreted by the fundamental theory of nanoindentation based on the Oliver-Pharr method. Consider a conical indenter with a angle  $\phi$  pressing against the film surface, then the elastic relation between the indentation force ( $P$ ) and depth ( $h$ ) can be written as [166]:

$$P = \left[ \left( \frac{2}{\pi} \frac{E}{1-\nu^2} \tan \phi \right) - \pi \sigma_i (\mu \sin \phi - \tan^2 \phi \cos \phi) \right] h^2 \quad (22)$$

where  $\sigma_i$  denotes the internal stress and  $\mu$  is a constant. From equation (22), it is clear that the internal stress will increase the indentation depth for constant force. As a result, the hardness and elastic modulus obtained from the load-displacement curve decreased. Therefore, the stress has a strong influence on the film hardness and elastic modulus.

The critical load in the nanoscratch test was measured to define the film adhesion in this work. It was found that the critical load for the Cu film was low. This low value may be due to two reasons, one is the limited thickness of the deposited Cu film and another possible reason is the limitations of the instrument used. The electroless NiP film showed a higher critical load than a Cu film of the same thickness, which is consistent with the qualitative tape testing results. It was also seen that the loading rate had a strong effect on the scratch result. The scratch groove made at the higher loading rate was more prone to failure as shown in Figure 5-13. Steinmanan et al. [167] also showed convincingly that critical load values were sensitive to some instrumental factors, such as loading rate, scan speed and film thickness. Beake et al. [168] pointed out that using different radius probes also altered the critical deformation, leading to different failure modes. Therefore, all the data collected under the same test conditions can be comparable, and the electroless NiP film shows better adhesion strength than electroless Cu of the same thickness even though it possesses higher tensile stress.

## 5.6 Conclusion

The internal stresses in electroless deposited Cu and NiP films were measured for various thicknesses. All of the Cu and NiP films were found to possess a high internal stress, which could be the main reason for weak adhesion. Moreover, the scratch tests showed that the critical load for NiP film on glass is much higher than that of copper. The scratch test on thin films is dependent on many parameters such as loading rate

and scratch speed, which make it very difficult to compare these results with those reported in the literature.

---

## **Chapter 6 Catalytic Surface Structure Effects on Electroless Cu plating**

---

### ***6.1 Introduction***

The electroless Cu or nickel deposition on glass requires a suitable surface on which to deposit. The important issue is that the surface must catalyse the oxidation of the reducing agent and then transfer the electrons to the  $\text{Cu}^{2+}$  ions in solution as described in chapter 2. Based on the results of the earlier chapters, it appeared that the adhesion failure of the coating occurred at the interface between the catalyst layer and the electroless plating. In order to investigate the reason for this, further experiments were conducted to study the effect of processing on the catalyst surface structure and its effect on the electroless plating. This section focuses on the Pd/Sn catalysts for electroless deposition.

### ***6.2 Literature review***

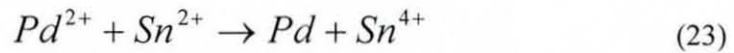
The technology of catalysing electroless deposition has evolved over the years with the aim to achieve uniform catalysis of a range of substrates with good adhesion. Previous studies have involved many different processes which are used to activate different substrates, but largely fall into the categories of Pd based catalyst and non-Pd catalyst.

#### ***6.2.1 Pd based catalysts***

Commercial Pd based catalysts have been especially formulated to provide consistent, reliable activation prior to electroless deposition. Pd based catalysts are of

considerable importance for the electroless metallisation of dielectric substrates such as plastic and ceramics as this produces a seed layer of palladium on the surface that activates the electroless deposition quickly. Table 6-1 shows a survey of some of the Pd catalysts that are used for electroless coating with examples of their applications.

A widely used Pd catalyst is based on a combination of Sn and Pd for which there are two main process routes: a two-step process which uses dilute solutions of first SnCl<sub>2</sub> then PdCl<sub>2</sub>; and a one-step process which uses a mixed SnCl<sub>2</sub>-PdCl<sub>2</sub> solution. The most extensively used system is the so-called SnPd mixed catalyst (also called SnPd or Sn/Pd). The catalysts are prepared by mixing PdCl<sub>2</sub>, with a large excess of SnCl<sub>2</sub>, in HCl solution. Pd particles are obtained by the following redox reaction:



The surface to be activated, i.e. catalysed, is immersed in the catalyst, depositing metallic Pd as well as Sn(IV). It is assumed that the metallic Pd acts as the catalyst for the subsequent electroless plating. In this system, tin not only acts as the reducing agent for Pd ions, it is also claimed to stabilize the small Pd nuclei (on the order of some nanometers in size) once they form, via strong Sn<sup>4+</sup> adsorption [71]. The resulting high positive charge density on the particles should, through electrostatic repulsion, prevent them from aggregating. Indeed, excess ionic tin on the surface can be detrimental and is usually removed. To do this, a solution known as an accelerator is used to remove the tin species from the surface before initiation of the plating reaction. However, if a self-accelerating electroless solution is employed, this is not required, as the tin species can be removed in the electroless bath..

**Table 6-1 Examples of Pd based catalysts in electroless deposition**

Catalyst	Application	Reference
Pd-Me (Me = Ag, Pt)	Synthesis of hydrogen peroxide with catalysts prepared by depositing metals by ELD	[167]
Na <sub>2</sub> PdCl <sub>4</sub>	The fabrication process of Cu nanowires by ELD	[168]
SnPd mixed catalyst (two-step and one step)	Nickel coating on activated mesoporous alumina membrane Cu or nickel coating on activated insulating material	[64, 132, 169]
PdCl <sub>2</sub> (tin-free)	Electroless metallisation of carbon substrates	[170]
Pd/ [C <sub>18</sub> H <sub>37</sub> ] <sub>4</sub> N <sup>+</sup> Br <sup>-</sup>	Microcontact printing to form micron-scale pattern by electroless deposition of Cu	[171]

An important aspect of the process is the catalytic activity of the PdSn catalyst, which can be estimated by measuring its activity for the electro-oxidation of formaldehyde or by the cyclic voltammetric response of a seeded electrode in an inert electrolyte [171, 174]. Formaldehyde oxidation is the reaction that is kinetically limited and strongly influenced by the catalyst. The cyclic voltammetric technique combined with transmission electron microscopy examination has been used to evaluate various accelerating solutions used to increase the activity as it is a useful and straightforward method for the direct evaluation of the catalytic activity of the PdSn colloids [174]. Osaka et al. [175] adsorbed the colloid on a Au electrode, then stripped it from the surface with a positive-going potential sweep. The charges under the stripping peaks could be taken as a measure of the quantity of Pd and Sn at the surface.

Although the SnPd mixed catalyst is widely used in the PCB industry, the use of Sn<sup>2+</sup> has some drawbacks with respect to the electrocatalytic activity of the Pd nuclei in the subsequent electroless plating sequence. So some articles reported the use of PdCl<sub>2</sub> to activate the surface by forming solid complexes between palladium ions and amine groups. Charbonnier et al. [176] have developed a Sn-free process where the surface

is only activated in a PdCl<sub>2</sub> solution after plasma pre-treatment. Moreover, van der Putten et al. [172] have reported a Sn-free process for use with polymer films modified by plasma treatment and graft copolymerisation with aniline followed by activation in a Pd-containing solution. The grafted polyaniline reduced Pd ions to metallic Pd, therefore avoiding the use of the SnCl<sub>2</sub> solution.

In general, all kinds of Pd based catalyst have been especially formulated to provide consistent, reliable activation prior to electroless deposition. A large difference in the morphologies of these different types of Pd catalysts is expected because of their different reduction mechanisms [177]. Moreover, the crystallisation processes of these Pd catalysts and Cu films significantly affect the surface morphologies that are obtained, the microstructures and crystal structures influence the resultant properties of the Cu films including electrical conductivity and electron/stress migration behaviours. Therefore, many mechanisms for Pd/Cu crystallisation have been proposed. It was found that growth and formation of the Cu clusters composed of smaller particles led to a better electroless Cu film [177], but there was no related experimental observation provided for the deposit adhesion and the effect of the catalytic structure. Therefore, the research herein focuses on the microstructural observation and characterisation of the interface crystallography of Pd catalysts combined with electroless deposited Cu films.

### **6.2.2 Non-Pd catalysts**

As well as Pd based catalysts noble metals, such as Ag, Au and Pt, have been used as alternative catalysts in electroless deposition. They can be either colloidal or in the form of nanoparticles. Due to the high cost of palladium, Shukla et al. [178] developed colloidal Ag as a catalyst to form a Cu mirror through pre-treatment with Ag slurry, without affecting the properties of the electroless Cu coating. Liu et al. [179] also reported that a thin layer of Ag colloids was anchored onto a glass surface through S-Ag bonds, resulting in a quicker deposition of Cu metal and a stronger adherence. Au nanoparticles were confined onto patterned films as a catalyst for the succeeding Cu electroless deposition [180].



### **6.3 Methodology and experimental procedures**

In order to understand the chemical composition that was formed during the initial deposition stage of different catalyst procedures, chemical analysis was carried out using XPS and static secondary ion mass spectrometry (SSIMS). Meanwhile, microstructure observation of the different morphologies caused by varied Pd/Sn treatments and Cu deposition were investigated using SEM and transmission electron microscopy (TEM) combined with energy dispersive x-ray (EDX).

XPS spectra were recorded using the same ESCALAB instrument and procedure described in chapter 4. Core level spectra were fitted by using XPSPEAK41 software; as part of this, the line width (full width at half-maximum, FWHM) and Lorentzian-Gaussian ratio of peaks was maintained constant for all components in a particular spectrum. Surface atomic ratios were calculated from the fitted peak areas normalised by relative atomic sensitivity factors.

Secondary ion mass spectrometry (SIMS) is a technique used to analyse the composition of solid surfaces and thin films by sputtering the surface of the specimen with a focused primary ion beam and collecting and analysing ejected secondary ions. While only charged secondary ions emitted from the material surface through the sputtering process are used to analyse the chemical composition of the material, these represent a small fraction of the particles emitted from the sample. These secondary ions are measured with a mass spectrometer to determine the elemental, isotopic, or molecular composition of the surface. SIMS is the most sensitive surface analysis technique, being able to detect elements present in the parts per billion range.

A time of flight SIMS (ToF-SIMS) IV instrument (ION-TOF GmbH, Münster, Germany) based at Nottingham University and fitted with a  $\text{Cs}^+$  primary ion beam source was used to investigate the surface chemistry of the electroless process at an ion beam energy of 25 keV. Samples were prepared not more than 24h before measurement. Pulsed low energy electrons (20 eV) were used to negate any charging effects due to the primary ion beam. The ion dose was maintained below  $1.0 \times 10^{12}$  ions/cm<sup>2</sup> and the primary ion beam was scanned over an area of  $200 \times 200 \mu\text{m}^2$ . The

spectra were fine-calibrated with the IonSpec (version 4.0) software using the exact masses of a standard set of small ions.

The microstructure of the deposits on glass substrates were examined using a Philips FEI Tecnai F20 Transmission Electron Microscope (TEM) operated at 5 kV and 1 mA. The Tecnai F20 was also used for direct higher resolution observation of the microstructural evolution of the different catalyst treated Cu coating on the glass surface. EDX analysis was carried out using an Oxford Instruments ISIS300 fitted to the Tecnai F20 and was used to define the distribution of catalyst within the metallic layer to provide quantification of the major elements at the interface and, where possible, the inclusions. TEM samples were prepared using a dual beam FIB instrument. The surface was cut using the ion beam at a high current (20 nA and 30 kV). A thin lamella was then prepared by rough milling, followed by additional milling at a lower current of 50 pA to clean the surface of the cross-section of any redeposited material from rough milling. The lamella was then attached to a tungsten needle by platinum deposition.

## **6.4 Results**

### **6.4.1 XPS of catalytic surfaces**

As the adhesion failure appeared to occur at the interface between the catalyst and Cu layers as shown in chapter 4, more dedicated experiments were carried out to examine the effect of immersion time in the catalyst. In this experiment, all of the glass sheets were pre-treated in APTS solution for 1 hour and then immersed in the pre-dip solution for 1 min. After that, the glass was activated by dipping in the Pd/Sn catalyst for different times to coat the surface. Figure 6-1 shows Pd 3d and Sn 3d XPS spectra of the activated substrate for (A) 30 sec, (B) 2 min (C) 8 min in catalyst solution.

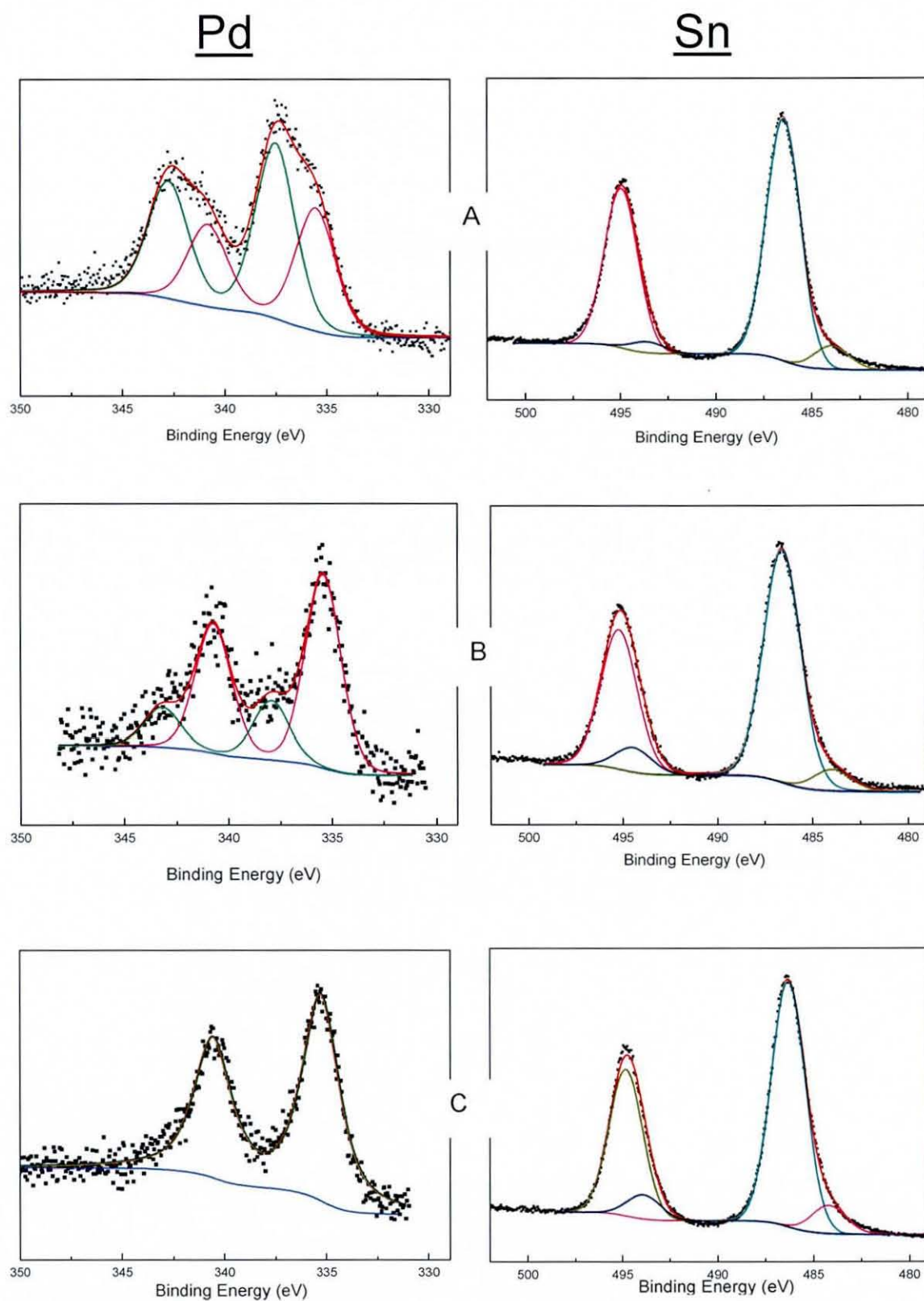


**Figure 6-1 Pd 3d and Sn 3d XPS core-level spectra of the activated substrate for (A) 30 sec (B) 2 min (C) 8 min exposure to the catalyst solution**

The Pd spectra present a doublet corresponding to Pd 3d<sub>5/2</sub> and Pd 3d<sub>3/2</sub> with a binding energy difference of about 5.3 eV. Each Pd spectrum ((A) and (B)) can be fitted with two spin-orbit-split doublets, while Pd spectrum (C) only presents one doublet. The main doublet with the Pd 3d<sub>5/2</sub> peak in (A) lying at 337.5 eV (green line) is attributed to Pd(II) and another peak at 335.4 eV (pink line) is attributed to Pd(0). The blue line shows the background of the spectrum and the orange line indicates the summation of the fitted peaks.

The corresponding Sn 3d XPS spectra shown on the right side of Figure 6-1 present a doublet corresponding to Sn 3d<sub>5/2</sub> and Sn 3d<sub>3/2</sub> with a binding energy difference of about 8.5 eV or 8.6 eV [71]. Each Sn spectrum can be fitted with two spin-orbit split doublets. The main doublet with the Sn 3d<sub>5/2</sub> peak lying at 486.5 eV (or 486.4 eV) is attributed to Sn(II) or Sn(IV) as the binding energy is very close to both of these species. The doublet where the Sn 3d<sub>5/2</sub> peak lies at 484.6 eV is assigned to metallic tin.

Table 6-2 lists the elemental ratios obtained from the areas of the XPS spectra, which allow the determination of the relative quantity of total Pd and Sn when the substrate was immersed for different time in solution. The ratio of Sn/Pd increased with increasing immersion time as did the amount of Pd metallic form compared to the Pd(II) state, while the metallic Sn / Sn(IV) ratio increased only slightly.

**Table 6-2 Ratios of elemental compositions for different catalyst immersion times**

	<b>Immersion time</b>	<b>Pd(0)/Pd(II)</b>	<b>Sn(0)/Sn(IV)</b>	<b>Sn/Pd</b>
A	30sec	0.7	0.10	4.6
B	2 min	3.3	0.12	8.43
C	8 min	All Pd(0)	0.13	10.7

Following the catalyst process, it was necessary to find out the nucleation and activity of the catalytic layer in the initial (0 to 1 min) immersion period in the electroless Cu solution. Therefore, XPS was employed to show the catalytic surface changes once it was immersed in the electroless Cu bath. Figure 6-2 shows Pd 3d and Sn 3d XPS

core-level spectra for (A) 15 sec, and (B) 1 min, in the electroless Cu solution. Before deposition of Cu, the glass was pre-treated with APTS solution for 1 hour, pre-dip for 1 min and catalyst for 2 min.

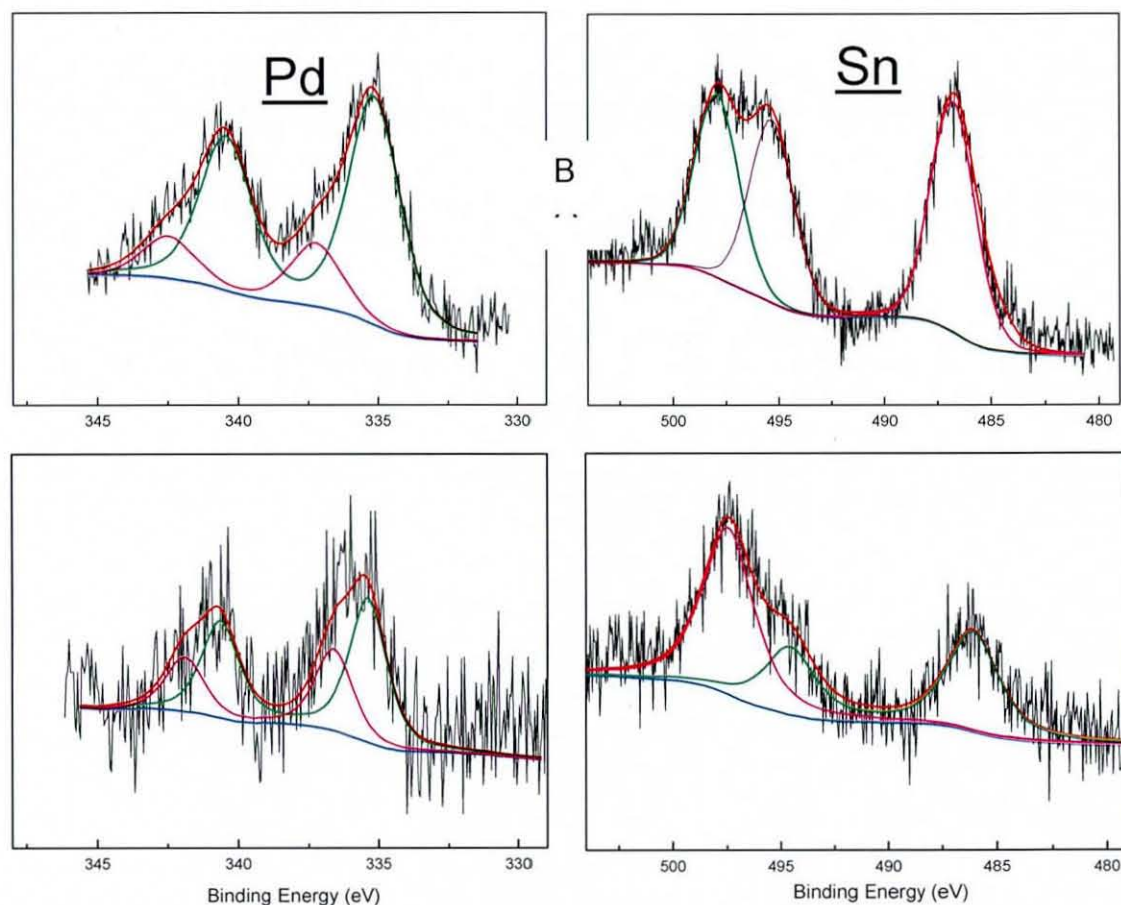


**Figure 6-2 Pd 3d, Sn 3d XPS core-level spectra after electroless Cu solution exposure for (A) 15 sec (B) 1 min**

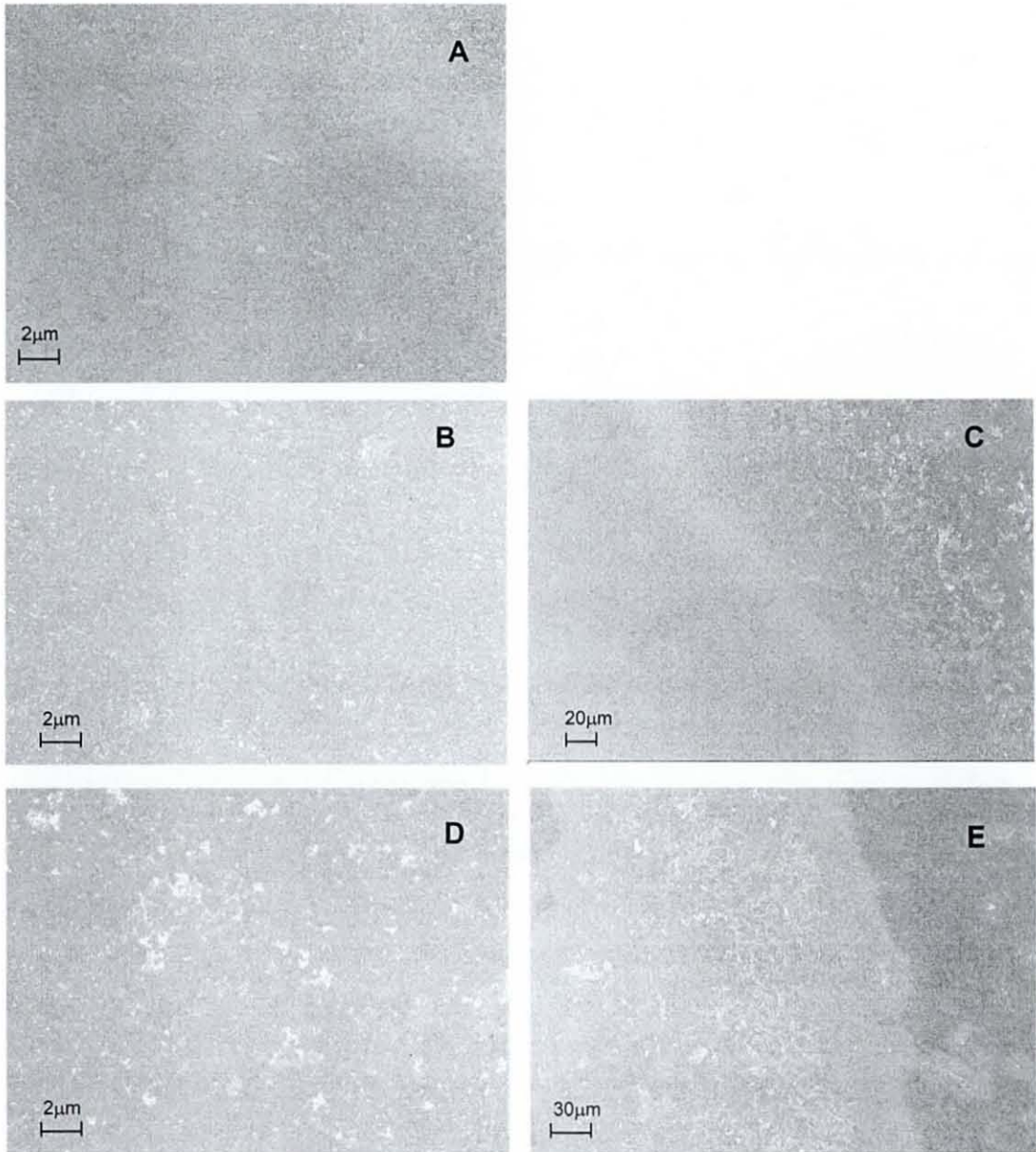
The shape of the Pd spectrum after 15 seconds in the electroless Cu solution (Figure 6-2A) was very similar to the catalyst one shown in Figure 6-1B. The Pd spectrum still presented a doublet corresponding to Pd 3d<sub>5/2</sub> and Pd 3d<sub>3/2</sub> with a binding energy difference of about 5.3 eV. The Pd spectrum was also composed of two spin-orbit split doublets. The main doublet with the Pd 3d<sub>5/2</sub> peak at 335.4 eV is attributed to Pd(0), while another peak is located at 337.3 eV. When the catalytic glass was immersed in the electroless Cu bath for 1 min (Figure 6-2B), the Sn signal decreased sharply compared to the value before plating. In addition, due to the low Pd signal,

the Pd spectrum could not be fitted easily with two spin-orbit split doublets as the background noise level was fairly high.

With increasing immersion time in the electroless Cu bath, the size of the Sn peaks decreased, but could still be seen. The spectra of Sn after a short time (15 sec / 1 min) in the electroless Cu bath can be fitted with one strong peak lying at 497.4 eV and one spin-orbit-split doublet located in 486.5 which is attributed to Sn(II) or Sn(IV). The peak at 497.4 eV is thought to be a sodium Auger peak presumably due to some contamination from the bath.

### **6.4.2 SEM of catalytic surfaces**

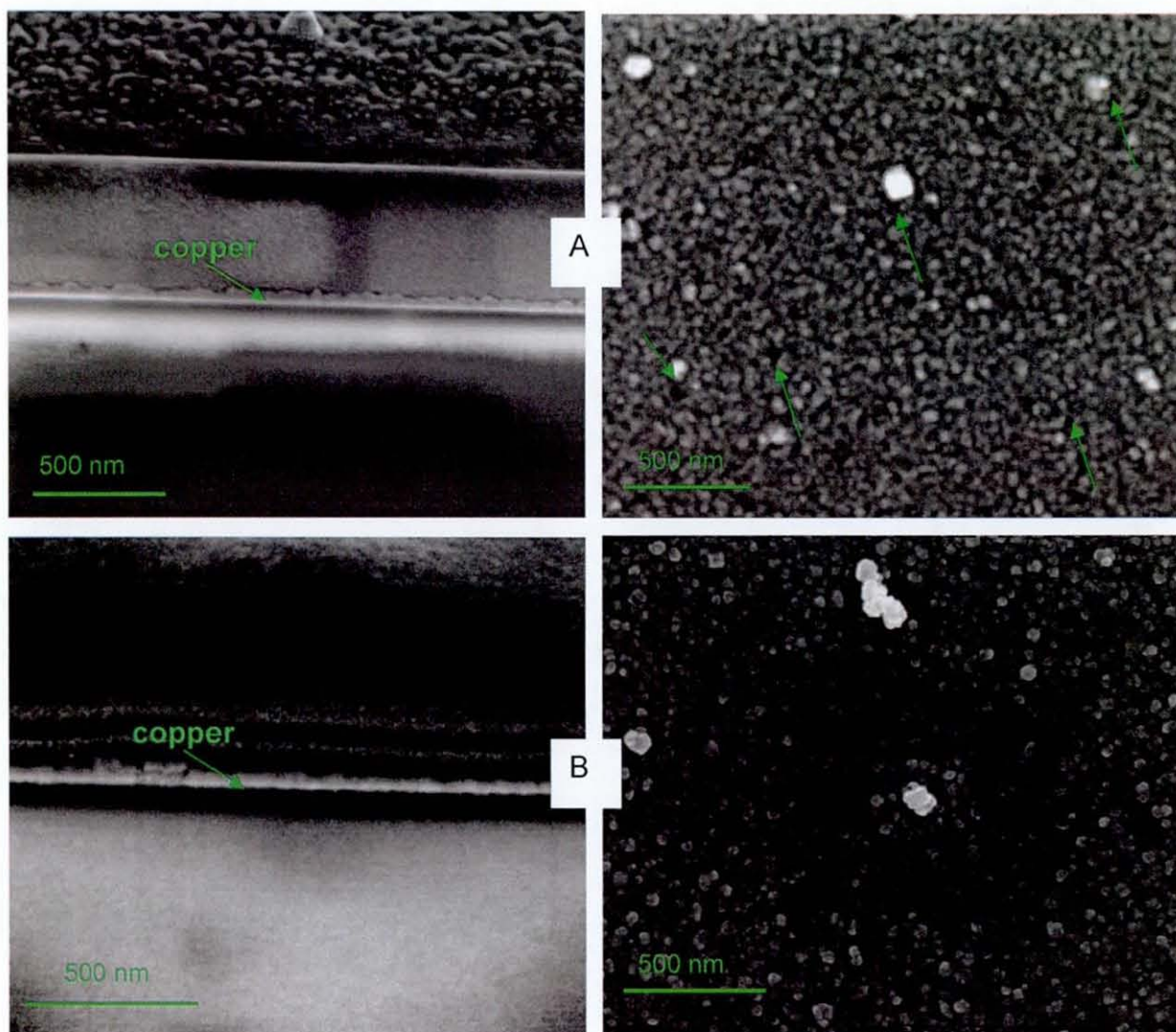
SEM was used to investigate the surface morphology for different catalytic surfaces. Figure 6-3 shows the absorbed catalyst particles for different immersion times in the catalyst solution. The deposition temperature was kept constant at a room temperature of 20-24 °C. Figure 6-3A shows the surface morphology of catalyst deposited after 30 sec. Since the deposition during the initial period is slow, limited catalyst particles were absorbed on the surface. The surface after catalyst deposition for 2 min is presented in Figure 6-3B. Obviously, the amount of the absorbed particles increases as the immersion time increases, leading to a uniform distribution of particles. In order to emphasise different morphologies between catalyst treated and non-catalyst treated surfaces, the interface was observed as shown in Figure 6-3C. To obtain this, a part of the glass was immersed into the catalyst solution, while another area did not contact the solution. As can be seen the untouched area, is almost smooth, while in the catalytic area, many particles can be found. After immersion in the catalyst solution for 8 min, the distribution of particles was not even over the surface, resulting in a patchy surface (Figure 6-3D). Figure E shows different morphologies of catalyst and non-catalyst treated areas. Some catalyst particles were found on the non-catalyst area presumably due to the rinsing process, however there was still an obvious boundary between the two sides.



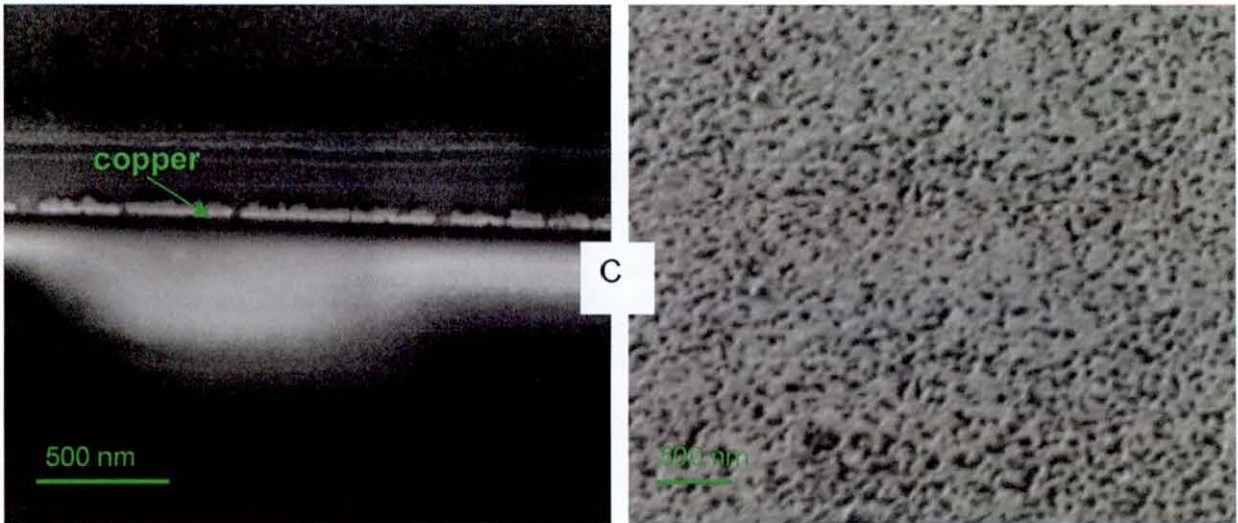
**Figure 6-3 SEM images of the catalytic surface with different immersion time (A) 30 sec (B,C) 2 min (D,E) 8 min in the catalyst solution**

SEM was also used to observe the surface morphology of electroless Cu deposits prepared with different catalyst immersion times. The samples were prepared in the electroless Cu bath for 5 min at 40°C. Figure 6-4 depicts the morphologies of the cross-section (left) and plan view (right) of electroless Cu deposited on glass with different catalyst immersion times: 0.5 min, 2 min and 8 min. It was found that, if the immersion time in the catalyst was short (e.g. 0.5 min), the Cu film was continuous and small Cu particles were observed as shown in Figure 6-4A, however, some voids

also appeared on the surface as are highlighted by the arrows. After increasing the catalyst immersion time to 2 min, the particle size of the Cu deposits became bigger and there were no black voids on the surface. Figure 6-4C shows when the catalyst time was as long as 8 minutes, in which case the Cu film had obvious breaks and voids. The surface morphology was further revealed by plan view images. All the glass surfaces were fully covered by Cu particles after 2mins (Figure 6-4B), while there were some voids and breaks visible after 8 mins (Figure 6-4C), consistent with the presented cross-sections.

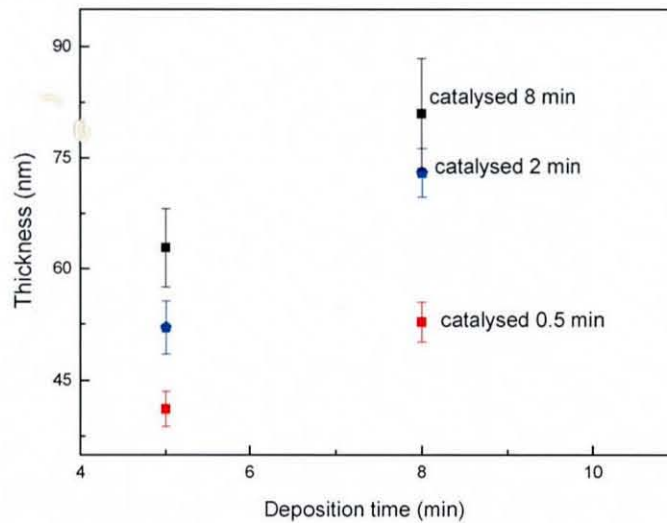






**Figure 6-4** SEM images of the cross-section (left) and plan view (right) of electroless Cu deposited on glass with different catalyst immersion time: (A) 0.5 min (B) 2 min (C) 8 min.

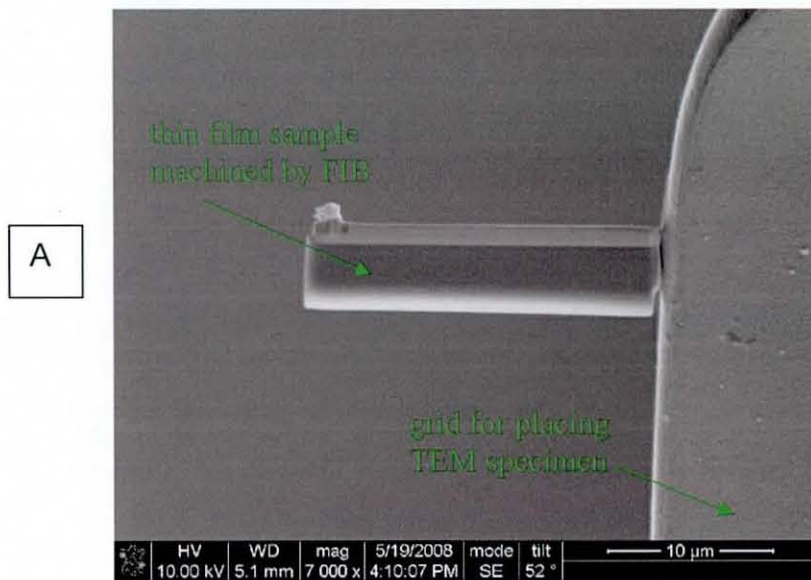
In order to estimate the effect of catalyst immersion time on the Cu deposition thickness, the thicknesses of deposits were measured by the software fitted on the FIBSEM. At least 6 different points were collected for each coating layer. The breaks and voiding regions of the electroless Cu with 8 min catalyst were not included in the thickness measurement. It was found that longer catalyst immersion times led to a thicker coating.

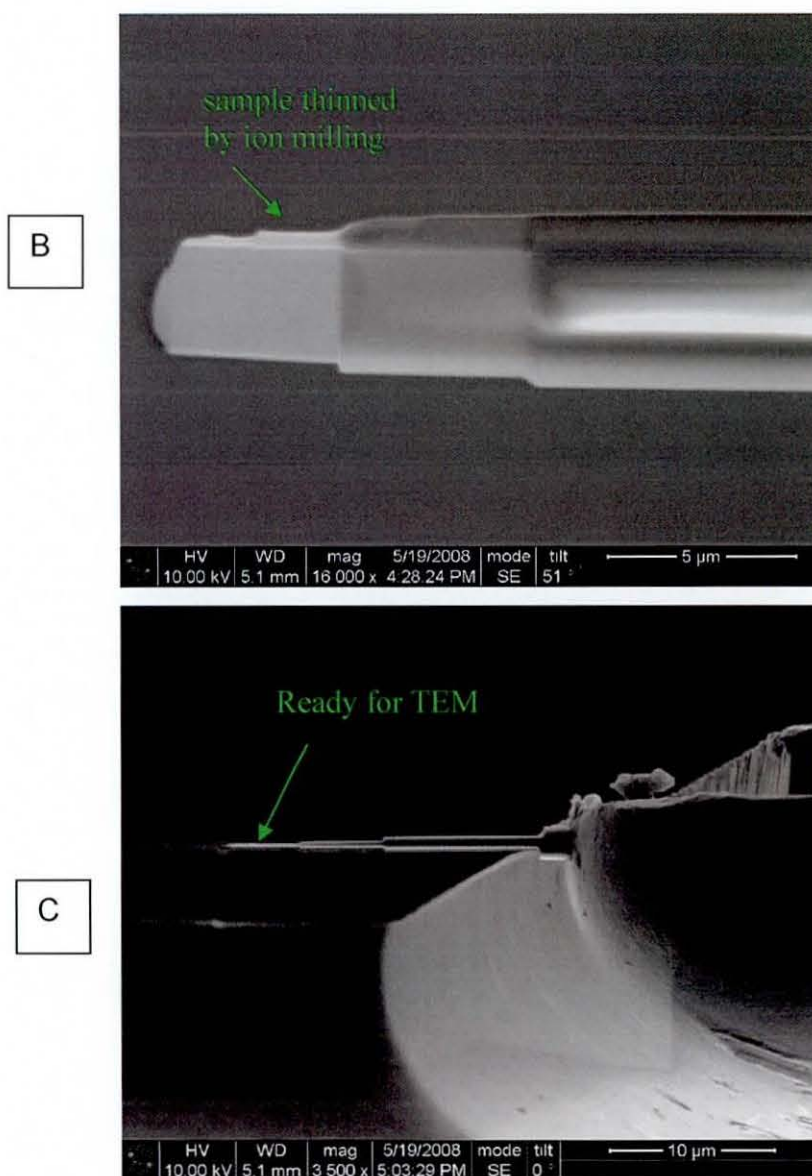


**Figure 6-5** Catalyst immersion time effect on Cu deposition thickness

### 6.4.3 TEM observations

Based on the SEM results showing the effect of catalyst treatment time on the morphology of the electroless Cu, TEM was used to obtain more detailed information on the microstructure between the glass and electroless deposits. The preparation of TEM samples was carried out in the FIB instrument. Once the area of interest was selected, it was coated with a Pt film about 1  $\mu\text{m}$  thick in order to protect the surface during ion milling. The width and depth of these trenches are generally in the 10  $\mu\text{m}$  to 20  $\mu\text{m}$  range. A thin slice 500 nm thick is routinely obtained. Several areas of interest may be thinned on the same specimen. Figure 6-6 shows a typical process for TEM sample fabrication of a thin film on glass substrate that was machined and thinned. First, the machined rectangle film sample was attached to a grid for TEM observation. Secondly, the thin film sample was thinned using ion milling. Finally, Ar gas was used to clear all the remnants on the sample.

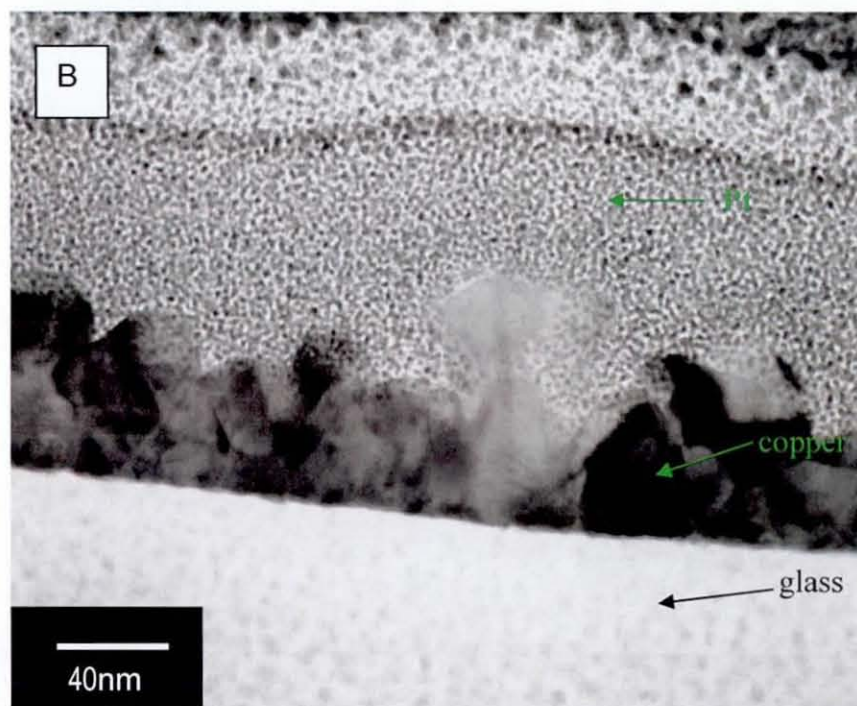
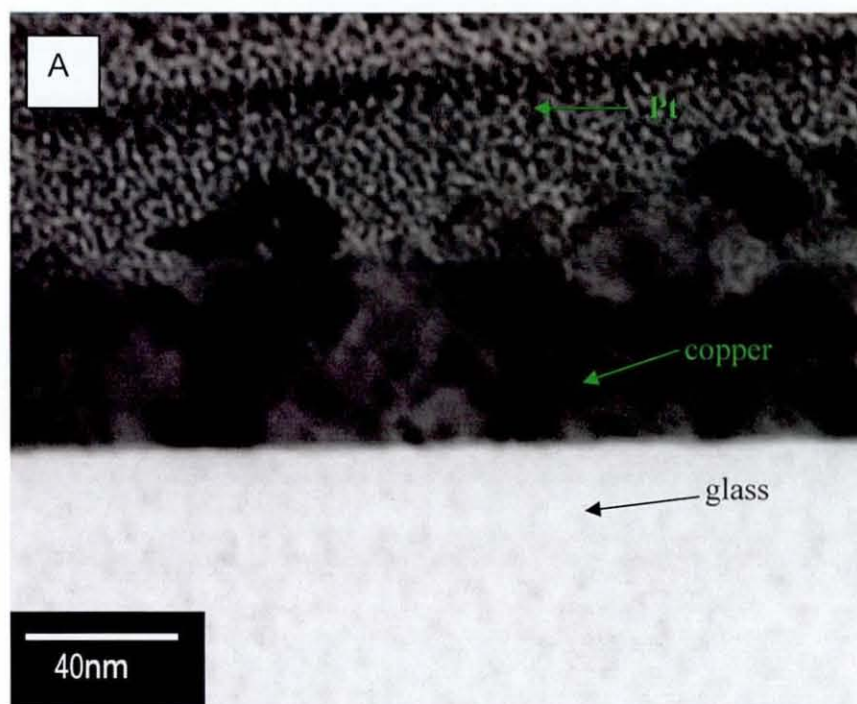




**Figure 6-6 SEM images of FIB machined TEM sample (A) FIB machined TEM sample adhered to grid, (B) Final thinning of the TEM sample, (C) Finished TEM sample**

In Figure 6-7 are TEM cross-section images of electroless Cu deposited on a glass substrate, which were catalysed for 0.5 min, 2 min and 8 min. Due to the basic mechanism of TEM, an ultrathin layer was needed for TEM observation, so all the coatings were prepared with 5 min electroless Cu deposition. As seen in Figure 6-7, the samples consist of the Pt coating at the top, glass at the bottom and the electroless Cu layer in the middle, which appears to be made of grains. The deposits in A and B consist of small and even grains and form a continuous film. The deposit in Figure 6-7C exhibits an uneven grain size distribution and small voids can be seen. The dimension of the voids and breaks are not as big as those seen in the SEM images

(Figure 6-4C), but this is probably because in the SEM images it was not easy to observe small amounts of Cu at the bottom. The grains on the substrate which had been catalysed for 8 min generally show a larger size than those on the substrates catalysed for only 0.5 or 2 min.



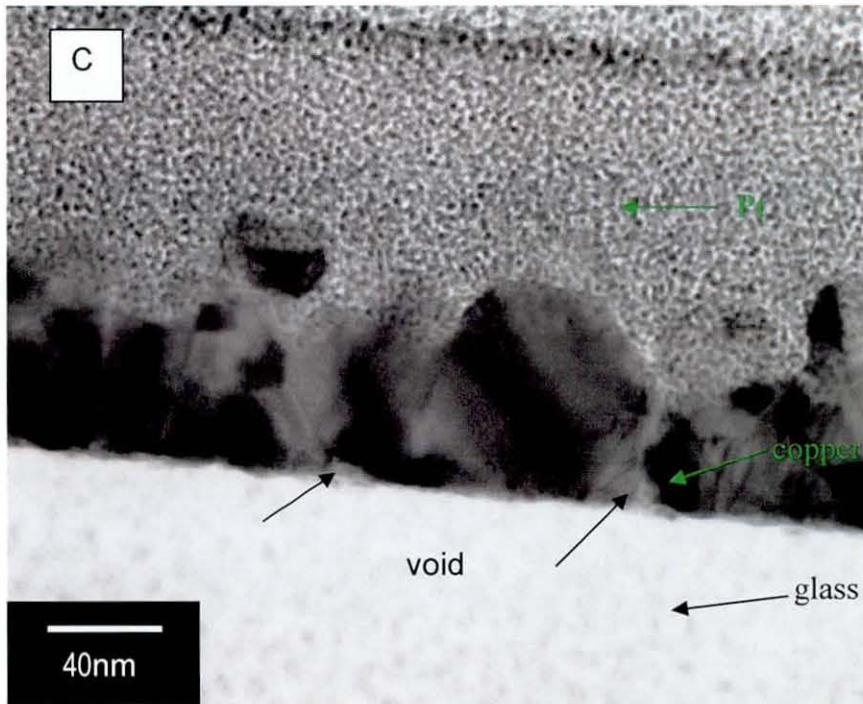
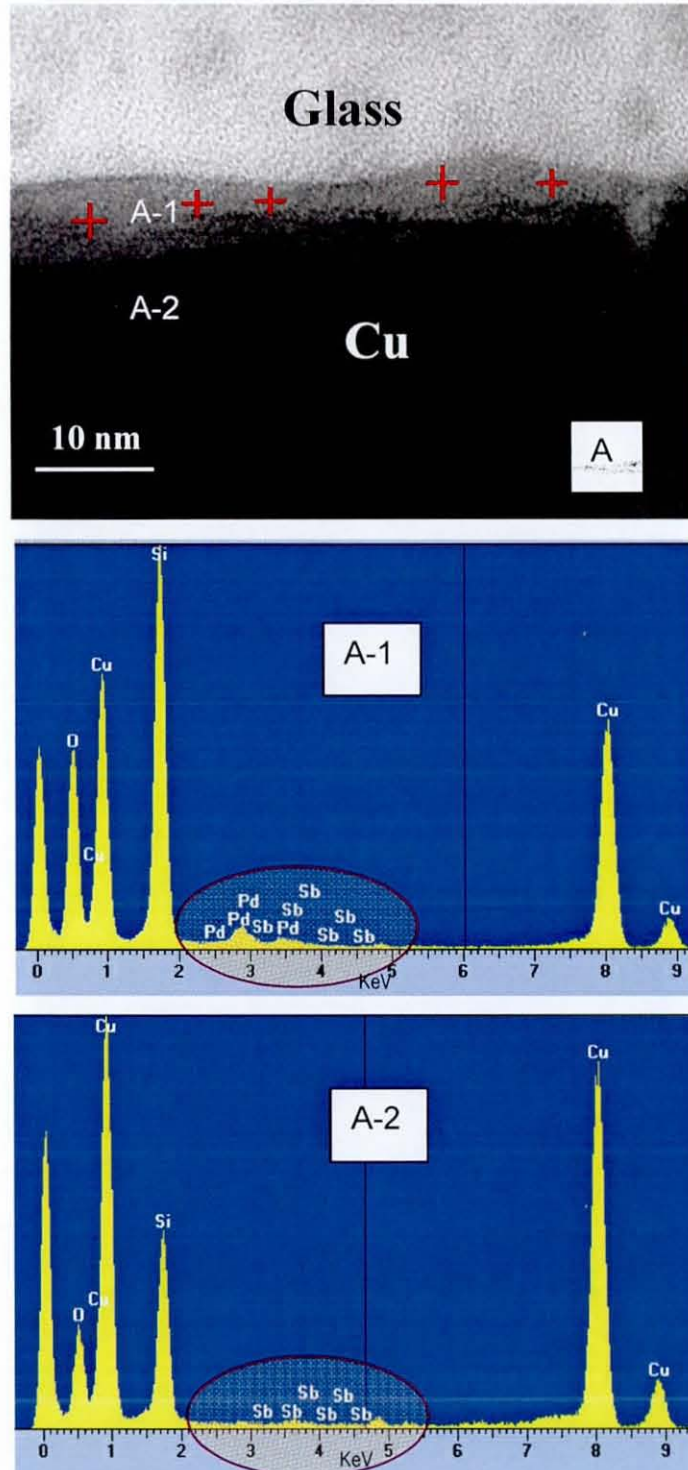


**Figure 6-7 TEM micrographs of electroless Cu deposited on glass with different catalyst immersion times: (A) 0.5 min, (B) 2 min, (C) 8 min**

The interface of different deposits prepared using different catalyst exposure times was also observed by high resolution TEM. Figure 6-8 shows TEM micrographs and corresponding EDX spectra of electroless Cu deposited on glass with catalyst immersion times: (A) 2 min and (B) 8 min. A continuous layer was seen between the Cu coating and glass, as shown with the red cross symbols in Figure 6-8A. After EDX analysis on several spots along this layer, it was concluded that this was the catalyst layer as there was an obvious Pd peak in the EDX spectrum (Figure 6-8A-1). For comparison, Figure 6-8A-2 presents the EDX result for a corresponding Cu area in Figure 6-8A, for which no Pd was observed. The thickness of the Pd layer was in the range of 2 nm to 8 nm.

EDX was also used to reveal the composition of the samples catalysed for 8 min. Figure 6-8B shows a number of areas that were analysed. The signal of Sb and Ce comes from the glass substrate. Due to the ultrathin layer of Pd, signals from both Cu and glass were also detected in the EDX spectra. Area 1 in the bright region is a void as there was no strong Cu peak or Pd peak in the spectrum. The EDX result collected from area 3 is presented in Figure 6-8B-1, and shows obvious Pd together with Cu

and Si. The spectrum obtained from area 4 is very similar to that of area 3. It was revealed that Cu particles were located at the bright areas, such as 2 and 5 as shown in Figure 6-8B-2. Based on this analysis, it was seen that there was a thin layer between the glass and Cu coating which was thought to be Pd, but with some voids such that it appeared discontinuous.



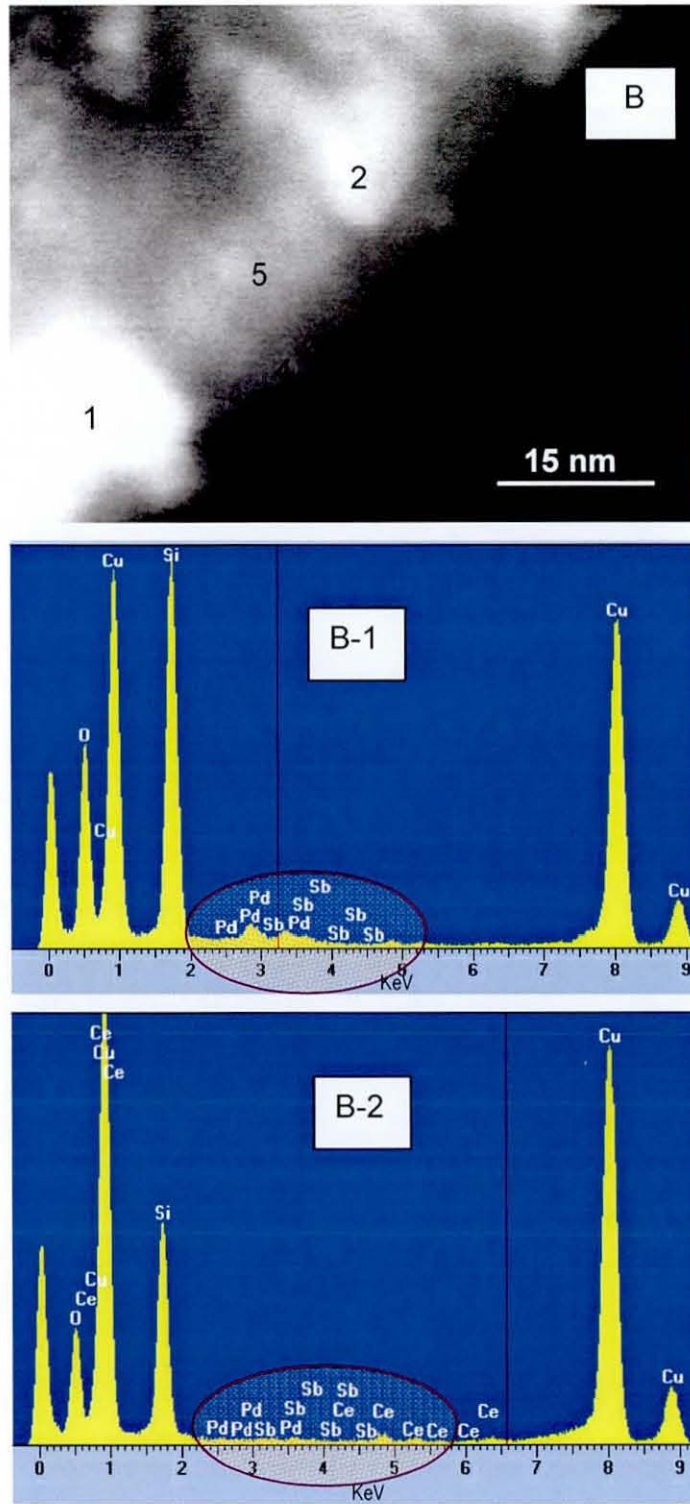


Figure 6-8 TEM micrographs and EDX spectra for electroless Cu deposited on glass with different catalyst exposure times: (A) 2 min and (B) 8 min

#### 6.4.4 SIMS analysis

In order to learn more about the composition of the electroless deposition layers, ToF-SIMS measurements were performed on the SAM surface, catalytic surfaces and electroless Cu deposits. The primary ion source was operated with an average current of 0.36 pA, a pulse width of 19.5 ns, and a repetition rate of 5 kHz. Negative spectra and positive spectra were acquired for three areas of  $500\mu\text{m}\times 500\mu\text{m}$  on every sample, keeping the primary ion dose of  $10^{12}$  ions  $\text{cm}^{-2}$ . Negative ion spectra were calibrated by using  $\text{H}_2\text{O}$  and OH peaks. Positive ion spectra were calibrated by using H, CH and  $\text{CH}_3$  peaks.

Figure 6-9 shows positive and negative ion SIMS spectra for glass surfaces before (A and B), and after (C and D), catalyst exposure for 2 min. In the positive spectrum before catalyst exposure (Figure 6-9A), peaks at mass-to-charge ratios ( $m/z$ ) of 15, 18, 26/27/28 /29, 30, 39/40/41/42/43/44, 52/53/54/55/56/57, 63/64/65/66/67/68/69/70 and 77/78/79 were assigned to  $\text{CH}_3^+$ ,  $\text{NH}_4^+$ ,  $\text{C}_2\text{H}_2^+/\text{C}_2\text{H}_3^+/\text{C}_2\text{H}_4^+/\text{C}_2\text{H}_5^+$ ,  $\text{CH}_2\text{NH}_2^+$ ,  $\text{C}_3\text{H}_3^+/\text{C}_3\text{H}_4^+/\text{C}_3\text{H}_5^+/\text{C}_3\text{H}_6^+/\text{C}_3\text{H}_7^+/\text{C}_3\text{H}_8^+$ ,  $\text{C}_4\text{H}_4^+/\text{C}_4\text{H}_5^+/\text{C}_4\text{H}_6^+/\text{C}_4\text{H}_7^+/\text{C}_4\text{H}_8^+/\text{C}_4\text{H}_9^+$ ,  $\text{C}_5\text{H}_3^+/\text{C}_5\text{H}_4^+/\text{C}_5\text{H}_5^+/\text{C}_5\text{H}_6^+/\text{C}_5\text{H}_7^+/\text{C}_5\text{H}_8^+/\text{C}_5\text{H}_9^+/\text{C}_5\text{H}_{10}^+$  and  $\text{C}_6\text{H}_5^+/\text{C}_6\text{H}_6^+/\text{C}_6\text{H}_7^+$  respectively. In the negative spectrum of APTS (Figure 6-9B), peaks at  $m/z$  of 41/42/43 and 60/61 came from the glass composition for  $\text{BO}_2^-$  and  $\text{SiO}_2^-$  species. It was confirmed that APTS coupled on the glass surface because a fragment of  $\text{CH}_2\text{NH}_2^+$  was detected. For both positive and negative spectra, the peak intensity was low for  $m/z$  over 100.

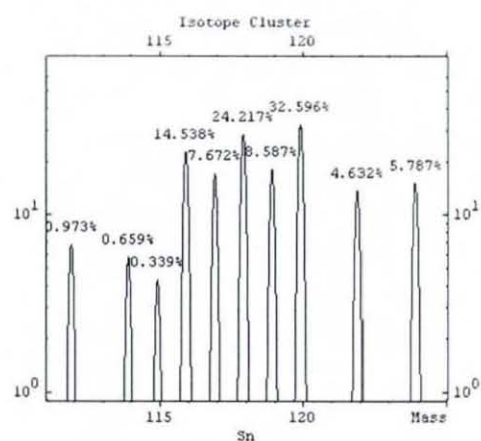
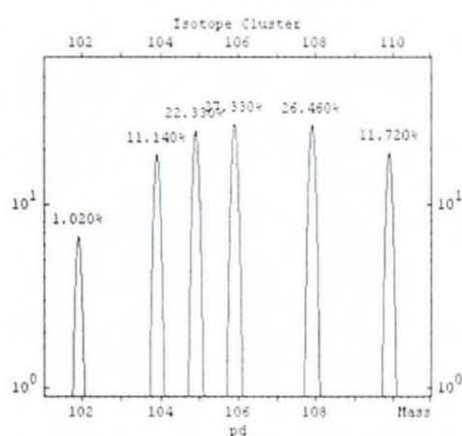
After the catalyst step, the spectra were significantly different. In the positive spectrum after catalyst exposure (Figure 6-9C) most of the peaks at  $m/z < 100$  corresponded to the hydrocarbon fragments  $\text{C}_x\text{H}_y$  identified earlier, so this range is not discussed here. Above  $m/z = 100$ , peaks at  $m/z$  104/105/106/108 and 116/117/118 /119/120/122/124 correspond to  $\text{Pd}^+$  and  $\text{Sn}^+$  according to the table of standard isotope peaks attached in Table 6-3. A few peaks appeared at  $m/z$  of 121/123/125, which were attributed to  $\text{PdNH}^+$ . There are two possible reasons for this assignment: there is no  $\text{Sn}^+$  peak at  $m/z$  121/123/125, meanwhile, if the isotopic abundance of Pd is considered, it is found that the intensity of peaks at  $m/z$  121/123/125 fits well with the presence of  $\text{PdNH}^+$ . New peaks at  $m/z$  131/132/133/134/135/137/139/141 probably



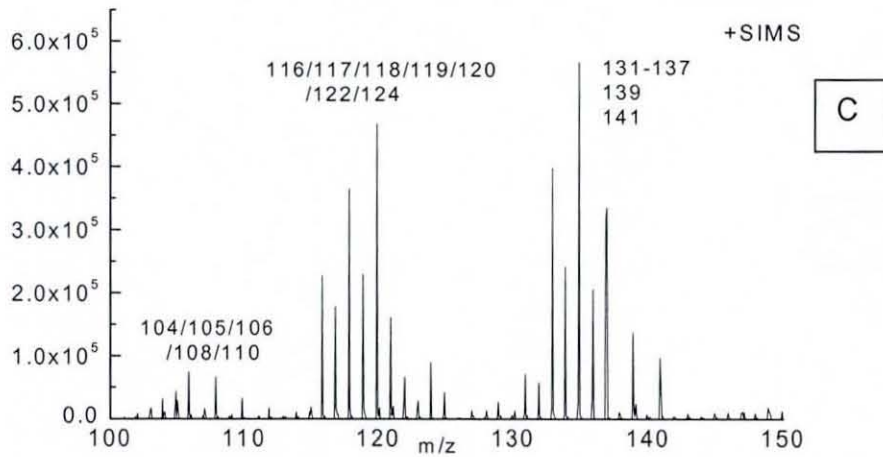
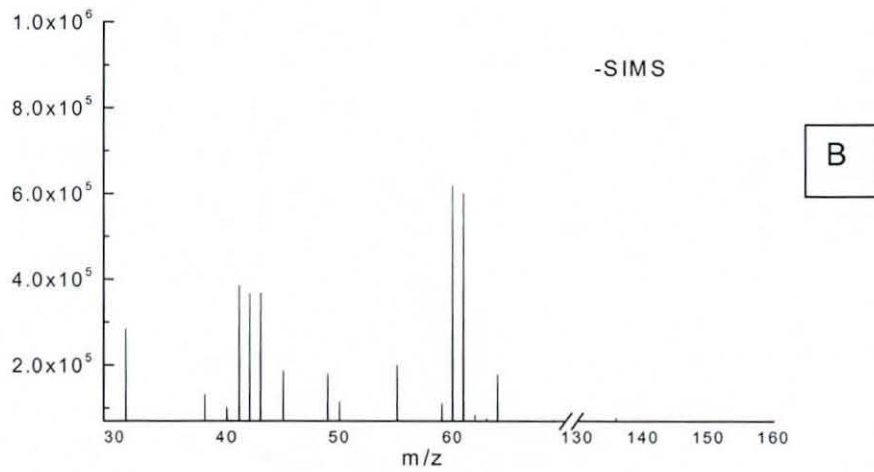
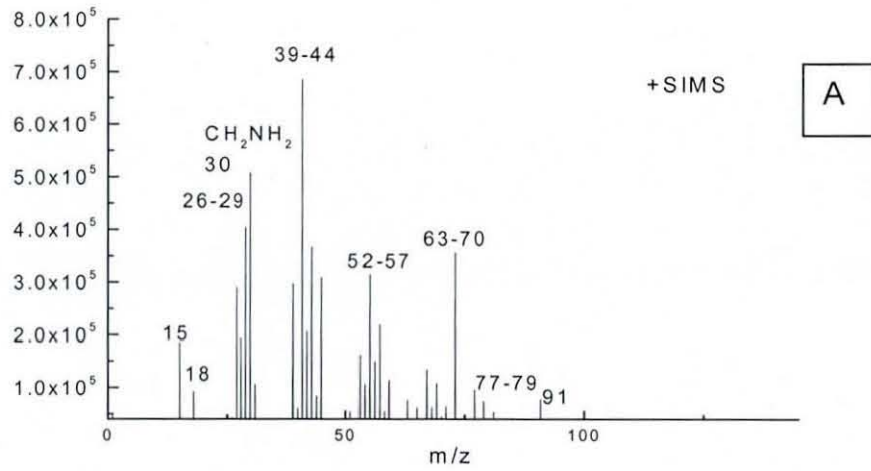
correspond to a mixture of  $SnOH^+$  and  $SnNH^+$  species. Comparing the negative spectrum before the catalyst step (spectrum B) with that after catalyst (spectrum D) shows strong peaks at  $m/z$  35/37 and 148/149/150/151/152 corresponding to  $Cl^-$  and  $SnO_2^-$  species.

Table 6-3 Isotope cluster of Pd and Sn

Pd m/z	Abundance	Sn m/z	Abundance
101.9056	1.020%	115.9017	14.538%
103.9040	11.140%	116.9030	7.672%
104.9051	22.330%	117.9016	24.217%
105.9035	27.330%	118.9033	8.587%
107.9039	26.460%	119.9022	32.596%
109.9052	11.720%	121.9034	4.632%
		123.9053	5.787%



Sources: IonSpec (version 4.0) software



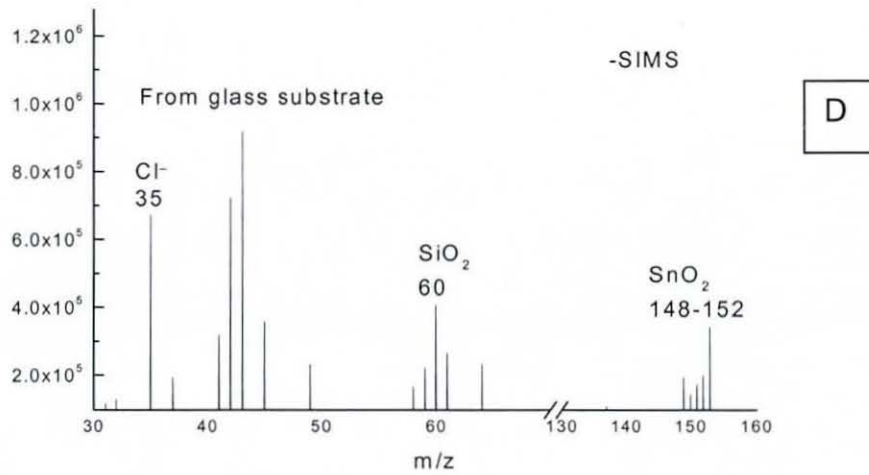
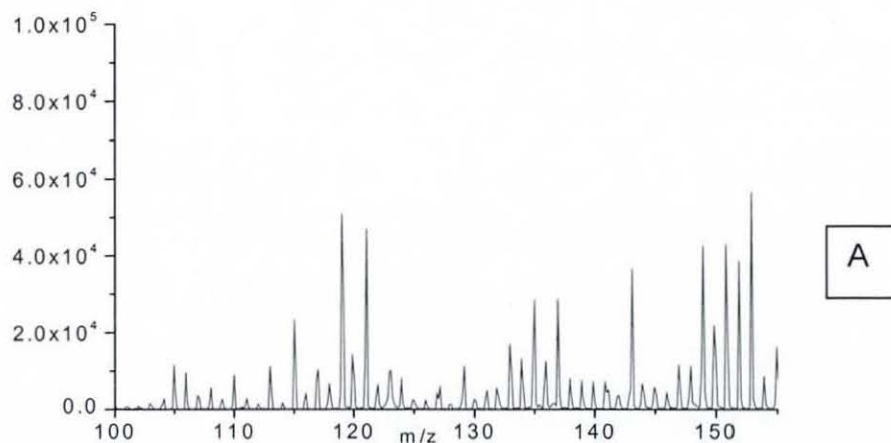
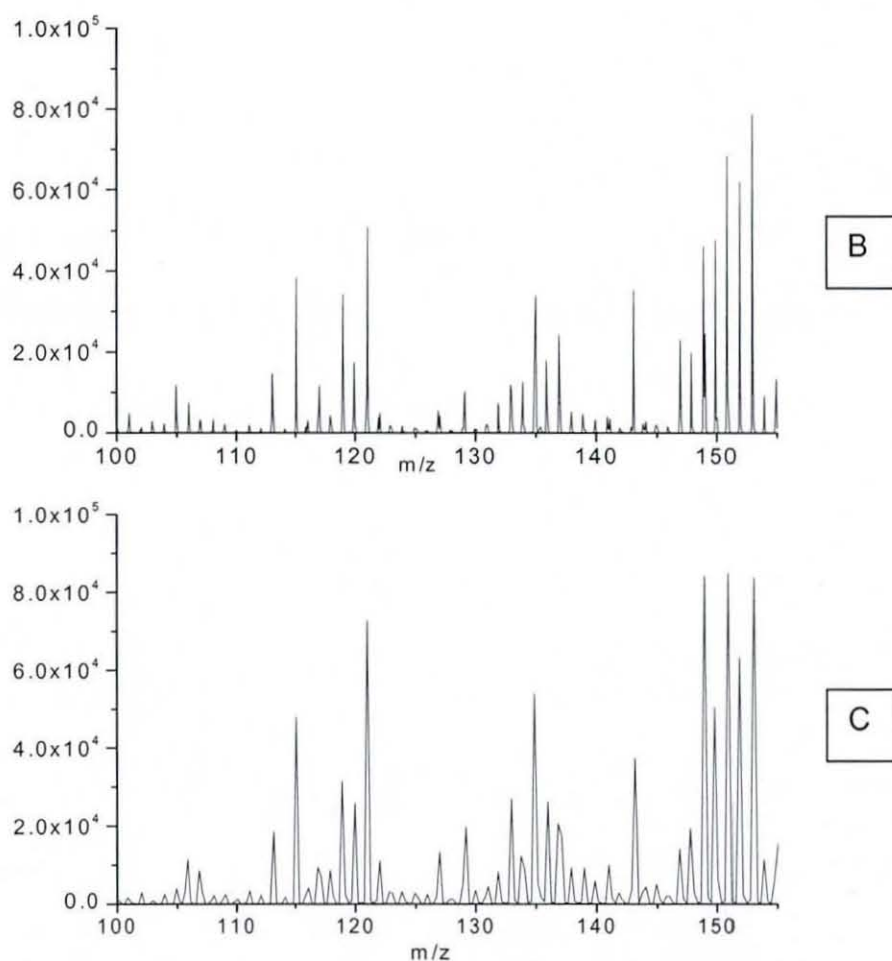


Figure 6-9 SIMS spectra of glass surfaces before (A,B) and after (C,D) catalyst steps

As the catalyst determined the adhesion and success of the following electroless deposition process, more SIMS analysis was done on the different catalytic samples to understand the effect of immersion time in the catalyst. Figure 6-10 shows the negative ion SIMS spectra for catalytic surfaces subjected to increasing immersion times from 0.5 min to 8 min. Obviously, the intensity of  $m/z$  at 148/149/150/151/152/154 corresponding to  $SnO_2^-$  increased with the immersion time, which is consistent with the XPS results that the amount of adsorbed Sn increased. The  $m/z$  peak at 153 probably corresponded to  $^{120}SnO_2H^-$ . Some peaks at  $m/z$  131/132/133/134/135/137/139/141 were thought to be due to a mixture of  $SnOH^+$  and  $SnNH^+$  species. Apart from this, peaks of  $m/z$  at 117/118/119/120/121 were evident, which were thought to be  $Sn^-$  and its isotope cluster.





**Figure 6-10 Negative ion SIMS spectra of glass surfaces following catalytic step durations of (A) 0.5 min, (B) 2 min, (C) 8 min**

Figure 6-11 shows the corresponding positive ion SIMS spectra for catalytic surfaces. In all the spectra, peaks at  $m/z$  105/106/107 and 116/117/118/119/120 correspond to  $Pd^+$ ,  $Sn^+$  and their isotopic peaks respectively. With increasing catalyst immersion time, the intensity of  $Pd^+$  remained stable. Peaks appeared at  $m/z$  121/122/123 and 124/125 that were attributed to  $PdNH^+$  and  $PdO^+$  respectively. It was seen that  $PdNH^+$  and  $PdO^+$  were reduced to a low intensity near the background level when the immersion time was up to 8 min. The peaks at  $m/z$  131/132/133/134/135/137/139/141 represented mixture fragments of  $SnOH^+$  and  $SnNH^+$ , and the intensity increased with increasing immersion time.

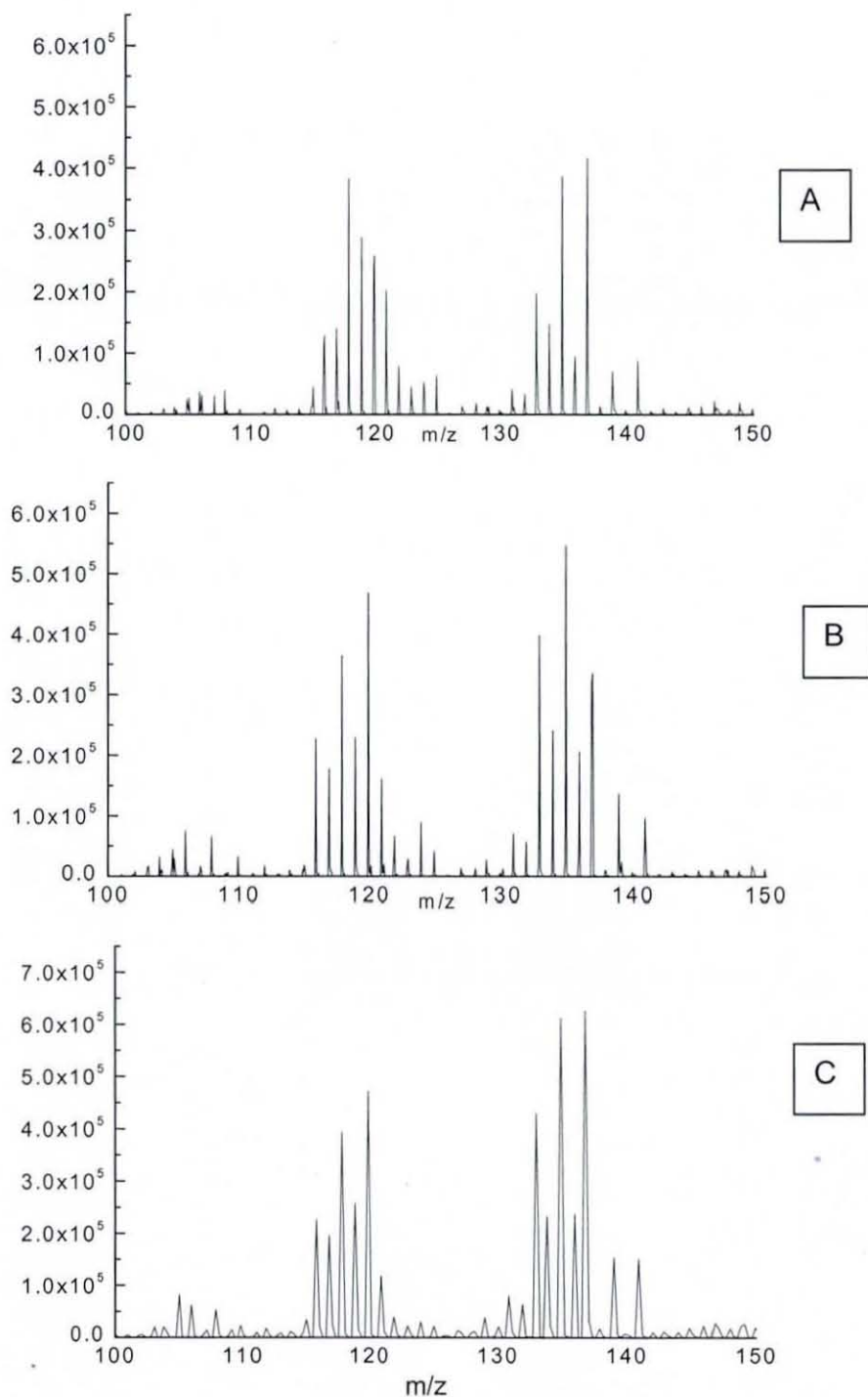


**Figure 6-11 Positive ion SIMS of glass surfaces following catalytic step durations of (A) 0.5 min, (B) 2 min, (C) 8 min**

Figure 6-12 presents the relationship between the intensity of  $PdNH^+$  and  $SnNH^+$  as a function of the catalyst immersion time obtained from the positive ion spectra in Figure 6-11.  $PdNH^+$  and  $SnNH^+$  were calibrated by the IonSpec software and the

strongest peak was selected for comparison, such as the peak at  $m/z$  121 for  $PdNH^+$  and peak at  $m/z$  135 for  $SnNH^+$ . It can be seen that  $PdNH^+$  decreased with increasing immersion time from 0.5 min to 8 min, while  $SnNH^+$  increased greatly. In the negative ion SIMS, both  $SnO_2^-$  and  $SnNH^+$  also increased greatly with increased catalyst immersion time.

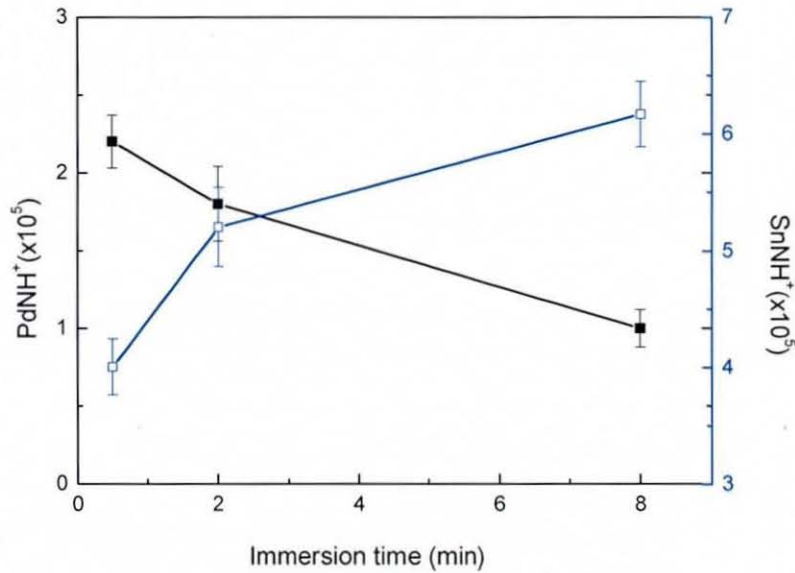


**Figure 6-12** The  $PdNH^+$  and  $SnNH^+$  intensity as a function of catalyst immersion time

SIMS was also used to investigate the surface chemical changes once samples were immersed in the electroless Cu bath. The samples were treated with APTS for 1 hour and pre-dip for 1 min, catalyst for 2 min and electroless Cu bath for 15 sec. Figure 6-13 shows both negative and positive ion SIMS spectra for short time immersion in the electroless Cu bath. Comparing these with the catalyst samples, it is clear to see that all the fragments which included Sn greatly decreased, such as  $SnO_2^-$  at  $m/z$  148-154 and  $Sn^+$  at  $m/z$  116-124. While the peaks for  $Pd^+$  ( $m/z$  105/106/108/110) became stronger than on any catalyst samples, indicating that some Sn ions were dissolved in the electroless Cu bath. The relative amount of detected Sn fragments decreased by approximately 10 times, compared with a catalytic surface.

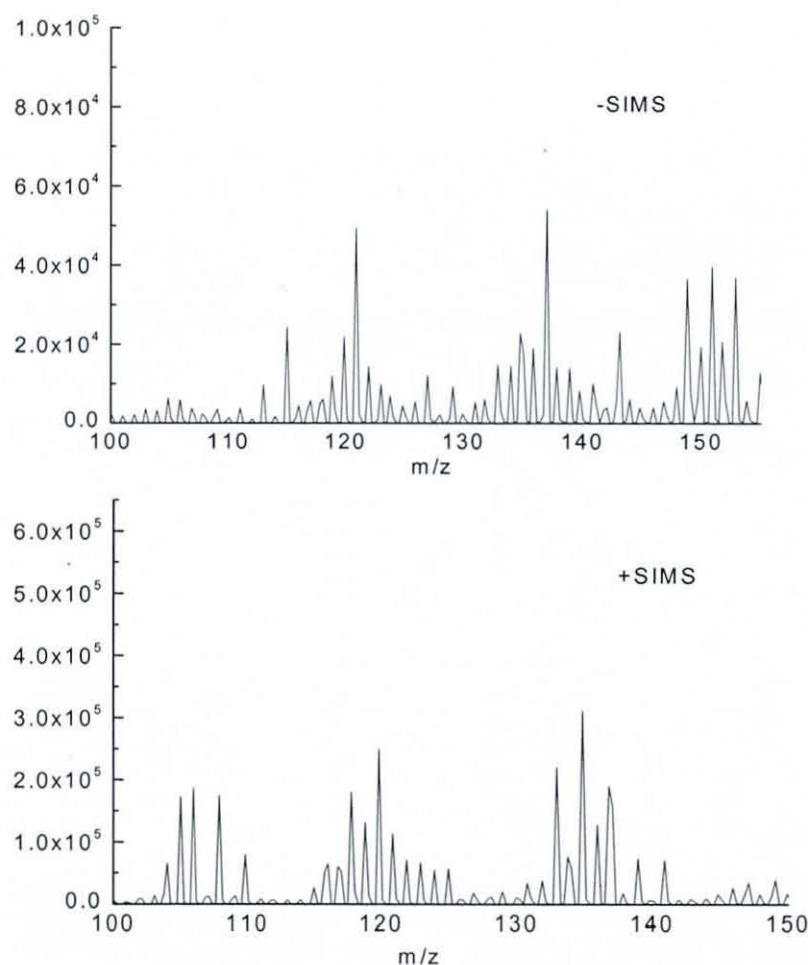


**Figure 6-13 Negative and positive ion SIMS spectra of the surface after electroless Cu solution exposure for 15 sec**

The delaminated surfaces of Cu peeled from the glass using tape were analysed by SIMS. Figure 6-14 shows both positive and negative spectra for the delaminated glass surface. Peaks of  $Pd^+$  at m/z 104/105/106/108 and peaks of  $Sn^+$  at m/z 116/117/118/119/120/122/124 can be seen. Compared with the catalytic surfaces, the intensity of all the Sn fragments decreased sharply. SIMS spectra for the delaminated Cu film showed only  $Cu^+$  and  $CuO^+$  fragments, and no interesting fragments came from Sn and Pd, so the spectra are not presented here.

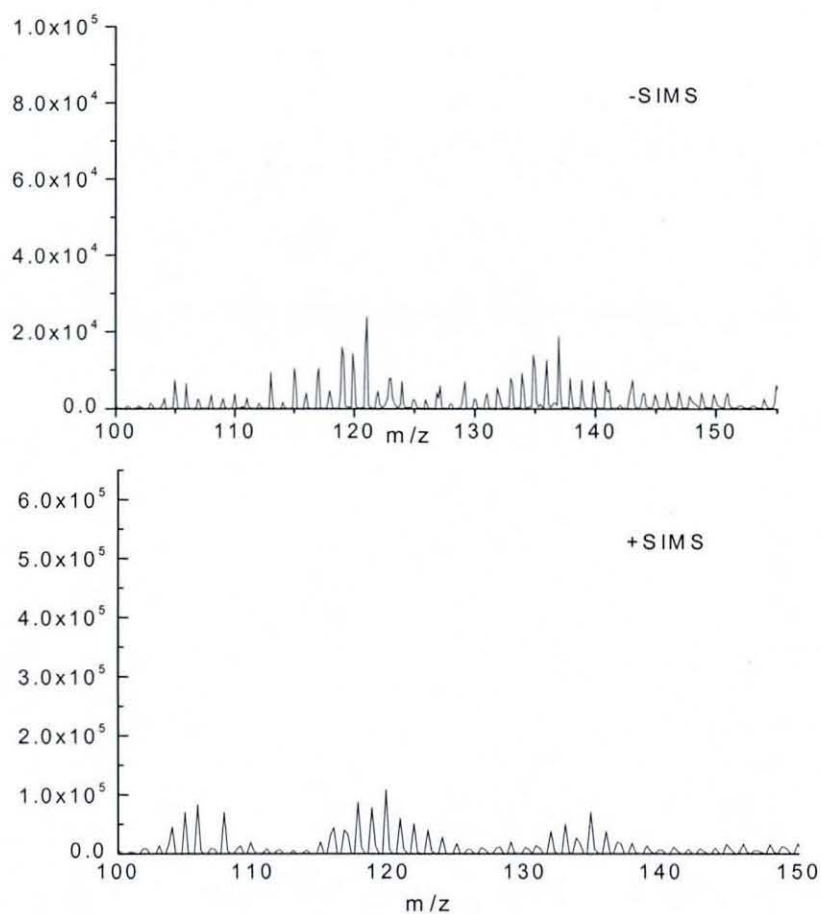


**Figure 6-14 Positive ion and negative ion spectra for the delaminated glass surface**

In general, due to the high sensitivity of the static-SIMS technique, many peaks are measured of which only the most intense ones are listed in Table 6-4. The observed fragments may either originate directly from the surface, or be formed during the ion formation process. After immersion of the sample in a Pd/Sn solution the signals from both  $\text{Si}^+$  and  $\text{Na}^+$  decreased considerably in intensity. The presence of Sn was revealed by  $\text{SnO}_2^-$ ,  $\text{SnNH}^+$  and  $\text{SnOH}^+$ . Table 6-4 summarises the surface fragments obtained from the glass surface treated under different conditions.



Table 6-4 Surface analysis results obtained from SIMS spectra

Process	Negative	Positive
Catalyst 30 sec	Cl(35), SiO <sub>2</sub> (60), Pd(104/105/106/108), Sn(116/117 /118/119/120/122/124), SnO <sub>2</sub> (148/149/150/151/152 /154)	Na(23), Pd(104/105/106/108), Sn (116/117/118/119/120/122/124), PdNH, PdN(121/122 /123/124/125), SnNH, SnOH(131/132/133/134 /135/137/139/141), PdCl <sub>2</sub> (176/177/179), SnCl <sub>2</sub> (189/190/191),
Catalyst 2 min	Cl(35), SiO <sub>2</sub> (60), Pd(104/105/106/108), Sn(116/117 /118/119/120/122/124), SnO <sub>2</sub> (148/149/150/151/152 /154)	Na(23), Pd(104/105/106/108), Sn(116/117/ 118/119/120/122/124), PdNH, PdN(121/122 /123/124/125), SnNH,SnOH(131/132/133/134/135/137/139/141),SnCl <sub>2</sub> (189/190/191)
Catalyst 8 min	Cl(35), SiO <sub>2</sub> (60), Pd(104/105/106/108), Sn(116/117 /118/119 /120/122/124), SnO <sub>2</sub> (148/149/150/151/152 /154)	Na(23), Pd(104/105/106/108), Sn(116/117/ 118/119/120/122/124), PdNH, PdN(121/122 /123/124/125), SnNH, SnOH(131/132/133/134/ 135/137/139/141), SnCl <sub>2</sub> (189 /190/191)
Electroless Cu for 15 sec	Cl(35), Cu(65/66), SiO <sub>2</sub> (60), Sn(116/117/118/119/ 120/122/ 124), SnO <sub>2</sub> (148/149/150/151/152/ 154)	Pd(104/105/106/108), Sn (116/117/118/119/ 120/122/124), SnNH, SnOH(131/132/133/ 134/135/137/139/141)
Delaminated glass surface	SiO <sub>2</sub> (60), Sn(116/117/118/119 /120/122/124)	Na(23), Pd(104/105/106/108), Sn(116/117/118/119 /120/122/124), SnNH, SnOH (131/132/133/ 134/135/137/139/141)
Delaminated Cu film	Cu(65/66), CuO(81/82)	

Note: some elements attributed to the glass substrate are not presented in this table.

## 6.5 Discussion

### Catalytic surface

As seen in the XPS results in Figure 6-1A and B, the Pd in these systems was found in two bonding environments, Pd<sup>2+</sup> located at 337.5 eV and Pd<sup>0</sup> located at 335.4 eV depending on the catalyst immersion time. For short times the surface showed high level of Pd(II) which reduced as the exposure time increased. With increasing immersion time to 2 min, Pd(0) became stronger than Pd(II) although the presence of Pd(II) as a residual species indicated that some unreduced Pd was still on the surface. All the Pd(II) was transferred to Pd(0) after 8 minutes immersion in the catalyst solution, as shown in Figure 6-1C. The Pd<sup>2+</sup> peak, located at 337.5 eV, is not thought to be due to Pd-O, since this bonding state occurs at 338.5 eV. It is believed then, that some of this Pd<sup>2+</sup> could be caused by Pd-N bonding [46, 181]: since nitrogen has lower electro-negativity than oxygen, the binding energy shift should be smaller. The SIMS results also revealed either PdNH<sup>+</sup> or PdN<sup>+</sup> species on the 30 s and 2 min catalyst immersion samples, but only relatively low levels of these species were observed on the catalysed sample for 8 min.

The increasing immersion time in the catalyst induced a slight increase in the Sn metallic form compared to the Sn(IV), but a much more obvious increase in the total adsorbed Sn was observed. The presence of some Sn in the metallic form implies that the core of the catalyst colloid particles contain some Pd-Sn metallic alloy, in agreement with other studies [71, 182] due to the following reaction that occurred within the catalyst [182]:



Due to the close B.E. values for Sn<sup>4+</sup> and Sn<sup>2+</sup>, it was not possible to say from the XPS which form of tin was present, however it is most likely to be Sn(IV) based on the expected mechanism of catalyst formation described earlier. It was shown from SIMS that the Sn was largely present as SnO<sub>2</sub>, rather than the SnCl<sub>4</sub> that was detected in Shukla's experiment [125].

It is interesting to note that, using the same colloidal solution, the composition of the surface differed according to the treatment period. The accepted model of the SnPd



In the catalyst surface with 30 sec treatment, the surface is only partially covered with catalyst particles where the Pd(0) atoms in the colloid are surrounded by Sn(IV). According to Lai's investigation [177], these are constructed of Pd nanocrystallites of only about 2-5 nm. In the model, the rest of the surface is covered with Pd ions from the catalyst solution that are attached to the amine groups of the SAM. This structure is expected to show both Pd(0) and Pd(II) in XPS as observed and also PdNH<sup>+</sup> and SnNH<sup>+</sup> in SIMS. When the catalyst immersion time increased to 2 min, the Pd(0) form increases, but there is still Pd(II) and a high concentration of Sn(IV) which can be explained by a higher coverage of catalyst particles. The surface is fully covered with catalyst particles, even multilayers at 8 min treatment. This structure is likely to show only Pd(0) and Sn(IV) in XPS, as found in the results. In addition, the amount of Pd-NH bonding will be negligible and the dominant attachment will be through Sn-NH bonding in agreement with the SIMS data.

This model is also consistent with the SEM and TEM micrographs that showed the Cu deposit morphology and coverage varied greatly because of different catalyst activities, which is also consistent with the observation of Horkans et al. [183]. At short catalyst immersion time (e.g. 30sec), some voids in the copper surface appeared which indicated insufficient activation sites for further electroless deposition due to the short catalytic period. With increasing catalyst immersion time to 2 min, there were no voids and electroless Cu deposited evenly on the catalytic surface. In the TEM Figure 6-8A (2 mins catalyst), it was clearly seen that a continuous Pd layer occurred between the glass and Cu layer. The appearance of this layer was probably because the number of well activated Pd grains was enough to construct a continuous layer, which was thought to offer effective bonding sites. The Cu film had obvious breaks and voids when the catalyst time was as long as 8 minutes, which showed that the structure of the Cu deposits was not benefitted by dense or multiple layers of catalyst. It was further confirmed from the TEM micrographs that more Pd particles were absorbed on the surface with increasing immersion time, resulting in an uneven distribution and aggregation of Pd particles on the surface (Figure 6-8).

### Activation of the catalyst surface

As described earlier, the Sn(IV) coating of the catalyst particles is not able to initiate electroless plating and an activation step is therefore required to remove some of this



work, it appears that the catalyst – Cu/Ni bond was weaker than the catalyst/SAM bond. The Cu film adhesion was weak for both 30 sec and 8 min catalyst treatments. For short period (30 sec) catalyst treatment, the Pd was not adequately deposited on the glass surface so that Cu particles were not able to adhere across all areas, providing limited points of contact. It might be expected that the 8 min catalyst treated surface is more suitable to copper deposition, due to greater coverage of catalyst particles. However, for a long time catalyst treatment, the higher concentration of Pd is thought to result in more rapid reaction in the initial period in the electroless Cu bath, leading to high levels of hydrogen bubbles and internal stress. This can explain why Cu deposits with some voids were observed in the 8 min catalyst treated samples. Meanwhile, it was reported that if tin existed on the surface and electroless Cu plating follows, an intermediate layer of Sn-Cu may be formed [184]. This layer may be brittle and weaken the bond between the glass and the Cu deposit. This is another possible interpretation of the failure location between Cu and catalyst. It is possible that with excess catalyst present that the Sn could not be as effectively removed before Cu plating started.

## **6.6 Conclusion**

The different catalyst structure effects on electroless Cu deposition were investigated and it was found that a catalytic surface with an excess or small number of activation sites was not beneficial for achieving electroless Cu deposits with good surface morphology and adhesion. A surface covered with a more uniform layer of catalyst particles, largely consisting of Pd(0) would be expected to provide good adhesion of the Cu coating.

---

## Chapter 7 Metallisation of Laser Machined Glass

---

### **7.1 Introduction**

As discussed in chapter 4 following peel tests, the glass side of the samples showed no trace of Cu metal, while the stripped Cu side showed only evidence of Cu, with no Pd or Sn. This indicated that failure occurred at the Cu-catalyst interface. These results revealed that improvement of catalyst adsorption and plating on smooth surfaces is unlikely to enable the formation of strong mechanical or chemical bonding between the glass surface and electroless Cu. It was therefore proposed that if the substrate surface was not as smooth ( $Ra = 0.7$  nm) as the CMZ glass discussed here, the adhesion between interfaces could be improved. This theory was tested by plating experiments onto laser machined glass.

As part of the overall investigation of glass as a substrate material, excimer laser machining was used to create tracks in the glass with roughened surfaces and microvias. Subsequently, it was found that by combining laser machining with electroless deposition that circuit patterns could be readily created. In this section, the results of electroless Cu deposition on excimer laser machined glass tracks and vias will be presented. In addition, work to investigate the electroplating of Cu onto the electroless Cu layer to build up the thickness will be shown.

## **7.2 Literature review**

In order to meet the requirements for substrate manufacturing, the thickness of the Cu pads and tracks on the glass surface should be in the range of 5 to 35 microns depending on the final application. Using electroless deposition it is only possible practically to deposit about two microns thick Cu films due to the low deposition rate. Therefore, a further deposition step is essential to complete the glass substrate circuit board. Electroplating is a potential method to build up the thickness and fill the vias in various applications in the PCB industry [10, 185]. The requirement for miniaturization of printed circuit boards has increased with the continuing downsizing of electronic devices. However, conventional multi-layered PCBs have limitations for higher packaging densities. In order to improve this, a build-up process rather than the traditional subtractive etching process has been adopted as a new multi-layered PCB manufacturing process. The build-up process consists of metallisation of via-holes to connect conductive layers and the plating of Cu into gaps in a photoresist to create tracks and pads. The traditional process is complicated because planarization must be accomplished by polishing after the formation of the insulation layer. Accordingly, the layer-to-layer connection with via-holes or fine bumps has been developed.

Available techniques for filling micro-vias are electroplating deposition, conductive paste and high pressure injection of a molten material [3]. Compared to the other techniques, electrochemical deposition is more suitable to create wires of high aspect ratio (length to diameter). As the conductor patterns become finer, filling of via-holes by Cu electroplating has become an effective method because of its low cost and high accuracy. Many research articles have confirmed that via-filling can be achieved by Cu electroplating [185, 186]. In this section, Cu electroplating is mainly reviewed in relation to via filling, especially focusing on some new improvements to electroplating baths.

The properties of electroplated Cu depend on a number of parameters, namely: ionic concentrations, pH value, temperature and the deposition voltage [98, 111]. Speed of deposition is related to the concentration of the solution and the voltage applied between cathode and anode, i.e. current density through the solution. Therefore, the



optimisation of these parameters can lead to metallic layers with the desired structural, electronic, and optical properties.

Unfortunately, voids are often formed in the trenches of microvias plated with additive-free baths, since the electric current lines are concentrated on the surface and in the corner of the wafer patterns [187, 188]. Because of the bigger size of trenches and via-holes used in conventional PCBs rather than via-holes for ULSI, void-free filling in sub-micron trenches and via-holes is difficult to accomplish by additive-free electroplating of Cu [185].

Chloride ions ( $\text{Cl}^-$ ), polyethylene glycol (PEG), bis (3-sulfopropyl) disulfidedisodium (SPS), Janus Green B (JGB) and thiourea (TU) are commonly used as additives to enhance plating performance [187, 189]. Miura [190] reported void-free filling in 40–180  $\mu\text{m}$  via-holes in epoxy resin using a high throwing power bath with  $\text{Cl}^-$ -PEG-SPS-JGB. Cu was deposited to approx. 0.5  $\mu\text{m}$  by electroless Cu plating and then this was electroplated with Cu. Despite the successful use of the process in build up technology, the behaviour of these additives during the Cu electrodeposition process is still incompletely understood because of the complexity resulting from interactions between the effects of the multiple additives. Therefore, investigations for understanding additive effects on the Cu electrodeposition inside submicrometer trenches have been carried out by many researchers. Many reports have shown that the addition of PEG with  $\text{Cl}^-$  inhibits Cu deposition, whereas SPS accelerates the deposition when it is added together with PEG and  $\text{Cl}^-$ . JGB is recognised as a levelling agent, flattening the bumps of Cu deposits on the surface, or to influence the filling properties. Table 7-1 shows a survey of the main additives for Cu electroplating baths [190, 191].

**Table 7-1 Compositions of typical Cu electroplating baths with various additives [190]**

Bath name	CuSO <sub>4</sub> •5 H <sub>2</sub> O (mol L <sup>-1</sup> )	H <sub>2</sub> SO <sub>4</sub> (mol L <sup>-1</sup> )	PEG (2000) (ppm)	Cl <sup>-</sup> (ppm)	SPS (ppm)	JGB (ppm)
Additive-free	0.26	2.0				
PEG	0.26	2.0	100			
Cl-PEG	0.26	2.0	100	50		
Cl-PEG-SPS	0.26	2.0	100	50	1-1000	
Cl-PEG-SPS-JGB	0.26	2.0	100	50	1-5	1-50

Honma et al. [185, 190, 192] confirmed that the Cu sulphate concentration in a Cu electroplating bath is one of the key factors affecting filling of the micro vias. The high Cu concentration bath gave a high deposition rate, while the lower concentration bath was suitable to form a thick film. In general, the control of Cu plating conditions including current density, concentration and combination of additives were considered to be key factors to via filling. The influence of current density on the filling of vias was also presented by Kobayashi [186]. It was found that the thickness at the centre of the via-holes decreased under conditions of high current density. However, the thickness was more uniform with decreasing current density.

### **7.3 Methodology and Experimental**

An excimer laser was used for machining of glass because of its good machined quality with high accuracy. The preparation of these samples was carried out by another PhD student working on the glass substrate project [11]. The excimer laser was employed to form tracks and microvias in 50 and 100 µm thick CMZ glass as it is effective laser machining for making glass-based microcomponents and devices [193]. The experimental equipment comprised of a KrF excimer laser machine (203 EMG Lambda Physik model), precision optics and XYZ Motion Master sample table. The KrF excimer laser machine was used at 248 nm wavelength, 400 mJ maximum pulse energy and 300 Hz maximum repetition rate. By placing a mask in the optics, different size and shape features could be machined e.g. circular and square and by

translating the sample under the laser spot at a fixed stage speed, tracks could be machined.

Electroless Cu was deposited onto the roughened surface using the procedure described in chapter two, including cleaning, APTS, pre-dip, catalyst and electroless deposition. For roughened glass, it was still found that the APTS treatment was required in order to help initiate the plating process. It was found that by using electroless deposition it was difficult to get more than two microns thick Cu films on glass substrates. Therefore, a further electrodeposition step is essential to complete the glass substrate by building up a much thicker metal layer.

In the present work, electroplating was initially investigated to fill the microvias and build up the Cu thickness across the surface. Electroplating of Cu requires an electrolyte containing Cu ions and two electrodes as shown in Figure 7-1. The anode was a Cu plate and electroless Cu as a conductive seed layer both on the smooth glass and within microvias was used as the cathode.

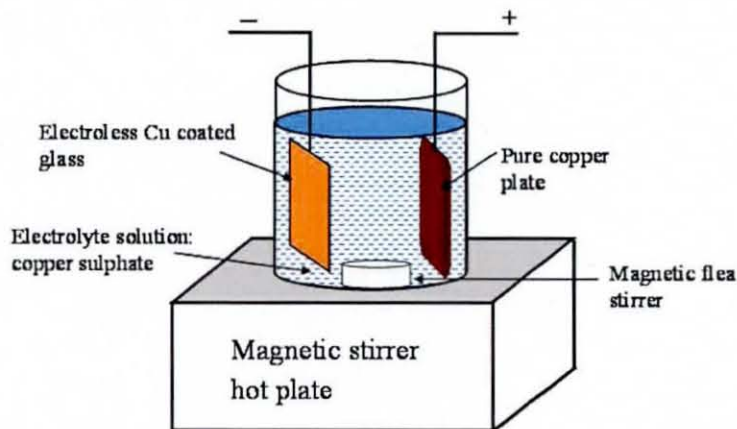


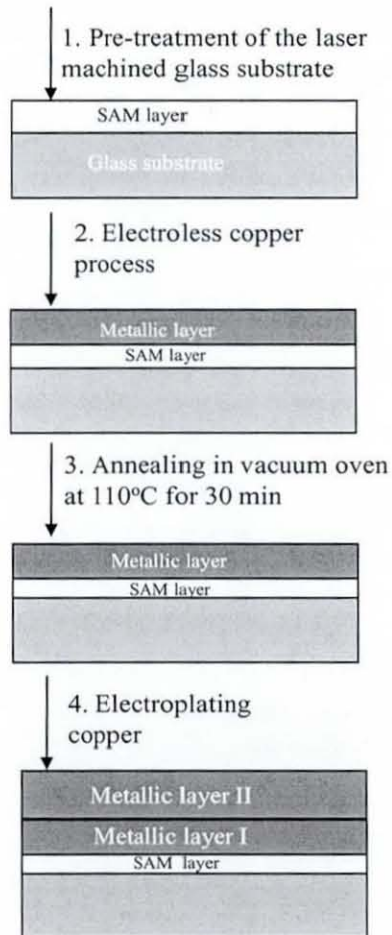
**Figure 7-1 Schematic diagram showing the main parts of a simple Cu electroplating process**

Within the time constraints of the current project it was not possible to investigate the effect of additives on the plating process. A basic bath was therefore used. The compositions and operating conditions of the Cu electroplating bath are shown in Table 7-2, which is a popularly used process.

**Table 7-2 Compositions and operating conditions of Cu electroplating bath**

Bath chemicals & operating conditions	Concentration
CuSO <sub>4</sub> •5H <sub>2</sub> O	0.26 mol/dm <sup>3</sup>
H <sub>2</sub> SO <sub>4</sub>	2.0 mol/dm <sup>3</sup>
Temperature	30°C
Agitation	Magnetic stirring

The full electrodeposition procedure for glass is listed in Figure 7-2. The annealing process in step 3 was used, as many researchers presumed annealing could decrease the cupric oxidation and improve the conductivity of the cathode material.

**Figure 7-2 Process flow diagram of electrodeposition of Cu on laser machined glass**

## 7.4 Results and Discussion

### 7.4.1 Electroless Cu on tracks and holes

By varying the laser machining parameters including repetition rate, pulse energy and ablation time, tracks with different roughness could be obtained and these were used for subsequent plating experiments. The Zygo white light interferometer was used to measure thin film thickness together with surface profile and surface structure analysis, without contacting the surface. The Zygo was also used to determine the roughness and surface metrology of Cu deposited on tracks. In general, the value of roughness in the laser machined tracks was in the  $Ra$  range of  $0.9\ \mu\text{m}$  to  $1.8\ \mu\text{m}$ , and it was found that the roughness slightly decreased after electroless deposition. Figure 7-3 shows a typical surface morphology of a laser machined groove. Clearly, the surface was roughened by the excimer laser ablation. The width and depth of the laser machined grooves varied with the laser machining process. The width of the grooves ranged from about  $100\ \mu\text{m}$  to  $1\ \text{mm}$  and depth was in the range of  $1\text{-}15\ \mu\text{m}$ .

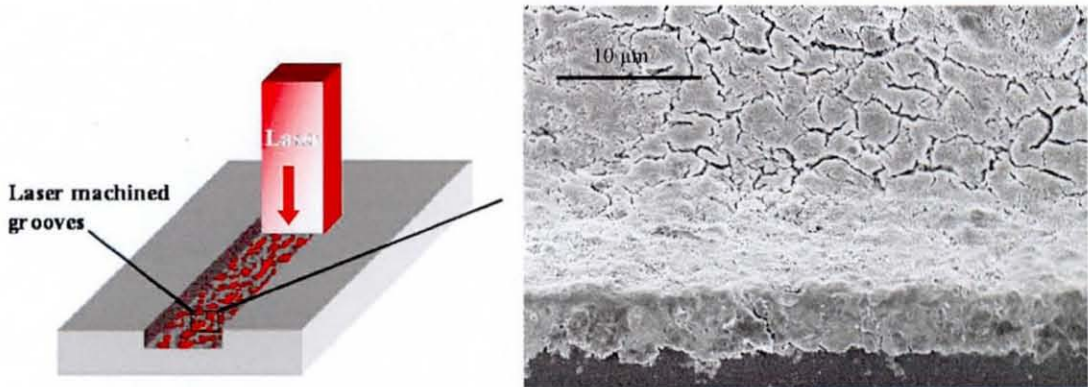
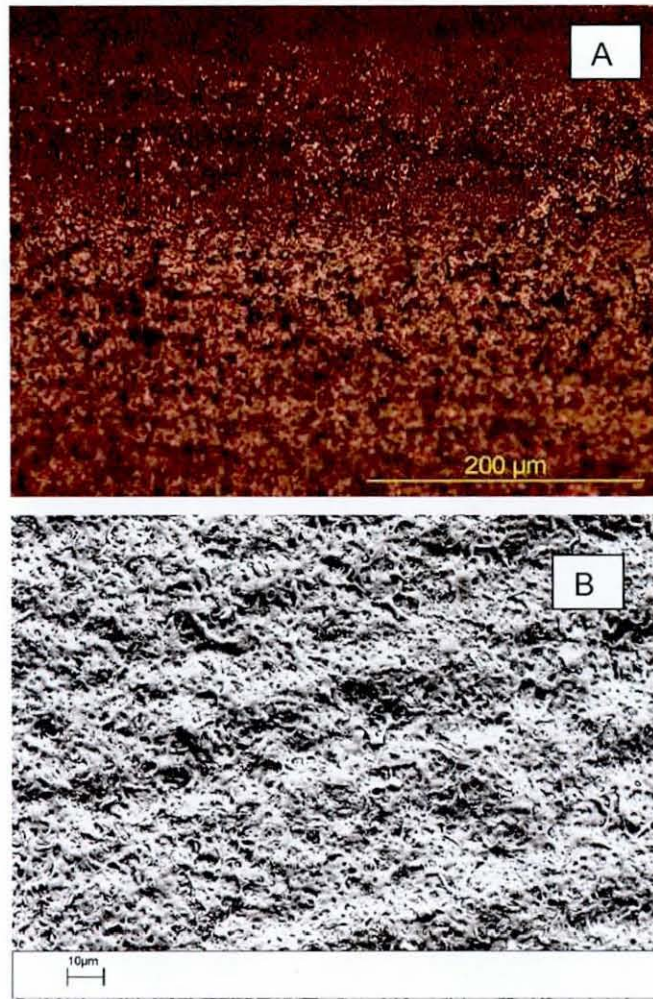


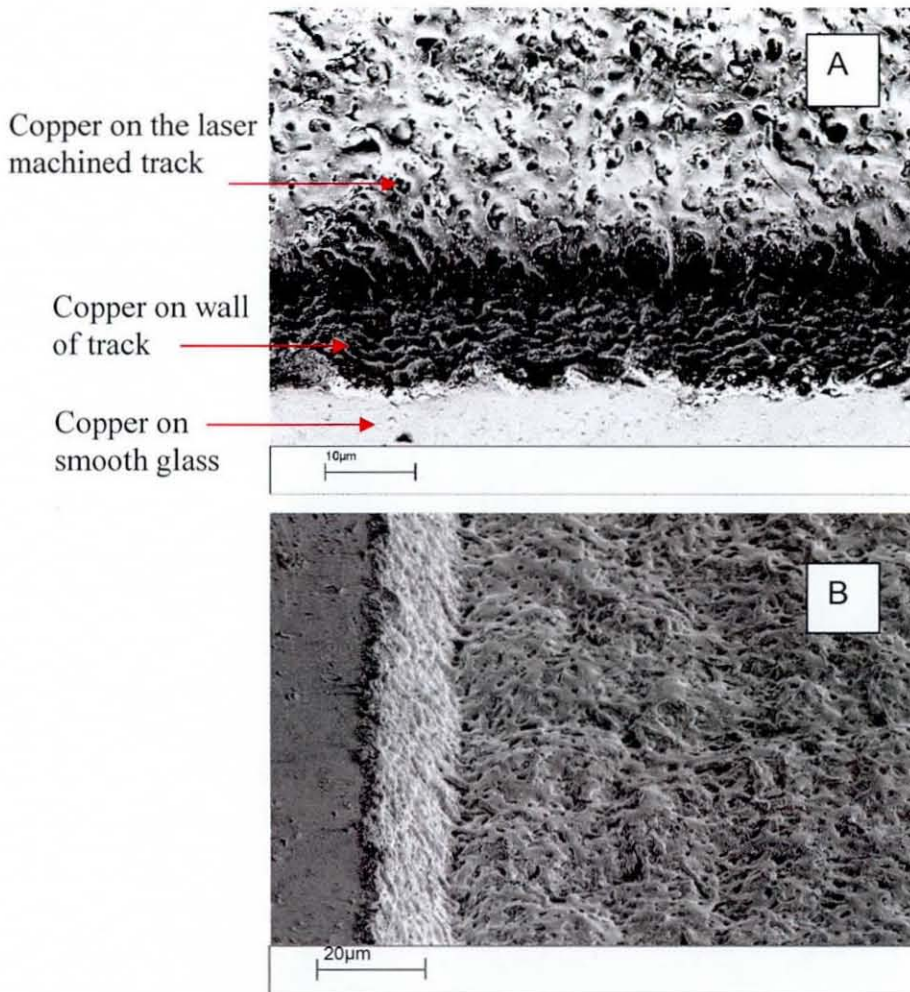
Figure 7-3 Diagram of laser machined groove

Figure 7-4 shows an optical micrograph (A) and SEM micrograph (B) of electroless Cu deposits within laser machined grooves. The  $Ra$  of the sample shown in Figure 7-4 was  $1.54\ \mu\text{m}$  which was machined at  $4.5\ \text{J}/\text{cm}^2$  fluence with a  $15\ \text{Hz}$  repetition rate, and after deposition the  $Ra$  was  $1.3\ \mu\text{m}$ . The  $Ra$  of unprocessed glass was  $2\ \text{nm}$ . Unlike for the smooth glass surfaces, the Cu particle shape and size could not be seen in the images.



**Figure 7-4 Optical microscope image (A) and SEM image (B) of electroless Cu deposited on a groove machined in glass**

SEM inspection of the electroless Cu deposited glass surface (Figure 7-5) showed clearly the different roughness of the laser machined track compared to the plain glass. It can be seen that the Cu formed a thin continuous layer over the original smooth surface of the glass and down the rougher side walls and base of the groove. Due to the high energy used during the laser machining process, the structure of the glass surface changed, and the surface of grooves appeared random similar to grain recrystallisation.



**Figure 7-5 SEM micrograph of Cu deposited on the laser machined groove and wall (A) view of side wall (B) plan view**

As an important factor for glass substrates, the electroless Cu deposition on laser machined vias in glass was also investigated using the above procedure. Both through-holes and partially drilled blind vias were used. Figure 7-6 shows optical and SEM images of Cu coated apertures with 100 µm diameter entry holes. Figure 7-6 A shows that the glass surface was fully covered with Cu in the electroless bath for 10 min. With increasing the plating time to 30 min, the Cu film started to peel off the smooth glass surface areas, as shown before, and finally led to thicker Cu deposited in the holes with almost no Cu left on the smooth glass as shown in Figure 7-6 B and C. The thicknesses of the electroless coatings were approximately 1.4-1.6 µm after 35 min. These images highlight the adhesion differences between the roughened and smooth areas of glass: the high thickness of Cu deposited in this case, led to the film peeling from the smooth areas, but remained adhered to the apertures.

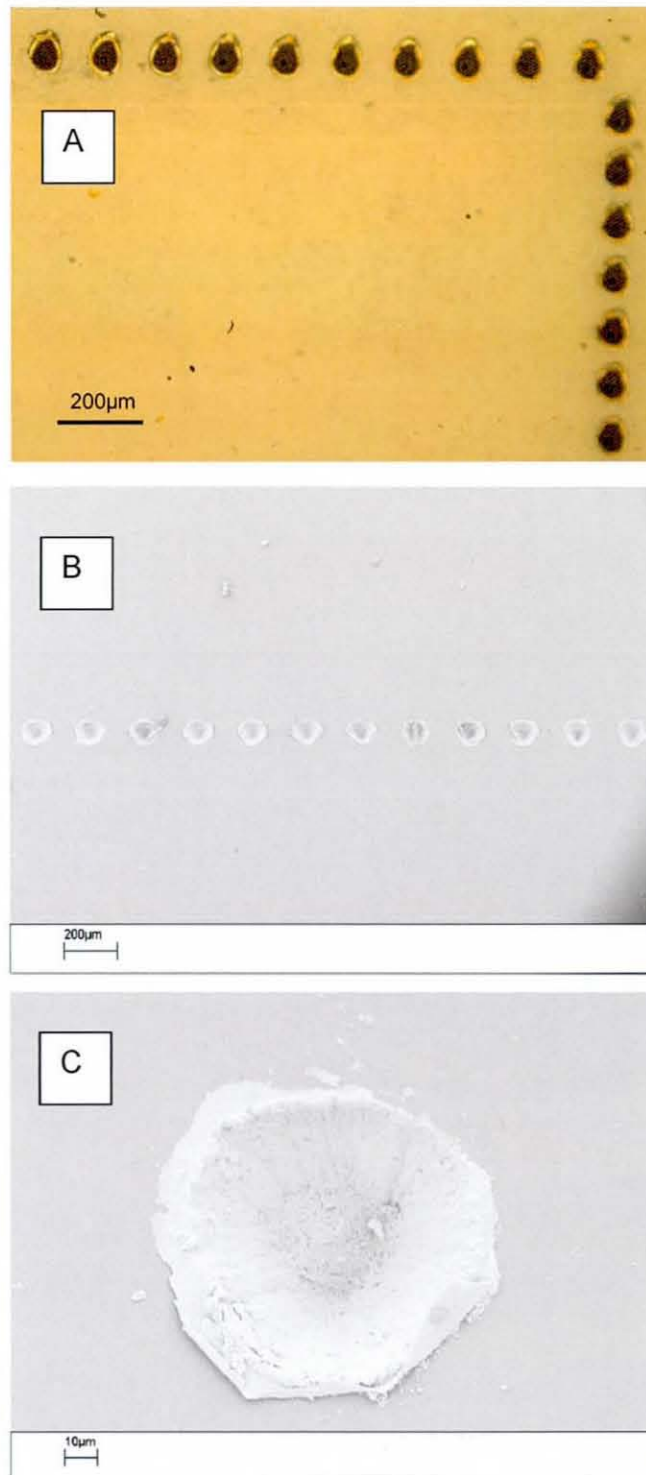


**Figure 7-6 Optical and SEM image of electroless Cu metallised through hole (A) and (B,C) blind apertures**

It is seen that adhesion to the roughened areas was significantly better than across the smooth glass such that thicker coatings of 1.5 µm could be prepared without peeling



off the surface during a tape peel test. The surface morphology produced by the laser machining process was rougher than smooth glass, which enabled strong bonding, presumably due to increased surface area and mechanical interlocking as shown schematically in Figure 7-7.

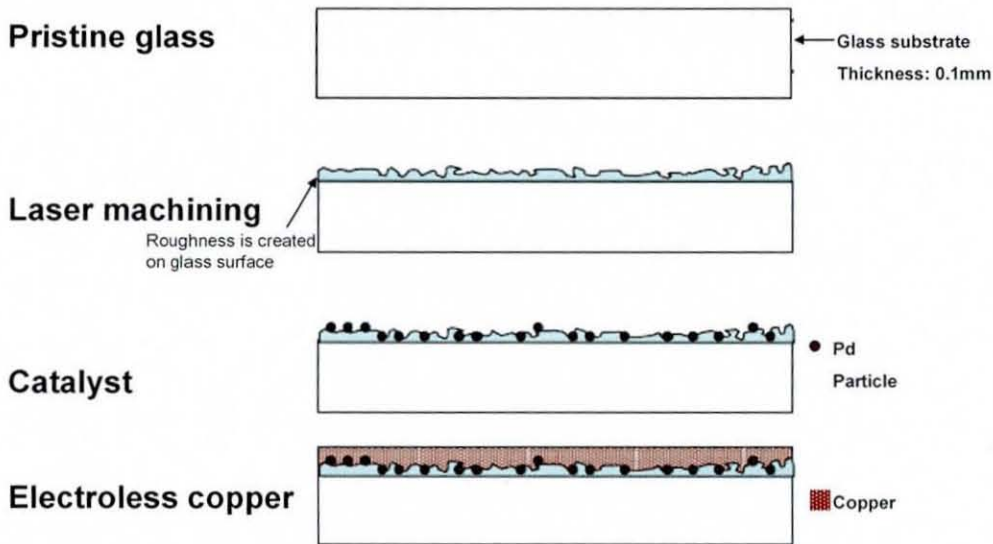
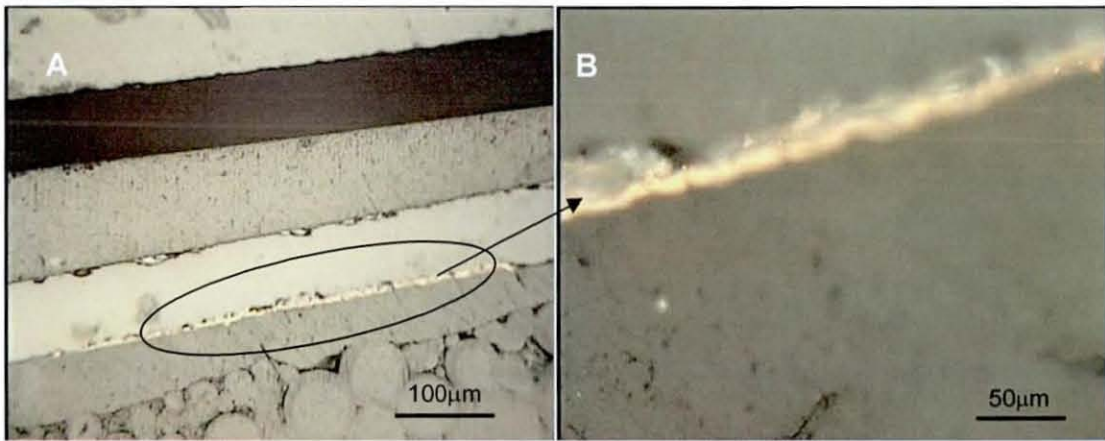


Figure 7-7 Electroless Cu deposition process flow for laser machined glass

#### 7.4.2 Further electroplating of Cu on tracks and holes

The adhesion of the electroless Cu coatings to the smooth glass substrate was the main problem identified before glass metallisation. For smooth glass, the electroplated Cu layer was easily peeled off, while the adhesion to the laser roughened glass area was fairly good.

To increase the Cu thickness on the smooth glass surface, electroplating was tested as it was thought that this may deposit with less stress leading to better adhesion [111]. However, this was not the case, and as the Cu was electroplated, it began to peel away as the thickness increased. Electroplating of laser roughened glass was therefore trialed. Figure 7-8 shows cross-section images of electroplated Cu deposited on grooves which were machined with an energy of 250 mJ, stage speed of 50  $\mu\text{m}/\text{sec}$  and the pulse frequency of 25 Hz. The thickness of electroplated Cu in the track was around 8-10  $\mu\text{m}$  and as presented in Figure 7-8B, the Cu deposit was a continuous layer with a rough surface.



**Figure 7-8 Optical microscope images of a cross section through electroplated Cu on a track**

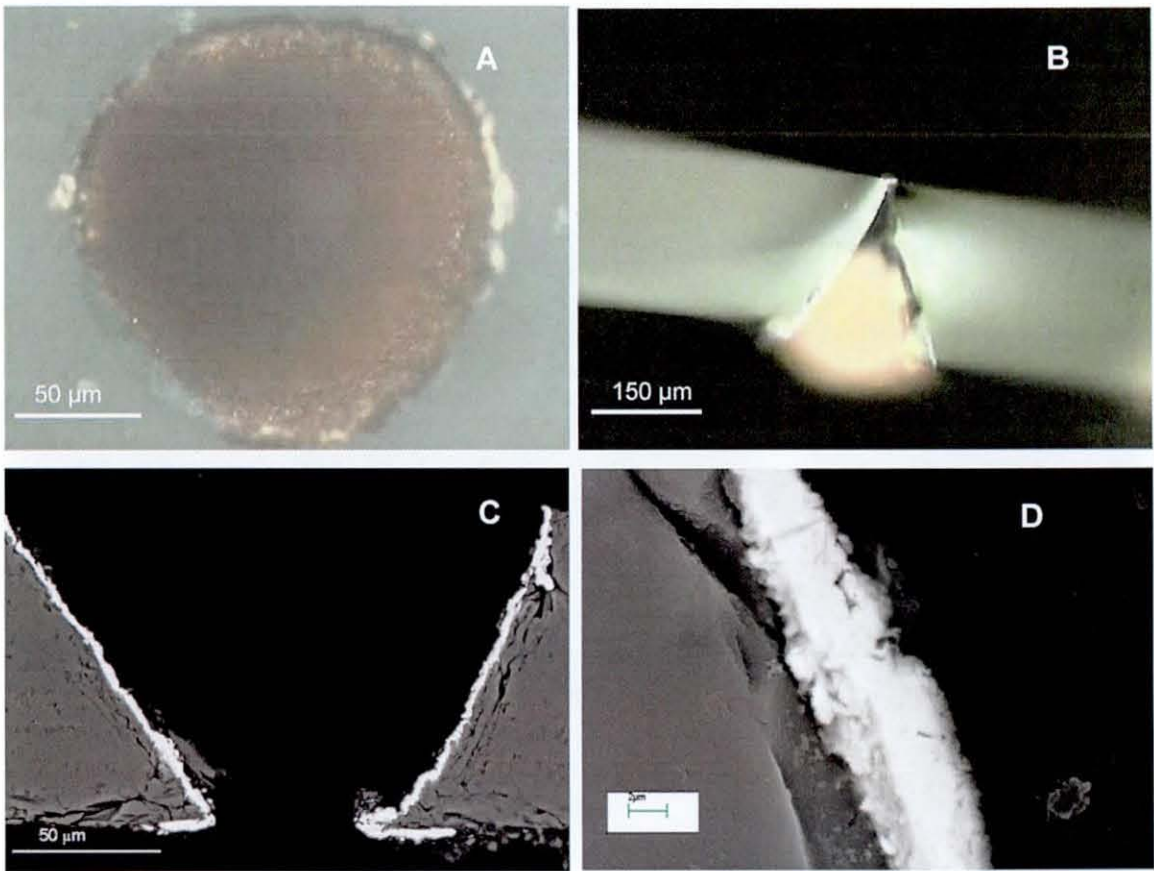
The Cu deposit thickness was varied by changing experimental parameters such as current density, plating time and work area. Table 7-3 lists some electroplated Cu deposit thicknesses on laser machined holes for which the hole diameters were about 150-170  $\mu\text{m}$ . As is well known the deposition thickness increases with increase of current density and electroplating time. With a higher current density ( $1.5\text{-}1.7 \text{ A/dm}^2$ ) applied, the maximum thickness achieved was only 2.4-4.3  $\mu\text{m}$  which is far from that needed to fully fill vias.

In addition to building up Cu on grooves, hole-filling is also important to complete the glass substrate. Therefore, investigation of the electroplating of Cu into the holes was carried out. Figure 7-9 shows view of a via metallised in the proposed way and shows the Cu coating of the via interior walls to a thickness of 3-5  $\mu\text{m}$ . The entry diameter was about 150  $\mu\text{m}$  and exit diameter is about 70-80  $\mu\text{m}$ .

**Table 7-3 Electroplated Cu thickness on laser machined holes**

	Electroplating time	Current density	Cu thickness
1	2 min	0.15 A/dm <sup>2</sup>	tiny
2	5 min	0.15 A/dm <sup>2</sup>	170 nm
3	10 min	0.15 A/dm <sup>2</sup>	340-650 nm
4	15 min	0.15 A/dm <sup>2</sup>	0.8-1.4 $\mu$ m
5	2 min	0.3 A/dm <sup>2</sup>	Less than 100 nm
6	5 min	0.3 A/dm <sup>2</sup>	260-440 nm
7	10 min	0.37 A/dm <sup>2</sup>	580-900 nm
8	15 min	0.3 A/dm <sup>2</sup>	1.0-1.7 $\mu$ m
9	2 min	1.5 A/dm <sup>2</sup>	400-530 nm
10	5 min	1.7 A/dm <sup>2</sup>	850-1000 nm
11	10 min	1.5 A/dm <sup>2</sup>	1.9-2.5 $\mu$ m
12	15 min	1.5 A/dm <sup>2</sup>	2.4-4.3 $\mu$ m

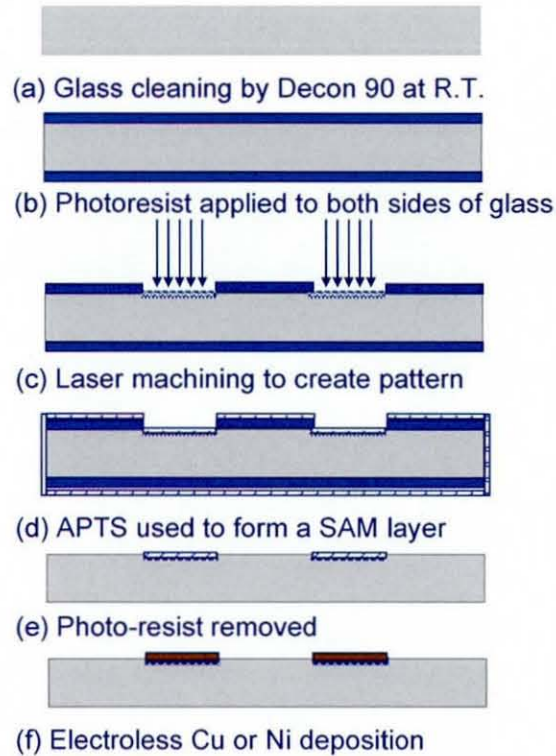
Compared with the image of electroless Cu in the vias, it was confirmed that the interior surface of the holes was covered with electroplated Cu, but for the electroplating conditions used, the hole was only partly filled. While this initially appeared successful, it was found that this process was limited in the thickness that could be deposited: as Cu was plated within the via, it was also plated onto the seed layer covering the smooth glass and, as described above, as the thickness increased this led to a reduction in adhesion to these smooth areas such that the coating eventually peeled off in the plating bath after only a short period of deposition. This highlights the need to find methods to improve the adhesion of the electroless coating to the smooth glass, or to use additional resist layers to restrict the areas to be electroplated.



**Figure 7-9 Optical microscope images (A,B) and SEM micrographs (C, D) of a via metallised with electroless and electroplated Cu**

### **7.4.3 Circuit pattern formation**

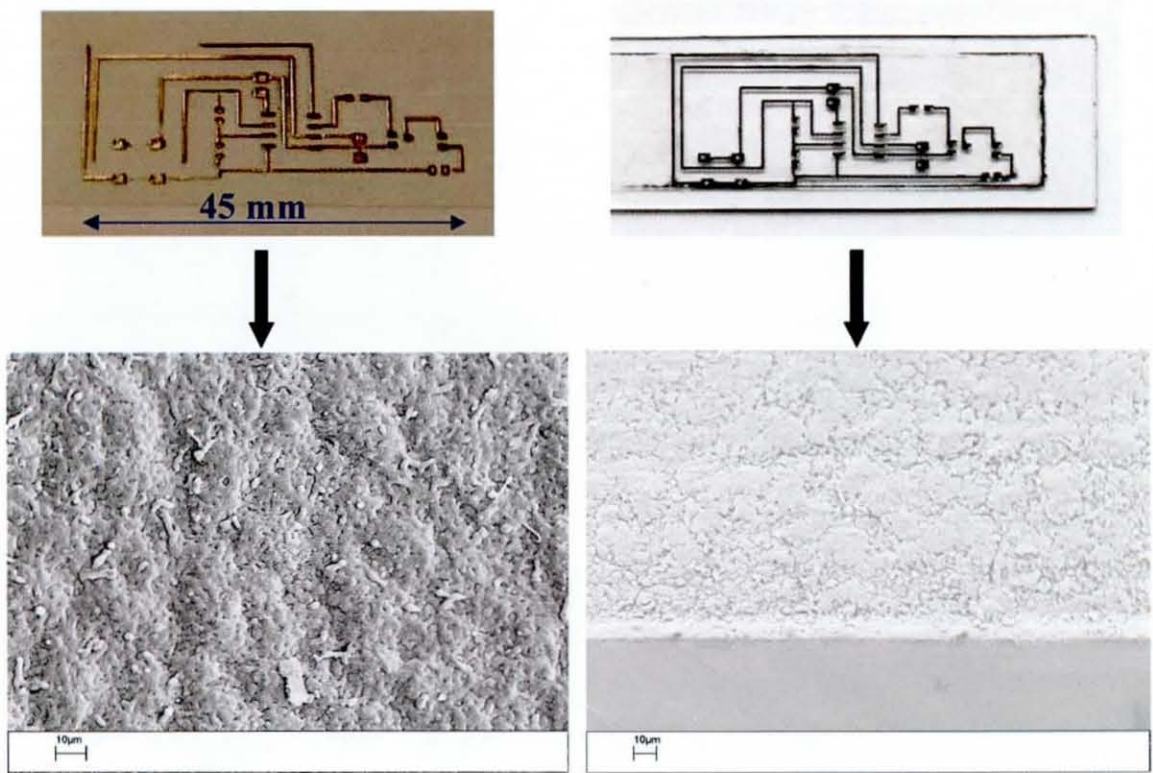
Combining the techniques described above, it was possible to prepare circuit patterns. The process of fabricating a Cu pattern on glass is shown in Figure 7-10. To begin with, the glass was initially laminated with a dry film photoresist layer (Ordyl ALPHA 940). This was then excimer laser machined to remove the photoresist and ablate the glass underneath to produce a pattern of tracks and pads. The sample was then prepared for metallisation by immersing it in the APTS solution – in this case the presence of the photoresist pattern enabled only the laser machined glass to be functionalised. After rinsing, the photoresist was stripped from the surface and then the entire sample was exposed to the catalyst solution. As only the laser machined areas of the surface had been activated with APTS the catalyst only adsorbed on these regions and was washed cleanly from the smooth glass. Subsequent electroless Cu or nickel plating was selectively deposited on the activated, laser machined areas and was well adhered due to the roughened nature of the tracks.



**Figure 7-10 Process flow diagram showing the fabrication of a Cu or NiP pattern**

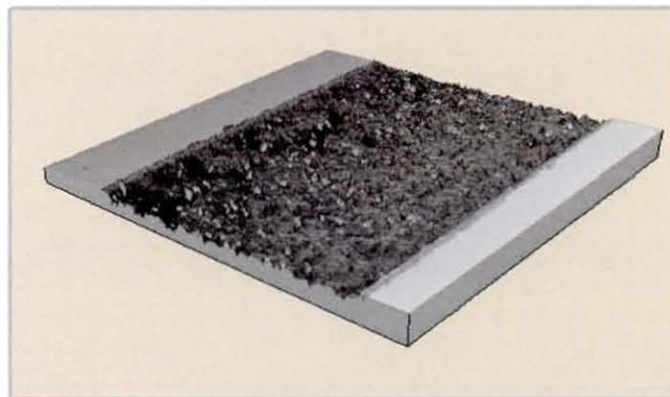
Most electroless processes were the same as those described in chapter 2. But some parameters were modified, the main one being to use  $5 \times 10^{-3}$  mol/l APTS solution in methanol (5%) and water (95%) instead of the usual mixture of methanol (95%) and water (5%). This was because the high concentration of methanol tended to remove the photoresist. After the APTS step, 100% methanol was used to remove the photoresist layer and then samples were immersed in DI water for 3 min followed by the pre-dip.

Figure 7-11 shows two large single layer patterns that were produced in this way and corresponding SEM images of two different coatings on the glass surface. The left side of the figure is electroless Cu coated (approx thickness of  $1.9 \mu\text{m}$ ) and the right side is electroless nickel coated (approx thickness of  $3.7 \mu\text{m}$ ). It is clearly seen that there are different surface morphologies. The Cu coating looks more uniform, and the top view of the nickel looks flat due to the thicker coating deposited.



**Figure 7-11** Circuit pattern created using proposed technique and surface morphology

Figure 7-12 presents 3D images of one of the tracks and shows clearly the difference in roughness between the track and the surrounding area. The track had a maximum depth of  $7.8\ \mu\text{m}$ . The  $R_a$  of the electroless Cu was approximately  $1.02\ \mu\text{m}$ . The thickness of the electroless Cu was around  $1.9\ \mu\text{m}$  and a small ridge could be seen at the edge of the track where the Cu was built up, indicating the selectivity of the process to the roughened area.



**Figure 7-12** Surface profile of electroless Cu deposited on grooves in glass

### **7.5 Conclusion**

The electroless Cu thickness on roughened grooves prepared using the excimer laser could be increased to at least 1.5  $\mu\text{m}$  with good adhesion. Based on the electroless Cu layer, electroplating Cu was applied to these surfaces and could be built up to a thickness of 8-10  $\mu\text{m}$  with strong adhesion, which meets the requirements for substrate manufacturing, for Cu pads and tracks. Combination of electroless deposition and laser machining enabled circuit patterns to be created.

---

## Chapter 8 Conclusion

---

In this chapter, summaries are drawn from the results and discussion presented in previous chapters, and potential further research highlighted in order to enable the realisation of glass substrates.

The contributions of this work to the electrical application are briefly stated here:

- Homogenous Cu and NiP films were deposited on glass by electroless plating, but the thickness was limited due to low plating rate and weak adhesion to the smooth glass. The electroless NiP deposition rate was almost 8 times higher than that of electroless Cu on the glass substrate. Thicker layers of Cu could be built up by further electroplating, although adhesion was still an issue.
- A SAM (self-assembled monolayer) of APTS was found to be essential to enable electroless plating of the glass, and the structure of the SAM is an important factor for determining the strength of adhesion between the glass and metal layer. One hour for APTS treatment was optimum, and it was found that extended immersion time in the silane solution did not improve the adhesion to the glass surface.
- The adhesion of the electroless coatings to glass were determined qualitatively using tape peel tests and more quantitatively using scratch tests. The effect of process times and conditions for electroless plating on adhesion were identified and it was found that with the optimised conditions, electroless Cu layers up to 160 nm and electroless nickel layers up to 700 nm could be deposited on smooth glass with good adhesion.
- The location of the failure between the metal coating and glass was revealed by XPS and SIMS and found to be between the catalyst and copper. SEM



micrographs further showed that there were many nano-scale voids on the delaminated copper layers. Further study of the PdSn catalyst structure enabled a model of the process to be developed and reasons for the weak adhesion proposed.

- The electroless Cu and NiP films were found to possess high internal stress that contributed to the adhesion of the coating to the glass. Nanoindentation tests revealed the hardness and elastic modulus of these thin films.
- The electroless Cu thickness on roughened grooves was increased to at least 1.5  $\mu\text{m}$  with good adhesion. For electroless NiP, it could be 3.7  $\mu\text{m}$ . Electroplating Cu was applied to electroless Cu deposited surfaces and the thickness on the roughened area could be built up to 8-10  $\mu\text{m}$  with good adhesion, which meets the requirements for substrate manufacturing, for Cu pads and tracks. Combination of electroless deposition and laser machining enabled circuit patterns to be created.

Further research work has been identified as a result of this study.

- Catalyst structure effects on conductive substrates: electroless deposition is also applied to a wide range of metal substrates, so this experiment could be used to further understand the Pd/Sn catalytic mechanism and its influence on electroless deposition.
- For the electrical applications, the solderability and reliability of the metallic layer on glass substrate needs to be investigated in more detail.
- In order to fulfil requirements for double layer or multilayer glass substrates, it is necessary to find methods to fill up the micro vias and further work using other materials such as conductive pastes should be investigated.

Overall, the research has thoroughly investigated the deposition of electroless coatings on glass and identified the process limits and reasons for poor adhesion to the smooth surface. Methods to improve adhesion have been investigated and combination of the electroless deposition with laser machining to roughen the surface and define patterns has been shown as a promising way forward. It is hoped that this work will lead to further development of glass substrates for future applications in high density electrical interconnect.

---

## References

1. Archambeault, B.R., *PCB design for real-world EMI control* 2002, Boston, Mass. ; London: Kluwer Academic Publishers.
2. Honma, H., *Advanced plating technology for electronic devices*. Electrochemistry, 2006. 74(1): p. 2-11.
3. Brown, W.D. and Ulrich, R.K., *Advanced electronic packaging*. 2005, Chichester: John Wiley.
4. Lunt, B.M., *Electronic physical design* 1st ed. 2004: Upper Saddle River, N.J. : Merrill.
5. Lau, J.H., *Flip chip technologies for high density interconnects*. 1995: McGraw-Hill.
6. Tong, H.-M., *Microelectronics packaging: present and future*. Materials Chemistry and Physics, 1995. 40(3): p. 147-161.
7. Reichl, H., Schubert, A., and Topper, M., *Reliability of flip chip and chip size packages*. Microelectronics Reliability. 40(8-10): p. 1243-1254.
8. Hwang, S.H., Cho, M.H., Kang, S.K., Lee, T.W., Park, H.H., and Rho, B.U., *Two-dimensional optical interconnection based on two-layered optical printed circuit board*. IEEE Photonics Technology Letters, 2007. 19(5-8): p. 411-413.
9. David, A.H., Karen Williams, Paul P. Conway, Fuad M. Khoshnaw, Cui, X., and Bhatt, D., *Challenges in the manufacture of glass substrates for High Density Interconnect*. Circuit World, 2007. 33(1): p. 22-30.
10. Tummala, R.R., Raj, P.M., Aggarwal, A., Mehrotra, G., Koh, S.W., Bansal, S., Tiong, T.T., Ong, C.K., Chew, J., Vaidyanathan, K., and Rao, V.S., *Copper interconnections for high performance and fine pitch flipchip digital applications and ultra-miniaturized RF module applications*. 56th Electronic Components & Technology Conference 2006, Vol 1 and 2, Proceedings, 2006: p. 102-111.
11. Bhatt, D., Williams, K., Hutt, D.A., and Conway, P.P., *Process optimisation and characterization of excimer laser drilling of microvias in glass*. 2007 9th Electronics Packaging Technology Conference, Vols 1 and 2, 2007: p. 196-201.

12. <http://www.engineeringtoolbox.com>.
13. <http://emtoolbox.nist.gov/Main/Main.asp>, *Web Site Home: Engineering Metrology Toolbox*.
14. Khan, N., Rao, V.S., Lim, S., We, H.S., Lee, V., Wu, Z.X., Rui, Y., Ebin, L., Chai, T.C., Kripesh, V., and Lau, J., *Development of 3D silicon module with TSV for system in packaging*. 58th Electronic Components & Technology Conference, Proceedings, 2008: p. 550-555.
15. Frohlich, H., *Theory of dielectrics : dielectric constant and dielectric loss*. 2nd ed. 1958: Clarendon.
16. Cui, X.Y., Bhatt, D., Hutt, D.A., Williams, K., and Conway, P.P. *Copper Deposition and Patterning for Glass Substrate Manufacture*. in *9th Electronics Packaging Technology Conference*. 10th -12th December 2007. Singapore
17. Bhatgadde, L.G., *A review of electroless plating techniques for electronics*. Transactions of the Metal Finishers Association of India, 1997. 6(3): p. 229-233.
18. Murarka, S.P., *Multilevel interconnections for ULSI and GSI era*. Materials Science and Engineering, 1997. R19: p. 87-151.
19. Aithal, R.K., Yenamandra, S., Gunasekaran, R.A., Coane, P., and Varahramyan, K., *Electroless copper deposition on silicon with titanium seed layer*. Materials Chemistry and Physics, 2006. 98(1): p. 95-102.
20. Cho, J.S.H., Kang, H.K., Wong, S.S., and Shachamdiamand, Y., *Electroless Cu for VLSI*. Mrs Bulletin, 1993. 18(6): p. 31-38.
21. Neal, A.W., *Printed circuit board*. 1983, New York: Wiley.
22. Shacham-Diamand, Y., Dubin, V., and Angyal, M., *Electroless copper deposition for ULSI*. Thin Solid Films, 1995. 262: p. 93-103.
23. Riedel, W., *Electroless nickel plating*. 1991: Finishing Publications.
24. Riedel, W., *Electroless nickel: introduction, fundamentals, limitations*. Galvanotechnik, 1990. 81(3): p. 842-844.
25. Tsai, T.K. and Chao, C.G., *The growth morphology and crystallinity of electroless NiP deposition on silicon*. Applied Surface Science, 2004. 233(1-4): p. 180-190.
26. Honma, H., Oyamada, K., and Koiwa, I., *Advanced plating technology for electronic devices*. Electrochemistry, 2006. 74(1): p. 2-11.

27. Agarwala, R.C., Agarwala, V., and Sharma, R., *Electroless Ni-P based nanocoating technology - A review*. Synthesis and Reactivity in Inorganic Metal-Organic and Nano-Metal Chemistry, 2006. 36(6): p. 493-515.
28. Krishnan, K.H., John, S., Srinivasan, K.N., Praveen, J., Ganesan, M., and Kavimani, P.M., *An overall aspect of electroless Ni-P depositions - A review article*. Metallurgical and Materials Transactions a-Physical Metallurgy and Materials Science, 2006. 37A(6): p. 1917-1926.
29. Seshan, K., *Handbook of thin-film deposition processes and techniques : principles, methods, equipment, and applications*. 2000, Park Ridge, N.J: Noyes Publications.
30. Smith, D.L., *Thin film deposition: principles and practice*. 1995, New York: McGraw-Hill.
31. Milton, O., *Material science of thin films*. 2001, London: Academic press.
32. Pulker, H.K., *Coating on glass*. 1984: Elsevier.
33. Mahan, J.E., *Physical Vapor Deposition of Thin Films* 2000: John Wiley & Sons.
34. Chan, K.Y., Tou, T.Y., and Teo, B.S., *Thickness dependence of the structural and electrical properties of copper films deposited by dc magnetron sputtering technique*. Microelectronics Journal, 2006. 37(7): p. 608-612.
35. Wu, Y.L., Hsieh, M.H., and Hwang, H.L., *Characterization of low temperature photo-assisted metal-organic chemical vapor deposited copper films using hexafluoroacetylacetonate copper(I) trimethylvinylsilane as precursor*. Thin Solid Films, 2005. 483(1-2): p. 10-15.
36. Kim, S., Choi, D.-J., Yoon, K.-R., Kim, K.-H., and Koh, S.-K., *Characteristics of chemical-vapor-deposited copper on the Cu-seeded TiN substrates*. Thin Solid Films, 1997. 311(1-2): p. 218-224.
37. Sricharoenchaikit, P., *Thin Metal-Film Formation Using Electroless Plating*. Journal of the Electrochemical Society, 1993. 140(7): p. 1917-1921.
38. Shacham-Diamand, Y. and Lopatin, S., *Integrated electroless metallization for ULSI*. Electrochimica Acta, 1999. 44(21-22): p. 3639-3649.
39. Dubin, V.M. and shacham-Diamand, Y., *Selective and Blanket Electroless Copper Deposition for Ultralarge Scale Integration*. J. Electrochem. Soc., 1997. 144: p. 898.

40. Schlesinger, M. and Paunovic, M., *Modern Electroplating*. 4th ed. 2000, Chichester: Wiley Interscience. 674.
41. Pienkos, T., Proszynski, A., Chocyk, D., Gladyszewski, L., and Gladyszewski, G., *Stress development during evaporation of Cu and Ag on silicon*. *Microelectronic Engineering*, 2003. 70(2-4): p. 442-446.
42. Boo, J.H., Jung, M.J., Park, H.K., Nam, K.H., and Han, J.G., *High-rate deposition of copper thin films using newly designed high-power magnetron sputtering source*. *Surface & Coatings Technology*, 2004. 188: p. 721-727.
43. Yoshida, A., Sato, H., Uchida, M., Wakahara, A., Hoshino, A., and Machida, H., *Copper film prepared with ArF excimer laser*. *Applied Surface Science*, 2001. 169: p. 493-495.
44. Lampeonnerud, C., Jansson, U., Harsta, A., and Carlsson, J.O., *Chemical Vapor-Deposition of Copper on Si(111) and SiO<sub>2</sub> Substrates*. *Journal of Crystal Growth*, 1992. 121(1-2): p. 223-234.
45. Lindroos, S., Ruuskanen, T., Ritala, M., and Leskel, M., *Growth of Cu thin films by the successive ionic layer adsorption and reaction (SILAR) method*. *Thin Solid Films*, 2004. 460(1-2): p. 36-40.
46. Xu, L., Liao, J., Huang, L., Ou, D., Guo, Z., Zhang, H., Ge, C., Gu, N., and Liu, J., *Surface-bound nanoparticles for initiating metal deposition*. *Thin Solid Films*, 2003. 434(1-2): p. 121-125.
47. Norkus, E., Vaskelis, A., and Pauliukaite, R., *Polarographic determination of formaldehyde according to the anodic oxidation wave in alkaline solutions*. *Electroanalysis*, 1999. 11(6): p. 447-449.
48. Mishra, K.G. and Paramguru, R.K., *Kinetics and mechanism of electroless copper deposition at moderate-to-high copper ion and low-to-moderate formaldehyde concentrations*. *Metallurgical and Materials Transactions B-Process Metallurgy and Materials Processing Science*, 1999. 30(2): p. 223-229.
49. Mishra, K.G. and Paramguru, R.K., *Kinetics and mechanism of electroless deposition of copper in a bath of low copper and high formaldehyde concentrations*. *Transactions of the Indian Institute of Metals*, 1997. 50(4): p. 241-247.
50. Vaskelis, A., Norkus, E., and Jaciauskiene, J., *Kinetics of electroless copper deposition using cobalt(II)-ethylenediamine complex compounds as reducing agents*. *Journal of Applied Electrochemistry*, 2002. 32(3): p. 297-303.

51. Li, J. and Kohl, P.A., *The Acceleration of Nonformaldehyde Electroless Copper Plating*. Journal of The Electrochemical Society, 2002. 149(12): p. C631-C636.
52. Ohno, I., Wakabayashi, O., and Haruyama, S., *Anodic-Oxidation of Reductants in Electroless Plating*. Journal of the Electrochemical Society, 1985. 132(10): p. 2323-2330.
53. Shacham-Diamand, Y., Inberg, A., Sverdlov, Y., Bogush, V., Croitoru, N., Moscovich, H., and Freeman, A., *Electroless processes for micro- and nanoelectronics*. Electrochimica Acta, 2003. 48(20-22): p. 2987-2996.
54. Mishra, K.G. and Paramguru, R.K., *Kinetics and mechanism of electroless deposition of copper*. Journal of the Electrochemical Society, 1996. 143(2): p. 510-516.
55. Matsuoka, M., Murai, J., and Iwakura, C., *Kinetics of Electroless Copper Plating and Mechanical-Properties of Deposits*. Journal of the Electrochemical Society, 1992. 139(9): p. 2466-2470.
56. Bindra, P., Light, D., and Rath, D., *Mechanisms of Electroless Metal Plating .1. Mixed Potential-Theory and the Interdependence of Partial Reactions*. Ibm Journal of Research and Development, 1984. 28(6): p. 668-678.
57. Hasan, N.M., dos Santos Filho, S.G., and Schwarzacher, W., *Growth and Density Time Dependence of Electroless Cu Films Deposited onto Au Using Cu-EDTA-HCHO Bath*. Electrochemical and Solid-State Letters, 2005. 8(10): p. C145-C147.
58. Zouhou, A., Vergens, H., and Duverneuil, P., *Determination of electroless kinetic: a QCM study*. Microelectronic Engineering, 2001. 56: p. 177-180.
59. Bindra, P. and Roldan, J., *Mechanisms of Electroless Metal Plating .2. Formaldehyde Oxidation*. Journal of the Electrochemical Society, 1985. 132(11): p. 2581-2589.
60. Wiese, H. and Weil, K.G., *Catalysis of Electroless Copper Deposition*. Journal of the Electrochemical Society, 1987. 134(8B): p. C437-C437.
61. Wanner, M., Wiese, H., and Weil, K.G., *Impedance Studies of Copper in Alkaline-Solutions, Especially During Electroless Plating*. Berichte Der Bunsen-Gesellschaft-Physical Chemistry Chemical Physics, 1988. 92(6): p. 736-745.

62. Wiese, H. and Weil, K.G., *On the Mechanism of Electroless Copper Deposition*. Berichte Der Bunsen-Gesellschaft-Physical Chemistry Chemical Physics, 1987. 91(6): p. 619-626.
63. Ramasubramanian, M., Popov, B.N., White, R.E., and Chen, K.S., *A mathematical model for electroless copper deposition on planar substrates*. Journal of the Electrochemical Society, 1999. 146(1): p. 111-116.
64. Donahue, F.M., Wong, K.L.M., and Bhalla, R., *Kinetics of Electroless Copper Plating: 4. Empirical Rate Law for HCOH-EDTA Baths*. Journal of the Electrochemical Society, 1980. 127(11): p. 2340-2342.
65. Schoenbe.Ln, *Use of Organic Additives to Stabilize and Enhance Deposition Rate of Electroless Copper Plating*. Journal of the Electrochemical Society, 1972. 119(11): p. 1491-&.
66. Weber, C.J., Pickering, H.W., and Weil, K.G., *The effect of additives on the microstructure of electroless copper*. Electrochemical Science and Technology of Copper, Proceedings, 2002. 2000(30): p. 130-138.
67. Weber, C.J., Pickering, H.W., and Weil, K.G., *STM study on the effect of cyanide during electroless copper deposition*. Proceedings of the Symposium on Fundamental Aspects of Electrochemical Deposition and Dissolution Including Modeling, 1998. 97(27): p. 51-59.
68. Lee, C.-L., Huang, Y.-C., and Kuo, L.-C., *Catalytic effect of Pd nanoparticles on electroless copper deposition*. J Solid State Electrochem, 2007. 11: p. 639-646.
69. Li, Z.F. and Ruckenstein, E., *Strong Adhesion and Smooth Conductive Surface via Graft Polymerization of Aniline on a Modified Glass Fiber Surface*. Journal of Colloid and Interface Science, 2002. 251(2): p. 343-349.
70. Ma, Z.B., Wang, J.H., Zhang, W.W., and He, A.H., *Investigation of nucleation and adhesion of diamond films on mirror-smooth glass substrates*. Surface and Coatings Technology, 2004. 184(2-3): p. 307-310.
71. Nicolas-Debarnot, D., Pascu, M., Vasile, C., and Poncin-Epaillard, F., *Influence of the polymer pre-treatment before its electroless metallization*. Surface and Coatings Technology, 2006. 200(14-15): p. 4257-4265.
72. Ahn, J.G., Kim, D.J., Lee, J.R., Chung, H.S., Kim, C.O., and Hai, H.T., *Improving the adhesion of electroless-nickel coating layer on diamond powder*. Surface and Coatings Technology, 2006. 201(6): p. 3793-3796.

73. Horn, H., Beil, S., Wesner, D.A., Weichenhain, R., and Kreutz, E.W., *Excimer laser pretreatment and metallization of polymers*. Nuclear Instruments and Methods in Physics Research Section B: Beam Interactions with Materials and Atoms, 1999. 151(1-4): p. 279-284.
74. Pan, C.T., *Selective electroless copper plating micro-coil assisted by 248 nm excimer laser*. Microelectronic Engineering, 2004. 71(3-4): p. 242-251.
75. Shafeev, G.A., *Laser-assisted activation of dielectrics for electroless metal plating*. Applied Physics A: Materials Science & Processing, 1998. 67(3): p. 303-311.
76. Comyn, J., *Adhesion science*. 1997, Cambridge: Royal Society of Chemistry.
77. Egitto, F. and Matienzo, L., *Plasma Modification of Polymer Surfaces for Adhesion Improvement*. IBM Journal of Research and Development, 1994. 38(4): p. 423-439.
78. Zhang, Q., Wu, M., and Zhao, W., *Electroless nickel plating on hollow glass microspheres*. Surface and Coatings Technology, 2005. 192(2-3): p. 213-219.
79. Hsu, H.H., Teng, C.W., Lin, S.J., and Yeh, J.W., *Sn/Pd catalyzed and electroless Cu deposition on TaN diffusion barrier layers*. Journal of the Electrochemical Society, 2002. 149(3): p. C143-C149.
80. Russell, S.W., Li, J., Strane, J.W., and Mayer, J.W., *The Effect of Copper on the Titanium-Silicon Dioxide Reaction and the Implications for Self-Encapsulating, Self-Adhering Metallization Lines*. Advanced Metallization and Processing for Semiconductor Devices and Circuits - Ii, 1992. 260: p. 763-768.
81. Chou, N.J., Dong, D.W., Kim, J., and Liu, A.C., *An XPS and TEM Study of Intrinsic Adhesion between Polyimide and Cr Films*. Journal of the Electrochemical Society, 1984. 131(10): p. 2335-2340.
82. Yoshiki, H., Alexandruk, V., Hashimoto, K., and Fujishima, A., *Electroless Copper Plating Using ZnO Thin Film Coated on a Glass Substrate*. J. Electrochem. Soc., 1994. 141(5): p. L56-L58.
83. Yoshiki, H., Hashimoto, K., and Fujishima, A., *Adhesion mechanism of electroless copper film formed on ceramic substrates using ZnO thin film as an intermediate layer*. Journal of the Electrochemical Society, 1998. 145(5): p. 1430-1434.



84. Charbonnier, M., Goepfert, Y., Romand, M., and Leonard, D., *Electroless plating of glass and silicon substrates through surface pretreatments involving plasma-polymerization and grafting processes*. Journal of Adhesion, 2004. 80(12): p. 1103-1130.
85. Ramanath, G.C., G. Ganesan, P. G. Guo, X. Ellis, A. V. Stukowski, M. Vijayamohanamb, K. , *Self-assembled monolayers as interfacial adhesion enhances and diffusion barriers for intergrated circuits*. Appl. Phys. Letters, 2003. 83(2): p. 383-385.
86. Li, Z.F. and Ruckenstein, E., *Conductive surface via graft polymerization of aniline on a modified glass surface*. Synthetic Metals, 2002. 129(1): p. 73-83.
87. Aw, K.C., Salim, N.T., Gao, W., and Li, Z., *Characterization of spin-on-glass very-low-k polymethylsiloxane with copper metallization*. Thin Solid Films, 2006. 504(1-2): p. 243-247.
88. Chen, Y.J., Kang, E.T., Neoh, K.G., and Huang, W., *Electroless metallization of glass surfaces functionalized by silanization and graft polymerization of aniline*. Langmuir, 2001. 17(23): p. 7425-7432.
89. Gao, J., Tang, F., and Ren, J., *Electroless nickel deposition on amino-functionalized silica spheres*. Surface and Coatings Technology, 2005. 200(7): p. 2249-2252.
90. Sawada, S., Masuda, Y., Zhu, P.X., and Koumoto, K., *Micropatterning of copper on a poly(ethylene terephthalate) substrate modified with a self-assembled monolayer*. Langmuir, 2006. 22: p. 332-337.
91. Gawrilov, G.G., *Chemical(electroless) nickel-plating*. 1979, Surrey: Portvullis Press.
92. *Joint Committee on Powder Diffraction Standards*, <http://openlibrary.org/a/OL1816966A/>.
93. Yu, M., Zhang, J., Li, D., Meng, Q., and Li, W., *Internal stress and adhesion of Cu film/Si prepared by both MEVVA and IBAD*. Surface and Coatings Technology, 2006. 201(3-4): p. 1243-1249.
94. Shiue, S.-T., Yang, C.-H., Chu, R.-S., and Yang, T.-J., *Effect of the coating thickness and roughness on the mechanical strength and thermally induced stress voids in nickel-coated optical fibers prepared by electroless plating method*. Thin Solid Films, 2005. 485(1-2): p. 169-175.

95. Donahue, F.M., Wong, K.L.M., and Bhalla, R., *Kinetics of Electroless Copper Plating: 2. Mixed Potential Analysis*. Plating, 1973. 60(43).
96. Goldie, W., *Electroless Copper Deposition*. Plating, 1965. 51: p. 1069-1074.
97. Dumesic, J., Koutsky, J.A., and Chapman, T.W., *Rate of Electroless Copper Deposition by Formaldehyde Reduction*. Journal of the Electrochemical Society, 1974. 121(11): p. 1405-1412.
98. Kanani, N., *Electroplating and electroless plating of copper & its alloys*. 2003: Finishing Publications.
99. Palasantzas, G., Koch, S.A., and De Hosson, J.T.M., *Growth front roughening of room-temperature deposited copper nanocluster films*. Applied Physics Letters, 2002. 81(6): p. 1089-1091.
100. Winau, D., Koch, R., Fuhrmann, A., and Rieder, K.H., *Film Growth-Studies with Intrinsic Stress Measurement - Polycrystalline and Epitaxial Ag, Cu, and Au Films on Mica(001)*. Journal of Applied Physics, 1991. 70(6): p. 3081-3087.
101. Abermann, R. and Koch, R., *In situ Study of Thin-Film Growth by Internal-Stress Measurement under Ultrahigh-Vacuum Conditions - Silver and Copper under the Influence of Oxygen*. Thin Solid Films, 1986. 142(1): p. 65-76.
102. Alfred Wagendristel and Wang, Y., *An introduction to physics and technology of thin films*. 1994, Singapore: World Scientific.
103. Dixit, P., Xu, L.H., Miao, J.M., and Pang, H.L., *Mechanical and microstructure characterization of high aspect ratio electroplated through wafer copper interconnects*. Electronics Packaging Technology Conference EPTC, 2006: p. 29.
104. Serre, C., Yaakoubi, N., Martine, S., Morante, J.R., Esteve, J., and Montserrat, J., *Electrochemical deposition of Cu and Ni/Cu multilayers in Si Microsystem Technologies*. Sensors and Actuators A 2005. 123-124: p. 633-639
105. Zhu, P.X., Masuda, Y., and Koumoto, K., *Seedless micropatterning of copper by electroless deposition on self-assembled monolayers*. Journal of Materials Chemistry, 2004. 14(6): p. 976-981.
106. Liu, H.D., Zhao, Y.P., Ramanath, G., Murarka, S.P., and Wang, G.C., *Thickness dependent electrical resistivity of ultrathin (<40 nm) Cu films*. Thin Solid Films, 2001. 384(1): p. 151-156.

107. Campbell, D.S., *The use of Thin Films in Physical Investigations*. 1966, New York: Academic Press. 299.
108. Lim, J.W., Mimura, K., and Isshiki, M., *Thickness dependence of resistivity for Cu films deposited by ion beam deposition*. Applied Surface Science, 2003. 217: p. 95-99.
109. Abrantes, L.M. and Correia, J.P., *On the Mechanism of Electroless Ni-P Plating*. Journal of the Electrochemical Society, 1994. 141(9): p. 2356-2360.
110. Balaraju, J.N., Narayanan, T., and Seshadri, S.K., *Electroless Ni-P composite coatings*. Journal of Applied Electrochemistry, 2003. 33(9): p. 807-816.
111. Lowenheim, F.A., *Electroplating*. 1978, New York: Mcraw-Hill.
112. Kar, K.K. and Sathiyamoorthy, D., *Influence of process parameters for coating of nickel-phosphorous on carbon fibers*. Journal of Materials Processing Technology, 2009. 209(6): p. 3022-3029.
113. Papini, M., *Chemical, Structural and Optical Characterization of Ni-P Chemical Conversion Coatings for Photothermal Absorption of Solar-Energy*. Solar Energy Materials, 1986. 13(4): p. 233-265.
114. Jiang, X.X. and Shen, W., *The fundamental and practice of electroless plating*. 2000, Beijing: National Defence Industry Press.
115. Chen, Z., Xu, X.D., Wong, C.C., and Mhaisalkar, S., *Effect of plating parameters on the intrinsic stress in electroless nickel plating*. Surface & Coatings Technology, 2003. 167(2-3): p. 170-176.
116. Mallory, G.O., *The Relationship between Stress and Adhesion of Electroless Nickel-Phosphorus Deposits on Zincated Aluminum*. Plating and Surface Finishing, 1985. 72(6): p. 86-95.
117. Matsuoka, M., Imanishi, S., and Hayashi, T., *Physical-Properties of Electroless Ni-P Alloy Deposits from a Pyrophosphate Bath*. Plating and Surface Finishing, 1989. 76(11): p. 54-58.
118. D.L.Smith, *Thin film deposition: principles and practice*. 1995, New York: McGraw-Hill.
119. Nacereddine, C., Layadi, A., Guittoum, A., Cherif, S.M., Chauveau, T., Billet, D., Youssef, J.B., Bourzami, A., and Bourahli, M.H., *Structural, electrical and magnetic properties of evaporated Ni/Cu and Ni/glass thin films*. Materials Science and Engineering: B, 2007. 136(2-3): p. 197-202.

120. Yoon, J.W., Park, J.H., Shur, C.C., and Jung, S.B., *Characteristic evaluation of electroless nickel-phosphorus deposits with different phosphorus contents*. *Microelectronic Engineering*, 2007. 84(11): p. 2552-2557.
121. Mittal, K.A., *Adhesion measurement of films and coatings*. 1995, Tokyo: VSP.
122. Ge, J., Turunen, M.P.K., and Kivilahti, J.K., *Surface modification and characterization of photodefinable epoxy/copper systems*. *Thin Solid Films*, 2003. 440(1-2): p. 198-207.
123. Barthel, E., Perriot, A., Dalmas, D., Sondergard, E., and Nael, P., *Surface mechanics of functional thin films on glass surfaces*. *Surface and Coatings Technology*, 2006. 200(22-23): p. 6181-6184.
124. Russell, S.W., Rafalski, S.A., Spreitzer, R.L., Li, J., Moinpour, M., Moghadam, F., and Alford, T.L., *Enhanced adhesion of copper to dielectrics via titanium and chromium additions and sacrificial reactions*. *Thin Solid Films*, 1995. 262(1-2): p. 154-167.
125. Shukla, S., Seal, S., Akesson, J., Oder, R., Carter, R., and Rahman, Z., *Study of mechanism of electroless copper coating of fly-ash cenosphere particles*. *Applied Surface Science*, 2001. 181(1-2): p. 35-50.
126. Carvalho, A., Geissler, M., Schmid, H., Michel, B., and Delamarche, E., *Self-assembled monolayers of eicosanethiol on palladium and their use in microcontact printing*. *Langmuir*, 2002. 18(6): p. 2406-2412.
127. Hozumi, A., Asakura, S., Fuwa, A., Shirahata, N., and Kameyama, T., *Preparation of a well-defined amino-terminated self-assembled monolayer and copper microlines on a polyimide substrate covered with an oxide nanoskin*. *Langmuir*, 2005. 21(18): p. 8234-8242.
128. Charbonnier, M., Alami, M., and Romand, M., *Plasma treatment process for palladium chemisorption onto polymers before electroless deposition*. *Journal of the Electrochemical Society*, 1996. 143(2): p. 472-480.
129. Vorobyova, T.N., *Adhesion interaction between electrolessly deposited copper film and polyimide*. *Journal of Adhesion Science and Technology*, 1997. 11(2): p. 167-182.
130. Herdt, G.C., Jung, D.R., and Czanderna, A.W., *Weak interactions between deposited metal overlayers and organic functional groups of self-assembled monolayers*. *Progress in Surface Science*. 50(1-4): p. 103-129.

131. Yoshino, M., Nonaka, Y., Sasano, J., Matsuda, I., Shacham-Diamand, Y., and Osaka, T., *All-wet fabrication process for ULSI interconnect technologies*. *Electrochimica Acta*, 2005. 51(5): p. 916-920.
132. Ruckenstein, E. and Li, Z.F., *Surface modification and functionalization through the self-assembled monolayer and graft polymerization*. *Advances in Colloid and Interface Science*, 2005. 113(1): p. 43-63.
133. Delamarche, E., Vichiconti, J., Hall, S.A., Geissler, M., Graham, W., Michel, B., and Nunes, R., *Electroless deposition of Cu on glass and patterning with microcontact printing*. *Langmuir*, 2003. 19(17): p. 6567-6569.
134. Chen, M.S., Brandow, S.L., Dulcey, C.S., Dressick, W.J., Taylor, G.N., Bohland, J.F., Georger, J.H.G., Pavelchek, E.K., and Calvert, J.M., *Channel-constrained electroless metal deposition on ligating self-assembled film surfaces*. *Journal of the Electrochemical Society*, 1999. 146(4): p. 1421-1430.
135. Arroyo-Hernandez, M., Martin-Palma, R.J., Perez-Rigueiro, J., Garcia-Ruiz, J.P., Garcia-Fierro, J.L., and Martinez-Duart, J.M., *Biofunctionalization of surfaces of nanostructured porous silicon*. *Materials Science and Engineering: C*, 2003. 23(6-8): p. 697-701.
136. Bull, S.J., G.-Berasetegui, E., and Sujeet, S., *An overview of the potential of quantitative coating adhesion measurement by scratch testing*, in *Tribology and Interface Engineering Series*. 2006, Elsevier. p. 136-165.
137. Lacombe, R., *Adhesion measurement methods*. 2005: Taylor & Francis.
138. Bull, S.J., G.-Berasetegui, E., and Sujeet, S., *Chapter 7 An overview of the potential of quantitative coating adhesion measurement by scratch testing*, in *Tribology and Interface Engineering Series*. 2006, Elsevier. p. 136-165.
139. Zhang, S., Sun, D., Fu, Y., and Du, H., *Toughness measurement of thin films: a critical review*. *Surface and Coatings Technology*, 2005. 198(1-3): p. 74-84.
140. Owens, D.K. and Wendt, R.C., *Estimation of Surface Free Energy of Polymers*. *Journal of Applied Polymer Science*, 1969. 13(8): p. 1741-&.
141. Arroyo-Hernandez, M., Perez-Rigueiro, J., Manso-Silvan, M., and Martinez Duart, J.M., *Bioactivity test for amine-based functionalized meso- and macro-porous silicon substrates*. *Materials Science and Engineering: C*, 2007. 27(5-8): p. 1211-1214.
142. *Standard Test Methods for Measuring Adhesion by Tape Test*. Vol. D3359-02 ASTM.

143. Dressick, W.J., Dulcey, C.S., Georger, J.H., and Calvert, J.M., *Photopatterning and Selective Electroless Metallization of Surface-Attached Ligands*. Chemistry of Materials, 1993. 5(2): p. 148-150.
144. Dressick, W.J., Dulcey, C.S., Haralson, Q.J., and Calvert, J.M., *Covalent Binding of Pd Catalyst to Ligating Self-Assembled Monolayer Films for Selective Electroless Metal Deposition*. J.Electrochem.Soc., 1994. 141: p. 210.
145. Kim, S., Jang, J.-H., Lee, J.-S., and Duquette, D.J., *Stress behavior of electrodeposited copper films as mechanical supporters for light emitting diodes*. Electrochimica Acta, 2007. 52(16): p. 5258-5265.
146. Riedel, S., Röber, J., Schulz, S.E., and Geßer, T., *Stress in copper films for interconnects*. Microelectronic Engineering, 1997. 37-38: p. 151-156.
147. Read, D.T. and Dally, J.W., *A New Method for Measuring the Strength and Ductility of Thin-Films*. Journal of Materials Research, 1993. 8(7): p. 1542-1549.
148. Shute, C.J. and Cohen, J.B., *Determination of Yielding and Debonding in Al-Cu Thin-Films from Residual-Stress Measurements Via Diffraction*. Journal of Materials Research, 1991. 6(5): p. 950-956.
149. Chuang, C.T., Chao, C.K., Chang, R.C., and Chu, K.Y., *Effects of internal stresses on the mechanical properties of deposition thin films*. Journal of Materials Processing Technology, 2008. 201(1-3): p. 770-774.
150. Mezin, A., *Coating internal stress measurement through the curvature method: A geometry-based criterion delimiting the relevance of Stoney's formula*. Surface and Coatings Technology, 2006. 200(18-19): p. 5259-5267.
151. Skomski, R., *Stress and strain in micro- and nano-structured interstitial magnets*. Scripta Metallurgica et Materialia, 1995. 33(10-11): p. 1831-1839.
152. Gunnars, J. and Alahelsten, A., *Thermal stresses in diamond coatings and their influence on coating wear and failure*. Surface & Coatings Technology, 1996. 80(3): p. 303-312.
153. Hanabusa, T., Kusaka, K., and Sakata, O., *Residual stress and thermal stress observation in thin copper films*. Thin Solid Films, 2004. 459(1-2): p. 245-248.
154. Gelfi, M., Bontempi, E., Roberti, R., Armelao, L., and Depero, L.E., *Residual stress analysis of thin films and coatings through XRD experiments*. Thin Solid Films, 2004. 450(1): p. 143-147.

155. Briscoe, B.J., Fiori, L., and Pelillo, E., *Nano-indentation of polymeric surfaces*. Journal of Physics D-Applied Physics, 1998. 31(19): p. 2395-2405.
156. Oliver, W.C. and Pharr, G.M., *Measurement of hardness and elastic modulus by instrumented indentation: Advances in understanding and refinements to methodology*. Journal of Materials Research, 2004. 19(1): p. 3-20.
157. Bull, S.J., *Failure Modes in Scratch Adhesion Testing*. Surface & Coatings Technology, 1991. 50(1): p. 25-32.
158. Prikryl, R., Cech, V., Kripal, L., and Vanek, J., *Adhesion of pp-VTES films to glass substrates and their durability in aqueous environments*. International Journal of Adhesion and Adhesives, 2005. 25(2): p. 121-125.
159. Ottermann, C.R., Bange, K., Braband, A., Heafke, H., and Gutmannsbauer, W., *MICROSCRATCH ANALYSIS OF THE ADHESION FAILURE FOR THIN OXIDE FILMS WITH DIFFERENT THICKNESS*. Material research society symposium proceeding, 1997. 436: p. 109.
160. Tsui, T.Y. and Pharr, G.M., *Substrate effects on nanoindentation mechanical property measurement of soft films on hard substrates*. Journal of Materials Research, 1999. 14(1): p. 292-301.
161. Ohring, M., *Materials science of thin films*. 2002, San Diego: Academic press. p764.
162. Okolo, B., Lamparter, P., Welzel, U., Wagner, T., and Mittemeijer, E.J., *The effect of deposition parameters and substrate surface condition on texture, morphology and stress in magnetron-sputter-deposited Cu thin films*. Thin Solid Films, 2005. 474(1-2): p. 50-63.
163. Choi, H.M., Choi, S.K., Anderson, O., and Bange, K., *Influence of film density on residual stress and resistivity for Cu thin films deposited by bias sputtering*. Thin Solid Films, 2000. 358(1-2): p. 202-205.
164. Beegan, D., Chowdhury, S., and Laugier, M.T., *Comparison between nanoindentation and scratch test hardness (scratch hardness) values of copper thin films on oxidised silicon substrates*. Surface & Coatings Technology, 2007. 201(12): p. 5804-5808.
165. Ma, D., Xu, K., He, J., and Lu, J., *Evaluation of the mechanical properties of thin metal films*. Surface and Coatings Technology, 1999. 116-119: p. 128-132.

166. Bai, M.W., Kato, K., Umehara, N., and Miyake, Y., *Nanoindentation and FEM study of the effect of internal stress on micro/nano mechanical property of thin CNx films*. Thin Solid Films, 2000. 377: p. 138-147.
167. Steinmann, P.A., Tardy, Y., and Hintermann, H.E., *Adhesion Testing by the Scratch Test Method - the Influence of Intrinsic and Extrinsic Parameters on the Critical Load*. Thin Solid Films, 1987. 154(1-2): p. 333-349.
168. Beake, B.D., Ogwu, A.A., and Wagner, T., *Influence of experimental factors and film thickness on the measured critical load in the nanoscratch test*. Materials Science and Engineering: A, 2006. 423(1-2): p. 70-73.
169. Javaid, R., Tanaka, D.A.P., Kawanami, H., and Suzuki, T.M., *Silica Capillary with Thin Metal (Pd and Pt) Inner Wall: Application to Continuous Decomposition of Hydrogen Peroxide*. Chemistry Letters, 2009. 38(2): p. 146-147.
170. Searson, P.C., Cammarata, R.C., and Chien, C.L., *Electrochemical Processing of Metallic Nanowire Arrays and Nanocomposites*. Journal of Electronic Materials, 1995. 24(8): p. 955-960.
171. O'Sullivan Eugene, J.M., *Characterization of PdSn catalysts for electroless metal deposition*. IBM J.RES.DEVELOP., 1988. 32(5): p. 591-595.
172. Vanderputten, A.M.T., Debakker, J.W.G., and Fokkink, L.G.J., *Electrochemistry of Colloidal Palladium - an Experimental-Study of Sol Formation and Electrocatalysis*. Journal of the Electrochemical Society, 1992. 139(12): p. 3475-3480.
173. Hidber, P.C., Helbig, W., Kim, E., and Whitesides, G.M., *Microcontact printing of palladium colloids: Micron-scale patterning by electroless deposition of copper*. Langmuir, 1996. 12(5): p. 1375-1380.
174. Svendsen, L.G., Osaka, T., and Sawai, H., *Behavior of Pd-Sn and Pd Catalysts for Electroless Plating on Different Substrates Investigated by Means of Rutherford Backscattering Spectroscopy*. Journal of the Electrochemical Society, 1983. 130(11): p. 2252-2255.
175. Osaka, T., Takamatsu, H., and Nihei, K., *A Study on Activation and Acceleration by Mixed PdCl<sub>2</sub>/SnCl<sub>2</sub> Catalysts for Electroless Metal Deposition*. J. Electrochem. Soc., 1980. 127: p. 1021.



176. Charbonnier, M. and Romand, M., *Tin-free electroless metallization of glass substrates using different PACVD surface treatment processes*. Surface and Coatings Technology, 2003. 162(1): p. 19-30.
177. Lai, C.H., Sung, Y.C., Lin, S.J., Chang, S.Y., and Yeh, J.W., *Atomic-scale observation on the nucleation and growth of displacement-activated palladium catalysts and electroless copper plating*. Electrochemical and Solid State Letters, 2005. 8(8): p. C114-C116.
178. Shukla, S., Seal, S., Rahaman, Z., and Scammon, K., *Electroless copper coating of cenospheres using silver nitrate activator*. Materials Letters, 2002. 57(1): p. 151-156.
179. Liu, Z.-C., He, Q.-G., Hou, P., Xiao, P.-F., He, N.-Y., and Lu, Z.-H., *Electroless plating of copper through successive pretreatment with silane and colloidal silver*. Colloids and Surfaces A: Physicochemical and Engineering Aspects, 2005. 257-258: p. 283-286.
180. Watanabe, S., Kimura, H., Sato, T., Shibata, H., Sakamoto, F., Azumi, R., Sakai, H., Abe, M., and Matsumoto, M., *Micro- and nanopatterned copper structures using directed self-assembly on templates fabricated from phase-separated mixed Langmuir-Blodgett films*. Langmuir, 2008. 24(16): p. 8735-8741.
181. CHARBONNIER, M., ALAMI, M., and ROMAND, M., *Electroless plating of polymers: XPS study of the initiation mechanisms*. JOURNAL OF APPLIED ELECTROCHEMISTRY 1998. 28: p. 449-453.
182. Froment, M., Queau, E., Martin, J.R., and Stremsoerfer, G., *Structural and Analytical Characteristics of Adsorbed Pd-Sn Colloids*. Journal of the Electrochemical Society, 1995. 142(10): p. 3373-3377.
183. Horkans, J., *Comparison of the Activity of PdSn Colloidal Catalysts with the Activity of Pure Metals for HCHO Oxidation - Enhancement of the Activity by Ionic Tin*. Journal of the Electrochemical Society, 1984. 131(8): p. 1853-1855.
184. Gui-xiang, W., Ning, L., Hui-li, H., and Yuan-chun, Y., *Process of direct copper plating on ABS plastics*. Applied Surface Science, 2006. 253(2): p. 480-484.
185. Kawasaki, J., Mihara, K., Kobayashi, T., and Honma, H., *Via-filling using electroplating for build-up printed circuit boards*. Electrochemical Technology Applications in Electronics Iii, 2000. 99(34): p. 51-55.

186. Kobayashi, T., Kawasaki, J., Mihara, K., and Honma, H., *Via-filling using electroplating for build-up PCBs*. *Electrochimica Acta*, 2001. 47(1-2): p. 85-89.
187. Josell, D., Baker, B., Witt, C., Wheeler, D., and Moffat, T.P., *Via filling by electrodeposition - Superconformal silver and copper and conformal nickel*. *Journal of the Electrochemical Society*, 2002. 149(12): p. C637-C641.
188. Kim, S.K., Josell, D., and Moffat, T.P., *Electrodeposition of Cu in the PEI-PEG-Cl-SPS additive system - Reduction of overfill bump formation during superfilling*. *Journal of the Electrochemical Society*, 2006. 153(9): p. C616-C622.
189. Lau, P.P., Wong, C.C., and Chan, L., *Improving electroless Cu via filling with optimized Pd activation*. *Applied Surface Science*, 2006. 253(5): p. 2357-2361.
190. Miura, S. and Honma, H., *Advanced copper electroplating for application of electronics*. *Surface & Coatings Technology*, 2003. 169: p. 91-95.
191. Hasegawa, M., Negishi, Y., Nakanishi, T., and Osaka, T., *Effects of additives on copper electrodeposition in submicrometer trenches*. *Journal of the Electrochemical Society*, 2005. 152(4): p. C221-C228.
192. Honma, H., *Plating technology for electronics packaging*. *Electrochimica Acta*, 2001. 47(1-2): p. 75-84.
193. Tseng, A.A., Chen, Y.T., Chad, C.L., Chad, C.L., Ma, K.J., and Chen, T.P., *Recent developments on microablation of glass materials using excimer lasers*. *Optics and Lasers in Engineering*, 2007. 45(10): p. 975-992.

